Experimental aeroelastic characterization based on integrated optical measurements

Mertens, C.

DOI
10.4233/uuid:366ceaef-39cf-4d87-9883-cf942b4971c4

Publication date
2023

Document Version
Final published version

Citation (APA)
Mertens, C. (2023). *Experimental aeroelastic characterization based on integrated optical measurements*. [Dissertation (TU Delft), Delft University of Technology]. https://doi.org/10.4233/uuid:366ceaef-39cf-4d87-9883-cf942b4971c4

EXPERIMENTAL AEROELASTIC CHARACTERIZATION BASED ON INTEGRATED OPTICAL MEASUREMENTS

EXPERIMENTAL AEROELASTIC CHARACTERIZATION BASED ON INTEGRATED OPTICAL MEASUREMENTS

Dissertation

for the purpose of obtaining the degree of doctor
at Delft University of Technology
by the authority of the Rector Magnificus prof.dr.ir. T.H.J.J. van der Hagen,
chair of the Board of Doctorates,
to be defended publicly on
Friday 30 June 2023 at 10:00 o'clock

by

Christoph MERTENS

Master of Science in Aerospace Engineering,
Delft University of Technology, The Netherlands
born in Hamburg, Germany.

This dissertation has been approved by the promotors.

Composition of the doctoral committee:

Rector Magnificus	chairperson
Dr.ir. B.W. van Oudheusden	Delft University of Technology, promotor
Dr. A. Sciacchitano	Delft University of Technology, copromotor
Dr. J. Sodja	Delft University of Technology, copromotor
Independent members:	
Prof.dr. A. Schröder	DLR, Germany
Prof.dr.ir. C.J. Simão Ferreira	Delft University of Technology
Prof.dr. G. Dimitriadis	University of Liège, Belgium
Prof.dr. L. David	University of Poitiers, France
Prof.dr. F. Scarano	Delft University of Technology, *reserve member*

This work has been carried out in the context of the HOMER (Holistic Optical Metrology for Aero-Elastic Research) project that has received funding from the European Union's Horizon 2020 research and innovation programme under grant agreement No 769237.

Keywords: experimental aeroelasticity, wind tunnel testing, flexible wing, gust response, unsteady aerodynamics, Lagrangian particle tracking, PIV

Printed by: Print Service Ede

Front & Back: created by the author with the DALL-E transformer language model

ISBN 978-94-6366-706-7

An electronic version of this dissertation is available at
http://repository.tudelft.nl.

CONTENTS

SUMMARY

This thesis presents a novel measurement approach for aeroelastic wind tunnel testing. The key novelty of this approach is the integrated measurement of aerodynamic and structural quantities using an optical technique. The considered approach consists of combined measurements of flow tracer particles and structural markers using a Lagrangian particle tracking system. Based on these measurements, the quantities of interest for the characterization of an aeroelastic interaction, which are the three forces in Collar's triangle (aerodynamic, elastic, and inertial), are determined.

Currently, measurements in aeroelastic wind tunnel tests are typically performed with individual sensors for each quantity of interest (pressure transducers, strain gauges, or accelerometers) that are installed inside the experimental model and/or with a force balance that measures the total loads acting on the model. The integrated optical measurement approach is an advancement over this existing measurement technology because it provides field measurements of the aeroelastic structural response and the unsteady flow field around the experimental model, based on which the aerodynamic and structural load distributions can be determined, without requiring an instrumentation of the model with sensors. This measurement approach is therefore an effective way to produce experimental reference data to support the development of novel aeroelastic prediction methods with a potential to accelerate the technological development process for innovations in aeronautics in the future.

The development and applications of the integrated optical measurement in this thesis are based on the measurements that were performed in three experimental campaigns in the wind tunnel. Each of the three experiments corresponds to one of the three main chapters of this thesis. All three experiments are performed on a large model scale, with dimensions on the order of 1 m, which is a scale of high practical relevance for aeroelastic wind tunnel testing. The complexity of the three experiments, in terms of the aeroelastic phenomena that are observed, is increased incrementally, from a rigid-body motion, over a linear aeroelastic test case, to a nonlinear aeroelastic test case. Based on the observations and findings of the previous experiments, the data analysis methods for the subsequent experiments are selected and applied.

The first measurements with the integrated approach are performed on the rigid-body motion of a pitching wing with an actuated flap. Based on these measurements, two novel implementations of a non-intrusive aeroelastic loads determination method using flow field data are applied and assessed in a comparison with the data measured with installed pressure transducers, achieving good results. Furthermore, the structural motion of the wing is characterized based on the position measurements of structural markers on the wing surface in terms of the harmonically varying angle of attack and flap deflection. These results are validated against the input signal for the actuators that produce the structural motion, showing a very good agreement.

The second wind tunnel experiment is performed to provide a proof of concept of an aeroelastic characterization based on measurements with the integrated optical approach. For this experiment, measurements of one spanwise section of a flexible wing that is subjected to unsteady inflow conditions, which are produced by a gust generator, are conducted. The unsteady aerodynamic loads are determined based on the flow field measurements and the inertial and elastic loads are determined based on the structural deformation measurements using a simplified structural model of the wing. The experimental approach is validated by using these results to quantify the equilibrium of forces in Collar's triangle, thereby serving as a proof of concept for the aeroelastic characterization based on integrated optical measurements.

The third and final experiment presented in this thesis is performed using a highly flexible wing geometry that is currently studied in the field of aeroelasticity as a benchmark case for the development of novel aeroelastic prediction methods. The aeroelastic response of the highly flexible wing to steady and periodic gust inflow conditions is analyzed with the integrated measurement approach. Two different angles of attack and two different gust excitation frequencies are studied, producing linear and nonlinear aeroelastic effects. Advancing the work performed in the context of the proof of concept study, the aeroelastic loads along the entire span of the highly flexible wing are characterized in this chapter. Furthermore, additional measurements of the structural and aerodynamic properties of the wing are conducted with a shape scan, a ground vibration test and infrared thermography measurements of the boundary layer on the suction side of the wing in the wind tunnel. The obtained results constitute a reference data set that is valuable for ongoing aeroelasticity research on improved nonlinear aeroelastic prediction methods.

Nomenclature

Latin Symbols

A	N	Aerodynamic force
c	m	Chord length
C	m	Circulation integration contour
C_ℓ	-	Section lift coefficient
C_m	-	Section pitching moment coefficient
C_p	-	Pressure coefficient
$\boldsymbol{C}$	-	Damping matrix
d	m	Distance
D'	$\mathrm{N\,m^{-1}}$	Drag per unit span
$\boldsymbol{D}$	-	Loading matrix
e	-	Euler's number
E	N	Elastic force
EI	$\mathrm{N\,m^{-2}}$	Flexural rigidity
f	-	Objective function
$\boldsymbol{f}$	-	Finite element external load vector
f_g	Hz	Gust frequency
f_p	Hz	Pitching frequency
f_s	Hz	Sampling frequency
$\boldsymbol{F}$	N	Force vector
i	-	Imaginary unit
I	N	Inertial force
$\boldsymbol{I}$	-	Identity matrix
k	-	Reduced frequency
$\boldsymbol{K}$	-	Stiffness matrix
L	N	Lift force
M'	N	Pitching moment per unit span
M	$\mathrm{N\,m}$	Bending moment in the beam
$\boldsymbol{M}$	-	Mass matrix
$\boldsymbol{n}$	m	Normal direction vector
N'	$\mathrm{N\,m^{-1}}$	Normal force per unit span

p	Pa	Pressure
$\boldsymbol{p}$	-	Position vector
P	-	Polynomial fit coefficients
q	$\mathrm{N\,m^{-1}}$	External loading on the beam
Q	N	Shear force in the beam
$\boldsymbol{r}$	-	Reference position vector
Re	-	Reynolds number
$\boldsymbol{R}$	-	Rotation matrix
s	m	Span width
$\boldsymbol{s}$	-	Circulation integration path vector
$\boldsymbol{S_C}$	$\mathrm{m^2}$	Control surface
t	s	Time
T	s	Period
u	$\mathrm{m\,s^{-1}}$	Flow velocity component in the x-direction
u_t	$\mathrm{m\,s^{-1}}$	Tangential velocity component
$\boldsymbol{u}$	$\mathrm{m\,s^{-1}}$	Flow velocity vector
v	$\mathrm{m\,s^{-1}}$	Flow velocity component in the y-direction
v_g	$\mathrm{m\,s^{-1}}$	Transversal gust velocity
U_∞	$\mathrm{m\,s^{-1}}$	Freestream velocity
V	$\mathrm{m\,s^{-1}}$	Flow velocity magnitude
$\boldsymbol{V_C}$	$\mathrm{m^3}$	Control volume
w	m	Out-of-plane beam deflection
x, y, z	m	Cartesian coordinates
x_{tr}	m	Boundary layer transition location
$\boldsymbol{x}$	m	Coordinate vector
X, Y, Z	m	Translations in coordinate transformation

GREEK SYMBOLS

α	°	Angle of attack
α_e	°	Effective angle of attack
α_g	°	Gust inflow angle
α_v	°	Inflow angle due to transversal wing motion
β	°	Gust vane angle
γ_b	$\mathrm{m\,s^{-1}}$	Bound vortex sheet strength
$\boldsymbol{\gamma}_{\mathrm{flux}}$	$\mathrm{m^2\,s^{-2}}$	Vorticity flux vector
Γ	$\mathrm{m^2\,s^{-1}}$	Circulation
Γ_p	$\mathrm{m^2\,s^{-1}}$	Partial bound circulation
Γ_b	$\mathrm{m^2\,s^{-1}}$	Total bound circulation
δ	°	Flap deflection angle
δ_{BL}	m	Boundary layer thickness
Δ	-	Difference
Δ_F	N	Force measurement residual
Δ_L	-	Lift coefficient residual
ε	-	Strain
ϵ	-	Measurement error

θ	°	Wing twist angle
μ	-	Sample mean
μ_d	$\mathrm{Pa\,s}$	Dynamic viscosity
μ_m	$\mathrm{kg\,m^{-1}}$	Mass per unit span
$\boldsymbol{\xi}$	-	Degrees of freedom vector
ρ	$\mathrm{kg\,m^{-3}}$	Fluid mass density
σ	-	Standard deviation
τ	Pa	Shear stress
ϕ	rad	Phase shift
Φ	$\mathrm{m^2\,s^{-1}}$	Velocity potential
φ, Θ, Ψ	°	Rotations in coordinate transformation
ω_g	$\mathrm{rad\,s^{-1}}$	Angular gust frequency
$\boldsymbol{\omega}$	$\mathrm{s^{-1}}$	Vorticity vector

SUPERSCRIPTS

$\tilde{x}$	Integration variable
$\dot{x}$	Temporal derivative
$\bar{x}$	Temporal average
$'$	Sectional force, per unit span

SUBSCRIPTS

aero	Aerodynamic
amp	Amplitude
B	Balance measurement
CP	Center of pressure
FA	Flow acceleration term
i	Sample index
lab	Laboratory coordinates
LE	Leading edge
m	Mean
ref	Reference
surf	Surface
TE	Trailing edge
tip	Wingtip
QS	Quasi-steady term
0	Steady term
∞	Freestream

ACRONYMS

CFD	Computational fluid dynamics
CVV	Coaxial volumetric velocimeter
DIC	Digital image correlation
DOF	Degree of freedom
eVTOL	Electrical vertical take-off and landing
FE	Finite element
FEM	Finite element model
FSI	Fluid-structure interaction
GVT	Ground vibration test
HFSB	Helium-filled soap bubbles
LCO	Limit-cycle oscillation
LED	Light-emitting diode
LPT	Lagrangian particle tracking
MAC	Modal assurance criterion
NASA	National Aeronautics and Space Administration
OJF	Open jet facility
PIV	Particle image velocimetry
PTV	Particle tracking velocimetry
RMS	Root mean square
STB	Shake-the-box
TRL	Technology readiness level

1

INTRODUCTION

Where it began
I can't begin to knowing
But then I know it's growing strong

Neil Diamond

1.1. MOTIVATION

In this day and age, the aeronautical industry is facing multiple major challenges. The civil aviation sector currently has a significant impact on the global climate, contributing around 3.5% to the anthropogenic global warming over the last decades (D. S. Lee et al., 2021), which makes the energy transition from fossil fuels to renewable energy sources an urgent requirement to adhere to the Paris Agreement (2015). The integration of novel propulsion systems with reduced emissions based on renewable energy challenges the status quo in aircraft design with new and innovative designs emerging in recent years, such as the *Flying V*[1], shown in Fig. 1.1(a). Additionally, significant advances in the more fundamental aeronautical disciplines, such as aerodynamics and structural engineering, are required to drastically improve the efficiency of future aircraft for sustaining the aspired economic growth of the sector (Grewe et al., 2021). At the same time, the energy transition has also sparked the innovation process of entirely new air transportation concepts, such as battery-powered, electrical vertical take-off and landing (eVTOL) aircraft that are intended for the regional or urban transport of passengers. As an example of a concept of such an aircraft, a photo of the eVTOL testbed LA-8 from NASA Langley (North et al., 2021) is shown in Fig. 1.1(b). Several companies are currently in the process of developing eVTOL aircraft for commercial use[2]. Considering all of these ongoing developments, it is thus evident that there is a high demand for technological innovation related to aeronautics in the coming decades, and a strong interest, politically as well as economically, to bring these concepts into practice in due time.

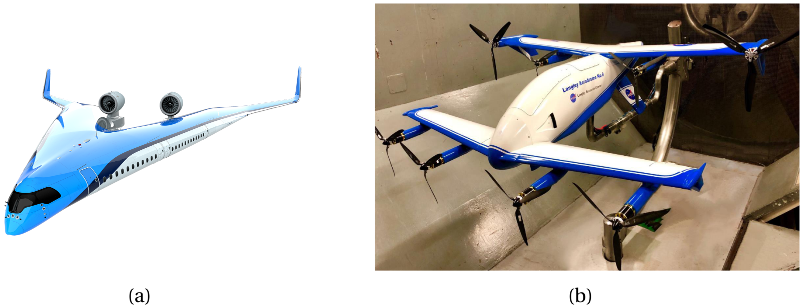
(a) (b)

Figure 1.1: (a) Flying V concept airplane (image credit: Edwin Wallet), (b) LA-8 eVTOL testbed in the wind tunnel at NASA Langley (from North et al., 2021)

A technical development process starts with the observation and assessment of the basic principles of a new technology in a fundamental research environment and ends with the implementation and use of the technology in the operational environment. These first and last steps, as well as the seven intermediate steps, are quantified in the Technology Readiness Level (TRL) scale, shown in Fig. 1.2, which was developed by NASA and has been adopted by the European research policy makers[3] (Héder, 2017).

---

[1] further information on the concept can be found at www.tudelft.nl/en/ae/flying-v (accessed 09.03.2023)

[2] a directory is administered by The Vertical Flight Society at https://evtol.news/aircraft (accessed 09.03.2023)

[3] the illustration is based on the TRLs as defined by the European Commission (accessed 09.03.2023)

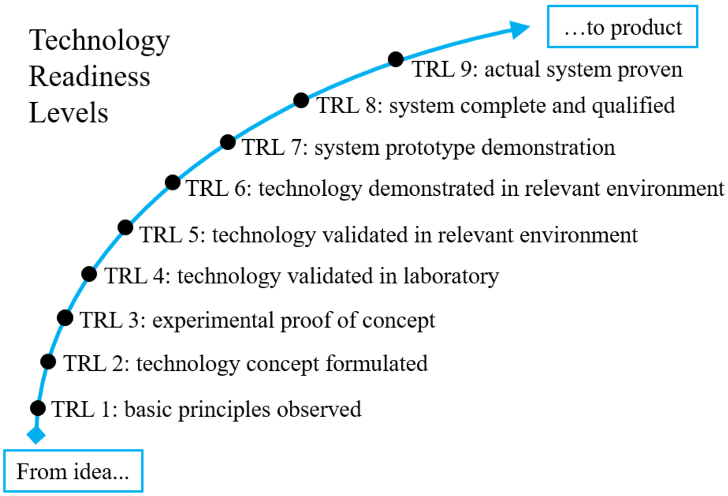

Figure 1.2: TRLs for the Horizon 2020 program of the European Commission (see Héder, 2017)

In the present day, the initial steps of technological development (TRL 1 and 2) are often performed with computer simulations because they allow a faster variation of the still relatively large parameter space. However, for all TRLs above 2, experimentation in the laboratory (TRL 3 and 4), which often includes wind tunnel experiments, or in a relevant operating environment (TRL 5 and above), is required to advance the technological development. Apart from that, experimental data is also required to validate the simulation tools that are used in the initial development phases. This is particularly relevant when the design problem is multidisciplinary and the accurate simulation of the operating environment is associated with a high computational cost, which is typical for aeronautical engineering technologies. In this case, the simulation tools that are used in the initial design phase usually employ simplified models to save computational efforts. This means that laboratory experiments, for example those performed in a wind tunnel, are a crucial step in the development process, where the computational predictions are validated before the first prototypes are built. A prominent example of a prototype that has experienced a catastrophic failure due to a complex physical phenomenon that had not been predicted accurately in the previous development steps is the Helios aircraft, shown in Fig. 1.3(a), which was developed by NASA and AeroVironment, Inc., in the 1990s. The Helios was a research prototype of a solar-electric aircraft with a wingspan of 75 m that completed several successful flights, including a flight setting an unofficial world record by flying at an altitude of nearly 30 km in 2001[4], before it crashed into the Pacific Ocean during a flight from Hawaii in June 2003 (see Fig. 1.3(b)). The reason for the crash of the Helios aircraft was a dynamic *aeroelastic* instability. The high flexibility of the wing structure had made the aircraft highly susceptible to small external disturbances, in this case a wind gust due to atmospheric turbulence, which ultimately led to the instability causing the structural failure (Noll et al., 2004).

---

[4] https://www.nasa.gov/centers/armstrong/news/FactSheets/FS-068-DFRC.html (accessed 09.03.2023)

(a) (b)

Figure 1.3: Photos of the Helios aircraft in flight (a) and after the crash (b), from Noll et al. (2004)

The field of study called *aeroelasticity*, to which this thesis contributes, is concerned with predicting and thus preventing the occurrence of such catastrophic instabilities on aircraft. Even though the Helios airplane was a research prototype, the use of more flexible lifting structures is a general trend in aviation, mainly driven by the desire to improve efficiency by saving structural weight. As a consequence, a variety of nonlinear aeroelastic effects (see, e.g., Dimitriadis, 2017), those related to the large wing deformations occurring on the Helios being one example, will need to be taken into account rigorously in the development process of future aircraft. The currently ongoing development of improved computational methods for predicting aeroelastic phenomena needs to be supplemented with reference data from wind tunnel experiments for validation. This reference data is challenging to obtain because it requires the simultaneous measurement of structural as well as fluid dynamic quantities. The complete characterization of an aeroelastic interaction involves the determination of both aerodynamic and structural loads. In this thesis, a novel approach to determining these quantities in wind tunnel experiments is introduced.

1.2. RESEARCH OBJECTIVE

Two of the most crucial engineering fields for designing and improving the efficiency of aircraft are structural mechanics and aerodynamics. At the intersection of these two fields lies the domain of aeroelasticity, covering the interaction of flexible structures with the aerodynamic forces acting on them. A popular concept to depict the domain of aeroelasticity and categorize the problems that occur within it is Collar's triangle of forces (see Fig. 1.4), introduced by A. R. Collar (1946). This schematic represents graphically the interaction of the three forces involved in aeroelasticity, which are the aerodynamic, elastic, and inertial forces. This domain can be divided into two subdomains, namely static aeroelasticity and dynamic aeroelasticity. The subdomain of static aeroelasticity is concerned with aeroelastic phenomena that are related to the structural response to (quasi-)steady aerodynamic forces. Dynamic aeroelastic phenomena comprise the interaction of unsteady aerodynamic forces with dynamic structural behavior, a typical example of a dynamic aeroelastic phenomenon is flutter, which is a growing oscillation of a structure that can lead to its destruction (as on the Helios aircraft).

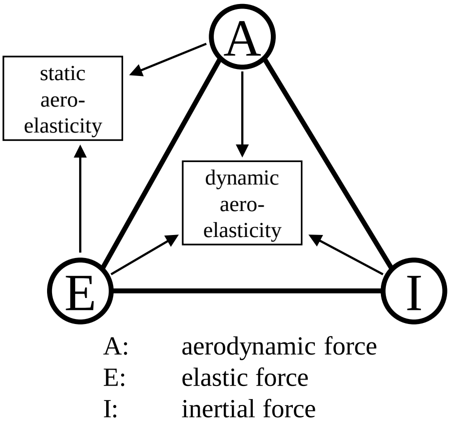

Figure 1.4: Illustration of Collar's triangle of forces

Analytical models exist to predict the occurrence of certain aeroelastic phenomena, such as flutter and divergence (Hodges & Pierce, 2011), but usually perform a linearization of the aeroelastic interaction before the analysis. However, in some situations, nonlinear aeroelastic effects are relevant, two examples of such effects are geometric nonlinearities of the structure due to large wing deformations and aerodynamic nonlinearities due to flow separation (Dimitriadis, 2017). In these situations, the accuracy of linear models may be insufficient, while the use of higher fidelity computational models (Bazilevs et al., 2013) is undesirable or practically impossible due to associated computational costs. A significant research effort is therefore being spent to develop novel cost-effective numerical analysis methods for predicting nonlinear aeroelastic phenomena that are not captured correctly by the conventional linear models (e.g., Bernhammer et al., 2017; Drachinsky and Raveh, 2020; Kantor et al., 2019).

The development of these methods is currently ongoing and requires reference data, typically obtained from wind tunnel experiments, for validation. However, the interaction of the three forces of different nature that comprise Collar's triangle makes the production of reference data in aeroelastic wind tunnel experiments challenging. A variety of techniques exists to measure the individual physical quantities that allow the determination of each of the forces locally (e.g., pressure transducers, accelerometers, strain gauges) or in an integral sense by mounting the wing to a load cell or a force balance; however their coordinated use results in complex setups and expensive experimental models. Additionally, installed sensors are invasive to the experimental model, potentially modifying its shape, mass, and stiffness distribution, which complicates the aeroelastic scaling of the wind tunnel model that is necessary to faithfully represent the behavior of full-scale aircraft (Bisplinghoff et al., 1955). The limited space that is available inside slender wing models furthermore typically results in a relatively low spatial resolution of the measurements. One example of an experimental model of an aircraft wing for aeroelastic wind tunnel testing that was instrumented with three different types of sensors is the model presented by Ballmann et al. (2008), shown in Fig. 1.5.

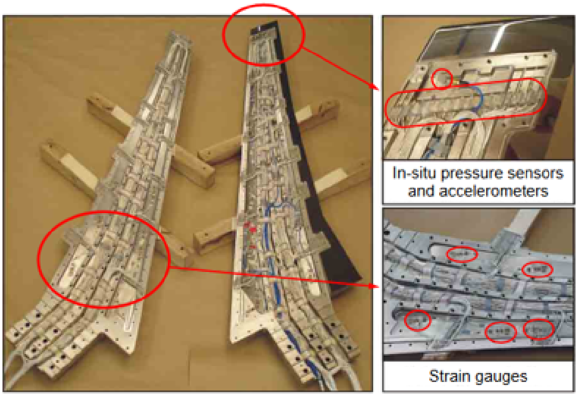

Figure 1.5: Heavily instrumented wing model for wind tunnel testing, from Ballmann et al. (2008)

The complex design of the interior structure of the wing model that is seen in Fig. 1.5, which is required to accommodate the sensors and their connections, significantly complicates the manufacturing and assembly of such a wing model, thus increasing the overall costs of the experiment. The amount of sensor instrumentation used in this particular study therefore remains an exception rather than the rule; most wind experimental models are less heavily instrumented. The review of Tang and Dowell (2016) provides an overview of several important experimental aeroelastic studies that include the analysis of the gust response, limit-cycle oscillations (LCOs), and other aeroelastic phenomena for different experimental models. One example is the seminal study of the aeroelastic behavior of a flexible high aspect ratio wing (Tang & Dowell, 2001), shown in Fig. 1.6(a). The results include the analysis of the frequency of a limit cycle oscillation that occurs over the range of flow velocities shown in Fig. 1.6(b). The experimental results were obtained by analyzing measurements with an accelerometer positioned inside the wing at mid-span and compared to a theoretical nonlinear prediction model.

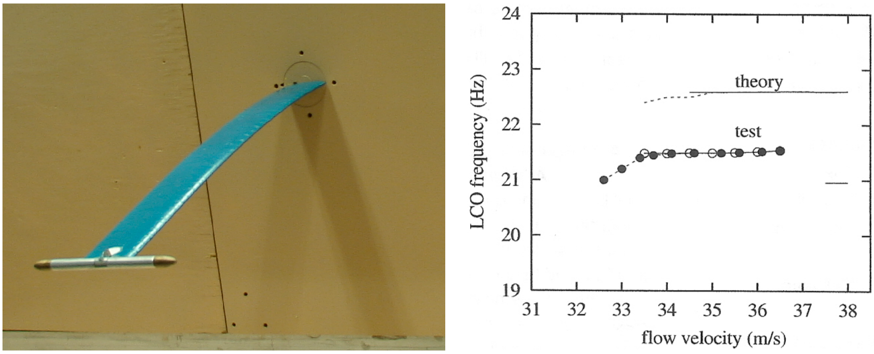

(a) wing model mounted in the wind tunnel (b) measured and theoretical LCO frequencies

Figure 1.6: Experimental study of a high aspect ratio wing, from Tang and Dowell (2001, 2016)

The experimental aeroelastic research conducted in the past decades, including the example shown in Fig. 1.6, thus typically produced measurement data that was limited to only a few discrete parameters, such as the wingtip deflection or the frequency of the dynamic motion of oscillating wings. Many important insights were generated based on those reference data sets in the past, but nevertheless, it is obvious that a larger amount of measurement data, potentially quantifying multiple parameters (structural and aerodynamic) simultaneously, could provide deeper insights into an aeroelastic interaction.

Modern optical measurement techniques, which provide non-intrusive field measurements, are a viable approach to overcoming some of the most significant limitations associated with the use of installed sensors. Firstly, the experimental model does not need to be instrumented with sensors for conducting these measurements, and secondly, the spatial resolution of the measurements is not limited by the model size but by the camera sensor. Examples of modern optical measurement techniques are particle image velocimetry (PIV, Raffel et al., 2018) and pressure-sensitive paint (PSP, T. Liu et al., 2005) for aerodynamic measurements, and photogrammetry (T. Liu et al., 2012) and digital image correlation (DIC, Pan, 2018) for structural measurements. On the other hand, a drawback of these optical techniques is that the determination of the quantities of interest, i.e., the aeroelastic forces, from the measured quantities, which are for example structural displacements or the flow velocity, is often not trivial. The topic of load determination based on optical measurement data has therefore been subject to considerable research efforts in recent years (Rival & van Oudheusden, 2017; van Oudheusden, 2013). Aside from this complication, a further issue with performing aeroelastic wind tunnel tests using optical techniques is that to perform simultaneous structural and aerodynamic measurements, two optical measurement techniques have to be used at the same time, which adds to the complexity of the experimental setups. So far, only a few, relatively recent studies found their way into the published literature that have followed the approach of combining optical techniques in a wind tunnel experiment to study aeroelastic phenomena. Among these is the study of Marimon Giovannetti et al. (2017), shown in Fig. 1.7, where PIV and DIC were used to simultaneously determine the deformation of a flexible wing and the resulting unsteady position of the wingtip vortex.

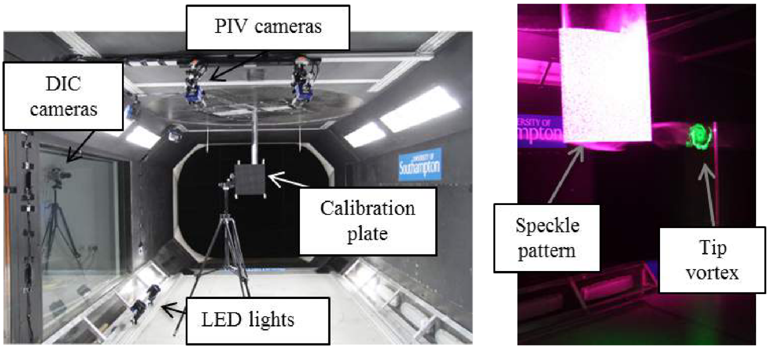

(a) calibration in the test section (b) combined measurement

Figure 1.7: PIV/DIC experiment at the University of Southampton, from Marimon Giovannetti (2017)

Similar to the study of Marimon Giovannetti et al. (2017), the deformation and aerodynamic loads on a flexible plate were investigated by Zhang et al. (2019) using DIC and PIV. A combination of PSP and a photogrammetry technique was used by Imai et al. (2022) to study transonic wing flutter while D'Aguanno et al. (2023) have used DIC and PIV to investigate shock-induced panel flutter. These existing studies indicate the capabilities of optical measurement techniques for the characterization of aeroelastic phenomena, but they do not overcome the complication of the coordinated use of several measurement and data processing systems. The objective of this work is to present a novel experimental aeroelastic characterization approach that facilitates a more efficient generation of experimental reference data from aeroelastic wind tunnel tests. Given the shortcomings and limitations of the existing experimental approaches, the following research objective can be formulated:

"Develop and prove the feasibility in wind tunnel testing of an experimental aeroelastic characterization approach that provides aerodynamic and structural loads based on integrated optical measurements using a single data acquisition system."

The outline of an approach that fulfills this research objective is illustrated in Fig. 1.8. The novelty of this approach is the full integration of the aerodynamic and structural measurements using only one system, which simplifies the aeroelastic measurements in comparison to the currently existing approaches that combine different systems. These integrated measurements are then processed into separate aerodynamic and structural data sets and the acting loads are determined to perform an aeroelastic characterization by quantification of the three forces in Collar's triangle. A particular challenge associated with the research objective lies in the proof of the feasibility of the approach for aeroelastic wind tunnel tests. These are frequently performed on relatively large model scales, with model dimensions on the order of meters, which complicates the optical measurements. Furthermore, many important aeroelastic phenomena, such as flutter, LCOs, gust response, or aeroservoelastic phenomena, involving the actuation of control surfaces, are inherently unsteady, thereby complicating the realization of the wind tunnel experiment and the optical measurements.

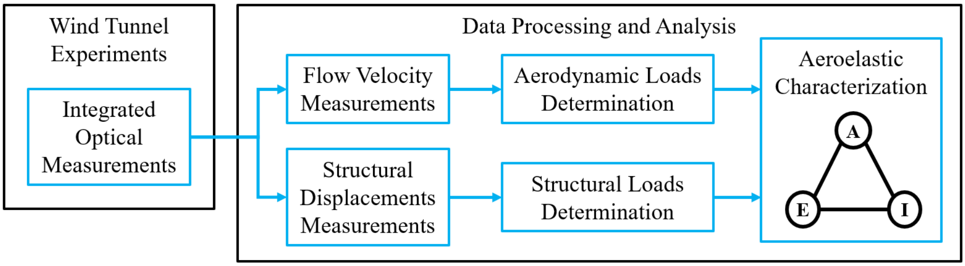

Figure 1.8: Schematic of the integrated measurement approach employed in this thesis

The thesis is structured as follows. In the following Chapter 2, the existing techniques to perform an aerodynamic and structural characterization using optical measurements are reviewed. This includes the description of the measurement principle as well as a discussion on the determination of the aerodynamic or structural loads based on the measurements. Furthermore, the suitability of the existing optical measurement techniques to be used in a novel integrated approach that fulfills the research objective is assessed and the implementation of an aeroelastic characterization in an experimental framework is described. In Chapter 3, the novel integrated aerodynamic and structural measurement approach is developed and demonstrated based on a wind tunnel test of a pitching wing with a movable trailing edge flap. In the following Chapter 4, the proof of concept of an aeroelastic characterization using the integrated measurement approach is delivered by determining the three forces in Collar's triangle on a flexible wing experimentally. In Chapter 5, the suitability of the approach for contributing to ongoing experimental aeroelasticity research is demonstrated by analyzing the gust response of a highly flexible benchmark wing model in a wind tunnel experiment. This experiment provides reference data for which there is a current demand in the field. In the final Chapter 6, conclusions are drawn and an outlook on future directions of research is provided. This outlook entails suggested improvements to the measurement approach as well as a discussion about future applications.

2

BACKGROUND

This chapter reviews the state-of-the-art in experimental methods to determine the aeroelastic loads based on optical measurements performed in the wind tunnel. An overview of the existing techniques for aerodynamic and structural measurements is given and these approaches are assessed with respect to their suitability to be used in an integrated optical measurement approach for the characterization of the aeroelastic loads. In an aeroelastic interaction, the relevant loads are the three components in Collar's Triangle, which are the aerodynamic, inertial, and elastic forces. For both aerodynamic and structural measurements, the determination of these loads involves dedicated post-processing procedures, using appropriate physical models to relate the obtained measurement data to the acting forces. Based on these experimentally determined loads, an aeroelastic characterization can be implemented.

The structure of this chapter follows the outline of the integrated measurement approach shown in Fig. 1.8. The first section, Sec. 2.1, covers the acquisition of the optical measurements in an aeroelastic wind tunnel experiment. Here, the existing aerodynamic and structural measurement techniques are first discussed separately, and subsequently assessed based on their suitability to be combined in an integrated optical approach. The outcome of this evaluation is the design of the integrated measurement approach that is developed and applied in the following chapters of this thesis. The products of the selected approach are measurements of the flow field and the structural displacements. To perform an aeroelastic characterization based on these measurements, the aerodynamic and structural loads need to be determined using physical models. The existing methods for the aerodynamic and structural loads determination are reviewed in the second section of this chapter, Sec. 2.2. In the final section, Sec. 2.3, two methods for the implementation of an aeroelastic characterization in the experimental framework are presented.

2.1. OPTICAL MEASUREMENT TECHNIQUES FOR EXPERIMENTAL AEROELASTICITY

In this section, the state-of-the-art in optical measurement technology that can be used for the characterization of aeroelastic loads is reviewed. Optical measurement techniques can be generally categorized as either field or point techniques, where field techniques measure incoherent (white) light with digital cameras, while point techniques measure coherent (laser) light with specific photosensors. Considering the research objective of this thesis, which requires the integrated measurement of aerodynamic and structural quantities, this section is exclusively focused on field techniques because they provide a possibility for this by acquiring structural and aerodynamic data in one image, whereas point measurement techniques, per definition, only measure one quantity at one specific location. For the aerodynamic measurements, two different field measurement approaches are discussed, either measuring the flow field or the surface pressure. For the structural measurements, different implementations of photogrammetric surface detection techniques are discussed. For integrating aerodynamic and structural measurements, existing work has been focused on combining surface pressure measurements with structural deformation measurements. Based on the discussion at the end of this section, combining flow field measurements with a particle tracking approach and structural displacement measurements with a point tracking approach emerges as a more appealing option because these measurements can be performed using only one measurement and data processing system.

2.1.1. AERODYNAMIC MEASUREMENT TECHNIQUES

Two different experimental approaches to aerodynamic measurements using optical techniques are reviewed in this section. The first approach is flow field-based, where optical measurements of the flow field are conducted and the loads are determined in a later data processing stage using physical relations between the loads and the flow velocity. The second method is the surface-based approach, where the pressure on the surface of the object under investigation is measured using pressure-sensitive paint. The flow field measurements have the advantage that they provide a direct and quantitative representation of the flow, in contrast to the surface pressure measurements that only quantify the imprint of the flow on the object. The pressure-sensitive paint measurements, on the other hand, have the advantage of providing a measured quantity that is more closely related to the aerodynamic loads, which reduces the post-processing efforts related to the load determination.

FLOW FIELD MEASUREMENTS

The most frequently used technique for measuring the flow field in wind tunnel tests is particle image velocimetry (PIV). A schematic of the experimental setup for a PIV experiment is shown in Fig. 2.1 and the measurement principle is discussed in the following. Based on the description of the principle of PIV by Raffel et al. (2018), the required equipment for performing a PIV experiment can be divided into hardware and software components. The hardware elements that are needed in a PIV experiment are the seeding of the flow with tracer particles, light sources for illuminating the particles, cameras for recording the optical measurements, and a timing system for the coordinated use of the light sources with the cameras. Using this equipment, a sequence of images of the illuminated tracer particles in the flow is acquired and subsequently used to determine the flow velocity field from the relative displacement of the particles between consecutive images. For this process, the software that is used for the analysis of the image data must consist of three components, which are the calibration between the particle position in the wind tunnel and the optical sensor, the evaluation of the flow velocity from the series of particle images, and the post-processing of the obtained result for removing invalid measurements and extracting the quantities of interest.

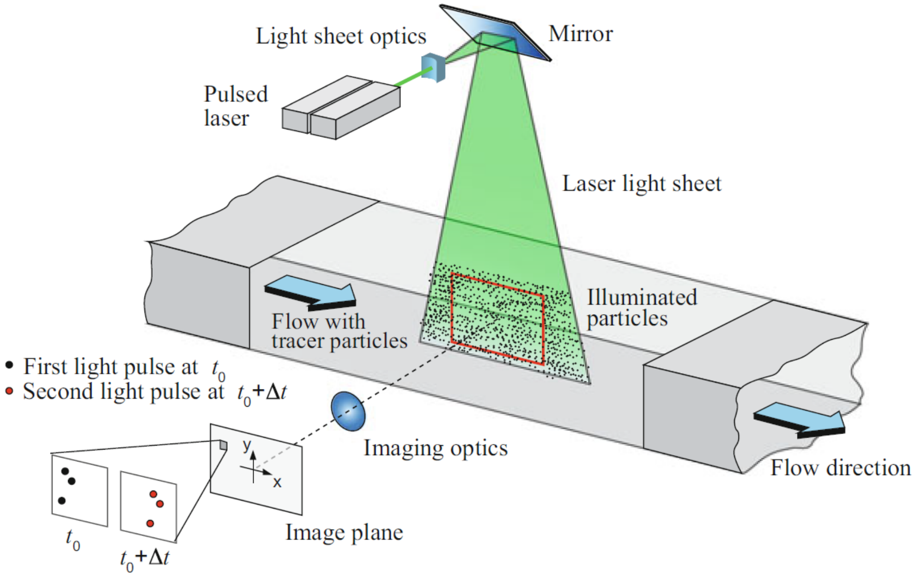

Figure 2.1: Schematic of a PIV experiment, from Raffel et al. (2018)

Since its introduction into the field in the 1980s, the PIV technique has consistently gained popularity and has undergone significant developments over the last decades, which can be reviewed in detail in the relevant textbooks (Adrian & Westerweel, 2011; Raffel et al., 2018) and review papers (for example Adrian, 1991, 2005; Westerweel et al., 2013). The advancements in two aspects of the measurement approach are particularly relevant for this thesis; namely, the increasing amount of physical information that is evaluated based on the particle images and the increasing scale of the measurement volume. Both aspects are discussed in the following.

The experimental setup in Fig. 2.1 represents a relatively simple PIV setup, where a single camera is acquiring images of particles in a light sheet. This means that information about the two velocity components can be evaluated in a measurement plane (planar PIV). Over the years, the addition of multiple cameras and the thickening of the light sheet first facilitated measurements of the third (out-of-plane) velocity component (stereoscopic PIV, Prasad, 2000) and later also volumetric velocimetry measurements with tomographic PIV (Elsinga et al., 2006), using typically four cameras that acquire images of the same area in the flow field from different angles. One commonality of all these approaches is that the flow velocity is evaluated from clusters of particles using spatial cross-correlations. A different evaluation approach for the particle images, which can reveal more detailed information about the flow, is particle tracking velocimetry (PTV). With this technique, the velocity of the individual particles in the flow is evaluated. This means that PTV is naturally a three-dimensional flow measurement technique. The PTV technique has been practiced in the field for more than 30 years (Nishino et al., 1989), but problems with the computational efficiency of the particle reconstruction algorithms and the relatively low achievable particle concentration have limited the usability of this technique. Those problems have traditionally been treated separately, as it is apparent for example from the two publications of Maas et al. (1993) and Malik et al. (1993). As a result of a lack of progress on both of these problems, tomographic PIV has been the more widely used volumetric measurement technique since the years after its introduction (Scarano, 2013).

A breakthrough in volumetric flow velocity measurement was achieved in this respect with the introduction of the Shake-The-Box (STB) algorithm by Schanz et al. (2016). The STB algorithm is a Lagrangian particle tracking (LPT) algorithm, which implies that a particle is tracked for several time steps, which allows for a more accurate determination of the particle position and velocity, at a higher particle density. In addition, it facilitates the experimental determination of the rate of change in velocity of a particle along its path, i.e., the Lagrangian acceleration (Schröder & Schanz, 2023). The novelty of the STB algorithm is the integration of the particle position reconstruction, using the iterative particle reconstruction algorithm of Wieneke (2012), in the particle tracking step of the image data analysis procedure, as illustrated in Fig. 2.2. The key step here is the prediction of the particle positions in the image based on the information of the particle tracks from the previous time steps. The true particle position is then found by “shaking” (iteratively varying) the predicted particle positions in space until the residual image is minimized. This approach thus uses the already available information on the particle dynamics to improve the efficiency of the LPT algorithm. What remains in the residual image are only the new particles that have entered the measured volume. Their position is determined with a triangulation approach and then the new tracks can be built, which are used in the predictions of the following time step. With this efficient algorithm, particle tracking at high particle densities is possible with a computational effort that is an order of magnitude smaller than tomographic PIV algorithms. On the other hand, the measurement principle of LPT requires the use of time-resolved data acquisition with high-speed cameras (frame rates on the order of kHz).

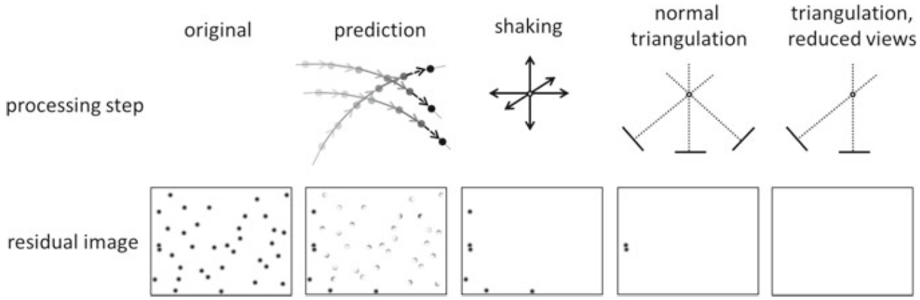

Figure 2.2: Image data analysis procedure of the STB algorithm, from Schanz et al. (2016)

The efficiency of the STB algorithm at high particle densities makes it suitable for applications in large measurement volumes. The need for flow velocity measurements in larger volumes arises because in many scenarios the experimental models cannot be downscaled arbitrarily, as the relevant similarity parameters have to be considered. This is particularly relevant for aeroelastic experiments, where both the aerodynamic and structural parameters have to be scaled. Many aeroelastic experiments are therefore conducted in relatively large wind tunnel facilities, with model scales on the order of meters. However, to conduct optical flow field measurements at this scale, not only the software must be suitable but also the hardware components (tracer particles, illumination, and cameras/imaging system). An important enabling development in this respect is the use of helium-filled soap bubbles (HFSB) as flow tracer particles (Bosbach et al., 2009). The HSFB have a diameter of around 0.5 mm, are neutrally buoyant, and scatter an order of 10^4 times more light than conventional micron-sized tracer particles for PIV (Scarano et al., 2015). The use of aerodynamically shaped seeding rakes producing a seeded stream tube makes HFSB usable in large-scale subsonic wind tunnel facilities (Caridi et al., 2016). Current designs of such seeding rakes cover a cross-sectional area of several square meters with several hundred bubble-producing nozzles, operating at a production rate of around 20,000 bubbles per second (Engler Faleiros, 2021; Engler Faleiros et al., 2019). The availability of HFSB for large-scale wind tunnel testing also relaxes the requirements for the light source, thanks to the high light-scattering intensity of the HFSB. Volumetric flow field measurements with HFSB can be conducted using pulsed light-emitting diode (LED) arrays as a light source (Schröder et al., 2022; Wolf et al., 2019), which are advantageous in terms of cost and ease of operation compared to the high-speed lasers that are traditionally used in PIV experiments.

In terms of the imaging system, an interesting development for large-scale volumetric flow field measurements is the coaxial volumetric velocimeter (CVV) by Schneiders et al. (2018). This device incorporates four high-speed cameras and a laser light source in a compact housing using a coaxial arrangement, with which flow measurements in a volume of ca. 10-15 liters can be achieved. The compactness of the CVV allows it to be mounted on a robotic arm, which facilitates the traversing of the CVV, and thus the automated combination of several measurements to one large flow field measurement, as first demonstrated by Jux et al. (2018) for the flow around a full-scale cyclist mannequin with a total measurement volume of around 2 m^3. Another example of a large-scale wind tunnel test with robotic PIV measurements is the study of the wake of the Delfly flapping-wing micro air vehicle by Martínez Gallar et al. (2019), which is shown in Fig. 2.3. In this study, data acquired in the wind tunnel from four different measurement volumes were combined to provide a representation of the quasi-periodic wake in a flow domain with a volume of ca. 60 liters, as shown in Fig. 2.3(b).

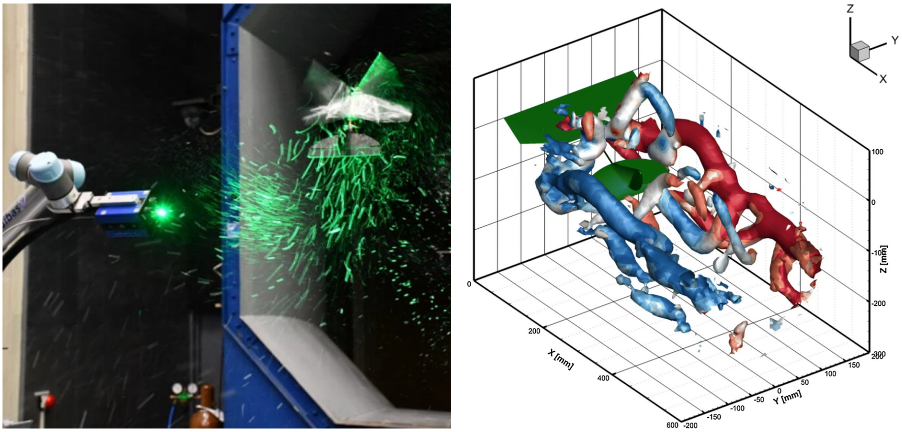

(a) robotic PIV measurement in the wind tunnel (b) isocontours of the measured vorticity

Figure 2.3: Large scale flow field measurements in the wake of the Delfly, from Martínez Gallar et al. (2019)

Concerning the applicability of robotic volumetric PIV to aeroelasticity, a considerable difference between the first application on the cyclist mannequin and the wake study of the Delfly is that the wake flow is unsteady. As such, it cannot be analyzed in the same fashion as done in Jux et al. (2018), where the LPT measurements were merged into a combined, time-averaged measurement. Temporal averaging is generally necessary because the particle concentration during the experiment is usually too low to extract meaningful information based on individual particle tracks. Instead, it is common to calculate an ensemble average of the particle tracks to obtain a statistical representation of the flow field on a Cartesian grid (Agüera et al., 2016). An unsteady flow phenomenon can be analyzed with this approach if a conditional average is performed, where several measurements over a small time span are considered to perform an ensemble average. As is the case in the study of Martínez Gallar et al. (2019), this approach is significantly simplified when the observed flow phenomenon is periodic, which allows a phase average to be performed. This property of the flow also facilitates the combination of several measurement volumes into one larger flow field, when the same phase angle reference is used for all measurements. These examples illustrate that also for aeroelastic investigations in relatively large-scale subsonic wind tunnel facilities, flow field measurements are feasible at the relevant scale for aeroelastic experiments, but the measurement capabilities are currently limited to (quasi-)steady and unsteady periodic phenomena.

SURFACE PRESSURE MEASUREMENTS

In contrast to flow field measurements, surface techniques measure aerodynamic properties directly on the object under investigation. The following discussion addresses the pressure-sensitive paint (PSP) technique for measuring surface pressure. A sketch of a typical PSP measurement setup is shown in Fig. 2.4(a). The model under investigation is coated with a layer of the PSP. The active element of the paint is a fluorescent molecule that is activated by oxygen, which is immersed in an oxygen-permeable polymer binder. This paint is then excited with a powerful light source, typically a high-intensity LED with a wavelength in the ultraviolet band. The amount of light that is emitted by the fluorescent molecules is proportional to the oxygen concentration, which relates to the surface pressure (T. Liu et al., 2005). This light emission is measured with a camera, where a filter is used to obtain the isolated signal from the PSP. The relation between the light intensity and the pressure is established for each paint composition by calibration in a pressure chamber. Each pixel of the camera thus effectively acts as a pressure transducer. Through post-processing of the optical measurement data, it is thus possible to determine the surface pressure distribution on the object in the wind tunnel with a high spatial resolution, which is limited only by the camera resolution. An example of such a pressure distribution that was obtained using PSP by Yorita et al. (2017) is shown in Fig. 2.4(b). It shows the pressure coefficient distribution on the DLR-F17 delta wing configuration (Schütte et al., 2010) at an angle of attack of $\alpha = 15^\circ$. The PSP measurements reveal a complex pressure distribution, which would be unfeasible to obtain with this level of detail when using installed pressure sensors.

The PSP technique became established for aerodynamic testing already in the 1990's (McLachlan & Bell, 1995). Applications of PSP in wind tunnel tests include wings and full aircraft models over a wide range of flow speeds, ranging from low subsonic (Brown et al., 1997) over transonic (Klein et al., 2005) to supersonic (McLachlan et al., 1995) and hypersonic applications (Nakakita & Asai, 2002). The low-speed flow regime can be identified as particularly challenging for the application of PSP because the pressure variations that occur in this regime are smaller, which implies that the accuracy limitations of the PSP technique lead to larger relative errors. Another common issue of all surface techniques, irrespective of the quantity that is measured, is the measurement error that is introduced through the deformation or displacement of the experimental model. This error is relevant when an intensity ratio is calculated between wind-on and wind-off measurements for conducting PSP measurements, and when the measured surface data is mapped on the three-dimensional object in post-processing. The model displacement and/or deformation is therefore measured experimentally in cases where these quantities are required to obtain accurate surface measurements. An optical technique that is frequently used for this purpose is photogrammetry, which is described in the following. This combination of PSP with structural measurements can be seen as the first step towards an integrated aerodynamic and structural measurement approach based on optical measurements, which is a topic that is further discussed in Sec. 2.1.3.

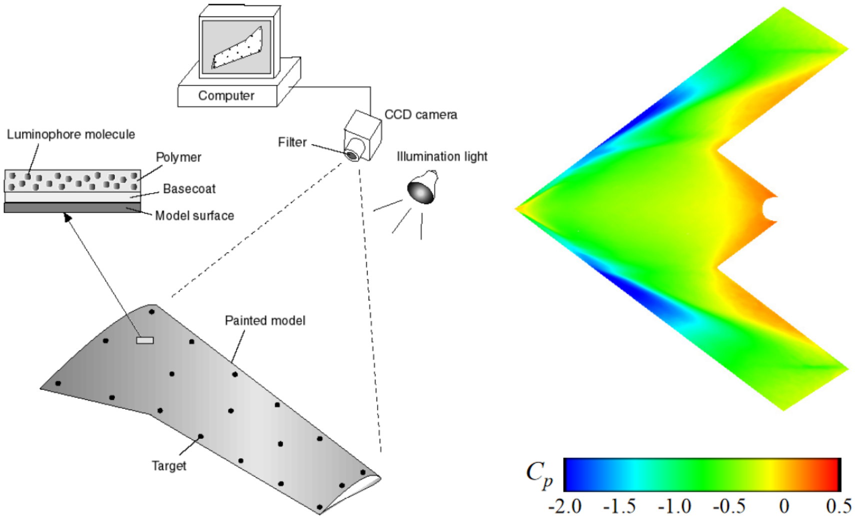

(a) Sketch of a measurement setup (T. Liu et al., 2005)

(b) Pressure on the suction side of a delta wing model (Yorita et al., 2017)

Figure 2.4: Principle and application of PSP in wind tunnel testing, (a) measurement setup and components, (b) pressure distribution on a delta wing model based on PSP measurements

2.1.2. STRUCTURAL MEASUREMENT TECHNIQUES

The following discussion provides an overview of optical field measurement techniques for structural dynamics. The discussion is limited to photogrammetric optical techniques, based on incoherent light, as only these techniques are relevant to the integrated measurement approach that is pursued in this thesis. Photogrammetric optical techniques are essentially surface detection techniques that can be distinguished depending on the type of targets that are used for the measurements and the data processing method. The approaches that are outlined in the following are digital image correlation (DIC), point tracking, and edge detection.

The most widely used approach for photogrammetric measurements in the wind tunnel environment is point tracking. In this approach, individual, typically circular targets are placed on the model under investigation and their position is reconstructed based on the images acquired with one or, more commonly, several cameras. A schematic of a photogrammetric measurement setup using two cameras (stereo photogrammetry) is shown in Fig. 2.5. Using a stereoscopic setup with at least two cameras, the position of the measured point on an object can be reconstructed in a three-dimensional space using triangulation, assuming that the placement of the cameras with respect to each other is known from a previously performed geometrical calibration. This data processing step is typically performed with a dedicated software tool. Given that the positions of the targets on the undeformed object under investigation are known, these measurements can then be used to quantify the displacements of the object surface at the discrete locations where the targets were placed.

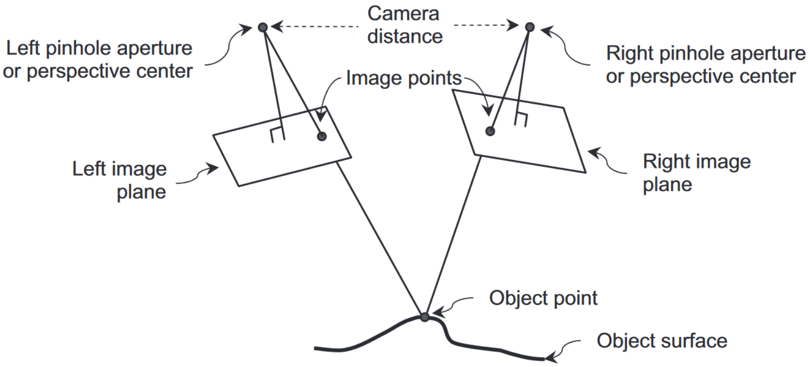

Figure 2.5: Principle of a stereo photogrammetry measurement setup, from Helfrick et al. (2011)

A strong asset of the photogrammetric point tracking approach, making this technique highly attractive for large-scale wind tunnel measurements, is its scalability. By adjusting the size of the targets for tracking, this technique can be applied on any relevant scale for aeronautical applications without major modifications of the measurement approach, which opens a wide range of applications, from scaled-wind tunnel tests (Schairer & Hand, 1999) to free flight (Burner et al., 2003), as reviewed by T. Liu et al. (2012). Two examples from their review are shown in Fig. 2.6.

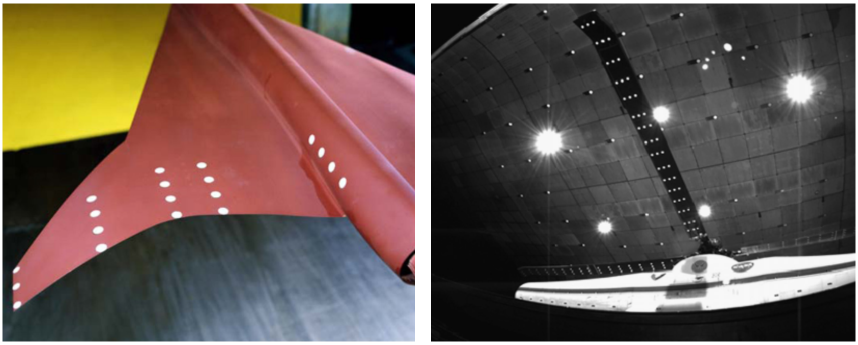

(a) aircraft model with target rows (b) full-scale UH-60A airloads rotor

Figure 2.6: Wind tunnel models for photogrammetric point tracking measurements, from T. Liu et al. (2012)

A remarkable example of large-scale photogrammetric measurements with an aeronautics application is the blade deformation study performed on a full-scale UH-60A helicopter rotor in the 40-by-80-ft wind tunnel of the National Full-Scale Aerodynamics Complex at NASA Ames by Barrows et al. (2011), shown in Fig. 2.6(b). The diameter of this rotor is approximately 16 m and the photogrammetry targets had a diameter of around 5 cm. 48 targets per rotor blade were used for photogrammetric displacement measurements, based on which the pitch angle and the elastic bending deformation of the four individual blades during the rotation period were determined.

Another photogrammetric technique that can be considered for aeroelastic experiments is DIC. An illustration of a stereo DIC measurement setup is shown in Fig. 2.7. The setup for this technique is in principle the same as for the point tracking, requiring also a geometrical calibration. The differences between the two approaches lie in the nature of the targets on the object surface and the data processing method. For DIC, a dense speckle pattern is applied to the surface, which consists of a fine, irregular grid of bright spots. These speckle patterns are recorded with the cameras before and after the loading is applied to the object. Applying a cross-correlation on small interrogation windows of the acquired images, it is possible to determine not only a high-resolution displacement field but also the deformation of the surface in terms of the strain field (Pan, 2018). This additional information obtained with the DIC technique is an advantage over the point tracking approach, where strain fields cannot be directly measured due to the relatively low target density.

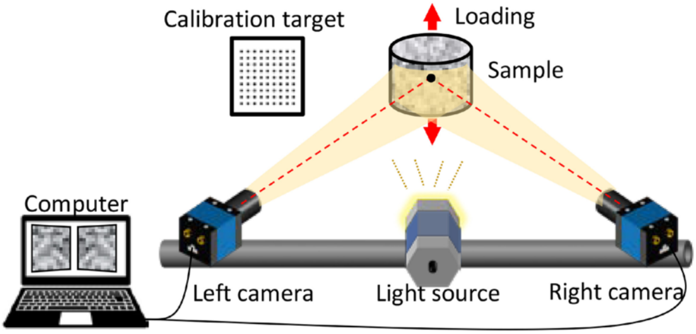

Figure 2.7: Schematic of a stereo DIC measurement setup, from Pan (2018)

The high spatial resolution of DIC makes this technique appealing for studying aeroelastic phenomena. One example is the study of P. Wu et al. (2010), which investigated the effects of different structural designs on the deformation characteristics of the flexible flapping wings of a micro air vehicle, as shown in Fig. 2.8. While this and similar studies (e.g., Ha et al., 2015) prove that high accuracy measurements of wing displacement and deformation can be obtained with DIC, there are only a few studies, including the study of Banks et al. (2015), that have applied the technique in large-scale wind tunnel facilities. A reason for this is the scaling of the speckle pattern that is required for the preparation of larger experimental models. The pattern needs to be magnified such that it appears similarly in the acquired images and the same cross-correlation data processing method can be used as in smaller-scale experiments. This, however, means that increasing the scale of the experimental reduces the spatial resolution of the DIC measurements unless it is possible to increase the camera resolution, thus diminishing the major advantage of the DIC technique over the point tracking approach.

As the third photogrammetric measurement approach, edge detection methods can be considered. While the measurement setup is essentially identical to the point tracking approach (see Fig. 2.5), this approach is used without applying targets on the object under investigation. Instead, optical features of the object itself are tracked, which

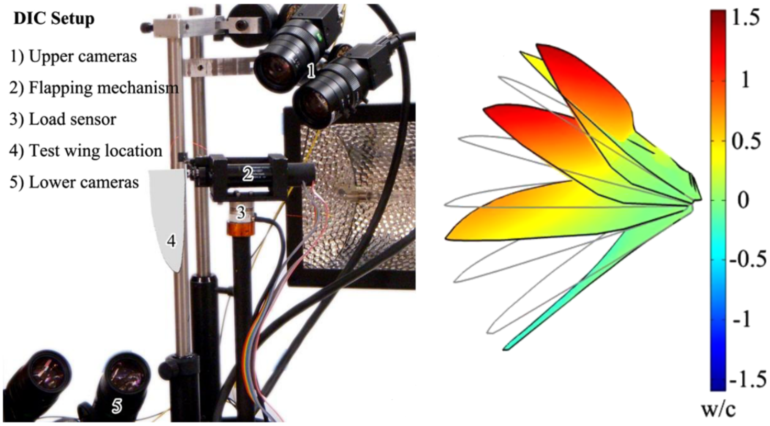

(a) measurement setup

(b) wing deformation measurement (reference shape shown in gray)

Figure 2.8: DIC study of a flexible flapping wing on a micro air vehicle scale, from P. Wu et al. (2010)

are typically the outer edges of the object. The fact that no targets on the experimental model are required has its advantages for certain applications, e.g., for the study of living animals (Heinold & Kähler, 2018). However, the amount of information that is obtained from edge detection methods is typically smaller and less straightforward to interpret than for point tracking data, which makes analyzing moving and deforming structures more difficult. Applications of the edge detection method are therefore typically rigid body motions or flexible objects with only a small number of deformation degrees of freedom (Baqersad et al., 2017).

In summary, photogrammetric point tracking appears as the most appealing of the discussed field measurement approaches in the context of large-scale aeroelastic wind tunnel experiments. The density of the obtained deformation measurements is higher and the results are easier to interpret than for the edge detection approach, while the application of the optical targets, particularly on large experimental models, and data analysis is simpler than for DIC measurements.

2.1.3. TECHNIQUES FOR AN INTEGRATED MEASUREMENT APPROACH

For the analysis of an unsteady aeroelastic phenomenon in a wind tunnel experiment, an exact synchronization of all the measurements that are conducted is crucial for the interpretation of the results. When acquiring optical measurements using several optical measurement systems simultaneously, considerable efforts would therefore have to be spent to synchronize these measurements. For a dynamic aeroelastic characterization, a clear advantage would be gained when both the structural and the aerodynamic response could be characterized based on closely related optical techniques, such that they can be realized with a single measurement and data processing system. Developing such an *integrated* measurement approach is a key part of the research objective of this thesis that was stated in Sec. 1.2. In this section, the existing measurement techniques that were introduced are assessed based on their suitability for integrating aerodynamic and structural measurements in one measurement approach. The following discussion thus provides arguments for the selection of the approach that is developed and applied in the following chapters in this thesis.

From the optical measurement techniques that were reviewed previously, the experimental practice that is currently the closest to an integrated aerodynamic and structural measurement approach is the combined use of PSP with photogrammetric point tracking. A combination of these two techniques was used already in the 1990s at NASA Langley (Bell & Burner, 1998). In such an approach, the PSP measurements are used to provide insight into the aerodynamic loads on the investigated wing model while the photogrammetry measurements facilitate a shape reconstruction of the moving and/or deforming wing, which in turn can be used to determine structural loads. There are however several drawbacks of this approach in the context of aeroelastic investigations. Firstly, the use of PSP for unsteady aeroelastic interactions is not currently established in the field. While unsteady PSP methods are currently under development, their use in the low-speed regimes in which aeroelastic experiments are frequently performed is non-trivial because the magnitude of the pressure variations is relatively small, which means that the PSP techniques comes with very high relative errors for this kind of application. Secondly, while the integration of photogrammetric point tracking into a PSP measurement is straightforward in the image data acquisition stage by placing targets for tracking on the wing model that are then detected in the PSP image, the rest of the measurement chain cannot be integrated into one process because of the dissimilarities between the two techniques. Both techniques require different calibrations, where the PSP needs to be calibrated to relate the surface pressure to the measured light sensitivity while the photogrammetry system needs a geometric calibration between the two-dimensional image data and the three-dimensional space. This furthermore implies that the data processing is performed with different software tools (see Fig. 2.9(a)). Finally, it should be noted that a three-dimensional photogrammetry measurement requires at least two cameras with the same field of view, which may be useful but is not strictly necessary for the PSP measurements. It follows, therefore, that this combination of techniques is not an ideal approach to performing aeroelastic analyses in low-speed, large-scale wind tunnel tests. As a result, while this approach has been applied on flexible wings in a few studies, for example by T. Liu et al. (2011), most existing studies have used the combined PSP-point tracking primarily for the relatively simple problem of correcting the analysis of the PSP images for the displacement of rigid wind tunnel models under the aerodynamic load with the results of the photogrammetric point tracking analysis.

A different approach is therefore followed in this thesis, which is the integration of optical flow field measurements using LPT in combination with photogrammetric point tracking. By ensuring that the targets for the point tracking on the surface of the wing model appear similarly sized to the flow tracer particles in the acquired images, the position, velocity, and acceleration of both flow tracers and structural markers can theoretically be evaluated using the same particle (or point) tracking algorithm. Moreover, by using two techniques that share the same measurement principle in one approach, it is also ensured that the calibration procedure is identical and that the same data processing software can be used for aerodynamic and structural measurements (see Fig. 2.9(b)).

The general feasibility of this approach for large-scale wind tunnel investigations has been recently demonstrated by Mitrotta et al. (2022), using the STB algorithm for tracking both flow tracer particles and structural markers on a flat plate in a wind tunnel environment. The image data of the flow tracers and the structural markers were hereby separated by applying temporal filters to the image data. As the time scale of the fluid motion is smaller than the time scale of the structural motion, a high-pass filter could be used to isolate the flow data and the reverse operation was performed with a low-pass filter to obtain image data that contains the isolates structural measurements. The key differences between the *combined* use of PSP and photogrammetry and the *integrated* use of LPT for aerodynamic and structural measurements are visualized in Fig. 2.9.

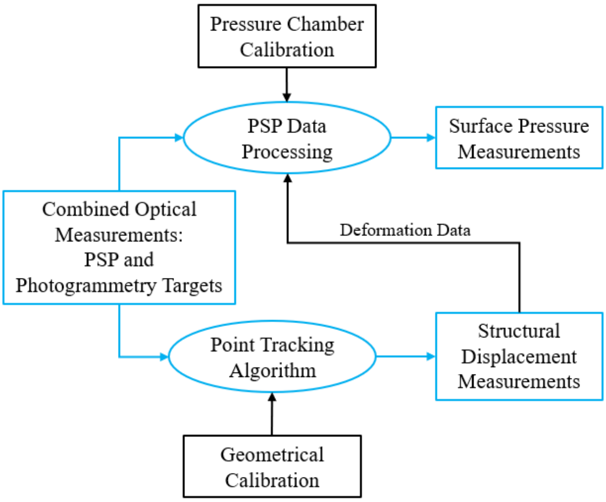

(a) combined measurement approach with PSP and point tracking

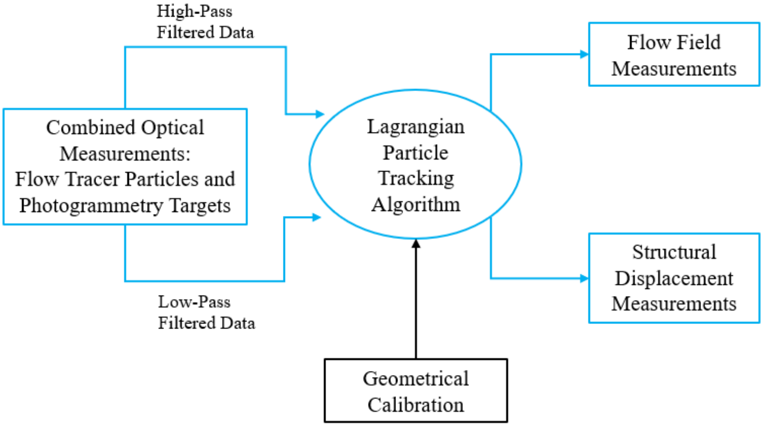

(b) integrated measurement approach with LPT and point tracking (used in this thesis)

Figure 2.9: Combination of aerodynamic and structural measurements into one measurement approach

One major difference between the two approaches is the aerodynamic output data, which is flow field data in the case of integrated LPT and photogrammetry measurements. This means that the aerodynamic loads need to be determined by post-processing of the flow field measurements using physical relations between the flow field and the acting loads. The existing methods for this aerodynamic characterization step are discussed in the following Sec. 2.2.1.

2.2. AEROELASTIC LOADS DETERMINATION BASED ON OPTICAL MEASUREMENTS

This section covers, in two respective subsections, the aerodynamic and structural loads determination based on the optical measurements that are obtained with the integrated approach. In particular, this involves the aerodynamic loads being inferred from the measurements of the flow velocity field and the structural loads being inferred from the discrete displacement measurements. For both loads determination procedures, aerodynamic as well as structural, a significant body of research exists of which an overview is presented. However, for the specific cases that are relevant to this thesis in terms of the input data that originates from the integrated measurements and the application to aeroelasticity, there are currently no existing standard procedures.

2.2.1. AERODYNAMIC LOADS DETERMINATION

In the context of aeroelasticity, an aerodynamic characterization involves the determination of the dynamically varying aerodynamic loads that act on lifting structures, such as wings or rotor blades. For the characterization of slender wings, the aerodynamic force is typically analyzed per wing section and split into two components, the sectional lift force L', acting perpendicular to the direction of the inflow U_∞, and the sectional drag force, D' in the direction of the inflow, as shown in Fig. 2.10.

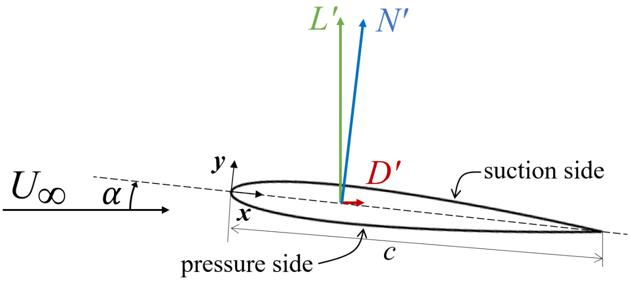

Figure 2.10: Sketch of a wing section with forces and coordinate system

In most aeronautics applications, the design operating conditions of wings impose that the angle of attack α between the inflow and the chord line c of the wing section is small, to ensure attached flow conditions under which the lift is much larger than the drag (typical values of the lift-to-drag ratio L'/D' are around 100, see Abbott et al., 1945). Considering the research objective of this thesis, the focus of this section will therefore be on the determination of the lift force as the dominant force in aeroelastic interactions, and the surface pressure, which is related to the lift as shown in the following.

One approach to determining the aerodynamic force on an object is by integrating the pressure and shear stress distributions over the surface. Applying this procedure to a wing section, the force normal to the chord line, per unit span, N', is obtained, when working in the coordinate system of the wing section (see Fig. 2.10):

$$N' = \int_0^c \left(p_{\text{pressure}} - p_{\text{suction}}\right) dx + \int_0^c \left(\tau_{\text{pressure}} \frac{dy_{\text{pressure}}}{dx} + \tau_{\text{suction}} \frac{dy_{\text{suction}}}{dx}\right) dx. \tag{2.1}$$

The second term in Eq. (2.1) is negligible for thin wings because the surface gradient is small and the shear stress τ is much smaller than the pressure in the flow regime that is relevant for aeronautics. The pressure difference between the lower (pressure) and the upper (suction) side is therefore the main contributor to the normal force.

The normal force is related to the lift and drag through the angle of attack:

$$N' = L' \cos\alpha + D' \sin\alpha\,, \tag{2.2}$$

where, for wings with $L' \gg D'$ at small angles of attack (assuming that $\cos\alpha \approx 1$), the first term is several orders of magnitude larger than the second. It is therefore customary to assume that $N' \approx L'$, which means that the following relation between lift and pressure is obtained (Katz & Plotkin, 2001):

$$L' = \int_0^c \left(p_{\text{lower}} - p_{\text{upper}}\right) dx. \tag{2.3}$$

In a wind tunnel experiment where flow velocity measurements are performed, the surface pressure has to be inferred from the flow field measurement in a post-processing scheme. Some approaches to perform this calculation are discussed in the following. A different way to determine the aerodynamic forces from the flow field measurement is the use of control volume approaches, which are discussed subsequently. In these approaches, the lift force is obtained without requiring knowledge of the surface pressure distribution.

FLOW FIELD-BASED SURFACE PRESSURE DETERMINATION

A relation between the static pressure p and the flow velocity $\boldsymbol{u}$ in an incompressible flow field is given by the Navier-Stokes momentum equation in the differential form (Batchelor, 1967):

$$\nabla p = -\rho \left(\frac{\partial \boldsymbol{u}}{\partial t} + (\boldsymbol{u} \cdot \nabla)\boldsymbol{u}\right) + \mu_d \nabla^2 \boldsymbol{u}. \tag{2.4}$$

It should be noted here that the implementation of this relation between the pressure and the measured flow velocity field is far from straightforward. The right side of Eq. 2.4 poses demanding requirements on the flow field measurement because the temporal and all spatial gradients of the flow field have to be measured accurately to be able to calculate the pressure gradient. To determine the pressure field, the pressure gradient then needs to be integrated numerically throughout the field from a reference point where the static pressure is known. Several authors have used such spatial integration approaches to determine the pressure field in the past (e.g., Baur and Könteger, 1999; Haigermoser, 2009; X. Liu and Katz, 2006), in studies that were mostly based on planar PIV measurements. More recently, Jux et al. (2020) used a similar approach to determine the time-averaged surface pressure on objects based on large-scale LPT measurements.

A related approach for the pressure field determination is the use of the Poisson equation for the pressure calculation (Gurka et al., 1999). In this approach, the divergence of Eq. (2.4) is taken, which results in the following expression:

$$\nabla^2 p = -\rho \nabla \cdot (\boldsymbol{u} \cdot \nabla)\boldsymbol{u}. \tag{2.5}$$

An advantage of this approach is that the temporal gradient and viscous terms drop out of the equation, as the mass conservation enforces a divergence-free velocity field in incompressible flow ($\nabla \cdot \boldsymbol{u} = 0$). Fujisawa et al. (2005) demonstrated the use of the Poisson approach to determine the loads on an unsteady cylinder, however without providing a detailed accuracy assessment. A more detailed study of the performance of this approach was conducted by de Kat and van Oudheusden (2011), who analyzed the turbulent wake flow of a square cylinder; the vorticity field measured with PIV and the pressure field obtained with the Poisson approach are shown in Fig. 2.11(a) and 2.11(b), respectively. In their study, a reasonable agreement (RMS error within 5%) between the PIV-based pressure fluctuations and the measurements with two pressure sensors that were installed on the cylinder was observed.

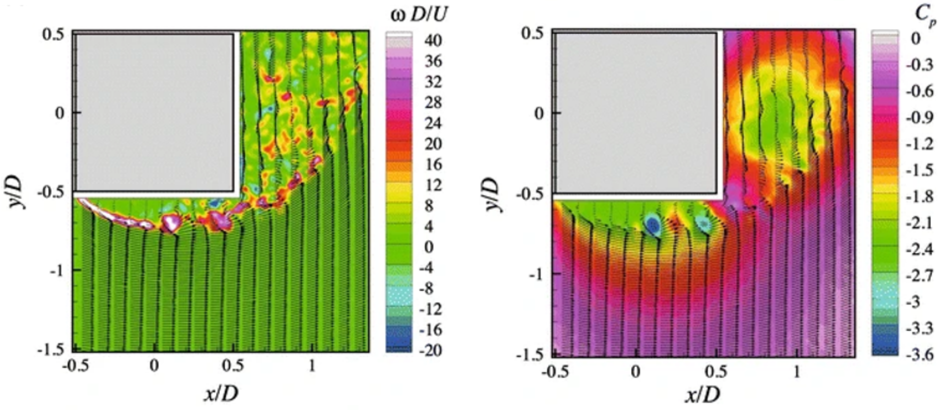

(a) vorticity field measured with PIV

(b) PIV-based pressure field

Figure 2.11: PIV-based pressure in the wake of a square cylinder, from de Kat and van Oudheusden (2011)

In contrast to the complex and potentially case-dependent, computationally expensive numerical integration schemes of the pressure gradient based on Eq. (2.4) (e.g., Wang et al., 2019), numerical solvers for the Poisson equation are standard tools in numerical analysis (Hoffman & Frankel, 2018). For this practical reason, the Poisson approach has found a more widespread use than the pressure integration, while none of the methods exhibits significant advantages over the other in terms of the accuracy of the pressure result (van Oudheusden, 2013).

One commonality of the pressure integration and the Poisson approach is that a reference pressure value has to be known at one or several locations on the boundary of the measured flow field to obtain the pressure field (Dirichlet boundary condition). This reference pressure is usually calculated from the flow field using Bernoulli's equation:

$$\frac{\partial \Phi}{\partial t} + \frac{1}{2} V^2 + \frac{p}{\rho} = \text{const.}\,, \tag{2.6}$$

where Φ is the velocity potential, defined by the relation $\boldsymbol{u} = \nabla \Phi$, V is the velocity magnitude, p is the static pressure and ρ is the fluid density at a given location in the flow field. Bernoulli's equation is valid everywhere in the flow field in incompressible, inviscid, and irrotational flow conditions. If the flow is additionally steady, Eq. (2.6) can be further simplified by ignoring the first term. When the static pressure in the undisturbed freestream p_∞ is known, an algebraic relation between the local flow velocity magnitude and the pressure can be given:

$$p = p_\infty + \frac{1}{2} \rho \left(U_\infty^2 - V^2 \right), \tag{2.7}$$

or in terms of the pressure coefficient C_p

$$C_p = \frac{p - p_\infty}{\frac{1}{2} \rho U_\infty^2} = 1 - \left(\frac{V}{U_\infty} \right)^2 . \tag{2.8}$$

The advantage of the use of this straightforward relation over the pressure determination based on the Navier-Stokes equation (Eqs. (2.4) or (2.5)) is that it is much less prone to measurement errors in the flow field because the requirements on the flow field measurement are relaxed, as only the local velocity magnitude is required, instead of all velocity components and gradients. The drawback of this approach is the limited applicability of Bernoulli's equation, which has inspired several researchers to perform a domain partitioning of the flow into regions where the flow conditions are such that Eq. (2.8) may be applied and the remaining domain where the pressure is determined using the pressure integration or Poisson approaches (Jux et al., 2020; Kurtulus et al., 2006).

The flow around a wing can be treated as mostly inviscid and irrotational, with the important exception of the boundary layer and potentially regions of separated flow near the surface of the wing or in the wake. This fact has been exploited by Ragni et al. (2009) to determine the surface pressure on a wing section from PIV measurements without using the Navier-Stokes equations, as shown in Fig. 2.12. In this study, the flow speed was outside the incompressible regime, such that the isentropic flow relations were used to determine the pressure from the flow velocity, which, similar to Eq. (2.8), provide an algebraic relation between the two quantities. The remaining problem of determining the surface pressure was then approached by an extrapolation of the pressure from the flow near the surface towards the actual surface pressure, which the authors performed as shown in Fig. 2.12(c). Special attention in such an approach is required in those regions where no (or erroneous) flow measurements are available or where the presence of the boundary layer violates the assumptions of the physical relation between flow velocity and pressure that was used.

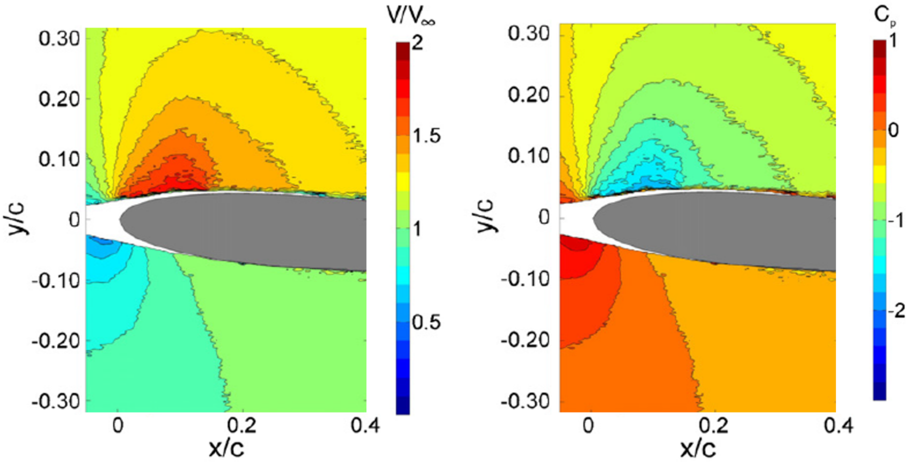

(a) flow field measurement

(b) PIV-based pressure field

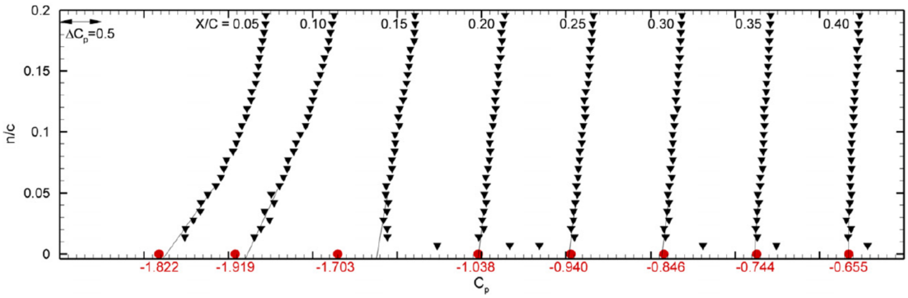

(c) extrapolation of the PIV-based surface pressure (black) in comparison to sensor data (red dots)

Figure 2.12: PIV-based surface pressure determination on a transonic wing, from Ragni et al. (2009)

In aeroelastic wind tunnel tests, the flow velocity is often low subsonic, justifying the incompressible flow assumption, which means that Bernoulli's principle is a suitable approach to determine the surface pressure on a wing with attached flow conditions. However, a problem is that aeroelastic phenomena are usually unsteady, which means that the temporal gradient of the velocity potential may contribute significantly and cannot always be neglected in Eq. (2.6). As the determination of the velocity potential is not straightforward based on experimental measurement data, some authors have chosen to neglect this term without any further consideration despite a degree of unsteadiness in the flow (Kurtulus et al., 2006). However, Villegas and Diez (2014b) have shown that this approach can lead to significant errors. Therefore, a particular challenge for unsteady aeroelastic phenomena lies in employing a robust and accurate method to model the effect of the unsteady term on the surface pressure in case Bernoulli's equation is used.

FLOW FIELD-BASED LIFT FORCE DETERMINATION

As an alternative to the spatial integration of the surface pressure, the aerodynamic force can be calculated directly from the flow field data using a control volume approach. The physical foundation for this approach is the Navier-Stokes momentum equation in its integral form which is applied to a fluid volume that fully encloses the object under investigation. Assuming an incompressible flow with constant density around an impermeable object, the following equation provides the relation between the instantaneous force $\boldsymbol{F}(t)$ on the object and the fluid dynamic quantities of a stationary control volume $\boldsymbol{V_C}$ surrounding it:

$$\boldsymbol{F}(t) = -\rho \iiint \frac{\partial \boldsymbol{u}}{\partial t} d\boldsymbol{V_C} - \rho \iint (\boldsymbol{u} \cdot \boldsymbol{n}) \boldsymbol{u} d\boldsymbol{S_C} - \iint p \boldsymbol{n} d\boldsymbol{S_C} + \iint \boldsymbol{\tau} \cdot \boldsymbol{n} d\boldsymbol{S_C}, \tag{2.9}$$

where $\boldsymbol{S_C}$ is the surface that bounds the control volume, with $\boldsymbol{n}$ being the vector normal to it. The specific use of this equation for the determination of aerodynamic forces based on PIV measurements of the flow field was introduced by Unal et al. (1997) and has since been applied in several other studies. One example is the study of Kurtulus et al. (2006), who used this approach to determine the unsteady aerodynamic lift and drag forces that act on a square cylinder, as shown in Fig. 2.13.

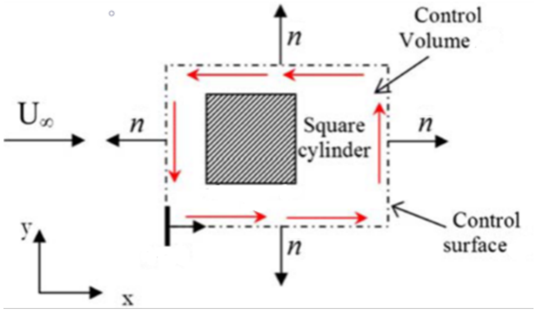

(a) control volume around a square cylinder

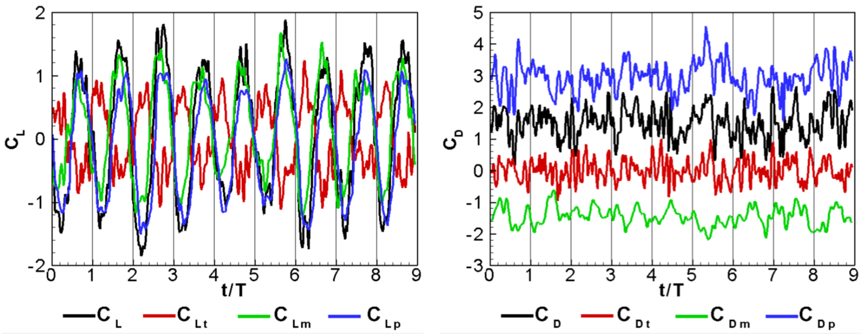

(b) unsteady lift coefficient (c) unsteady drag coefficient

Figure 2.13: Forces on a square cylinder with the control volume approach, from Kurtulus et al. (2006)

The lift and drag force coefficients that are shown with black lines in Fig. 2.13(b) and Fig. 2.13(c), respectively, are split into their respective components according to the different terms in Eq. (2.9). The shear stress term is not shown, because its contribution is negligible in high Reynolds number flow when the control volume boundaries are not placed directly at the object surface, as verified in the study by Kurtulus et al. (2006). The first term that is shown is the unsteady term (indicated by red lines in Fig. 2.13(b) and Fig. 2.13(c)), which is obtained by integrating the acceleration field over the control volume. Because this term is the only one that requires a volume integration, other researchers have derived a different expression for this term (derivative moment transformation, J.-Z. Wu et al., 2005) that depends only on the flow velocity at the surface of the volume, under the assumption that the volume of the object in the flow is small compared to the control volume (see Mohebbian and Rival, 2012). This relaxes the requirement on the flow field measurements, which are typically most difficult to obtain in the vicinity of the object under investigation due to light reflections and limited optical access. The second term is the convection term (indicated by green lines), which is calculated in a relatively straightforward way from velocity measurements at the control surface. More problematic is the third term on the right-hand side of Eq. (2.9), which is the pressure term (blue lines). Because the pressure on the control surface is not measured with PIV, it has to be calculated with the methods that were discussed in the previous section, which presents a significant additional post-processing effort. Despite this complication, the control volume approach based on Eq. (2.9) has been applied successfully in several studies of wings in steady and unsteady flow conditions (David et al., 2009; Gharali & Johnson, 2014; van Oudheusden et al., 2007; Villegas & Diez, 2014a).

To avoid the potential source of error that the additional data processing step of the pressure determination implicates, multiple vorticity-based formulations of the Navier-Stokes momentum equation for the determination forces based on flow velocity measurements were derived by Noca et al. (1997, 1999). In all of these formulations, the aerodynamic force is determined without requiring an explicit determination of the pressure. The most interesting vorticity-based formulation is the flux equation from Noca et al. (1999), which is given for thin, impermeable objects as:

$$\boldsymbol{F}(t) = \rho \iint \boldsymbol{n} \cdot \boldsymbol{\gamma}_{\mathrm{flux}} \, d\boldsymbol{S_C} \, , \tag{2.10}$$

where the vorticity flux vector $\boldsymbol{\gamma}_{\mathrm{flux}}$ is defined as

$$\begin{aligned} \boldsymbol{\gamma}_{\mathrm{flux}} = & \frac{1}{2} u^2 \boldsymbol{I} + \boldsymbol{u}\boldsymbol{u} - \frac{1}{2} \boldsymbol{u}(\boldsymbol{x} \times \boldsymbol{\omega}) + \frac{1}{2} \boldsymbol{\omega}(\boldsymbol{x} \times \boldsymbol{u}) \\ & - \frac{1}{2} \left[\left(\boldsymbol{x} \cdot \frac{\partial \boldsymbol{u}}{\partial t} \right) \boldsymbol{I} - \boldsymbol{x} \frac{\partial \boldsymbol{u}}{\partial t} + 2 \frac{\partial \boldsymbol{u}}{\partial t} \boldsymbol{x} \right] \\ & + \frac{1}{2} \left[\boldsymbol{x} \cdot (\nabla \cdot \boldsymbol{\tau}) \, \boldsymbol{I} - \boldsymbol{x} (\nabla \cdot \boldsymbol{\tau}) \right] + \boldsymbol{\tau} \, , \end{aligned} \tag{2.11}$$

where $\boldsymbol{\omega} = \nabla \times \boldsymbol{u}$ is the vorticity field, $\boldsymbol{I}$ is the identity matrix and $\boldsymbol{x}$ is a coordinate vector.

This implementation of the control volume approach has been applied in several studies (e.g., DeVoria et al., 2014; DeVoria and Ringuette, 2013), including multiple studies on unsteady wings (Simão Ferreira et al., 2011; Sterenborg, van Zuijlen, et al., 2014).

However, a drawback of this approach is that, despite avoiding the explicit determination of the pressure, the requirements on the flow field measurements are not significantly reduced compared to the conventional control volume formulation. The reason for that is that the vorticity-based formulation requires the evaluation of additional terms that include higher-order gradient operations and multiplications, which are prone to the amplification of measurement errors. In the comparative study of Rival and van Oudheusden (2017), it was therefore concluded that none of the two approaches has a clear advantage over the other in terms of a relaxation of the requirements on the flow field measurement or the required post-processing efforts.

A different method to determine the lift from flow field measurements is by application of the Kutta-Zhukovsky theorem (see Anderson Jr., 2011, chapter 3), which relates the section lift to the circulation Γ around an object:

$$L' = \rho U_\infty \Gamma \,. \tag{2.12}$$

The circulation is defined as the integral of the velocity along a closed contour C around the object, which is related to the surface integral of the enclosed vorticity according to Stokes' theorem:

$$\Gamma = -\oint_C \boldsymbol{u} \cdot d\boldsymbol{s} = -\iint \boldsymbol{\omega} \cdot d\boldsymbol{S_C} \,. \tag{2.13}$$

The circulation around a wing section, and hence the section lift, can thus be obtained from a measured flow field with a line integral of the velocity around the wing section, with the only additional requirements being the knowledge of the fluid density and the freestream velocity. As this straightforward method requires no spatial derivation of the PIV velocity measurements, it is less prone to measurement errors than the control volume methods. Consequently, the lift determination using PIV measurements based on the Kutta-Zhukovsky theorem has been applied successfully in different studies of static wings (e.g., T. Lee and Su, 2012; Lind et al., 2014).

Although the circulation theorem was originally derived under the conditions of irrotational and inviscid flow, it was found to yield results that are in good agreement with validation data also for flows around wings with moderate amounts of flow separation and unsteadiness (Sharma & Deshpande, 2012; Sterenborg, Lindeboom, et al., 2014). When considering the presence of vorticity in a rotational flow field, it can be concluded that the choice of the circulation contour becomes important in such a scenario as a direct consequence of Eq. (2.13). This is in contrast to the analysis of irrotational flows with the Kutta-Zhukovsky theorem, and to the control volume approaches in general, where the result for the aerodynamic force would be theoretically independent of the choice of the integration contour, such that it can be selected to introduce the smallest amount of measurement errors into the load determination procedure by using the measurement data with the smallest amount of measurement uncertainty. The effect of the integration contour on the result for the lift for viscous flow around a wing section was analyzed in detail by Olasek and Karczewski (2021), who compared the lift resulting from various integration contours with the ground truth in computational fluid dynamics (CFD) simulation data. They observed that a lift plateau forms when systematically varying the contour size, with the lift dropping sharply when the contour is located (partly) in the boundary layer and slowly dissipating when the contour is placed at a large distance from the wing. Consequently, they concluded that the integration contour corresponding to the maximum value for the lift from this plateau should be used, where lift variations due to measurement errors need to be excluded. A result from their study is presented in Fig. 2.14, where a comparison of the lift of a wing section from the Kutta-Zhukovsky theorem with the CFD ground truth at various angles of attack and two different Reynolds numbers is shown. The agreement between the curves is very good (differences consistently below 2%), even when the wing is in full stall for $\alpha \geq 14°$.

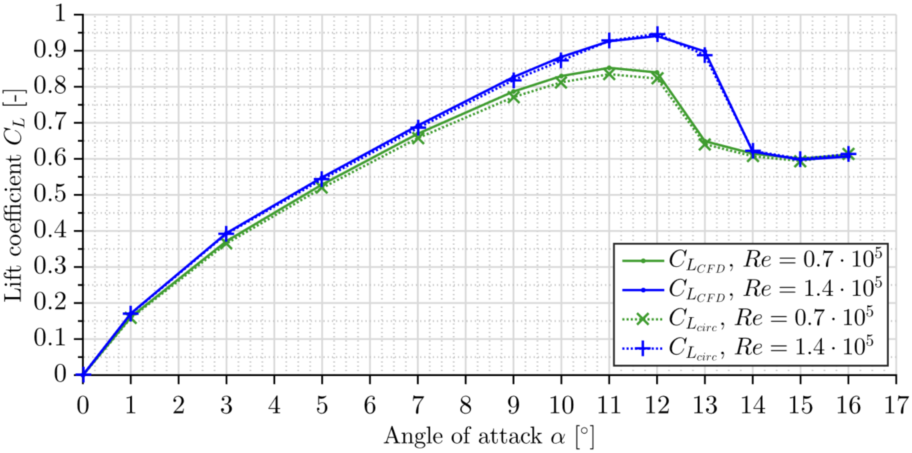

Figure 2.14: Comparison of the lift coefficient as determined with the Kutta-Zhukovsky theorem $C_{L_{circ}}$ with the ground truth $C_{L_{CFD}}$ for the flow around a wing section at various angles of attack for two different Reynolds numbers, from Olasek and Karczewski, 2021

While the preceding discussion demonstrates that the Kutta-Zhukovsky theorem can be considered the preferred approach to determine the lift force on wings from measured flow field data in steady flow conditions, the unsteady effects that occur on moving wings or wings in unsteady inflow are not captured by Eq. (2.12). Some authors have previously attempted to account for these effects using relatively simple physical models (Sterenborg, Lindeboom, et al., 2014; Yuan & Olinger, 2005), for example by using a potential flow model of the wing with a lumped vortex approximation of the wing section. Improvements over the quasi-steady formulation were observed in those studies, but a systematic assessment of these approaches based on experimental flow field measurements has not been performed.

A further load parameter that is of relevance in an aeroelastic characterization, which is closely related to the lift, is the pitching moment. While the moment determination is trivial when the pressure distribution is known, and alternatively can be determined with a control volume approach in a similar fashion as the lift (Chin & Lentink, 2019), its determination based on the circulation is currently not a standard practice.

2.2.2. STRUCTURAL LOADS DETERMINATION

When considering the role of experimentation in structural mechanics in the context of aeronautics, it should be noticed that a numerical structural model that is based on the model geometry usually exists already from the early design stages onward. Experiments are therefore typically conducted to provide reference data that can be used to validate or "update" these models. In practice, this means that the mass and stiffness parameters of the model are adjusted to match the experimental data, and/or the fidelity of the numerical model is increased when necessary. In the context of aeroelasticity in particular, numerical prediction models are used from early design stages onward to estimate the aeroelastic loads for the design and sizing of the components of an aircraft. The structural models that are used for aeroelastic predictions in the earlier phases of the design process are low-order models, where the entire aircraft ("stick" models, see Fig. 2.15) or complex parts, such as the wings, are simplified to one-dimensional beam structures (Murua et al., 2012; Riso & Cesnik, 2022; Stodieck et al., 2018).

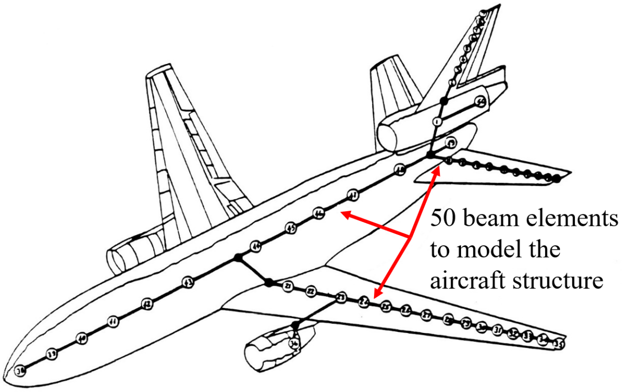

Figure 2.15: Illustration of a low-order structural model of an aircraft, adapted from Rommel and Dodd (1984)

Experimental data of the structural deformation under aeroelastic load that is obtained from optical measurements can thus be used for a comparison with the structural response results of the performed aeroelastic simulation. However, for the research of this thesis, it is part of the objective to perform an aeroelastic characterization based on the experimental data. This means that the structural deformation measurements need to be post-processed to derive the acting structural loads, which is an effort similar to the previously discussed procedures for the aerodynamic load determination. Two different types of structural loads are involved when performing an aeroelastic characterization, which are the elastic and inertial loads. A discussion of the possible approaches to performing the dynamic load determination is given in the following for both loads, elastic and inertial. For the determination of the respective loads, a numerical model of the mass (for inertial loads) and the stiffness (for elastic loads) of the structure is required. Considering the previously described context of aeroelastic simulation models, the complexity of the numerical structural models that are used within the scope of this thesis is limited to simple beam models.

ELASTIC LOADS DETERMINATION

The elastic loads determination based on discrete deformation measurements with a simplified structural model is illustrated in the following using the simple example of a one-dimensional Euler-Bernoulli beam model. Here, the relation between the deflection of the beam w along the beam coordinate z and an applied load q is given by the Euler-Bernoulli equation:

$$q(z) = \frac{d^2}{dz^2}\left(EI(z)\frac{d^2 w(z)}{dz^2}\right), \tag{2.14}$$

where EI is the flexural rigidity of the beam. This stiffness property needs to be known to be able to perform the elastic loads determination and can be derived from high-fidelity models of the structure or tests in the laboratory. Equation (2.14) states that the unknown external load on a beam is related to the fourth spatial derivative of the deflection. Considering the presence of random measurement errors, it is assumed that Eq. (2.14) cannot be applied directly to the measurement data when considering the amplification of the errors that are connected to the spatial differentiation of the sparse, discrete deformation measurements obtained with the point tracking approach.

One possible approach to determine the structural loads from optical deformation measurements is to perform an inverse modeling of the structure. Here, it is not attempted to derive the elastic loads directly from the deformation measurements, but instead, the solution of the structural model that best matches the experimental observations is found with an optimization (Gherlone et al., 2018). It should however be noted that most published literature on the subject of inverse structural modeling for loads and shape reconstruction is concerned with the analysis of experimental measurements of strain using installed sensors with the purpose of structural health monitoring (Tessler, 2007).

An inverse modeling approach that can be implemented regardless of whether the experimental measurement data is in terms of strain or deformation is by expressing the unknown external load on the structure with a limited number of degrees of freedom, for example using polynomials where the coefficients are the optimization variables (Gherlone et al., 2014). This approach can be considered to be more robust to experimental measurement errors than a direct loads estimation when the number of unknown variables is conform to the amount of measurement information that is available from the experiment. In an aeroelastic context, this approach to the loads determination can be implemented by performing an optimization for the unknown aerodynamic load that is applied to the structure, as first demonstrated experimentally by T. Liu et al. (2002) for a simplified beam structure. Among the few studies that have attempted to perform an aeroelastic loads determination based on such optical deformation measurements is the work of Roy et al. (2006), the results of which are visualized in Fig. 2.16. This study used a photogrammetry system to track the dynamic aeroelastic deformations of a thin flat plate under unsteady aerodynamic loading. Based on an analytical structural model of the plate geometry, an unsteady force distribution on the plate undergoing limit-cycle oscillations was determined. However, the authors did not provide an accuracy analysis of the determined loads but suggested further research on this method. Since then, this approach has not found widespread application in aeroelastic wind tunnel testing.

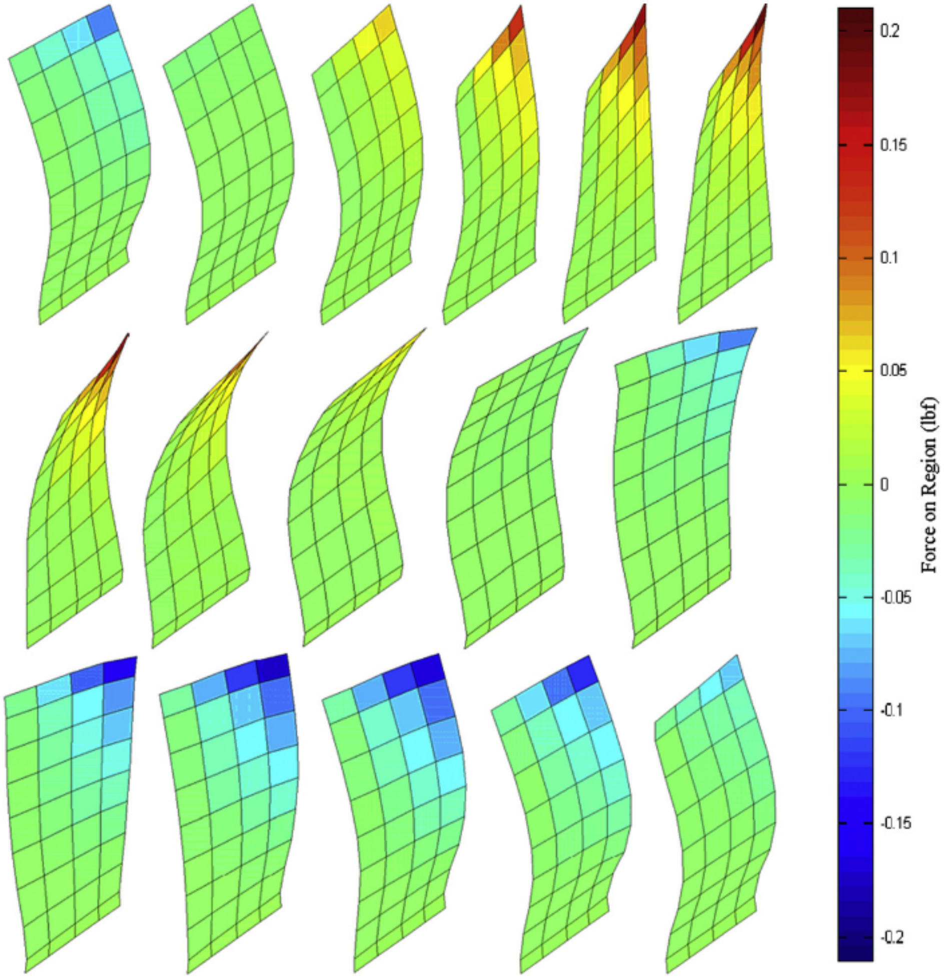

Figure 2.16: Deformation measurements (not to scale) and inversely determined loads, from Roy et al., 2006

In summary, it can be stated that the determination of elastic loads based on optical measurements is not common practice in the context of experimental aeroelasticity. Based on published literature, a viable approach is to use a beam model in combination with an inverse modeling approach, which related the structural response to the loading that is expressed in terms of a limited number of degrees of freedom.

INERTIAL LOADS DETERMINATION

When a structure is undergoing dynamic deformations, it experiences inertial loads in addition to the elastic loads. The inertial force per unit length, I' can be given in the following form for a one-dimensional beam:

$$I'(z,t) = \mu_m(z)\frac{\partial^2 w(z,t)}{\partial t^2}\,. \tag{2.15}$$

If an accurate mass distribution of the structure is available, the linear mass of the beam μ_m is known. The inertial force can in this case be obtained from measurements of the beam's acceleration, i.e., the second temporal derivative of the deflection. In aeroelastic wind tunnel testing, acceleration is one of the most frequently measured quantities through the use of accelerometer sensors installed inside the experimental model. In the context of optical measurements, measuring the acceleration may be considered challenging because the quantity that is measured optically is either the displacement or the local deformation. This means that two temporal derivatives have to be applied to the experimental data to obtain the acceleration. Similar to the considerations for the determination of the elastic load, the differentiation of the experimental data, which is typically performed using a finite difference scheme, is impaired by the presence of random measurement errors. However, two decisive factors make the determination of the inertial load based on deformation measurements considerably more attainable than the elastic load. The first factor is that the double-differentiation that is required for the inertial load determination is less critical in terms of the error amplification than the quadruple-differentiation that would be required for Eq. (2.14). The second factor is that the required differentiation is temporal and not spatial, which implies that the error amplification does not relate to the spatial resolution of the tracked points, but to the temporal resolution of the measurements. In the integrated measurement approach, high-speed cameras with frame rates of several kilohertz are used because these are required for the aerodynamic measurements. It thus assumed that the temporal resolution of the optical measurements is high enough to make use of commonly available temporal filters for obtaining the acceleration (see, e.g., Black et al., 2010; Walker et al., 2009; P. Wu et al., 2010). This makes the determination of the inertial loads from deformation measurements obtained with the integrated optical approach considerably less challenging than the determination of the elastic loads.

2.3. IMPLEMENTATIONS OF THE AEROELASTIC CHARACTERIZATION

In this section, the implementation of an aeroelastic characterization in an experimental framework is described. An experimental aeroelastic characterization involves the quantification of the three forces in Collar's triangle based on measurements performed in a wind tunnel. It is therefore a data processing step that follows after the aerodynamic and structural loads determination described in the previous section (see Fig. 1.8). The quantification of Collar's triangle of forces based on aerodynamic and structural measurements can be implemented in two different ways that are both outlined in this section, and applied in Chapter 4 and Chapter 5 of this thesis, respectively.

Generally, when analyzing an aeroelastic problem, it is common to formulate the equations of motion, which can be given in the following form:

$$(\boldsymbol{M}+\boldsymbol{M}_{\text{aero}})\,\ddot{\boldsymbol{\xi}}+(\boldsymbol{C}+\boldsymbol{C}_{\text{aero}})\,\dot{\boldsymbol{\xi}}+(\boldsymbol{K}+\boldsymbol{K}_{\text{aero}})\,\boldsymbol{\xi}=\boldsymbol{F}_{\text{external}}\,. \tag{2.16}$$

Here, the matrices $\boldsymbol{M}$, $\boldsymbol{C}$, and $\boldsymbol{K}$ relate to the structural properties of mass, damping, and stiffness, respectively, while the vector $\boldsymbol{\xi}$ contains the degrees of freedom of the aeroelastic system. The contribution of the aerodynamics in the equations of motion is split into three components via the introduction of the aerodynamic (added) mass $\boldsymbol{M}_{\text{aero}}$, the aerodynamic damping $\boldsymbol{C}_{\text{aero}}$, and the aerodynamic stiffness matrix $\boldsymbol{K}_{\text{aero}}$. The external force on the right side of Eq. (2.16) contains all remaining force contributions, for example due to propulsion, gust excitation, and gravity.

In the context of an experimental characterization, the aerodynamic loads, including the loads occurring due to gust excitation or control surface deflection, are determined as one force, which may be labeled as A. Similarly, the structural inertial contribution $\boldsymbol{M}\ddot{\boldsymbol{\xi}}$ can be labeled as I. The remaining structural load components due to stiffness and structural damping may then be labeled as $\boldsymbol{C}\dot{\boldsymbol{\xi}}+\boldsymbol{K}\boldsymbol{\xi}=E$. The structural damping, accounted for through the matrix $\boldsymbol{C}$, is usually small for typical structures and may be neglected. When also neglecting the other sources of external forces, the following expression results:

$$A+E+I=0\,, \tag{2.17}$$

which states that the sum of the forces in Collar's triangle is zero. This formulation is very useful in the context of an experimental aeroelastic characterization where these three forces are attempted to be analyzed individually. When all forces have been determined experimentally, the three forces can be added together and Eq. (2.17) can be used to perform an accuracy assessment of the measurement approach by quantifying the measurement residual, which is the difference of the sum from zero. This first approach to an aeroelastic characterization is visualized in Fig. 2.17 and applied in Chapter 4 of this thesis, in the context of a proof of concept study for the aerodynamic and structural loads determination method.

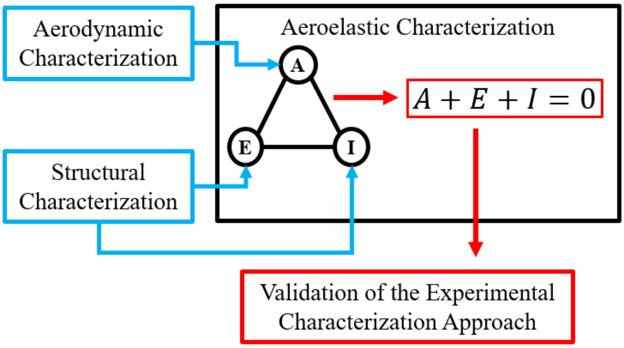

Figure 2.17: aeroelastic characterization approach applied in Chapter 4 of this thesis

As a second, alternative approach to an aeroelastic characterization, Eq. (2.17) can be used to calculate the third aeroelastic force in a situation where two of the forces have been determined experimentally, while the third force is more difficult to determine from experimental measurements. When considering the discussion of the previous sections, this typically applies to the elastic force, which requires the largest structural modeling effort for its determination based on optical measurements. Using Eq. (2.17), the elastic force can thus also be evaluated using the previously determined aerodynamic and inertial forces. This approach, visualized in Fig. 2.18, is followed in Chapter 5 for the aeroelastic characterization study of a highly flexible wing. Theoretically, a similar approach could be implemented that determines the aerodynamic force implicitly using only structural measurements. The development of such an approach is however outside of the scope of this thesis.

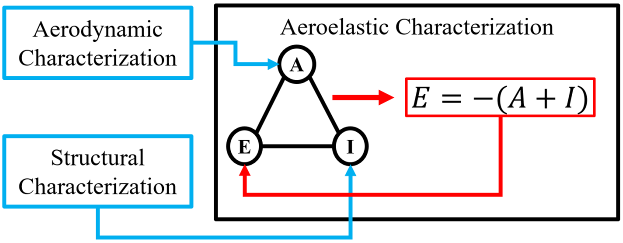

Figure 2.18: aeroelastic characterization approach applied in Chapter 5 of this thesis

3

DEVELOPMENT OF AN INTEGRATED OPTICAL MEASUREMENT APPROACH

In this chapter, the rigid body motion and unsteady aerodynamic loads of a pitching wing model that features an actuated trailing edge flap are determined based on integrated optical measurements with a Lagrangian particle tracking system. The flow field measurements are obtained by tracking HFSB flow tracers, while the structural measurements are performed by tracking markers on the model surface. The unsteady angle of attack and flap deflection angle of the wing are determined from the marker tracking data by fitting a rigid body model, that accounts for the motion degrees of freedom of the wing, to the measurements. For the determination of the unsteady aerodynamic loads from the flow field measurements, two different approaches are evaluated, which are both based on unsteady potential flow theory and produce results that are in good agreement with the reference measurements from pressure transducers.

Parts of this chapter have been published as: Mertens, C., Sciacchitano, A., van Oudheusden, B. W. and Sodja, J. (2021). An integrated measurement approach for the determination of the aerodynamic loads and structural motion for unsteady airfoils. *Journal of Fluids and Structures, 103*, 103293.

3.1. BACKGROUND

This chapter demonstrates a novel experimental approach that facilitates non-intrusive measurements of the structural motion and the aerodynamic loads that act on moving and/or deforming wings. As discussed in the previous chapter, optical measurement techniques for aeroelastic wind tunnel testing have already received considerable attention in the published literature. However, until now, the characterization of the structural and the aerodynamic response requires the simultaneous application of either multiple diagnostic techniques or multiple data processing tools. This complicates the experimental setup and increases the data processing effort and therefore limits the amount of information that can be extracted from the experiment. To relieve this complication, it was recently demonstrated that the STB algorithm of Schanz et al. (2016) is, in addition to the tracking of flow tracer particles, also suitable for tracking circular structural markers, and can therefore be used in a photogrammetric point tracking approach (Mitrotta et al., 2022). The same measurement principle is followed in this chapter to obtain simultaneous measurements of the unsteady flow field and structural marker positions on a pitching wing with an actuated flap. Subsequently, the unsteady angle of attack and flap deflection angle are determined from the measured marker positions using a regression approach based on the two degrees of freedom of the rigid body wing/flap motion, and the measurements of the unsteady flow field are used to determine the aerodynamic response in terms of the lift, pitching moment and surface pressure distribution based on unsteady potential flow theory. The results for the structural measurements are validated with the input signals of the actuators that produce the rigid body motion. The aerodynamic load results are compared to reference data based on measurements with differential pressure transducers.

3.2. EXPERIMENTAL SETUP AND PROCEDURES

3.2.1. WIND TUNNEL SETUP

The experiments are conducted in the Open Jet Facility (OJF) at the Delft University of Technology. The OJF is an open test section, closed return wind tunnel with an octagonal outlet (2.85 m × 2.85 m) and a nominal freestream turbulence intensity of 0.5%. For the experiments, the wind tunnel is operated at a freestream velocity of $U_\infty = 5.6\,\mathrm{m\,s^{-1}}$ (Reynolds number $\mathrm{Re} = \rho U_\infty c/\mu_d = 150{,}000$), and the investigated wing model is mounted vertically in the test section. The rectangular wing (chord length $c = 0.40\,\mathrm{m}$, span width $s = 1.45\,\mathrm{m}$) is equipped with two circular end plates, where the top plate is attached to a support frame and the bottom plate is mounted on a steel frame that also holds the pitching mechanism. The latter controls the angle of attack oscillations $\alpha(t)$ of the model around the pitch axis, which is located at $x/c = 0.3125$. The pitching motion is described by $\alpha(t) = \alpha_\mathrm{m} + \alpha_\mathrm{amp}\sin(2\pi t/T)$, where α_m is the mean angle, α_amp is the amplitude and T is the period of the pitching motion. The pitching frequency is $f_p = 0.39\,\mathrm{Hz}$, meaning that the length of the period is $T = 2.55\,\mathrm{s}$. This corresponds to a reduced frequency of $k = f_p \pi c U_\infty^{-1} = 0.09$, which is in the unsteady aerodynamics regime (Leishman, 2006). The setup is mounted on a rotation table that allows setting the mean angle. The main parameters of the experimental setup are summarized in Table 3.1. All relevant components of the wind tunnel setup are shown in Fig. 3.1.

Table 3.1: Overview of the experimental parameters

Parameter	Symbol	Value
Freestream velocity	U_∞	$5.6\,\mathrm{m\,s^{-1}}$
Chord length	c	0.40 m
Span width	s	1.45 m
Reynolds number	Re	150,000
Motion period	T	2.55 s
Reduced frequency	k	0.09
Mean angle	α_m	0.25°
Pitch amplitude	α_amp	4.00°

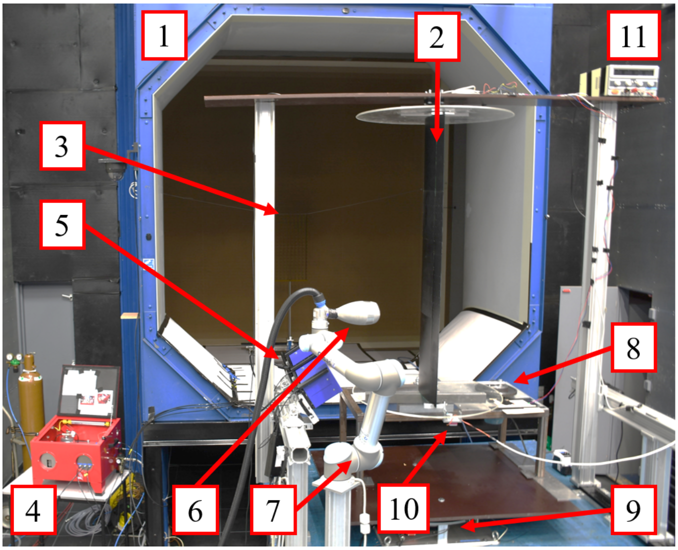

1. Wind tunnel nozzle exit
2. Wing model
3. HFSB seeding rake
4. HFSB fluid supply unit
5. LED arrays
6. MiniShaker Aero
7. Robotic arm
8. Pitching mechanism
9. Rotation table
10. Flap actuation servomotor
11. Servomotor power supply

Figure 3.1: Photo of the experimental setup in the wind tunnel test section, looking upstream

3.2.2. WING MODEL

The experimental model is a rigid wing with a NACA 0018 airfoil featuring a movable trailing edge flap that is hinged at $x/c = 0.75$, as illustrated in Fig. 3.2. The design of this model has been motivated in relation to the general framework of the "Smart Rotor" concept (Barlas & van Kuik, 2010), which aims at reducing construction, maintenance, and operation costs of wind energy systems by reducing the peak loads in wind turbine operation via active shape modification of the rotor blades. The model is equipped with 24 Honeywell HSCS-RRN-1.6MD-SA5 differential pressure transducers (measurement range ±160 Pa, nominal accuracy ±4 Pa) that are installed inside the model and connected to 48 surface pressure taps. The taps are located along a diagonal line oriented at 15° with respect to the inflow direction to reduce the effect of the upstream sensors on the downstream measurements. The sensors are used to measure the pressure difference between the model's top and bottom surfaces at specific chordwise positions. These measurements are used as a reference for the flow field-based load determination. The procedure to generate the reference data from the pressure transducer measurements is described in Sec. 3.2.4. The active load reduction capabilities of the model are provided by a controller that acts based on the aerodynamic load measured using only 8 of the 24 differential pressure sensors to improve the response time, as discussed in detail by Fernández Barrio et al. (2020). The measured sensor signals are integrated over the chord using a trapezoidal integration scheme to provide an estimate of the instantaneous lift force (see Eq. (2.3) in Sec. 2.2.1). Based on the measured lift, the controller sends a signal to a JR DS8711HV servomotor, which is mounted on the bottom end plate and attached to the movable trailing edge flap, to counteract the unsteady loads induced by the pitching of the model, to maintain a constant value of the lift.

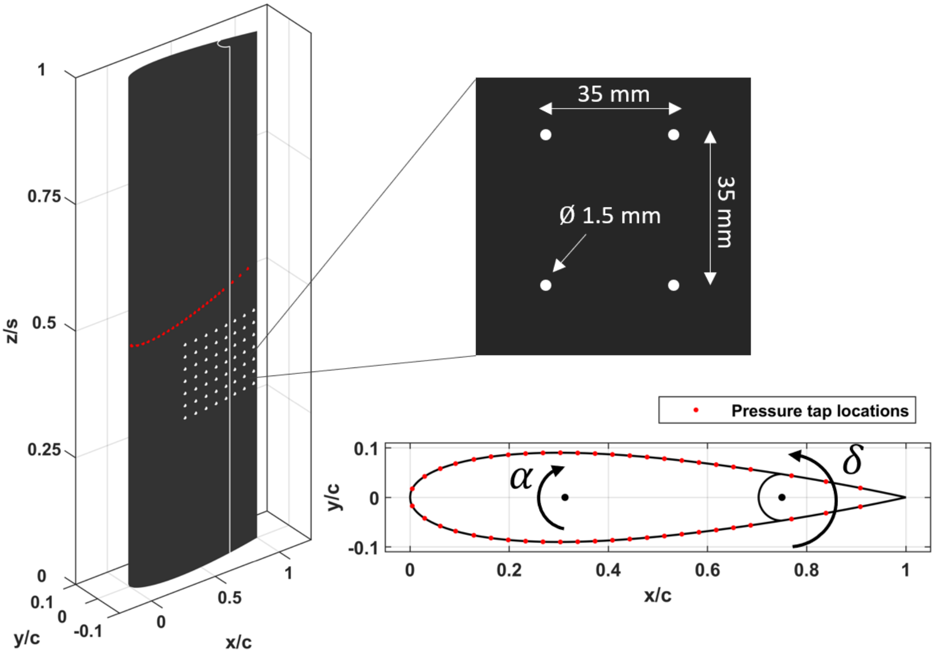

Figure 3.2: Illustration of the wing model with pressure tap locations (indicated in red) and marker grid

To perform the optical measurements of the structure, the wing model is painted black with a rectangular grid of 56 white markers (diameter 1.5 mm, spacing 35 mm) located between $0.35 < x/c < 1$ and below the line of pressure sensors at mid-span, as shown in Fig. 3.2. The location of the pitch axis and the flap hinge are indicated in Fig. 3.2 as well, along with the positive direction of rotation for the angle of attack α and the flap deflection angle δ. To prevent laminar boundary layer separation near the leading edge, a zig-zag turbulator strip (thickness 2 mm, width 12 mm, pitch 60°) is installed on both sides of the wing at $x/c = 0.1$. Results from two different experimental test cases are analyzed, one where the flap is fixed with respect to the wing and one with actuated trailing edge flap. The phase-averaged lift coefficient, $C_\ell = L'(\frac{1}{2}\rho U_\infty^2)^{-1}$, calculated from the measurements with the differential pressure transducers acquired over a total of 45 motion periods, is shown in Fig. 3.3 for the pitching wing with fixed flap and with the flap actuated by the controller. The error bars indicate the standard deviation of the phase-averaging procedure. With the employed controller settings, a reduction in the magnitude of the unsteady loads of about 80% is achieved, while the standard deviation is increased by about 40% due to the period-to-period variation in the flap motion, which is introduced by the controller as a result of the measurement noise in the pressure sensors signals.

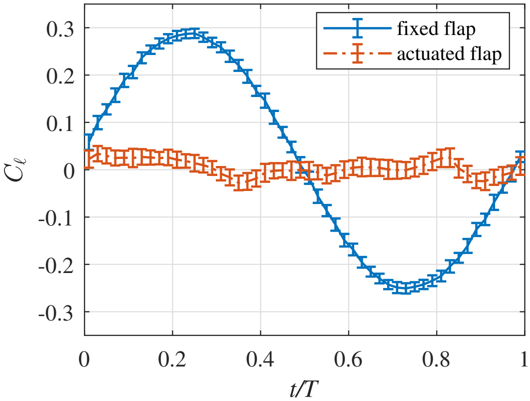

Figure 3.3: Phase-averaged lift coefficient over the period for the pitching wing with fixed and actuated flap

Integrated optical measurements are conducted for both test cases. For the test case with actuated flap, a separate test was performed on the pitching wing, where the controller output, which is the servomotor input signal, is stored. The recorded controller output is then phase-averaged and imposed on the servomotor during the optical measurements, which means that when the measurements are acquired for the test case with actuated flap, the controller itself is not active. This procedure improves the periodicity of the flap motion and prevents spurious flap deflection behavior when the pressure taps would become contaminated by the HFSB seeding.

3.2.3. LAGRANGIAN PARTICLE TRACKING SYSTEM

The system used for image recording of the integrated optical measurements is a LaVision MiniShaker Aero CVV probe (Schneiders et al., 2018) mounted on a Universal Robots UR5 robotic arm, which has six motion degrees of freedom and a maximum reach of 0.85 m. The controlled positioning of the CVV in space with the robotic arm enables the measurement of several adjacent volumes without performing repeated calibrations of the CVV. Furthermore, it also allows a simple merging of the measurement volumes during post-processing, which facilitates the measurement of flow fields around objects on a cubic meter scale (Jux et al., 2018). The CVV features four digital cameras for image acquisition, that are mounted in a compact housing (dimensions 130 mm × 90 mm × 80 mm). The flow is seeded with HFSBs that are generated by a 450 mm × 950 mm seeding rake with 200 bubble-producing nozzles, which nominally produce 30 000 bubbles per second each, as described by Engler Faleiros et al. (2019). To improve the seeding concentration and to minimize the influence of the seeding generator on the turbulence intensity of the freestream, the seeding generator is placed in the settling chamber of the wind tunnel, upstream of the wind tunnel nozzle. The cross-section of the seeded flow region in the test section resulting from this setup is ca. 200 mm × 200 mm. The illumination of the HFSB flow tracers is achieved using two LaVision LED-Flashlight 300 illumination units mounted side by side to illuminate a chordwise region of 800 mm length, corresponding to $-0.5 < x/c < 1.5$ of the wing chord. This results in a total measurement volume size of about 32 L. The spanwise region for the flow measurements is identical to the spanwise region with surface markers, as shown in Fig. 3.2. It is expected that at this position, the spanwise component of the flow velocity is negligible compared to the other two flow components which allows the sectional flow field to be analyzed in a spanwise-averaged manner.

Three different stations of the CVV probe with respect to the wing are used, as illustrated in a two-dimensional view from the top in Fig. 3.4. The CVV position near the trailing edge is located about 50% further away from the wing than the other two CVV positions, to capture all surface markers over the full pitching motion and flap deflection range. The distances d_1 and d_2 indicated in Fig. 3.4 are approximately 0.4 m, whereas d_3 is approximately 0.6 m. These distances are sufficient to limit the effect of the presence of the CVV probe on the flow velocity around the model to less than 1% within a radius of 0.2 m, corresponding to $0.5c$, around the wing (Jux et al., 2018). The larger distance d_3 partially impairs the quality of the flow field measurements from that CVV position, which exhibits larger values of random noise due to the low tomographic aperture angle of the CVV, as discussed in detail by Schneiders et al. (2018). The flow field measurements cover only one side of the wing, in view of the symmetry of the pitching geometry. For analyzing the loads, LPT measurements with a phase difference of $\Delta t/T = 0.5$ are combined, to reconstruct a flow field measurement that covers both sides of the wing.

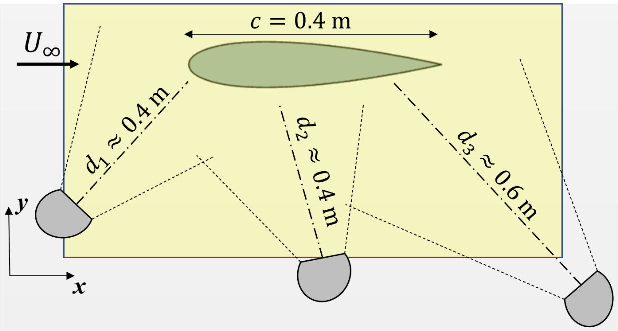

Figure 3.4: Sketch of the three CVV positions with respect to the wing and the illuminated volume

The particle images are acquired at a sampling frequency of $f_s = 700$ Hz and processed with the LaVision DaVis 10 software. The procedure for obtaining the flow field measurements from the images consists of applying a temporal high-pass filter to the images to remove light reflections (Sciacchitano & Scarano, 2014), performing a volume self-calibration (Wieneke, 2008), generating a non-uniform optical transfer function (Schanz et al., 2013) and then applying the STB algorithm (Schanz et al., 2016). The Lagrangian particle tracks that result from this procedure for the image data from 45 recorded pitching motion cycles per CVV position are allocated to 100 temporal bins, each spanning 1% of the pitching motion period T. Subsequently, the particle track data is ensemble-averaged spatially to a two-dimensional Cartesian grid with 5 mm grid spacing (i.e. 1.25% of the chord), based on a bin size of 20 mm × 20 mm with 75% overlap, hence producing phase-resolved flow field measurements in a spanwise-averaged sense. The ensemble averaging is performed using a top-hat filtering approach, as described by Agüera et al. (2016). Subsequently, a temporal sliding-average filter with a window size of 5% of the period is applied to each grid point to further reduce random errors in the unsteady flow field data. The measurement uncertainty of the flow fields is estimated by comparing the data in the overlapping regions of the adjacent measurement volumes, analogous to the procedure employed by Jux et al. (2018). The root mean square (RMS) of the discrepancies in the measured velocity magnitude is around 3% of the local velocity magnitude for the CVV positions 1 and 2, and around 7% for the CVV position 3. The data processing for the model position determination begins with removing the flow tracer information from the particle images by applying a temporal low-pass filter to the acquired images. A sliding minimum filter in time over a kernel of three images is used, as suggested by Mitrotta et al. (2022). In view of the relatively low pitching frequency and to reduce the processing time, only every seventh image from the series of acquired images is used in the subsequent position determination procedure. The resultant reduced sampling frequency of $f_s = 100\,\text{Hz}$ corresponds to $f_s \times T = 255$ images per pitching cycle. After the image filtering, the STB algorithm is used to perform Lagrangian particle tracking of the markers on the wing surface.

3.2.4. PRESSURE TRANSDUCER MEASUREMENTS DATA PROCESSING

The pressure transducer measurements are acquired over 45 complete pitching cycles at a sampling rate of $f_s = 32\,\text{Hz}$. Because the LPT measurements are conducted only on one side of the wing, a direct comparison between the loads derived from the flow field measurements and the differential pressure transducer data is not possible. To produce consistent reference data for the LPT-based loads, the pressure transducer measurements from two phase instants separated by $\Delta t/T = 0.5$, which correspond to one LPT-based load result, are combined to generate one reference data point, exploiting the symmetry of the airfoil shape. Based on the assumption that the aerodynamic load scales linearly with the angle of attack α for small values of α, it can be assumed that the LPT-based load, that is obtained from the two separate flow field measurements, will be equivalent to the mean value of the aerodynamic load at the two phase instants where the flow field was measured.

The procedure to generate the reference data for the lift coefficient C_ℓ from the differential pressure transducer measurements is illustrated in Fig. 3.5, for the time instant $t/T = 0.25$ and both experimental test cases, i.e., with fixed flap and with actuated flap. The results for C_ℓ, as calculated from the pressure transducer measurements by integrating the pressure difference along the chord (see Eq. (2.3)), at $(t/T)_1 = 0.25$, where $\alpha = \alpha_\text{m} + \alpha_\text{amp}$, are shown in blue together with C_ℓ measurements at $(t/T)_2 =$

$(t/T)_1 + \Delta t/T = 0.25 + 0.5 = 0.75$, where $\alpha = \alpha_\mathrm{m} - \alpha_\mathrm{amp}$, with the sign switched (shown in orange). Although the set of samples for each individual time instant is distributed relatively smoothly, the distribution of the combined ensemble of samples is bi-modal because of the non-zero mean angle α_m. The same procedure that is illustrated for $t/T = 0.25$ in Fig. 3.5 is applied at 25 time instants over the first half of the period $0 < t/T < 0.5$.

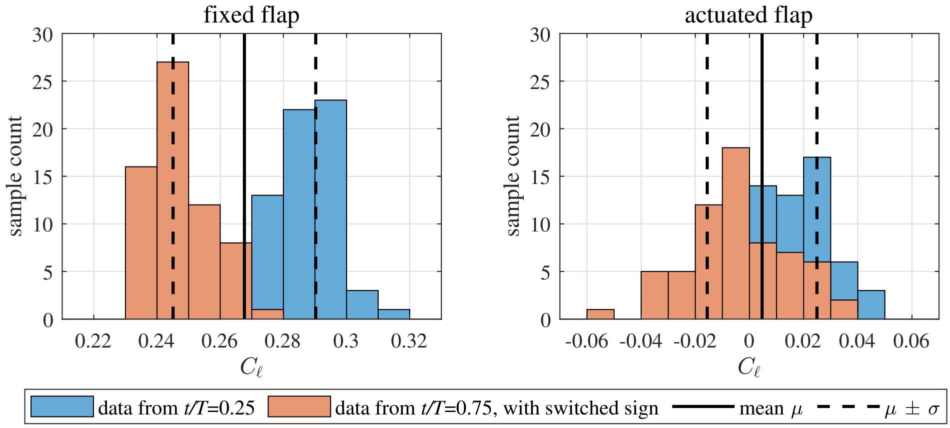

Figure 3.5: Visualization of the procedure for generating the reference data for the LPT-based loads from the differential pressure transducer measurements. Example given for the phase instant $t/T = 0.25$

The resulting lift coefficient C_ℓ over time is shown in Fig. 3.6, together with the lift coefficient of the two individual semi-periods. The reference data points are the sample mean μ for the respective time instant and the error bars indicate the standard deviation $\pm\sigma$, which is on average ±0.021 with fixed flap and ±0.023 with actuated flap.

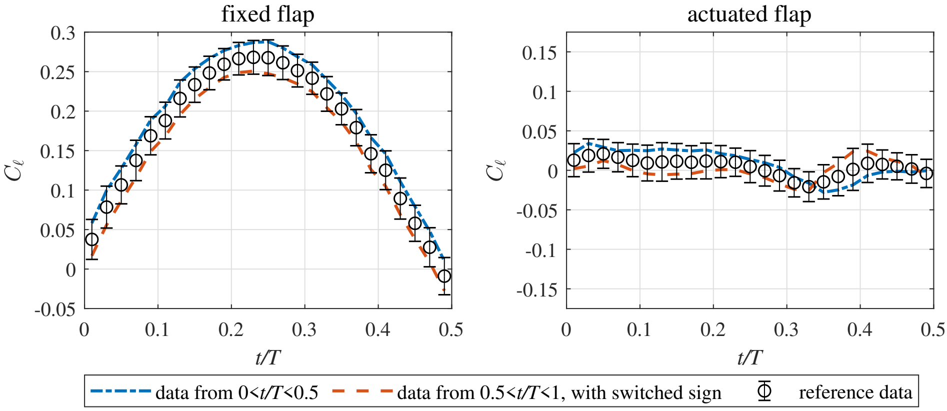

Figure 3.6: Results for the reference lift based on the pressure transducer measurements

The reference data is used for the comparison with the results of the LPT-based lift determination methods. Following a similar procedure as for the lift, sets of reference data are also determined for the pitching moment and surface pressure difference.

3.3. DETERMINATION OF ANGLE OF ATTACK AND FLAP DEFLECTION

The LPT measurements of the marker positions are analyzed to determine the angle of attack and flap deflection angle. The first step is the analysis of the measurements of the static wing to determine the model position in laboratory coordinates and to illustrate the outlier filtering approach. Subsequently, the measurements of the pitching wing with fixed flap are presented and the results for the pitching wing with actuated flap are discussed in detail. The latter case is more challenging to characterize experimentally as the number of available marker position measurements per motion degree of freedom is smaller, compared to the other configurations (i.e., static wing and fixed flap).

3.3.1. MARKER-BASED WING POSITION DETERMINATION

The marker position measurements are obtained in the laboratory coordinate system of the UR5 robot. The reference positions of the markers in the wing coordinate system are known and there are six unknown degrees of freedom (DOFs) for the coordinate transformation from the laboratory coordinates to the wing coordinates. The DOFs are found by minimizing the overall distance of the marker measurements to the nearest reference marker position for each individual measurement. This fitting procedure is described by the minimization of an objective function f:

$$\arg \min_{\varphi,\Theta,\Psi,X,Y,Z} f := \sum_{i=1}^{N} \left| \boldsymbol{R}(\varphi,\Theta,\Psi) \left(\boldsymbol{p}_i + \begin{bmatrix} X \\ Y \\ Z \end{bmatrix} \right) - \boldsymbol{r} \right|, \tag{3.1}$$

where N is the number of tracked markers, $\boldsymbol{p}_i$ is the position vector of the ith marker track in laboratory coordinates, X, Y, and Z are the translations of the coordinate transformation, and $\boldsymbol{r}$ is the position vector of the nearest reference marker in wing coordinates. φ, Θ and Ψ are the rotation angles of the coordinate transformation around the x, y, and z axes respectively, with the rotation matrix $\boldsymbol{R} = \boldsymbol{R}_z(\Psi)\boldsymbol{R}_y(\Theta)\boldsymbol{R}_x(\varphi)$:

$$\boldsymbol{R} = \begin{bmatrix} \cos\Psi & -\sin\Psi & 0 \\ \sin\Psi & \cos\Psi & 0 \\ 0 & 0 & 1 \end{bmatrix} \begin{bmatrix} \cos\Theta & 0 & \sin\Theta \\ 0 & 1 & 0 \\ -\sin\Theta & 0 & \cos\Theta \end{bmatrix} \begin{bmatrix} 1 & 0 & 0 \\ 0 & \cos\varphi & -\sin\varphi \\ 0 & \sin\varphi & \cos\varphi \end{bmatrix}. \tag{3.2}$$

The rotation Ψ around the vertical z-axis is directly related to the angle of attack, through $\alpha = -\Psi + \alpha_{\text{lab}}$. Note that α is defined as nose-up (clockwise) positive. The angle of the laboratory coordinate system with respect to the inflow, α_{lab}, is expected to be small based on the chosen experimental settings and can be determined by analyzing position measurements of the static wing at $\alpha = 0°$. This angle is defined by positioning the symmetric wing so that $C_\ell(\alpha) = 0$, which is verified by the measurements with the differential pressure transducers.

The result of the six DOFs fitting procedure is illustrated in Fig. 3.7 for marker tracking data from 100 images of the static wing at $\alpha = 0°$. The fitting procedure is effective despite the presence of outliers which mainly occur due to light reflections in the particle images at the trailing edge and the wing-flap junction. The average number of marker tracks per time step including the outliers is 54.9, which is about 98% of the number of reference markers on the model. The low tomographic aperture angle of the CVV results in a relatively large measurement noise along the direction of the CVV viewing axis (see Schneiders et al., 2018). The marker position measurements plotted as dots in Fig. 3.7 therefore appear as short line segments crossing the reference grid marker positions. The value for α_{lab} that is found from this analysis is $\Psi_{\alpha=0^\circ} = \alpha_{\text{lab}} = 0.04^\circ$.

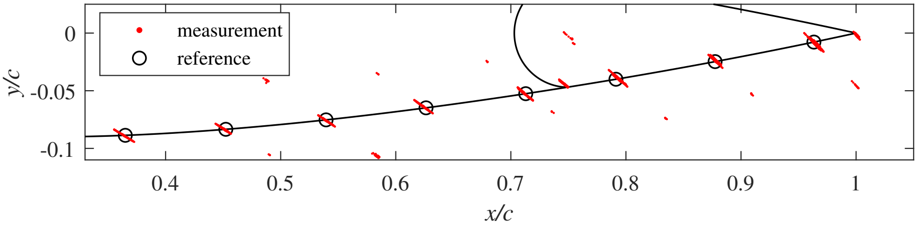

Figure 3.7: Fitting of marker position measurements of the static wing to the reference grid

After an initial application of the fitting procedure, outliers are removed from the marker tracking data by setting a threshold for the distance from the measurement point to the nearest reference marker. The outlier threshold that is used is two times the average distance of all measurements to their respective nearest reference marker. When the optimization is performed for the second time for the data shown in Fig. 3.7 after removing the outliers, the average number of marker tracks per time step reduces to 48.2, which is about 86% of the reference markers. The remaining average distance from the marker position measurements to the nearest reference marker is 3.01 mm before and 1.21 mm after the outlier filtering.

For the analysis of the pitching wing, the fitting procedure is performed in two steps. In the first step, the fitting is performed for 500 images of the time series using the six DOFs optimization procedure using Eqs. (3.1) and (3.2) as described above for the static test case. The origin of the wing coordinate system is placed at the rotation point x_r. The result of this first step of the analysis is shown in Fig. 3.8. It can be observed that all degrees of freedom in the optimization, except for the rotation Ψ around the vertical axis, are practically constant, with standard deviations of less than 1 mm for the translational DOFs and less than 0.1° for the rotational DOFs. Therefore, the results obtained for the five remaining DOFs X, Y, Z, φ, and Θ are averaged and then prescribed in the second step of the fitting procedure, such that in this step only Ψ is determined. The second step is performed with two iterations per time step, with the outlier filtering applied for the second iteration.

For the analysis of the pitching wing with actuated flap, the procedure is adjusted to allow for the additional degree of freedom corresponding to the flap deflection δ. This is achieved by deforming the reference marker grid in the optimization allowing for the variable flap deflection. Similar to the analysis of the pitching wing with fixed flap, the analysis is performed in two steps; after the determination of the five constant DOFs in the first step, the remaining two DOFs of the wing motion Ψ and δ are determined in the second step.

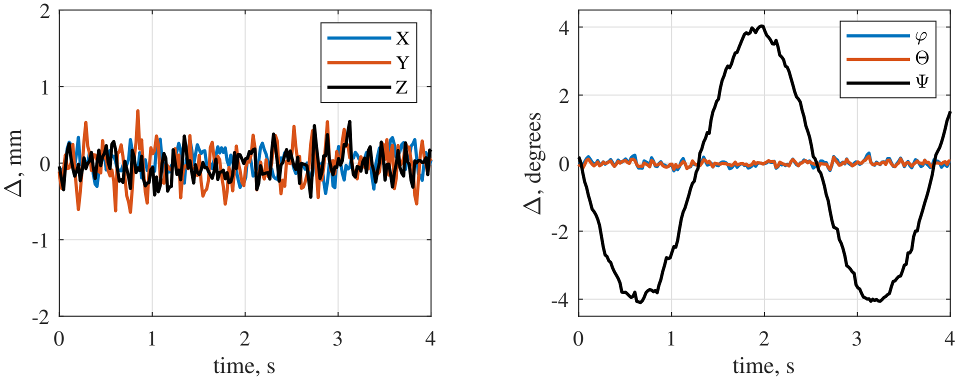

(a) translational DOFs (b) rotational DOFs

Figure 3.8: Variation in the results of the six DOFs fitting procedure for the pitching wing with fixed flap, with the Δ indicating the difference from the result for the static wing for the respective DOF

3.3.2. RESULTS

The results of the marker-based model position measurement for the pitching wing with actuated flap in terms of α and δ are shown in Figs. 3.9(a) and 3.9(b), respectively, in comparison with the corresponding validation data. The motion that is imposed by the pitching mechanism, as given in Table 3.1, is used as a reference for α, which is calculated from the measured rotation Ψ and the value that was found for α_{lab}. The measured flap deflection δ is compared to the reference flap angle which is calculated from the value of the control signal that is received by the servomotor that actuates the flap based on the kinematics of the flap hinge (see Fernández Barrio et al., 2020 for details on the flap actuation controller). The results from the marker-based position determination are sorted by phase for comparison with the reference data. Each measurement data point in Figs. 3.9(a) and 3.9(b) corresponds to the angles determined from the position measurement of the markers in one particle image.

The agreement between the determined α and the reference based on the motion imposed by the pitching mechanism is excellent, the RMS of the difference is 0.03°. The RMS of the difference between the determined flap deflection angle and the reference based on the servomotor input signal is with 0.44° somewhat larger. Some systematic differences to the reference and a higher level of random noise are expected in this case, because the servomotor that actuates the flap was operated closer to its power limit than the motor that drives the pitching mechanism, and the actual rotation imparted by the servomotor was not measured. The largest systematic difference occurs at the beginning of the pitching cycle because the signal sent to the servomotor to generate the flap motion was updated for every pitching cycle at $t/T = 0$, causing a small delay in the servomotor motion here. Apart from that, larger differences occur when the servomotor is moving slowly near the motion turning points, where the flap motion was affected by friction between the wing and the end plates, and when the servomotor is actuated at its maximum angular velocity, around $t/T = 0.4$ and $t/T = 0.8$. For the rest of the pitching cycle with $0.5 < t/T < 0.65$ and $0.85 < t/T < 1$, the agreement between the flap angle and the reference is similar to the agreement that is observed for α.

The obtained results for the wing position and flap deflection over the period are phase-averaged with a phase bin spanning 1% of the period, corresponding to the parameters used during the flow field processing. This correspondence facilitates the synchronous analysis of the phase-averaged model position and flow fields. The results obtained in this way are shown for both test cases at four phase instants in Figs. 3.10 and 3.11, respectively.

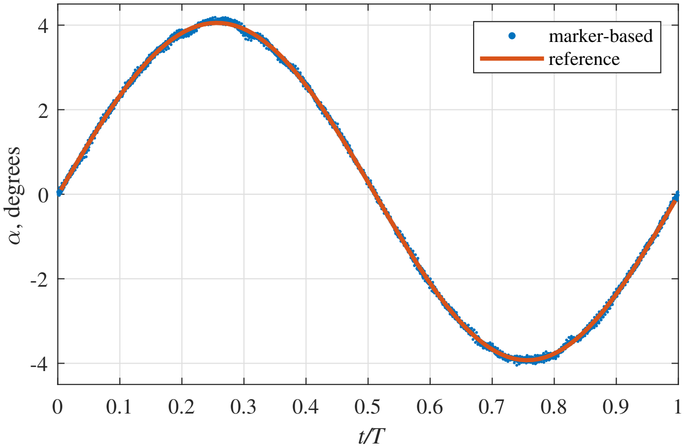

(a) angle of attack

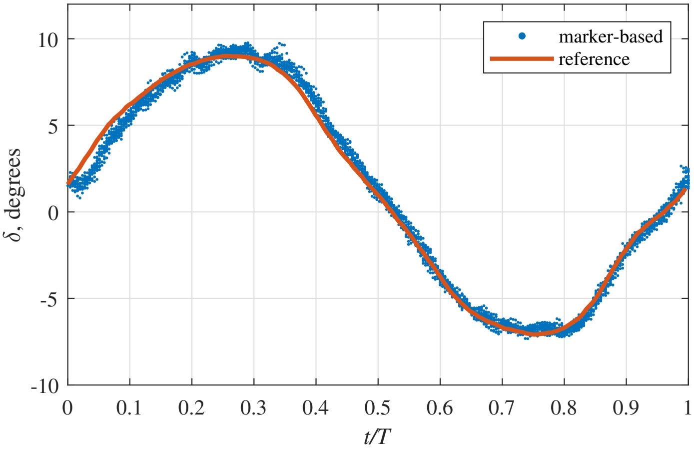

(b) flap deflection angle

Figure 3.9: Results for the angle of attack and flap deflection of the pitching wing based on the marker tracking data compared to kinematic input reference data

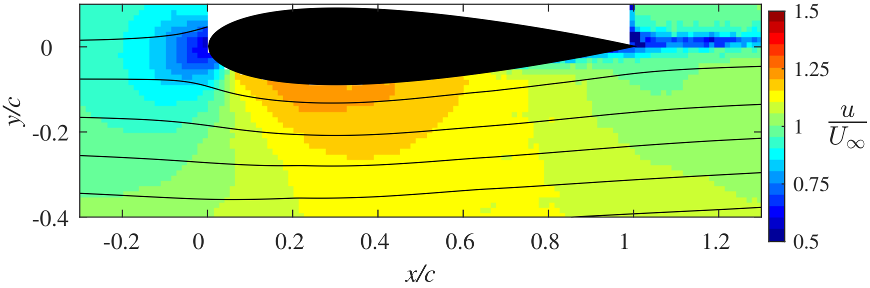

(a) $t/T = 0$

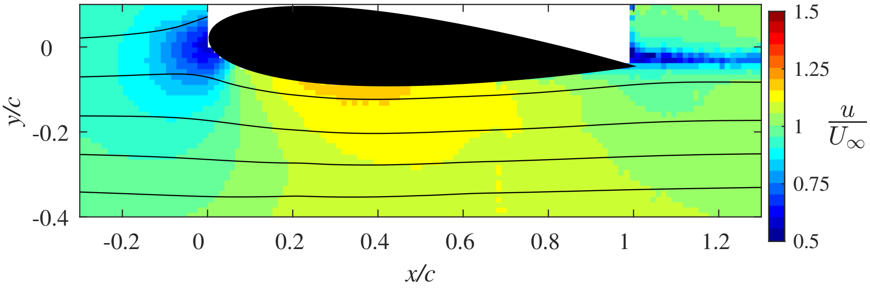

(b) $t/T = 0.25$

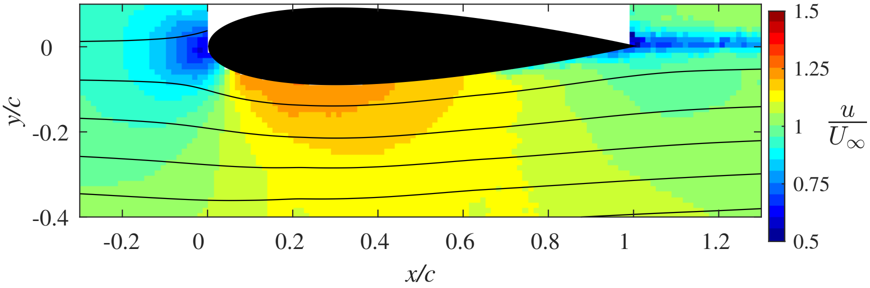

(c) $t/T = 0.5$

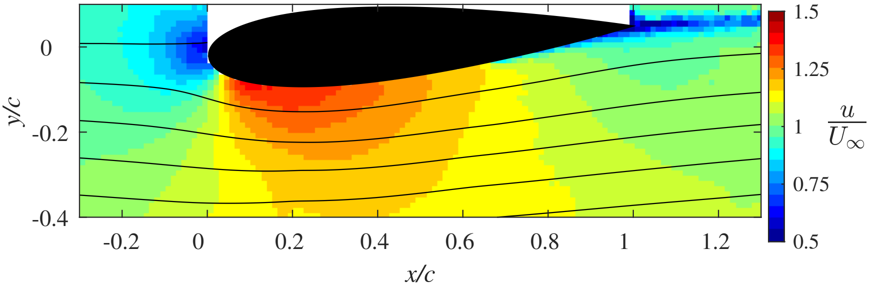

(d) $t/T = 0.75$

Figure 3.10: Flow field and marker-based wing reconstruction of the pitching wing with fixed flap

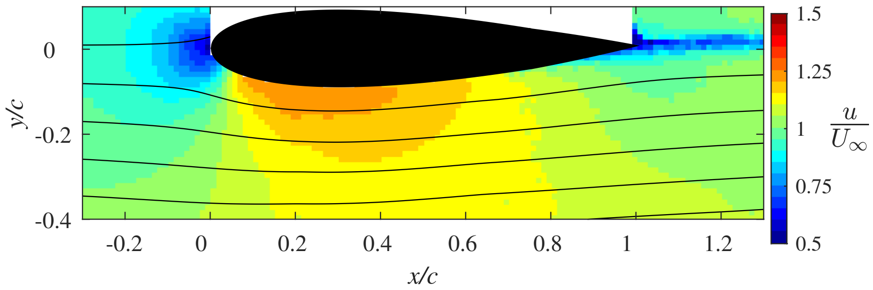

(a) $t/T = 0$

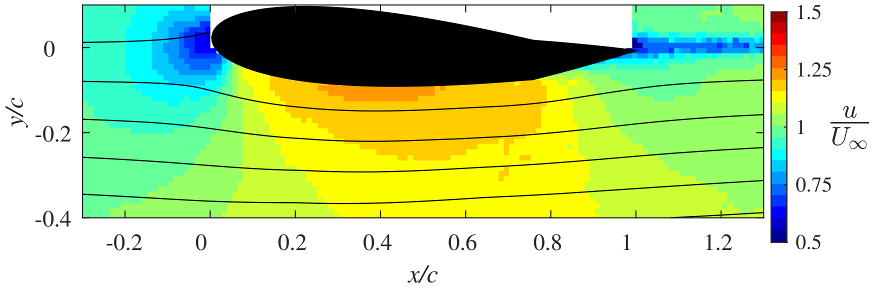

(b) $t/T = 0.25$

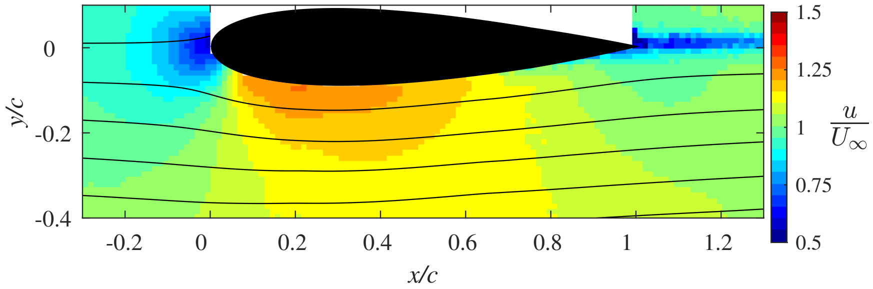

(c) $t/T = 0.5$

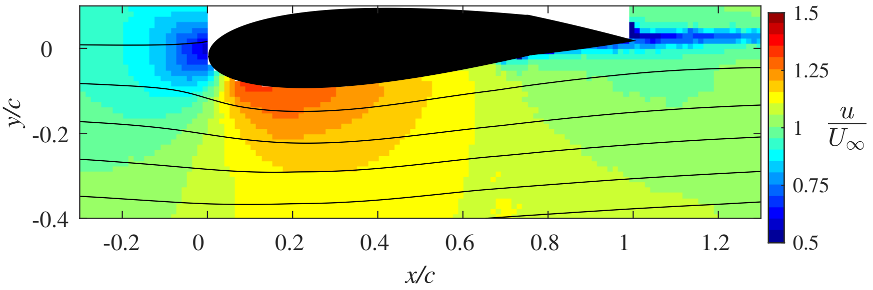

(d) $t/T = 0.75$

Figure 3.11: Flow field and marker-based wing reconstruction of the pitching wing with actuated flap

3.4. DETERMINATION OF UNSTEADY AERODYNAMIC LOADS

3.4.1. PRESSURE-BASED LOAD DETERMINATION METHOD

To calculate the aerodynamic loads on a wing section, it can be represented by a planar sheet of bound vortices along the chord line, following classical thin airfoil theory. Based on the assumption of small disturbances, the unsteady surface pressure difference along the chord $\Delta p(x,t)$ is related to the bound vortex strength distribution $\gamma_b(x,t)$ and the freestream velocity and density (see Katz and Plotkin, 2001, Eq. 13.35):

$$\Delta p(x,t) = \rho U_\infty \gamma_b(x,t) + \rho \frac{\partial}{\partial t}\int_0^x \gamma_b(\tilde{x},t)\,d\tilde{x}. \tag{3.3}$$

In the steady case, the first term in Eq. (3.3) would directly relate the value of the bound vortex strength distribution γ_b to the surface pressure difference. Therefore, this first term is labeled as the quasi-steady pressure difference, $\Delta p_{\mathrm{QS}}(x,t) = \rho U_\infty \gamma_b(x,t)$.

Assuming incompressible, inviscid, and irrotational flow, the quasi-steady surface pressure can be determined directly in a given flow velocity field using Bernoulli's equation (see Sec. 2.2.1):

$$C_{p,\mathrm{QS}} = 1 - \frac{V^2}{U_\infty^2}, \tag{3.4}$$

where V is the local velocity magnitude.

The quasi-steady *surface* pressure is challenging to evaluate from the velocity measurements due to the measurement errors and viscous effects that affect the near-wall region and is instead determined using a linear extrapolation of the flow pressure obtained from applying Eq. (3.4) in the vicinity of the wing, similar to the approach of Ragni et al. (2009). The procedure to determine the quasi-steady surface pressure on the wing from flow velocity measurements in the vicinity of the wing at different chordwise positions is described in the following.

For the chordwise positions with $x/c \leq 0.1$, it is assumed that the boundary layer region is thin, compared to the spatial bin size that is used during the ensemble averaging so that the flow measurements are not significantly affected by the presence of the boundary layer and Eq. (3.4) can be applied even close to the wing surface. Therefore, the surface pressure is determined in three steps that are applied for each vertical line of the Cartesian grid of the flow field measurement where $x/c < 0.1$:

1. Application of Eq. (3.4) to the flow measurement at the first grid point outside of the wing y_1, to determine C_{p,QS_1} at a distance of Δy_1 from the wing surface.
2. Application of Eq. (3.4) to the next following grid point away from the surface in y-direction, y_2 with C_{p,QS_2}, to approximate the pressure gradient $\frac{\partial C_{p,\mathrm{QS}_1}}{\partial y}$ with a backward finite difference as $\frac{\partial C_{p,\mathrm{QS}_1}}{\partial y} \approx \frac{C_{p,\mathrm{QS}_1} - C_{p,\mathrm{QS}_2}}{y_1 - y_2}$.
3. Extrapolation of the pressure on the wing surface $C_{p,\mathrm{QS}_\mathrm{surf}}$ from the nearest grid point with $C_{p,\mathrm{QS}_\mathrm{surf}} = C_{p,\mathrm{QS}_1} - \frac{\partial C_{p,\mathrm{QS}_1}}{\partial y}\Delta y_1$.

For the determination of $C_{p,\mathrm{QS}_{\mathrm{surf}}}$ downstream of $x/c = 0.1$, it is assumed that the application of Eq. (3.4) close to the wing surface yields erroneous results due to the presence of a thickened boundary layer. It is therefore necessary to exclude these data points from the analysis. The development of the boundary layer thickness on the wing can be roughly estimated using an empirical expression for the turbulent boundary layer on a flat plate with zero pressure gradient $\delta_{BL}(x)$ (White, 2006):

$$\delta_{BL}(x) \approx 0.16 \frac{x}{\mathrm{Re}_x^{1/7}}. \tag{3.5}$$

Despite the streamwise pressure gradient on a wing being non-zero, the relatively small angles of attack that are considered in this study justify the use of Eq. (3.5) as a first estimation of the turbulent boundary layer thickness on the wing for the purpose of excluding the grid points that are likely affected by the presence of the boundary layer from the surface pressure determination analysis. After that, the determination of the surface pressure follows the same procedure as for $x/c \leq 0.1$. This procedure is illustrated in Fig. 3.12 for the chordwise positions where x/c is 0.1, 0.3 and 0.5. For the flow field measurements from the most downstream position of the CVV, where $x/c > 0.65$, more measurement noise is observed. To reduce the sensitivity of the surface pressure result to individual data points, the pressure gradient is not determined from a finite difference in this region, but with a linear regression of multiple data points instead, in this case over 10 data points. This approach also diminishes the modeling errors associated with the application of Eq. (3.5) to a region of non-zero pressure gradient, which would affect the measurements at y_1 and y_2. The result of the linear regression is used to extrapolate the surface pressure in the chordwise region with $x/c > 0.65$, as illustrated in Fig. 3.12 for $x/c = 0.7$ and $x/c = 0.9$.

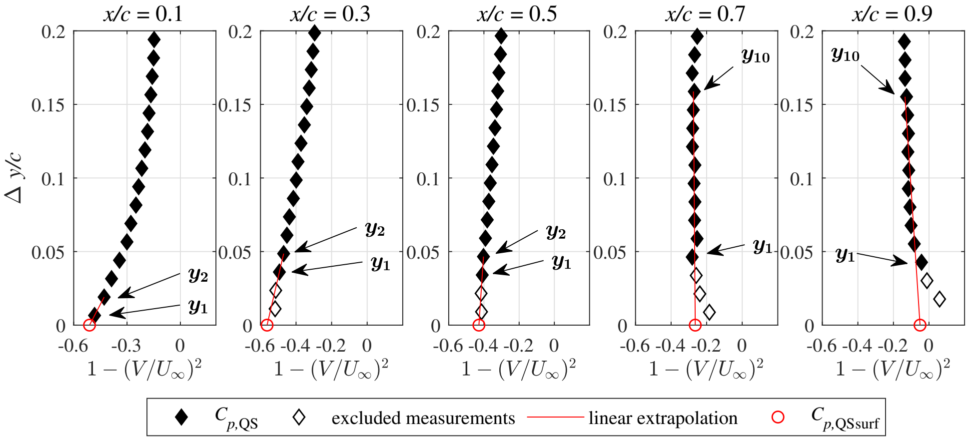

Figure 3.12: Extrapolation method for the quasi-steady surface pressure. Exemplary data from the pitching wing with fixed flap at $t/T = 0$ for five different chordwise positions

Once the quasi-steady surface pressure $C_{p,\mathrm{QS}_{\mathrm{surf}}}$ is determined for one side of the wing over the entire pitching motion period, the quasi-steady pressure difference on the wing $\Delta C_{p,\mathrm{QS}}$ is determined by subtracting measurements of $C_{p,\mathrm{QS}_{\mathrm{surf}}}$ with a phase difference of $\Delta t/T = 0.5$. This step is required as LPT measurements are conducted only on one side of the wing and exploits the fact that the airfoil is symmetric (see Sec. 3.2.4).

When the quasi-steady pressure difference is known, the unsteady surface pressure difference can be calculated with Eq. (3.3). First, the vortex-sheet strength distribution along the chord is determined from the measurement of the quasi-steady pressure difference:

$$\gamma_b(x,t) = \frac{\Delta p_{\mathrm{QS}}}{\rho U_\infty} = \frac{\Delta C_{p,\mathrm{QS}} U_\infty}{2}. \tag{3.6}$$

With this result for $\gamma_b(x,t)$, the unsteady surface pressure difference follows from Eq. (3.3). From the pressure difference, the aerodynamic loads are determined by spatial integration. If the considered angles of attack α are small, so that $\cos(\alpha) \approx 1$ and the influence of the tangential force on the lift is negligible, the unsteady lift per unit span $L'(t)$ and the lift coefficient $C_\ell(t)$ are obtained by chordwise integration of the pressure difference (see Eq. (2.3) in Sec. 2.2.1):

$$C_\ell(t) = \frac{L'(t)}{\frac{1}{2}\rho U_\infty^2 c} = \frac{\int_0^c \Delta p(x,t)dx}{\frac{1}{2}\rho U_\infty^2 c}. \tag{3.7}$$

The nose-up pitching moment per unit span $M'(t)$ and the moment coefficient $C_m(t)$ are similarly obtained by spatial integration of the pressure difference:

$$C_m(t) = \frac{M'(t)}{\frac{1}{2}\rho U_\infty^2 c^2} = \frac{\int_0^c (x_{\mathrm{ref}} - x)\Delta p(x,t)dx}{\frac{1}{2}\rho U_\infty^2 c^2}. \tag{3.8}$$

The location of the reference axis for the moment is taken to correspond to the rotation axis of the pitching wing so that $x_{\mathrm{ref}}/c = 0.3125$.

3.4.2. CIRCULATION-BASED LOAD DETERMINATION METHOD

To circumvent the explicit determination of the surface pressure, the aerodynamic loads can be expressed in terms of the circulation instead. In the considered case of a pitching wing with unsteady flow conditions, the circulation in the flow field is due to the bound vortex strength $\gamma_b(x,t)$, as well as the vorticity shed in the wake. The wake vorticity is produced as a result of the changes in bound circulation following Kelvin's theorem for the conservation of circulation. In the unsteady thin airfoil theory, it is assumed that vorticity is shed into the planar wake at the trailing edge and convected downstream at freestream velocity (Leishman, 2006).

The bound vortex strength relates to the bound circulation as:

$$\Gamma_p(x,t) = \int_0^x \gamma_b(\tilde{x},t)d\tilde{x}, \tag{3.9}$$

where $\Gamma_p(x,t)$ is the partial circulation between the leading edge and the chordwise position x so that the total bound circulation is $\Gamma_b(t) = \Gamma_p(c,t)$.

It follows that the lift can be expressed in terms of the circulation when a chordwise integral is applied to the pressure difference according to Eq. (3.3):

$$L'(t) = \int_0^c \Delta p(x,t)\,dx = \rho U_\infty \Gamma_b(t) + \rho \int_0^c \frac{\partial}{\partial t}\Gamma_p(x,t)\,dx\,. \tag{3.10}$$

The first term on the right-hand side of Eq. (3.10) is equivalent to the Kutta-Zhukovsky theorem for steady flows (see Eq. (2.12) in Sec. 2.2.1), whereas in the unsteady case, the bound circulation is time-dependent. This term can therefore be labeled as the quasi-steady lift contribution:

$$L'_{\mathrm{QS}}(t) = \rho U_\infty \Gamma_b(t)\,. \tag{3.11}$$

The second term relates to the flow acceleration effect and is labeled as:

$$L'_{\mathrm{FA}}(t) = \rho \int_0^c \frac{\partial}{\partial t}\Gamma_p(x,t)\,dx\,. \tag{3.12}$$

The unsteady lift $L'(t)$, as the sum of the quasi-steady and the flow acceleration terms, can hence be calculated from the bound circulation distribution, which is obtained from line integrals of the measured flow velocity based on Eq. (3.9). The circulation determination procedure is described in the following, preceded by a systematic analysis of the effect of the integration path.

Three exemplary integration paths are shown in Fig. 3.13(a). Path I is placed at a distance of $0.05c$ from the wing surface, which means that the upstream segment of the integration path is located at $x/c = -0.05$, the downstream segment at $x/c = 1.05$ and the streamwise segment is located at $y/c = -0.14$, to additionally account for the thickness of the wing. Integration paths II and III are placed at a distance of $0.15c$ and $0.25c$ from the wing, respectively. The paths do not form a closed integration contour, as flow field data is only available for one side, and therefore the obtained result from the corresponding partial line integral that is shown in Fig. 3.13(b) is labeled as pseudo-circulation, Γ'. Similar to the pressure-based approach, flow fields separated by half a period are thus combined in the circulation-based loads determination. For the results of the line integration shown in Fig. 3.13(b), it is necessary to subtract the respective mean value, $\bar{\Gamma}'$, from the pseudo-circulation, to facilitate a direct comparison of the results obtained from the different integration paths.

Overall, the sensitivity of the pseudo-circulation to the position of the integration path observed in Fig. 3.13 is small. A phase lag is observed with increasing distance to the wing, such that the result obtained with path III is shifted in phase by about 1% of the period with respect to the result obtained with path I. Furthermore, it appears that the amplitude of the pseudo-circulation $\hat{\Gamma}'$ is reduced with increasing distance of the integration path to the wing so that $\hat{\Gamma}'$ is approximately 3.5% smaller for path III when compared to the result obtained with path I.

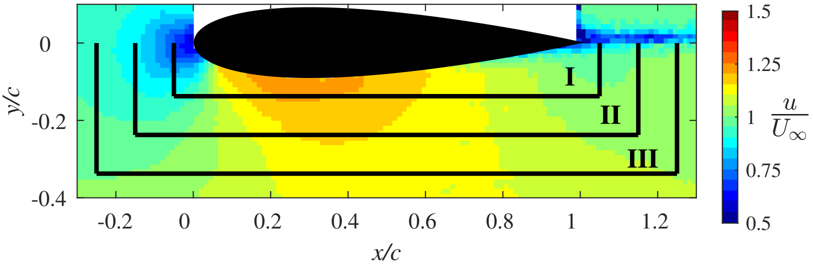

(a) position of three example integration contours

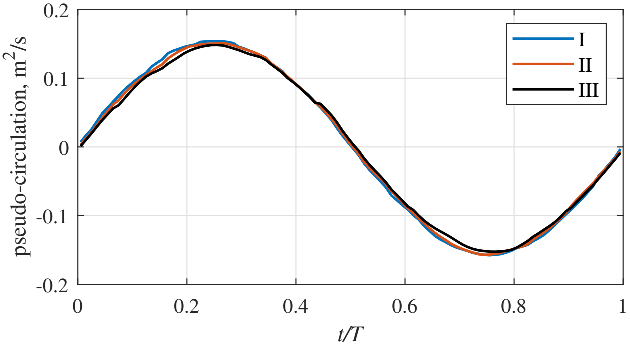

(b) results for the pseudo-circulation for the three contours

Figure 3.13: Effect of the integration path on the measured circulation around the wing

The effect of varying the position of the integration path is further analyzed by varying the distance to the wing for each one of the three line segments, while the other two distances remain constant at $0.15c$. The results are shown in Fig. 3.14, expressed in terms of the amplitude $\hat{\Gamma}'$ normalized with the reference, for which the result obtained with integration path II is used, and the lag t_{lag}, which is determined by cross-correlation with the reference. No strong systematic effect of the line segment positions on the circulation can be observed Fig. 3.14, apart from the lag, which varies as a result of varying the position of the downstream line segment (Fig. 3.14(c)). The wake of the unsteady wing contains the history of the shed vorticity, such that a phase shift of the circulation is observed when a larger fraction of the wake is included within the surface that is defined by the integration path. In Fig. 3.14(c), the dashed line describes a lag proportional to the freestream velocity, $t_{\text{lag}} = \Delta x / U_\infty$, which is in good agreement with the experimental results and therefore supports the assumption of the wake vortex sheet being shed at the trailing edge and convected downstream at U_∞. In unsteady potential flow, the circulation is independent of the positions of the upstream and streamwise segments of the integration path. This is in accordance with the measurement results shown in Fig. 3.14(a) and Fig. 3.14(b), where the largest effects are observed for the upstream and streamwise line segments when the integration path is very close to the wing, with a distance of less than $0.1c$. Additionally, small effects are observed when the integration path is close to the edge of the measurement volume, with distances larger than $0.2c$.

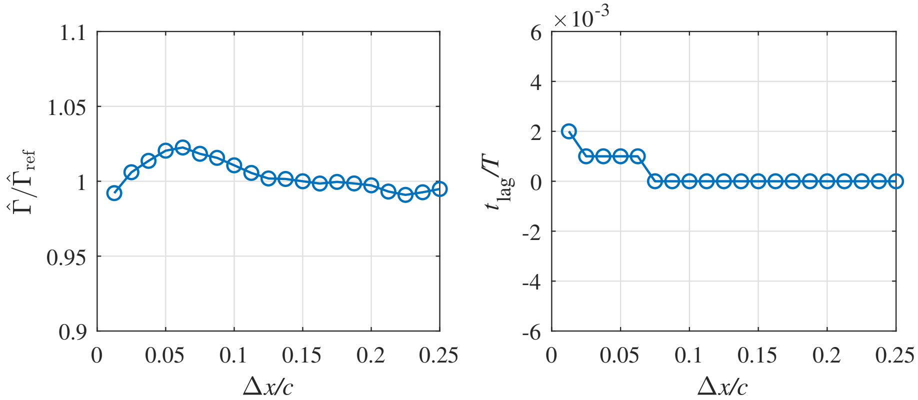

(a) variation of the upstream segment of the integration path

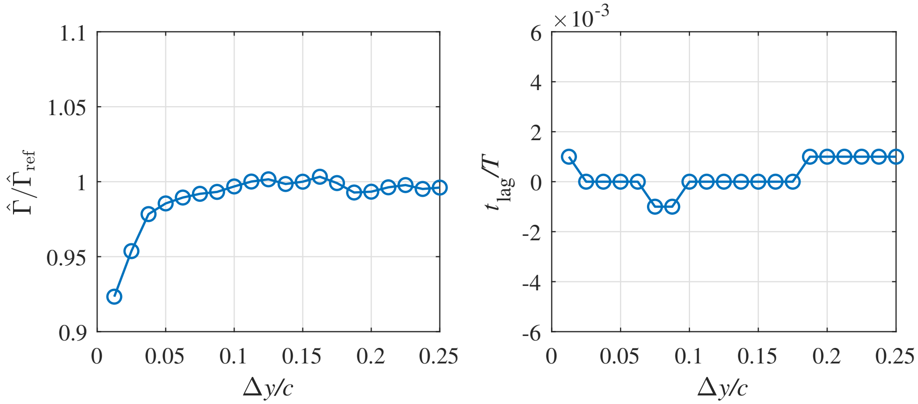

(b) variation of the streamwise segment of the integration path

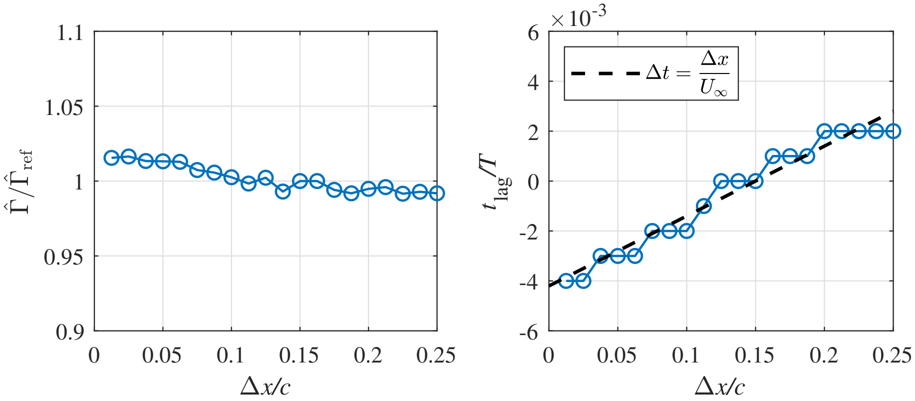

(c) variation of the downstream segment of the integration path

Figure 3.14: Sensitivity of the circulation to the location of the integration path

Based on these observations, the bound circulation $\Gamma_b(t)$ is determined in four steps:

1. Eight line integrals of velocity are calculated, for the entire period, using different integration paths with a distance to the wing between 0.1 and 0.2 chord lengths.
2. The obtained results are shifted backwards in phase by $t_{\text{lag}} = \Delta x / U_\infty$, according to the respective distance to the wing Δx.
3. The eight shifted results are averaged to one result over the period to reduce the level of random error.
4. Results with a phase difference of $\Delta t/T = 0.5$ are subtracted to determine the bound circulation.

To determine the partial bound circulation $\Gamma_p(x,t)$, a similar approach is followed, only that in step 1 the position of the downstream boundary is fixed at the particular chordwise position x, while the positions of the upstream and the streamwise boundaries are varied. A phase shift is therefore not applied for the determination of the circulation distribution, so step 2 is omitted. Steps 3 and 4 are applied in the same way as described above. After the application of these circulation determination procedures, $\Gamma_p(x,t)$ and $\Gamma_b(t)$ are known and the unsteady lift can be directly calculated using Eq. (3.10). The determination of the pitching moment from the circulation, without explicit knowledge of the pressure distribution, requires the additional steps described in the following.

The pitching moment can be calculated from the result for the unsteady lift $L'(t)$ and the chordwise center of pressure x_{CP}:

$$M'(t) = (x_{\text{ref}} - x_{\text{CP}}(t))L'(t), \tag{3.13}$$

with the chordwise center of pressure defined as

$$x_{\text{CP}}(t) = \frac{\int_0^c x\Delta p(x,t)dx}{\int_0^c \Delta p(x,t)dx} = \frac{\int_0^c x\Delta p(x,t)dx}{L'(t)}. \tag{3.14}$$

Because Eq. (3.14) requires prior knowledge of the unsteady pressure distribution, it is convenient to introduce a separate center of pressure for each of the two terms of the unsteady lift. Equation (3.13) is then replaced by

$$M'(t) = (x_{\text{ref}} - x_{\text{CP,QS}}(t))L'_{\text{QS}}(t) + (x_{\text{ref}} - x_{\text{CP,FA}}(t))L'_{\text{FA}}(t), \tag{3.15}$$

where the center of pressure of the quasi-steady lift contribution is

$$x_{\text{CP,QS}}(t) = \frac{\int_0^c x\Delta p_{\text{QS}}(x,t)dx}{\int_0^c \Delta p_{\text{QS}}(x,t)dx} = \frac{\rho U_\infty \int_0^c x\gamma_b(x,t)dx}{\rho U_\infty \int_0^c \gamma_b(x,t)dx} = \frac{\int_0^c x\gamma_b(x,t)dx}{\Gamma_b(t)} \tag{3.16}$$

and the center of pressure of the lift due to flow acceleration effects is

$$x_{\text{CP,FA}}(t) = \frac{\int_0^c x\Delta p_{\text{FA}}(x,t)dx}{\int_0^c \Delta p_{\text{FA}}(x,t)dx} = \frac{\rho \int_0^c x\frac{\partial}{\partial t}\Gamma_p(x,t)dx}{\rho \int_0^c \frac{\partial}{\partial t}\Gamma_p(x,t)dx} = \frac{\int_0^c x\frac{\partial}{\partial t}\Gamma_p(x,t)dx}{\int_0^c \frac{\partial}{\partial t}\Gamma_p(x,t)dx}. \tag{3.17}$$

The calculation of $x_{\text{CP,FA}}(t)$ with Eq. (3.17) is possible using the knowledge of the temporal behavior of the circulation $\Gamma_p(x,t)$. The computation of $x_{\text{CP,QS}}(t)$ with Eq. (3.16) would additionally require a further processing step to obtain the bound vortex strength distribution as the gradient of the bound circulation, $\gamma_b(x,t) = \frac{\partial}{\partial x}\Gamma_p(x,t)$. To avoid the possible introduction of errors associated with the computation of gradients from the experimental data, Eq. (3.16) is further modified with an integration by parts:

$$x_{\text{CP,QS}}(t) = \frac{\int_0^c x\gamma_b(x,t)dx}{\Gamma_b(t)} = \frac{\Gamma_b(t)c - \int_0^c \Gamma_p(x,t)dx}{\Gamma_b(t)} = c - \frac{\int_0^c \Gamma_p(x,t)dx}{\Gamma_b(t)}. \tag{3.18}$$

The pitching moment is thus determined from the measured circulation using the three Eqs. (3.15), (3.17), and (3.18), and from the result for the lift obtained with Eq. (3.10).

3.4.3. RESULTS

PRESSURE-BASED LOAD DETERMINATION

In Fig. 3.15, the surface pressure difference along the chord for the pitching wing with fixed flap is shown for four phase instants. The largest differences between the LPT-based pressure and the reference appear in the leading edge region, for $x/c < 0.1$. It is assumed that these larger differences are the result of insufficient spatial resolution of the flow field measurement to accurately capture the flow around the leading edge, which is characterized by relatively large spatial velocity gradients. Downstream of $x/c = 0.1$, the LPT-based results are in good qualitative agreement with the reference data. The somewhat larger differences that appear around $x/c = 0.2$ and around $x/c = 0.7$ are considered measurement artifacts due to the merging of the flow field data from the three measurement volumes. The agreement of the LPT-based results with the reference data is improved compared to the quasi-steady formulation when the unsteady pressure formulation is adopted, which is expected because the reduced frequency of the pitching motion is in the unsteady aerodynamics regime. The unsteady effects are the largest when the magnitude of the pitch rate is maximal, thus around $t/T = 0$ and $t/T = 0.5$. For example, at $t/T = 0.05$, the RMS of the difference to the reference data downstream of $x/c = 0.1$ is reduced by about 65% when the unsteady term is included.

The aerodynamic loads, in terms of the lift and pitching moment coefficients, as determined by a chordwise integration of the pressure difference are shown in Figs. 3.16 and 3.17. Here, it can be observed that the qualitative behavior of the quasi-steady and unsteady loads over the period is very similar, but the inclusion of the unsteady term introduces a phase shift of the signal. The phase shift is negative for the lift and positive for the moment, which can be explained by the fact that the unsteady term affects the load distribution mostly in the region downstream of the reference axis for the pitching moment computation that is located at $x_{\text{ref}}/c = 0.3125$, as seen in Fig. 3.15. This means that an increase in lift due to the inclusion of the unsteady term corresponds to a negative nose-up pitching moment and vice-versa. For the lift coefficient C_ℓ in Fig. 3.16, including the unsteady term results in a phase shift of $\Delta t/T = -2.2\%$, and the RMS error ϵ_{RMS}, calculated from the difference to the reference, is reduced by 33%. For the moment around the pitch axis C_m in Fig. 3.17, the phase difference between the quasi-steady result and the unsteady result is $\Delta t/T = 5.2\%$, and ϵ_{RMS} of the unsteady result is 54% lower than ϵ_{RMS} of the quasi-steady result.

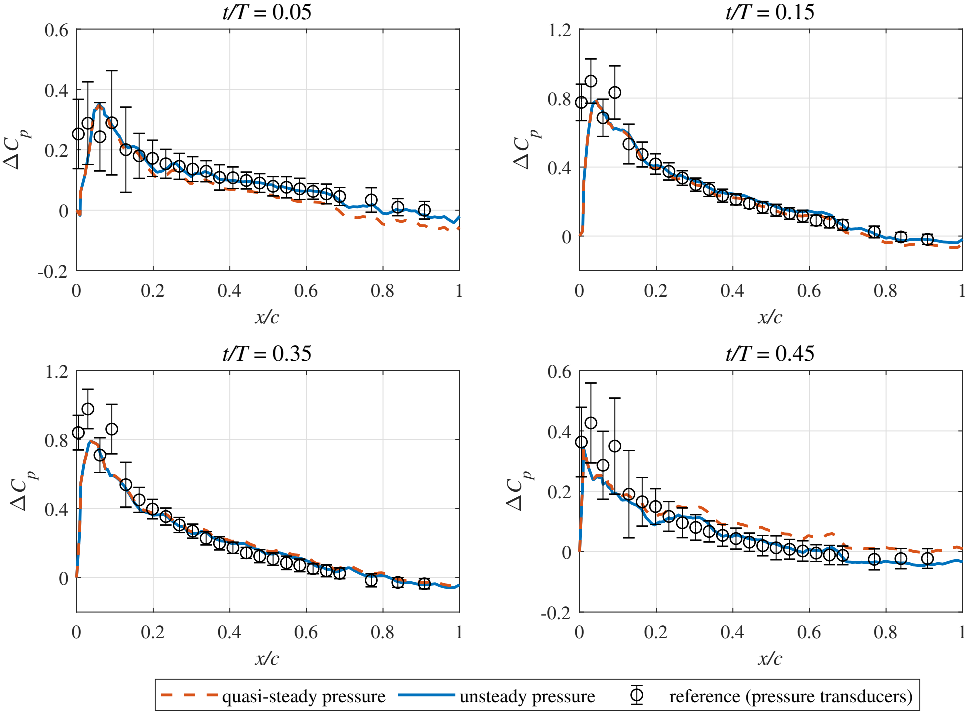

Figure 3.15: Comparison of the LPT-based surface pressure difference with the reference data from the pressure transducers at four different phase instants for the pitching wing with fixed flap

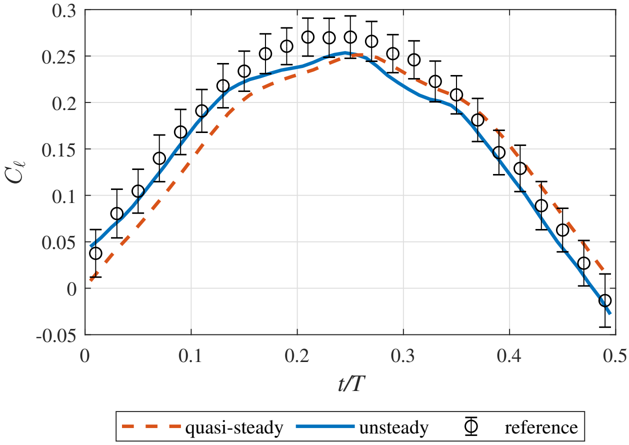

Figure 3.16: Comparison of the lift as determined with the pressure-based approach with the reference data from the pressure transducers for the pitching wing with fixed flap

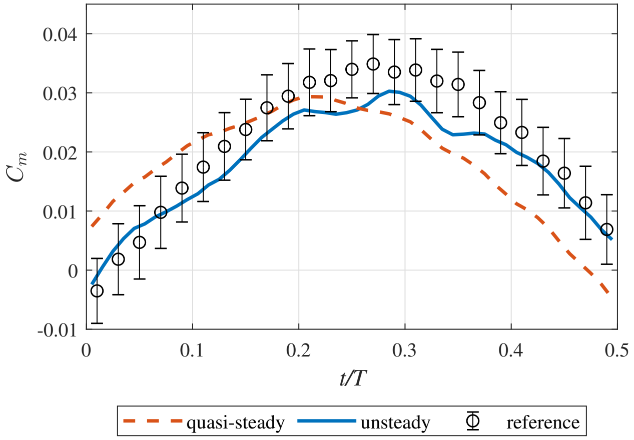

Figure 3.17: Comparison of the moment around the pitch axis as determined with the pressure-based approach with the reference data from the pressure transducers for the pitching wing with fixed flap

The results for the chordwise distribution of the pressure difference at four phase instants for the pitching wing with actuated flap are shown in Fig. 3.18. The effect of the actuated flap is evident, as the pressure difference becomes negative downstream of the mid-chord, with a local extremum at approximately $x/c = 0.75$, which is the flap hinge point. Furthermore, the magnitude of the suction peak near the leading edge is reduced as a result of the change in the effective camber of the wing due to the flap deflection. Only eight reference data points from the installed pressure transducers are available for comparison with the LPT-based results due to the particular setup of the flap actuation controller (see Sec. 3.2.4). Similar to the test case with fixed flap, the largest differences are observed for the largest magnitudes of ΔC_p. The effect of the unsteady term, which is calculated as the temporal gradient of the chordwise integral of bound circulation, is smaller than for the test case with fixed flap. That is because the controller is designed to keep the lift constant, therefore the flap motion tends to suppress the circulation variation and, hence, compensates for an increase in the suction peak near the leading edge with a corresponding negative peak in the pressure difference further downstream, which means that the unsteady effects are only observed in the center region of the wing around $x/c = 0.5$. In this region, the agreement with the reference data is marginally improved when the unsteady pressure formulation is used, compared to the quasi-steady formulation.

The aerodynamic loads from the pressure-based approach for the pitching wing with actuated flap are shown in Figs. 3.19 and 3.20. No large differences are observed between the results when using the quasi-steady or the unsteady pressure formulation, for neither the lift nor the pitching moment, which is in line with the observations for the pressure distributions themselves.

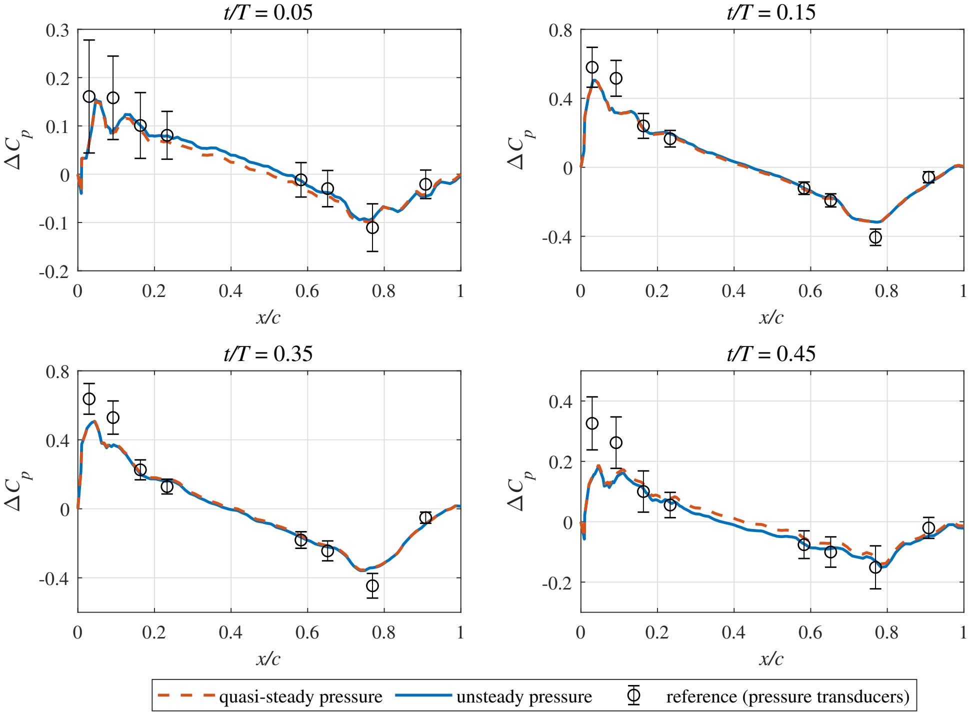

Figure 3.18: Comparison of the LPT-based surface pressure difference with the reference data from the pressure transducers at four different phase instants for the pitching wing with actuated flap

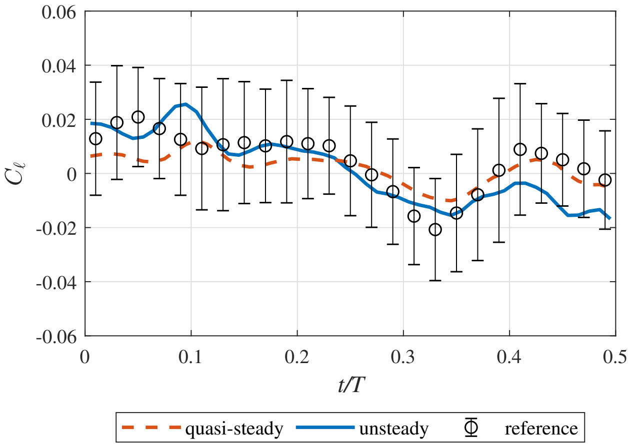

Figure 3.19: Comparison of the lift as determined with the pressure-based approach with the reference data from the pressure transducers for the pitching wing with actuated flap

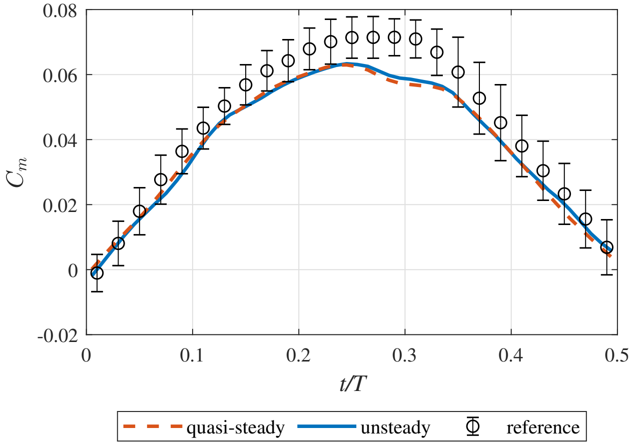

Figure 3.20: Comparison of the moment around the pitch axis as determined with the pressure-based approach with the reference data from the pressure transducers for the pitching wing with actuated flap

CIRCULATION-BASED LOAD DETERMINATION

The results for the circulation-based aerodynamic loads on the pitching wing with fixed flap are shown in Figs. 3.21 and 3.22. The quasi-steady result for the lift is in good agreement with the reference data, which is further improved when the unsteady formulation is used in which the result is shifted in phase by $\Delta t/T = -2.2\%$. For the pitching moment, the amplitude is underestimated by the circulation-based approach, so that only 75% of the amplitude of the reference data is reached, whereas for the lift 101% of the load amplitude is observed. This means that the center of pressure that was calculated with Eq. (3.18) is located too far downstream, closer to the pitch axis, that was used as the reference axis for the calculation of the moment. The phase shift in the moment signal of $\Delta t/T = 5.7\%$, which is produced by the unsteady formulation with respect to the quasi-steady result, is not large enough to reduce the remaining lag error with respect to the reference data below $\epsilon_t = -3.1\%$ of the period.

The aerodynamic loads for the pitching wing with actuated flap are shown in Figs. 3.23 and 3.24. The quasi-steady and the unsteady formulation for the lift both provide results that are in very good agreement with the reference. While including the flow acceleration effects has an evident effect on the results, the agreement with the reference is not significantly improved with this method. As discussed previously, the unsteady effects are expected to be negligible in this case, as the controller aims to maintain the circulation constant. For the pitching moment, the amplitude of the circulation-based results is smaller than the amplitude of the reference, similar to the pitching wing with fixed flap, but less pronounced. In this case, the amplitude reaches 91% of the reference. In contrast to the observations for the pitching wing with fixed flap, no significant lag error is observed in the pitching moment results. The unsteady formulation is shifted in phase by $\Delta t/T = 0.4\%$ with respect to the quasi-steady result, which reduces the RMS of the difference to the reference by 15%.

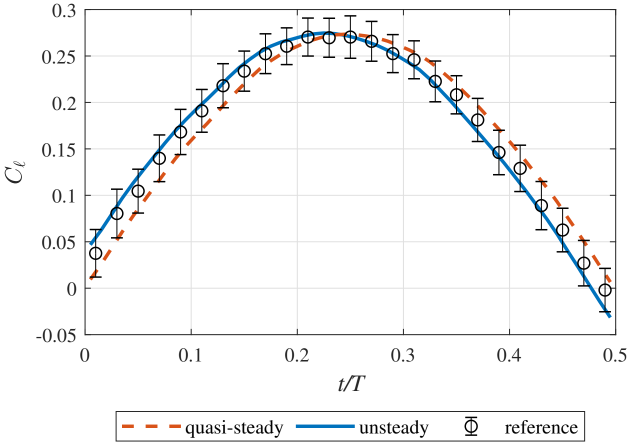

Figure 3.21: Comparison of the lift as determined with the circulation-based approach with the reference data from the pressure transducers for the pitching wing with fixed flap

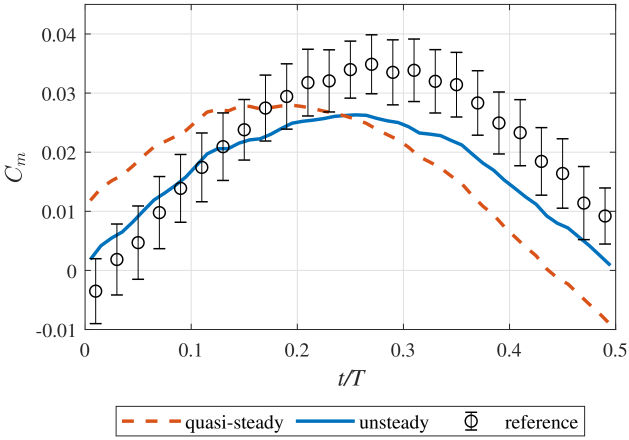

Figure 3.22: Comparison of the moment around the pitch axis as determined with the circulation-based approach with the reference data from the pressure transducers for the pitching wing with fixed flap

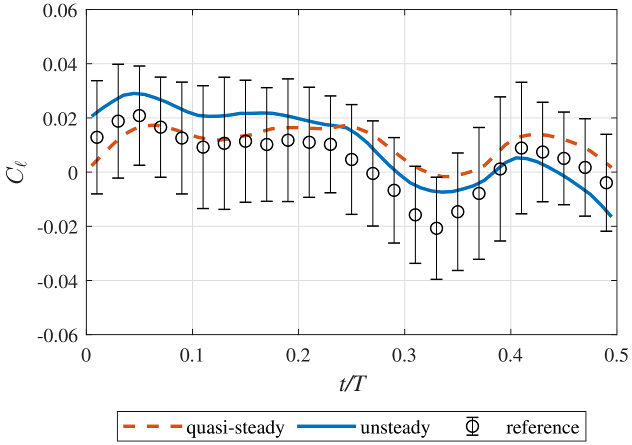

Figure 3.23: Comparison of the lift as determined with the circulation-based approach with the reference data from the pressure transducers for the pitching wing with actuated flap

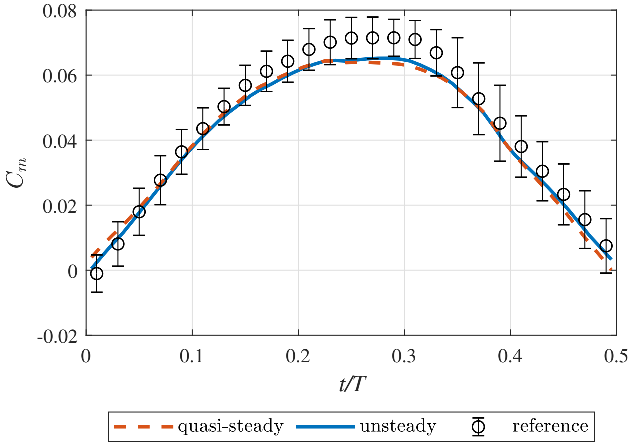

Figure 3.24: Comparison of the moment around the pitch axis as determined with the circulation-based approach with the reference data from the pressure transducers for the pitching wing with actuated flap

3.4.4. COMPARISON OF THE METHODS

The agreement of the results for the aerodynamic loads as determined using the pressure- and circulation-based methods with the reference obtained from the surface pressure transducer measurements is summarized in Tab. 3.2. The RMS error ϵ_{RMS} is computed from the difference between LPT-based load measurement and reference data. It is additionally given as a percentage of the maximum absolute value of the corresponding reference signal. The lag error ϵ_t is determined by cross-correlation with the reference signal and given both in seconds and as a percentage of the period. The amplitude error ϵ_{amp} is determined by calculating the RMS error from the difference between the measurement and the reference after the measured signal has been shifted in phase according to ϵ_t. The examination of the presented results yields the following observations:

- The consideration of the flow acceleration effects in an unsteady formulation for the loads is highly effective for increasing the agreement with the reference data for the pitching wing with fixed flap, compared to the quasi-steady formulation. Similar improvements are observed for both load determination methods and originate primarily from a shift of the quasi-steady result in phase.

- For the pitching wing with actuated flap, the improvements due to the consideration of the flow acceleration effects are negligible. In this case, the flap is actuated by a controller that is designed to keep the loads constant, which also diminishes the unsteady effects on the load variation. Therefore, both quasi-steady and unsteady approaches yield accurate and comparable results, with RMS errors of less than 0.01 in lift and moment coefficients.

- For the pitching wing with fixed flap, the circulation-based approach yields more accurate results for the lift, when compared with the results from the pressure-based approach. In contrast to the pressure-based approach, the circulation-based approach does not use measurements near the wing surface, where measurement resolution problems are expected due to the presence of large velocity gradients and a turbulent boundary layer. The low measurement resolution was found to be most problematic for the pressure-based approach in the wing nose region. Furthermore, the sensitivity of the circulation-based approach to individual flow velocity measurements is reduced by varying the integration path and averaging the result, so that the level of random error is decreased.

- For the pitching wing with fixed flap, the pressure-based approach yields more accurate results than the circulation-based approach for the evaluation of the pitching moment. The circulation-based approach underpredicts the pitching moment magnitude and exhibits a relatively large phase error in this case. It is noted that this lag is not a result of the selected approach to include the unsteady term, because the phase shift due to the consideration of flow acceleration effects is very similar to the pressure-based approach. Instead, a larger lag error is already observed in the quasi-steady circulation-based result for the pitching moment. The determination of the pitching moment with the circulation approach requires the integration of measurements near the surface so that the low measurement resolution can cause an accumulation of errors here.

- For the pitching wing with actuated flap, the absolute measurement error is smaller for both methods, compared to the pitching wing with fixed flap. In the pressure-based approach, this can be explained by the reduced magnitude of the suction peak, which is the main cause of the measurement resolution issues due to the large local velocity gradients near the leading edge of the wing. Compared to the test case with fixed flap, the presence of a negative peak in the pressure distribution and the associated measurement resolution problems cause a reduction of the error for the lift and an increase of the error for the moment. In comparison with the circulation-based approach, the pressure-based approach is slightly more accurate for the lift and the circulation-based approach is slightly more accurate for the pitching moment. However, the differences and overall errors are small enough so that both methods can be considered equivalent in this case.

Table 3.2: Summary of the comparison of the aerodynamic loads with the reference data from the pressure transducers. ϵ_{RMS}: RMS difference to the reference. ϵ_t: time lag to the reference. ϵ_{amp}: remaining RMS difference after correcting for the lag by shifting the signal by ϵ_t.

	pitching with fixed flap			pitching with actuated flap		
	ϵ_{RMS}	ϵ_t	ϵ_{amp}	ϵ_{RMS}	ϵ_t	ϵ_{amp}
pressure-based quasi-steady lift	0.028 10.4%	0.047 s 1.9%	0.018 6.8%	0.007 33.2%	0.010 s 0.4%	0.007 33.0%
pressure-based unsteady lift	0.018 6.8%	−0.009 s −0.4%	0.018 6.6%	0.008 39.7%	−0.038 s −1.5%	0.008 39.1%
circulation-based quasi-steady lift	0.017 6.4%	0.036 s 1.4%	0.004 1.3%	0.009 43.4%	0.045 s 1.8%	0.008 39.7%
circulation-based unsteady lift	0.010 3.7%	−0.020 s −0.8%	0.004 1.4%	0.009 42.8%	0.003 s 0.1%	0.009 42.8%
pressure-based quasi-steady moment	0.009 25.3%	−0.144 s −5.7%	0.004 11.4%	0.007 10.0%	−0.010 s −0.4%	0.007 9.8%
pressure-based unsteady moment	0.004 12.6%	−0.008 s −0.3%	0.004 12.5%	0.007 9.5%	−0.003 s −0.1%	0.007 9.5%
circulation-based quasi-steady moment	0.013 36.6%	−0.224 s −8.8%	0.004 12.5%	0.005 7.1%	−0.017 s −0.7%	0.005 6.5%
circulation-based unsteady moment	0.007 20.1%	−0.078 s −3.1%	0.006 16.3%	0.004 6.1%	−0.007 s −0.3%	0.004 6.0%

Overall, it is established that both unsteady aerodynamic load determination approaches, namely pressure-based and circulation-based, produce accurate results, in the two considered test cases with large and small lift variations, respectively. Neither of the two approaches appears as clearly superior to the other. Instead, it appears that the accuracy of the results for both approaches is compromised in different ways by deficiencies in the flow field measurement resolution. The pressure-based approach strongly depends on the flow measurements near the wing surface, where the measurement resolution is insufficient to accurately capture the flow behavior. Furthermore, the presence of the boundary layer on the wing increases the complexity of the implementation of the pressure-based method. In the circulation-based approach, flow measurements near the surface are not used in the determination of loads. Moreover, it is possible to reduce the sensitivity of the obtained loads to individual flow measurements by averaging the circulation result obtained with several integration paths. On the other hand, it is noted that the direct insights into the pressure distribution from the pressure-based approach provide information on possible measurement resolution issues that are not directly made available with the circulation-based approach.

3.5. Concluding Remarks

An experimental approach was introduced to obtain the structural motion and aerodynamic loads on an unsteady wing model using an integrated optical measurement approach. The approach consists of simultaneously conducting optical measurements of the flow and the structure with a volumetric flow measurement device and the application of a Lagrangian particle tracking algorithm for the image data processing of both flow and structure.

The position of the unsteady wing was measured with the optical system by using structural markers on the experimental model. The image processing and marker tracking analysis was performed with the same particle tracking algorithm that is used for the analysis of the flow tracer particles. Next, the position of the wing model in space was found by fitting the measurements of the marker positions to the structural marker grid that was painted on the model. Based on the considered experimental test case of a pitching wing with actuated flap, it can be concluded that the position determination method is suitable for reliably measuring the position and shape of moving and deforming objects, as long as the structural behavior can be described in terms of a few degrees of freedom.

The unsteady aerodynamic loads in terms of the lift and the pitching moment were determined from the flow field measurement using two implementations of an aerodynamic loads determination method that makes use of unsteady aerodynamics theory. The pressure-based and the circulation-based load determination approaches were both adapted with formulations from unsteady potential flow and thin airfoil theory to extract the unsteady aerodynamic loads. It was shown that adopting the unsteady formulations reduces the difference between the flow field-based load measurements and reference pressure data by more than 50% for the pitching wing without flap actuation, compared to results using quasi-steady formulations. It was also shown that both methods correctly predict the reduction of the unsteady effects when the flap is actuated.

None of the two methods could be identified as providing superior results compared to the other, as it was observed that the two methods are affected differently by measurement resolution issues, and the agreement of the results from both methods with the reference is overall very good, with typical errors of less than 0.01 in the lift and moment coefficients. However, the circulation-based method has the advantage of a simpler implementation and is therefore considered preferable for future applications. Both approaches for the aerodynamic loads determination that were introduced are connected to less data processing effort and pose lower measurement requirements on the flow field measurements than existing alternative methods that are based on the Navier-Stokes momentum equation.

Although the analysis of the pitching wing with an actuated flap was performed in a two-dimensional sense, the measurement data was obtained in three-dimensional space. The integrated optical measurement approach that was introduced in this chapter can therefore be applied to three-dimensional problems without further complications. This is demonstrated in the following chapters of this dissertation.

4

PROOF OF CONCEPT: AEROELASTIC CHARACTERIZATION OF A FLEXIBLE WING

In this chapter, an experimental aeroelastic characterization of a flexible wing using the integrated optical measurement approach is demonstrated. The aerodynamic, elastic, and inertial components in Collar's triangle of forces acting on a wing section are determined based on measurements of the structural and the aerodynamic response to steady and unsteady periodic inflow conditions. The aerodynamic lift force is determined from the flow velocity fields with the circulation-based approach that was introduced in the previous chapter. A finite element beam model of the wing is used to determine the inertial and the elastic force of the aeroelastic interaction from the deformation measurements. The obtained results for the aeroelastic characterization are assessed according to their agreement with each other based on the equilibrium of forces in Collar's triangle.

Parts of this chapter have been published as: Mertens, C., de Rojas Cordero, T., Sodja, J., Sciacchitano, A., and van Oudheusden, B. W. (2022). Aeroelastic Characterization of a Flexible Wing Using Particle Tracking Velocimetry Measurements. *AIAA Journal, 60*(1), 276–286.

4.1. BACKGROUND

The determination of all three forces in Collar's triangle based on integrated aerodynamic and structural measurements is performed in this chapter. By analyzing the temporal behavior of the three forces acting on a wing section, the proof of concept of an aeroelastic characterization is demonstrated. The experimental model that is investigated is a flexible wing subjected to steady and unsteady inflow conditions in a wind tunnel experiment. The considered unsteady inflow condition is a harmonically oscillating stream, produced by a gust generator that is mounted in the wind tunnel upstream of the wing. Optical measurements of the unsteady flow field and the structural motion are performed with the integrated measurement approach that was introduced in the previous chapter, where the LPT measurements of the flow are performed using HFSB as flow tracers, while the measurements of the structural motion are achieved by tracking surface markers using the same measurement and data processing system. After the LPT measurements of the flow and the structural motion are obtained, physical models need to be applied to determine the three forces comprising Collar's triangle. In this chapter, the proof of concept of an aeroelastic characterization for the investigated static and dynamic aeroelastic test cases is provided by using the circulation-based aerodynamic load determination method that was introduced in the previous chapter and a simplified beam model for the determination of the structural loads.

4.2. PHYSICAL MODELS FOR THE LOADS DETERMINATION

4.2.1. DETERMINATION OF THE AERODYNAMIC FORCE

The lift per unit span L' of a wing section in steady flow can be determined from the Kutta-Zhukowsky theorem (see Sec. 2.2.1, Eq. (2.12)), where the circulation bound to the airfoil Γ_b is obtained from a measured flow velocity field $\boldsymbol{u}$ with a line integral over a closed path C around the airfoil using Eq. (2.13). In unsteady inflow conditions, the flow acceleration effects on the unsteady lift have to be considered in addition to the quasi-steady lift due to the bound circulation. The unsteady lift determination is therefore performed with the circulation-based approach described in Sec. 3.4.2 using Eq. (3.10), where the partial bound circulation along the chord $\Gamma_p(x,t)$ is obtained similarly to the overall bound circulation $\Gamma_b(t)$, by line integrals of the measured flow velocity. As discussed in Ch. 3.4.2, the value of Γ_p at a given chord position x_i is obtained by performing a line integral of the velocity along a contour that encloses the chord of the wing from the leading edge until x_i, at which point the line integration path begins and ends on the airfoil surface.

4.2.2. DETERMINATION OF THE INERTIAL FORCE

The dominant motion degree of freedom of the considered aeroelastic interaction is the out-of-plane deflection w, in the direction perpendicular to the chord line of the flexible wing. For the purpose of this demonstration study, a simplified one-dimensional model of the wing, considering only the out-of-plane deflection, is used to perform the characterization of the aeroelastic interaction, while the other motion degrees of freedom are not taken into account. The out-of-plane inertial force per unit span I' on the wing can be determined as the product of mass per unit length and the out-of-plane acceleration along the spanwise coordinate z:

$$I'(z,t) = -\mu_m(z)\,\ddot{w}(z,t)\,, \tag{4.1}$$

where $\mu_m(z)$ is the mass per unit span, and $\ddot{w}$ is the second temporal derivative of the out-of-plane wing deflection. In the case of steady flow around the wing, $\ddot{w} = 0$ and thus $I'(z) = 0$. In the case of a harmonic gust excitation at a frequency of ω_g (see Sec. 4.3.1), it can be assumed that the dynamic response of the wing follows the harmonic excitation with the same frequency. This means that the steady-state dynamic response of the wing can be written as

$$w(z,t) = w_0(z) + w_{\mathrm{amp}}(z)\,e^{(i\omega_g t+\phi)}\,, \tag{4.2}$$

where $w_0(z)$ is the mean deflection, which is identical to the wing deflection in response to the steady inflow, and $w_{\mathrm{amp}}(z)$ is the steady-state dynamic deflection amplitude. The second temporal derivative of Eq. (4.2) is then

$$\ddot{w}(z,t) = -\omega_g^2\,w_{\mathrm{amp}}(z)\,e^{(i\omega_g t+\phi)}\,. \tag{4.3}$$

The inertial load $I'(z)$ as given in Eq. (4.1) is determined by performing a sinusoidal curve-fitting to the LPT-based marker displacements from their respective mean values over the period, to determine $w_{\mathrm{amp}}(z)$ as well as the phase shift ϕ, and thus $\ddot{w}(z)$ according to Eq. (4.3).

4.2.3. DETERMINATION OF THE ELASTIC FORCE

For the determination of the elastic force as a part of the aeroelastic characterization, only the shear force acting normally on the wing surface is considered. The flexible wing is therefore modeled as an Euler-Bernoulli beam, where the analysis is restricted to the bending deflection $w(z)$ across the span. The wing is clamped at the root so that $w(z=0) = 0$ and $w'(z=0) = 0$ are used as Dirichlet boundary conditions in the model. The Euler-Bernoulli equation that establishes a relation between the deflection and the external load on the wing $q(z)$ in the static case is:

$$\frac{d^2}{dz^2}\left(EI(z)\frac{d^2 w(z)}{dz^2}\right) = q(z)\,, \tag{4.4}$$

while the shear force $Q(z)$ and the bending moment $M(z)$ in the beam are:

$$Q(z) = -\frac{d}{dz}\left(EI(z)\frac{d^2 w(z)}{dz^2}\right) \tag{4.5}$$

$$M(z) = -EI(z)\frac{d^2 w(z)}{dz^2}\,. \tag{4.6}$$

The effective flexural rigidity $EI(z)$ is determined by extracting the values from the Timoshenko beam model of the same wing that was used by Rajpal et al. (2021). The effective flexural rigidity varies along the span therefore a finite element beam model is used to solve Eq. (4.4).

In the static case, the governing equation of the FE model is:

$$\boldsymbol{K}\boldsymbol{\xi} = \boldsymbol{D}\boldsymbol{f}\,, \tag{4.7}$$

where $\boldsymbol{K}$ is the stiffness matrix, $\boldsymbol{D}$ is the loading matrix, $\boldsymbol{f}$ is the external force vector, and the vector $\boldsymbol{\xi}$ contains the values of the nodal degrees of freedom, which are the deflections and the rotations. The continuous beam deflection $w(z)$ is calculated from the discrete values of the degrees of freedom by using Hermite splines, and $\boldsymbol{f}$ is determined by sampling the distribution of the external load $q(z)$ at the nodes of the FE model (more details on the implemented FE method can be found in Sec. 3.5.3 in Hodges and Pierce, 2011). The presence of measurement noise impedes the direct determination of the elastic force with Eq. (4.7) from the LPT measurements of the surface markers. Instead, the elastic force is determined by performing an optimization of the external load $q(z)$, such that the corresponding beam deflection $w(z)$ best matches the measurements. Due to the relatively small spanwise region where measurements are available in this particular experiment, it is necessary to make an assumption of the behavior of the external load across the span to achieve meaningful results with this approach. It is therefore assumed that the external load on the beam is constant across the span with $q(z) = q_0$ so that q_0 is the only optimization variable. This means that the lift reduction effects on the wing loading due to downwash near the wingtip are not taken into account, which can be justified by the relatively large aspect ratio of the wing.

Following the optimization procedure for q_0 in the static case, the shear force and the bending moment in the beam are determined with Eq. (4.5) and Eq. (4.6), which can be solved analytically in the case of a given constant external load in the static case, when considering the Neumann boundary conditions $Q(z = s) = 0$ and $M(z = s) = 0$ at the free end:

$$Q(z) = -\int q_0\, dz = -q_0(z - s)\,, \tag{4.8}$$

$$M(z) = \int Q(z)\, dz = -\frac{q_0}{2}(z^2 - 2zs + s^2)\,. \tag{4.9}$$

In the case that the wing is moving dynamically, the governing equation for the Euler-Bernoulli beam is enhanced with the inertia term:

$$\frac{\partial^2}{\partial z^2}\left(EI(z)\frac{\partial^2 w(z,t)}{\partial z^2}\right) + \mu(z)\frac{\partial^2 w(z,t)}{\partial t^2} = q(z,t)\,, \tag{4.10}$$

and equivalently for the FE model of the beam:

$$\boldsymbol{K}\boldsymbol{\xi}(t) + \boldsymbol{M}\ddot{\boldsymbol{\xi}}(t) = \boldsymbol{D}\boldsymbol{f}(t)\,, \tag{4.11}$$

where $\boldsymbol{M}$ is the mass matrix, as determined from the mass distribution properties of the experimental model.

If the assumed loading is given by $\boldsymbol{f}(t) = \boldsymbol{f}_0 + \boldsymbol{f}_{\text{amp}} e^{i\omega_g t+\phi}$, for a linear system the response is the superposition of the static and the steady-state dynamic response $\boldsymbol{\xi}(t) = \boldsymbol{\xi}_0 + \boldsymbol{\xi}_{\text{amp}} e^{i\omega_g t+\phi}$. The relation between the dynamic wing response amplitude $\boldsymbol{\xi}_{\text{amp}}$ and the external load amplitude $\boldsymbol{f}_{\text{amp}}$ does not depend on the time explicitly:

$$\left(\boldsymbol{K} - \omega_g^2 \boldsymbol{M}\right) \boldsymbol{\xi}_{\text{amp}} = \boldsymbol{D} \boldsymbol{f}_{\text{amp}}. \tag{4.12}$$

Similar to the steady case, Eq. (4.12) is used to optimize for the amplitude q_{amp} of a sinusoidal, spanwise constant external load by fitting the FE model beam deflection to the wing deformation amplitude that is obtained from the experimental measurements. In this case, it is not trivial to derive analytical expressions for the shear force and the bending moment in the beam so that in the test case with unsteady inflow, these quantities are computed from the deflection with Eq. (4.5) and Eq. (4.6).

4.2.4. CLOSURE OF COLLAR'S TRIANGLE

After the aerodynamic, inertial, and elastic forces are determined from the integrated measurements with the three described methods, the results can be combined in an internal validation procedure, where the physical agreement of the three different models with each other can be quantified. To visualize the different forces acting on the wing, a free body diagram of a wing section between the spanwise positions z_1 and z_2 is illustrated in the free body diagram in Fig. 4.1.

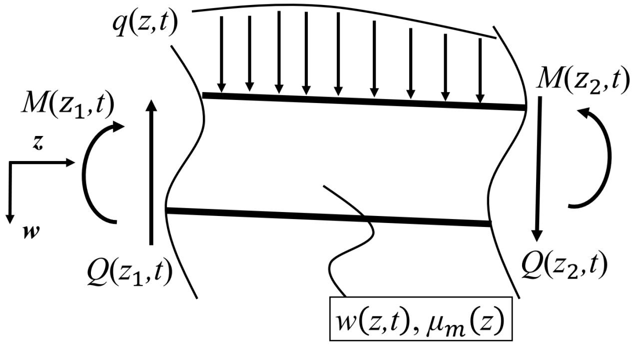

Figure 4.1: Free body diagram of a wing section

The equilibrium of the forces acting on the wing section in the direction of the deflection w in Fig. 4.1 is as follows:

$$\int_{z_1}^{z_2} q(z,t)\,dz - Q(z_1,t) + Q(z_2,t) - \int_{z_1}^{z_2} \mu_m(z)\,\ddot{w}(z,t)\,dz = 0. \tag{4.13}$$

The three forces in Collar's triangle that are involved in a dynamic aeroelastic interaction (aerodynamic force A, elastic force E, inertial force I), can be recognized in Eq. (4.13):

$$A = \int_{z_1}^{z_2} L'(z,t)\,dz = \int_{z_1}^{z_2} q(z,t)\,dz, \tag{4.14}$$

$$E = -Q(z_1,t) + Q(z_2,t), \tag{4.15}$$

$$I = \int_{z_1}^{z_2} I'(z,t)\,dz = -\int_{z_1}^{z_2} \mu_m(z)\ddot{w}(z,t)\,dz, \tag{4.16}$$

which means that the dynamic equilibrium of forces $A+E+I=0$ is given by Eq. (4.13) for the investigated wing segment. This requirement is verified by calculating a measurement residual, defined as $\Delta_F = A+E+I$, which is then used to quantify the error of the considered approach (see Sec. 2.3).

4.3. EXPERIMENTAL SETUP AND PROCEDURES

4.3.1. WIND TUNNEL SETUP

The experiment is conducted in the OJF (see Sec. 3.2.1) at a freestream velocity of $U_\infty = 14\,\mathrm{m\,s^{-1}}$, corresponding to a Reynolds number of $\mathrm{Re} = 230{,}000$ based on the chord of the wing. The experimental setup is shown in Fig. 4.2. A gust generator (Lancelot et al., 2017) is mounted at the wind tunnel outlet, which can generate various types of unsteady inflow conditions for the model in the test section. Two experimental test cases are considered: one test case with steady inflow, where the gust generator is not operated, and a second test case with periodic unsteady inflow, where the gust generator is operated continuously with a sinusoidal variation of the gust vanes angle β according to $\beta(t) = 5^\circ \times \sin(\omega_g t)$, where $\omega_g = 2\pi f_g$ is the angular frequency of the gust vane motion. The selected frequency of $f_g = 2\,\mathrm{Hz}$ corresponds to a reduced frequency of $k = f_g \pi c U_\infty^{-1} = 0.11$, which is similar to the reduced frequency in Ch. 3. To perform the LPT measurements of the flow, the freestream is seeded with the HFSB seeding system that is described in Sec. 3.2.3, which is placed in the wind tunnel settling chamber.

4.3.2. FLEXIBLE WING MODEL

The experimental model is a rectangular wing with a chord length of $c = 0.25\,\mathrm{m}$, a span width of $s = 1.75\,\mathrm{m}$ and a NACA 0010 profile, that is oriented at a geometric angle of attack of $\alpha = 5^\circ$ with respect to the freestream. The wing was constructed in-house out of carbon fiber reinforced epoxy unidirectional tailored laminates. Its inner structure is formed by two spars and thirteen ribs, and the outer skin is divided into three spanwise regions of equal length with different laminate thickness and stiffness properties. The laminate properties were optimized to minimize the structural weight and maximize the compliance of the wing. The design and manufacturing procedure of the flexible wing model is described in detail by Rajpal et al. (2021). To enable the LPT measurements of the wing displacement, a rectangular grid of white circular markers is spray-painted on the surface of the wing model using a laser-cut template. The markers have a diameter of 1.5 mm and the grid spacing is 30 mm. The marker grid on the wing is detailed in Fig. 4.3.

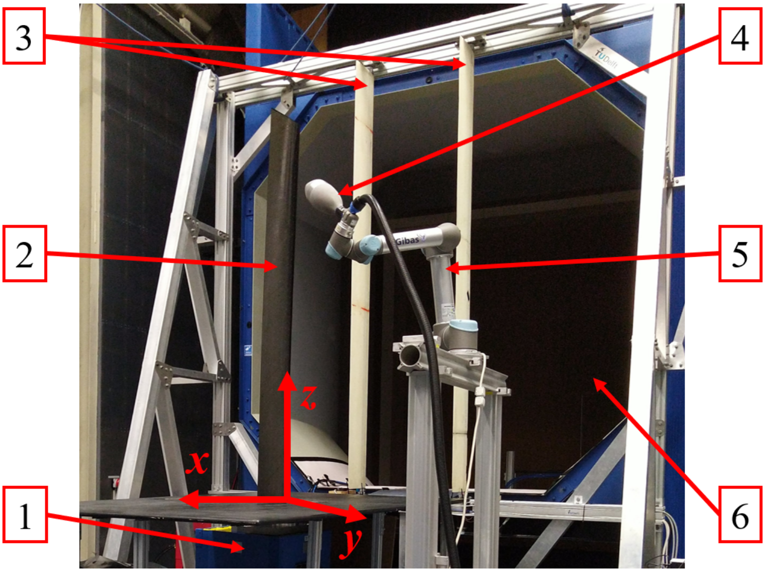

Figure 4.2: Photo of the wind tunnel setup. 1: six-component balance, 2: flexible wing model, 3: gust generator mounted at the wind tunnel nozzle exit, 4: CVV, 5: robotic arm, 6: HFSB seeding generator (not visible in the photo, placed in the wind tunnel settling chamber)

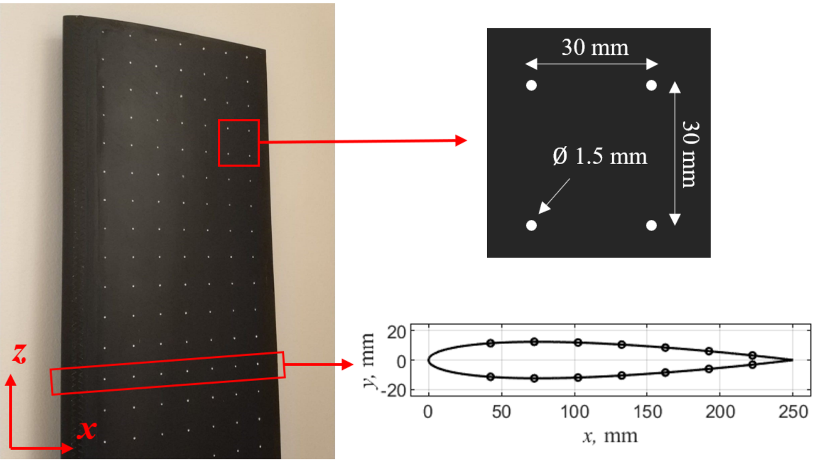

Figure 4.3: Photo of the flexible wing with details of the marker grid and the chordwise marker distribution

The flexible wing model is clamped to a six-component balance using an aluminum plug which is glued to the bottom of the wing. The mass of the wing without the aluminum plug is 1.44 kg. The dynamic motion amplitude of the flexible wing in response to the unsteady inflow generated by the gust vanes is increased by inserting a wingtip mass of 0.40 kg, which reduces the frequency of the wing's first bending mode from 5.4 Hz to 3.3 Hz, which is closer to the gust excitation frequency f_g, thus generating increased dynamic wing deformations. The maximum observed out-of-plane wingtip deflection is around 40 mm, corresponding to around 2% of the span.

The measurements of the six-component balance on which the wing is mounted are used for validation purposes of the loads at the root of the wing, as determined with the beam model based on the LPT measurements. Additionally, the wing model is equipped with a LUNA HD6 fiber optic strain sensor, that is mounted at mid-chord on the inside of the pressure side of the wing, from the root until $z = 1.65$ m or 94% of the span. The strain measurements from the optical fiber installed in the wing are obtained with a LUNA ODiSI data acquisition system and are used for validating the strains that are obtained from the FE beam model after fitting the model to the LPT marker measurements.

4.3.3. LPT DATA ACQUISITION AND PROCESSING

The same LPT measurement system that is described in Sec. 3.2.3 is used for the image data acquisition in this experiment. In contrast to the experiment described in Ch. 3, the CVV is used together with its coaxial illumination component, which consists of an optical fiber with a diverging lens at the end to illuminate the particles in the field of view of the cameras. As the illumination source, a Quantronix Darwin-Duo Nd:YLF laser (25 mJ pulse energy at 1 kHz, wavelength of 527 nm) is connected to the other end of the optical fiber. The optical measurements of the flow and the structure are conducted with the maximum acquisition frequency of the CVV of $f_s = 821$ Hz and with the maximum camera sensor size for that acquisition frequency, which is 704 × 540 pixel. Six different positions of the CVV with respect to the wing are used to obtain the flow measurements around the investigated wing section, with three different chordwise positions of the CVV on the pressure and suction side, respectively. To achieve this, the optical measurement setup is installed successively on both sides of the wing. The combined size of the measurement volumes with this procedure is around 15 L. For the case of steady inflow, 15 000 images are acquired per individual measurement volume. For the dynamic inflow case, 98 520 images are acquired over 240 motion periods per measurement volume.

The processing of the acquired image data begins with the separation of the flow tracers from the structural markers in the particle images, visualized in Fig. 4.4. This step improves the performance of the LPT algorithm because the appearance of the structural markers and the flow tracers in the images is not identical. The removal of the structural information from the integrated measurement images is achieved with a temporal high-pass filter (Sciacchitano & Scarano, 2014), exploiting the different time scales of the structural motion and that of the flow. In principle, the reverse operation can be applied to obtain the image data of the structural markers without the flow tracer information using a temporal low-pass filter (Mitrotta et al., 2022); however, this step is not directly necessary for this experiment, because the studied phenomena are either steady or periodic and thus repeatable over time. This means that the isolated structural marker information can be simply obtained by acquiring images without operating the HFSB seeding generator. This approach is advantageous because it allows the modification of the camera sensor size to the maximum of 704 × 636 pixel, which permits the simultaneous measurement of all markers along the chord on one side of the wing with just one acquisition at a sampling frequency $f_s = 500$ Hz.

(a) flow and structure (b) flow tracers (c) structural markers

Figure 4.4: Separating the integrated optical measurements into flow and structure data with temporal filters

After separating the flow and structural information, the next step is to apply the particle tracking algorithm. The used method for obtaining the LPT measurements consists of three steps, that are performed separately for the flow and the structure: first, a volume self-calibration (Wieneke, 2008) is performed, then an optical transfer function (Schanz et al., 2013) is generated, and subsequently, the STB algorithm (Schanz et al., 2016) is applied. The results are obtained in terms of individual Lagrangian particle tracks, with the position, velocity, and acceleration of each particle over time, for both the structural markers and the flow tracers in separate files. Once the track data of the flow tracers are obtained, the velocities of the flow tracer tracks are ensemble-averaged to a three-dimensional Cartesian grid with a spacing of 2.5 mm, using a top-hat filter approach with cubic bins of 10 mm × 10 mm × 10 mm, as described by Agüera et al. (2016). For the measurements obtained in the case of steady inflow, the particle tracks obtained from all acquired images are combined in the ensemble-averaging procedure. For the measurements with dynamic periodic inflow, the particle tracks are ensemble-averaged in a phase-averaged sense based on the recorded signal of the gust generator motion, where the particle tracks are assembled in 100 temporal bins, each spanning 1% of the gust excitation period $T = {f_g}^{-1}$.

The particle tracks of the structural markers are processed in two different post-processing procedures for the cases of steady and unsteady inflow, respectively. In the case of steady inflow, the marker track positions within a radius of 10 mm are averaged to obtain the mean position of the observed grid of markers in space. This step is necessary to overcome the relatively large random error in the position measurement of the markers, which has a typical value on the order of 1 mm (see Sec. 3.3.1). The same procedure is then repeated for a reference measurement of the marker positions without wind tunnel operation. Subsequently, the difference between the two grids is calculated, to obtain the static deflection of the wing. The physical model is then fitted to these results to determine the elastic forces. For the analysis of the test case with unsteady inflow, only the amplitude of the deflection around the mean is required in the physical model for the determination of the inertial force and the elastic force, as the considered linear elastic theory suggests that the mean value of the deflection is given by the result for the case of steady inflow. The marker position measurements over time are phase-averaged in 100 temporal bins, which is identical to the processing of the flow field so that the combination of the model position with the flow fields is coherent. The mean value of these position measurements per marker over the entire period is then subtracted from the phase-averaged positions to obtain the dynamic displacement of the respective marker over the cycle. In both test cases, no significant relation is observed between the chordwise position of the marker and the deflection, indicating negligible twist of the wing, allowing the marker information to be averaged along the chord to further reduce the influence of measurement noise before applying the physical models. The physical model for the determination of the inertial force requires the acceleration, which is computed from a sinusoidal fit to the phase-averaged position measurements in time. An overview of the complete data processing procedure is illustrated in Fig. 4.5.

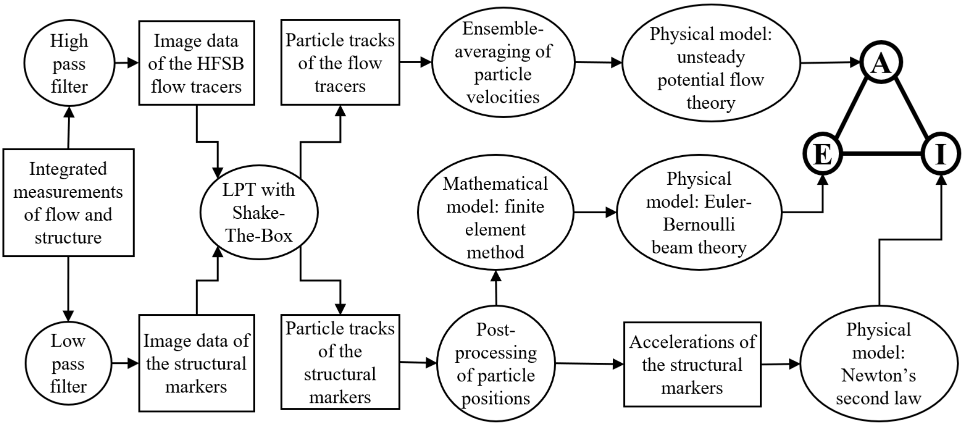

Figure 4.5: Data processing procedure for the aerodynamic and structural measurements

4.4. RESULTS

4.4.1. STEADY INFLOW

For the test case with steady inflow, the aerodynamic force is determined from the measured flow field and the elastic force is determined from the marker position measurements, while the inertial force is zero. The reaction force and moment at the root in the FE model, which is used to determine the elastic force in the investigated wing section, can be validated against the balance measurements. The strain that results from the application of the determined external force to the beam model is compared with the optical strain fiber measurements. The elastic force on the segment is in equilibrium with the aerodynamic force in the absence of inertial forces so that a comparison of the two forces is performed and the residual of the considered approach is computed.

ELASTIC FORCE

The result for the deflection $w(z)$ of the FE beam model as matched to the LPT marker displacement measurements with an optimization (as described in Sec. 4.2.3) is shown in Fig. 4.6. The standard deviation in the displacement of the seven chordwise markers that are used to produce one average displacement per spanwise position (that is indicated in the plot) has values in the range of $0.28\,\mathrm{mm} < \sigma < 0.61\,\mathrm{mm}$. After updating the value of the external load q_0 to achieve the best match of the beam model with the displacement measurements, the agreement between the beam deflection and the chordwise-averaged marker displacement is very good, with an RMS value of the difference between measurement and model of 0.10 mm.

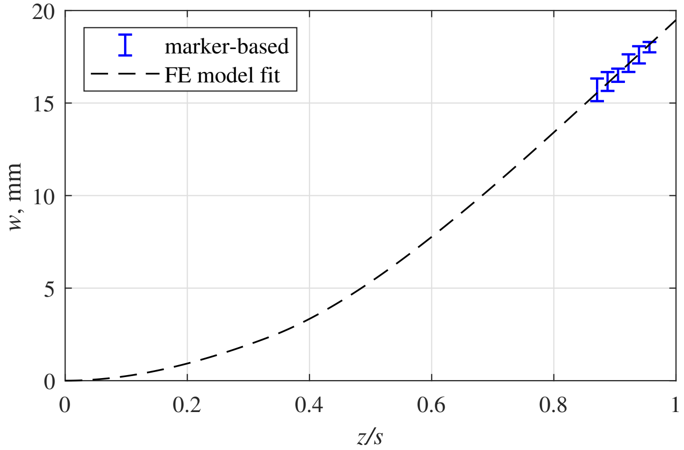

Figure 4.6: Deflection along the span of the FE beam model and LPT marker position measurements for the flexible wing at $U_\infty = 14\,\mathrm{m\,s^{-1}}$ and $\alpha = 5°$

The result for the deflected shape can be validated against the measurements from the optical strain fiber, that is installed inside the skin on the pressure side of the wing. For this purpose, the strains according to the beam model are computed from the deflection line by using the equation for the strain of an Euler-Bernoulli beam:

$$\varepsilon = -\frac{d^2 w}{dz^2} d_1\,, \tag{4.17}$$

where $d_1 = 11\,\mathrm{mm}$ is the distance of the optic fiber from the elastic axis of the beam, which is assumed to be at the chord line of the wing. The comparison between the strain measurement and the model strain is shown in Fig. 4.7. The cross-sectional stiffness properties of the wing change at $z/s = 1/3$ and $z/s = 2/3$ (see Rajpal et al., 2021), which results in a discontinuity of the strain in the beam model at these locations. In contrast, the strain fiber is installed on the inside of the surface at the pressure side of the wing, where the stiffness properties only change at $z/s = 1/3$; therefore, the strain that is measured with the optical fiber is only discontinuous at that location and not at $z/s = 2/3$. Apart from this difference, the agreement between the model and the measurement is very good.

The result for the external load q_0 can be used to calculate the shear force and the bending moment at the root of the flexible wing with Eq. (4.8) and Eq. (4.9), respectively. The value for the root shear force can be directly compared to the force measurement of the balance, as shown in Tab. 4.1, where the mean value and one standard deviation of the balance measurements are given. For the comparison of the bending moment with

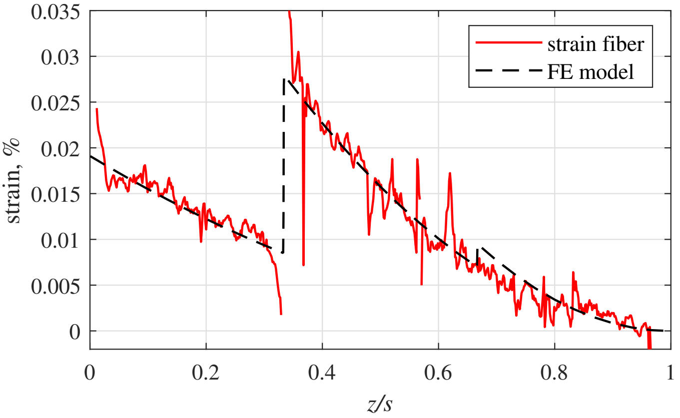

Figure 4.7: Comparison of the strain between the FE beam model that was fitted to the LPT marker positions and the optic fiber measurements

the balance measurement, the distance from the center of the balance to the root of the wing $d_2 = 334\,\mathrm{mm}$ has to be considered.

The root bending moment from the balance is determined from the balance measurements of the shear force and the moment under the assumption that no external bending moment is applied on the wing:

$$M(z=0)_\mathrm{B} = M_\mathrm{B} - Q_\mathrm{B} d_2\,. \tag{4.18}$$

A modeling assumption that is considered a source of the observed differences in shear force and bending moment in Tab. 4.1 is that of a constant external load along the span. The validity of this assumption can be assessed by calculating the spanwise center of pressure z_CP:

$$z_\mathrm{CP} = \frac{M(z=0)}{Q(z=0)}\,. \tag{4.19}$$

The balance measurements in Tab. 4.1 reveal that z_CP is located slightly further inward on the wingspan than in the assumed case of a spanwise-constant load, where z_CP is located at mid-span, differing by less than 5%, which indicates that the constant-load assumption is not the dominant source of error in the considered approach.

Table 4.1: Root loads from the FE model fitted to the non-intrusive structural measurements in comparison with balance measurements

Quantity	Non-intrusive w/ FE model	Balance measurement	Difference
Root shear force	$-17.34\,\mathrm{N}$	$-15.82 \pm 1.73\,\mathrm{N}$	9.64%
Root bending moment	$-15.18\,\mathrm{Nm}$	$-13.20 \pm 0.84\,\mathrm{Nm}$	14.94%
Center of pressure	$0.5 \times s$	$0.477 \times s$	4.84%

AERODYNAMIC FORCE

A section of the ensemble-averaged flow field at $U_\infty = 14\,\mathrm{m\,s^{-1}}$ and $\alpha = 5°$, located at $z/s = 0.90$, is shown in Fig. 4.8, together with the position of the wing section that is determined from the marker position measurements. Furthermore, the black rectangle in the plot indicates an exemplary rectangular integration contour for the calculation of the circulation around the airfoil. The shown integration contour is positioned such that a minimum distance of 25 mm, equivalent to $0.1c$, to the surface of the wing is observed in all directions.

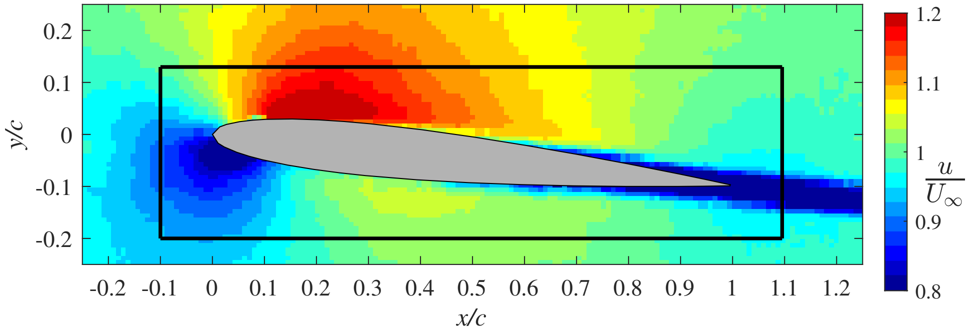

Figure 4.8: Flow field, airfoil position and an example circulation integration contour at $z/s = 0.90$

The circulation measurement that is obtained from the flow field is used to calculate the section lift with the Kutta-Zhukovsky theorem for all spanwise sections where flow measurements were conducted, as shown in Fig. 4.9. To reduce the sensitivity of the lift to the random error in the flow velocity measurements, the lift for each spanwise position is computed as the average of the lift values that are obtained when varying the distance of the rectangular circulation integration contour to the wing surface from $0.05c$ to $0.2c$ in $0.025c$ increments, similar to the procedure described in Sec. 3.4.2. The spanwise average of the standard deviation of the circulation obtained with the different integration contours is $\sigma = 0.004\,\mathrm{m^2\,s^{-1}}$, which is less than 1% of the spanwise average of the circulation, $\Gamma_b = 0.523\,\mathrm{m^2\,s^{-1}}$. The variations in the lift that result from using the different circulation integration contours are used to indicate the lift uncertainty in Fig. 4.9, where the error bars represent one standard deviation.

The aerodynamic force that is exerted on the investigated wing segment can be compared with the elastic force, which is determined from the marker measurements with the FE model. When considering the wing segment between $z_1/s = 0.85$ and $z_2/s = 0.9$, the aerodynamic force on the segment can be calculated from the lift distribution shown in Fig. 4.9 with a trapezoidal integration:

$$A = \int_{z_1}^{z_2} L'(z)\,dz = 0.7691\,\mathrm{N}, \tag{4.20}$$

while the elastic force on the segment with $q_0 = 9.91\,\mathrm{N\,m^{-1}}$ is:

$$E = -Q(z_1) + Q(z_2) = q_0(z_1 - z_2) = -0.8672\,\mathrm{N}. \tag{4.21}$$

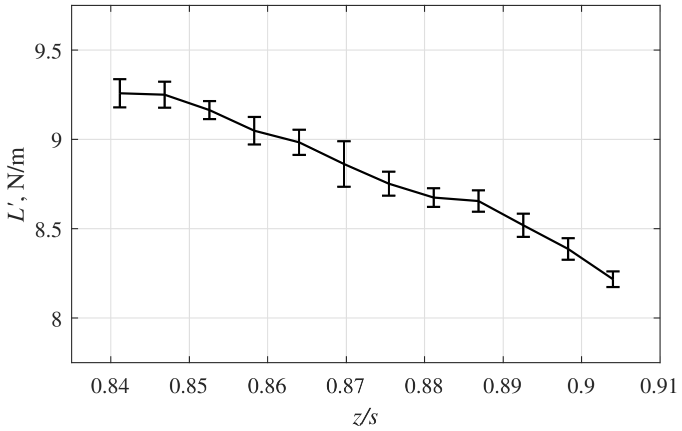

Figure 4.9: Lift from the Kutta-Zhukovsky theorem in the investigated wing section

According to the equilibrium of forces in Collar's triangle for the case of static aeroelasticity, the two forces A and E on the segment are equivalent in the absence of structural motion and hence inertial forces, which leads to the quantification of the observed measurement residual as $\Delta_F = A + E = -0.0981\,\mathrm{N}$. This value for the measurement residual is used to calculate a relative error of the considered approach for the case of steady inflow. To provide a reference force, the balance measurement of the shear force at the root is scaled by the fraction of the investigated wing section, which is $(z_2 - z_1)/s = 0.05$. This yields a reference force value of $F_{\mathrm{ref}} = -0.791\,\mathrm{N}$, and the corresponding relative error is $\epsilon = \Delta_F / F_{\mathrm{ref}} = 12.41\%$ for the case of steady inflow. This error is accredited to the difference between the elastic properties of the wing and the beam model and to the drop in lift towards the tip due to downwash effects, which is observed in Fig. 4.9 but not considered in the structural model.

4.4.2. UNSTEADY PERIODIC INFLOW

For the dynamic aeroelastic test case with unsteady periodic inflow, all three forces in Collar's triangle have to be considered. The analysis of the dynamic structural motion is based on the assumption of a linear elastic response to a sinusoidal external forcing. The result of a sinusoidal fit to the marker position measurements can be used to validate this assumption and to determine the acceleration and hence the inertial force on the investigated wing segment. The amplitude of the marker displacement measurements is used to determine the amplitude of the dynamic elastic force with the FE model. The unsteady aerodynamic force is determined from the measured flow fields and is subsequently compared to the inertial and elastic forces according to the equilibrium of forces in Collar's triangle.

INERTIAL FORCE

For the determination of the inertial force, the acceleration is determined from the phase- and chordwise averaged marker displacement measurements by fitting a sinusoidal curve to the measurements. The result is shown in Fig. 4.10 for the spanwise position at $z/s =$

0.90, where the sinusoidal fit is seen to be a very good representation of the actual measurements, with an RMS of the difference between the fit and the measurements of around 0.2 mm, which is less than the typical standard deviation of the measurements during the phase- and chordwise averaging of the marker measurements, which is around 0.3 mm.

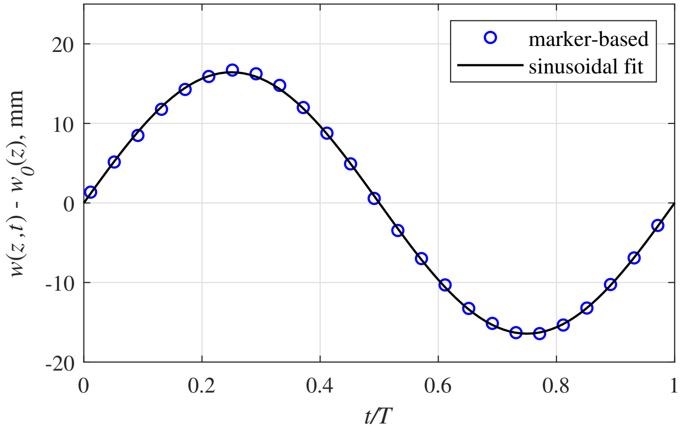

Figure 4.10: Phase-averaged marker-based displacement from the static reference and sinusoidal fit for *z/s* = 0.90

The discrete amplitude measurements that are obtained at the spanwise positions of the fiducial markers are used to estimate the continuous behavior of the wing motion in the investigated region. Because the measurements are performed near the tip, it can be assumed that the wing deformations in the sense of spanwise curvature are small and the measured amplitudes can be fitted with a linear curve, which is shown in Fig. 4.11.

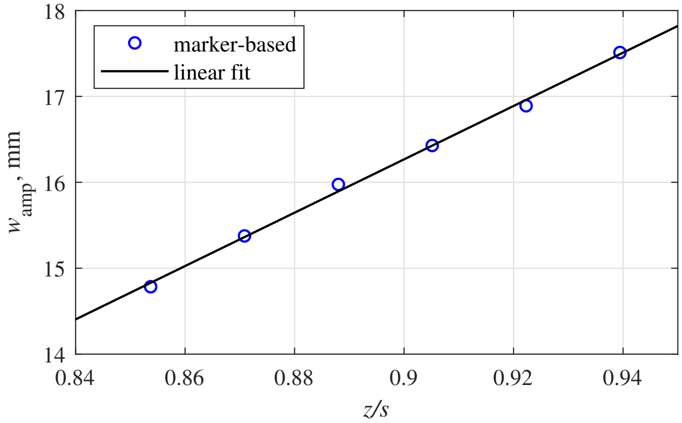

Figure 4.11: Marker-based displacement amplitudes in the investigated region and linear fit

With the obtained linear relation between the spanwise position on the investigated wing segment and the amplitudes of the sinusoidal fit according to Eq. (4.2), it is possible to determine the acceleration of the wing between z_1 and z_2 with Eq. (4.3) and thus the inertial force with Eq. (4.1). Furthermore, the amplitude at $z/s = 0.875$ resulting from the linear fit is used for the determination of the elastic force in the following.

ELASTIC FORCE

For the determination of the elastic force in the dynamic case, the amplitude of the sinusoidal forcing q_{amp} is determined from the observed wing motion amplitude w_{amp}. For that, the FE formulation of the dynamic beam bending motion in Eq. (4.12) is solved in an optimization procedure for q_{amp} that minimizes the difference in displacement amplitude between the model and the measurements. With the resulting FE degrees of freedom $\boldsymbol{\xi}_{\text{amp}}$ that are the best fit to the experimental data, the dynamic behavior of the FE model degrees of freedom is given as $\boldsymbol{\xi}_{\text{amp}} e^{i\omega_g t+\phi}$, where the phase is aligned with the sinusoidal fit of the marker measurements such that $\phi = 0$. From this result for $\boldsymbol{\xi}(t)$, the continuous time-dependent deflection $w(z,t)$ is calculated with the Hermite spline interpolation for each time step. Then, the shear force and bending moment along the span are obtained with Eq. (4.5) and Eq. (4.6), respectively, from the deflection by using a second-order accurate finite difference scheme. With the results of this procedure, the dynamic component of the shear force and the bending moment for comparison with the dynamic component of the balance measurements can be computed over the period. The comparison is shown in Fig. 4.12 for the force and in Fig. 4.13 for the moment, where the mean value has been subtracted from the balance measurements.

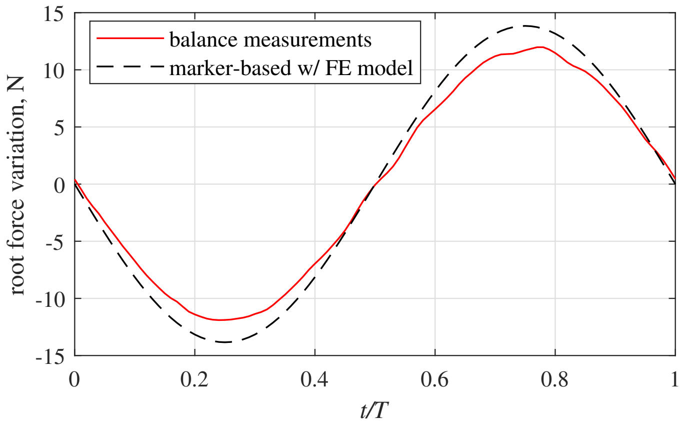

Figure 4.12: Comparison of the root shear force from the FE model with the balance measurements

The RMS value of the difference between the model and the measurement is 1.43 N for the shear force and 1.26 N m for the bending moment, corresponding to a relative error of 17.10% and 15.01%, respectively, using the RMS of the balance measurements as a reference. The phase alignment between the model and the measurement is very good for both the force and the moment, with phase differences of less than 0.5% of the period determined by cross-correlating the signals.

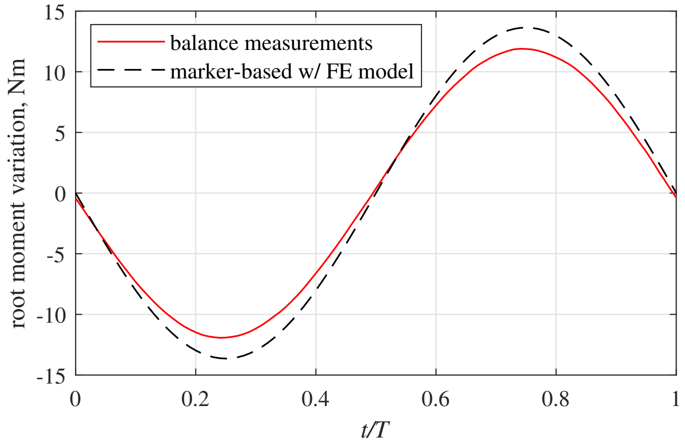

Figure 4.13: Comparison of the root bending moment from the FE model with the balance measurements

AERODYNAMIC FORCE

The phase-averaged unsteady flow field and the corresponding wing position as determined from the marker tracks are shown for four phase instants in Fig. 4.14. The effect of the impinging gusts is evident in the plots, with a visibly enlarged and reduced region of accelerated flow over the suction surface of the wing at $t/T = 0.25$ and $t/T = 0.75$, respectively.

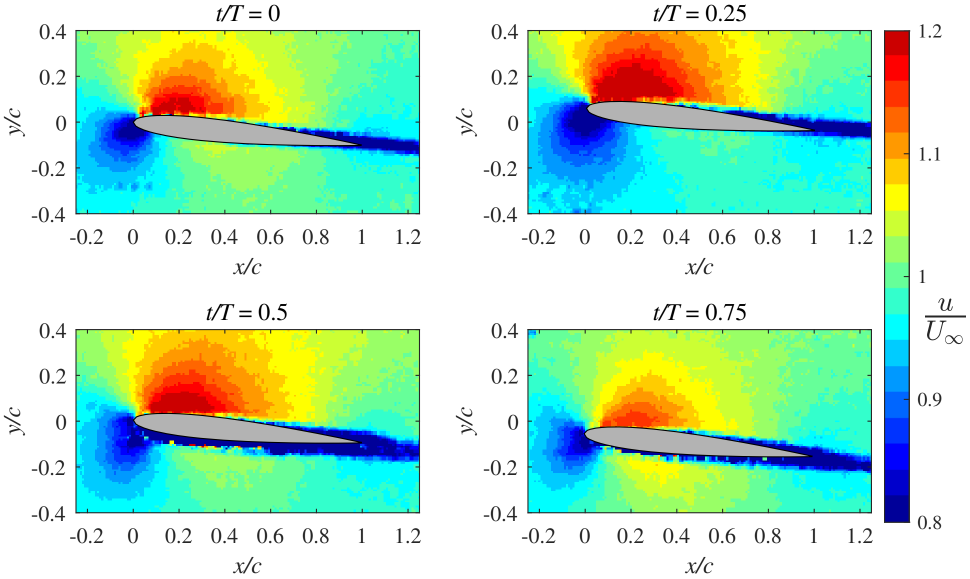

Figure 4.14: Flow field and airfoil position for four different phase instants at $z/s = 0.88$

The calculation of the unsteady lift with Eq. (3.10) requires the determination of the partial circulation $\Gamma_p(x,t)$, which is obtained by performing line integrals of the measured velocity for each phase instant. Similar to the test case with steady inflow, the procedure described in Sec. 3.3.1 is followed, where the position of the integration path is varied to reduce the effect of the random error in the flow velocity measurements on the result for the circulation. Only the positions of the line segments that are upstream, above, and below the airfoil are varied, while the downstream segment remains fixed at the particular x-location on the airfoil, to determine the value of $\Gamma_p(x,t)$ at that specific location. To determine the overall bound circulation around the airfoil $\Gamma_b(t) = \Gamma_p(x = c, t)$, the downstream segment of the integration path also remains fixed just behind the trailing edge of the airfoil, so that the varying circulation that is shed into the wake in the unsteady case following Kelvin's theorem is not affecting the determined result for the bound circulation $\Gamma_b(t)$. The mean value over the period of the standard deviation of the circulation obtained with different integration contours as described above is $\sigma = 0.024\,\mathrm{m}^2\,\mathrm{s}^{-1}$, which is increased by a factor of around six with respect to the standard deviation of the circulation that is obtained with a similar procedure for the test case with steady inflow. This increase results from the higher level of random error in the phase-averaged measurements of the unsteady periodic inflow when compared to the steady case because the number of acquired images is approximately 15 times smaller for a time span of 1% of the period in the unsteady inflow case than in the case with steady inflow. To reduce the level of random error in the measurement, the determined time series of $\Gamma_p(x,t)$ is fitted with a sinusoidal curve for each chordwise position. Additionally, the partial circulation is averaged across the span in the region z_1 to z_2 so that the average lift per unit span on the investigated wing segment is determined. The result is shown for four different phase instants in Fig. 4.15.

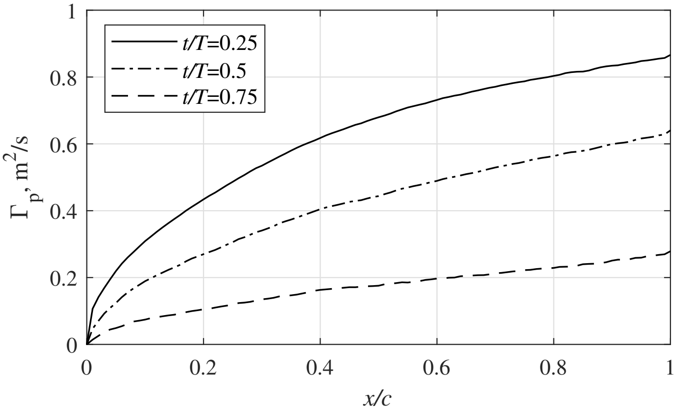

Figure 4.15: Partial bound circulation along the chord for three different phase instants

By using the Kutta-Zhukovsky theorem together with the overall bound circulation around the airfoil $\Gamma_b(t)$, as determined from the unsteady flow fields, the quasi-steady lift is obtained. To determine the unsteady lift, the additional flow acceleration term is computed from the time series of the circulation distribution with Eq. (3.10). Both lift curves over the period are shown in Fig. 4.16. The unsteady lift curve as determined from the sinusoidal fit is similar to the quasi-steady lift curve. As a result of including the flow acceleration term in Eq. (3.10), the amplitude of the unsteady lift is decreased by 0.7% compared to the quasi-steady lift, and the curve is shifted by −2.70% of the period. The lag of the lift with respect to the dynamic motion of the wing is reduced from 3.62% to 0.92% of the period when including the flow acceleration term, which leads the quasi-steady lift in phase.

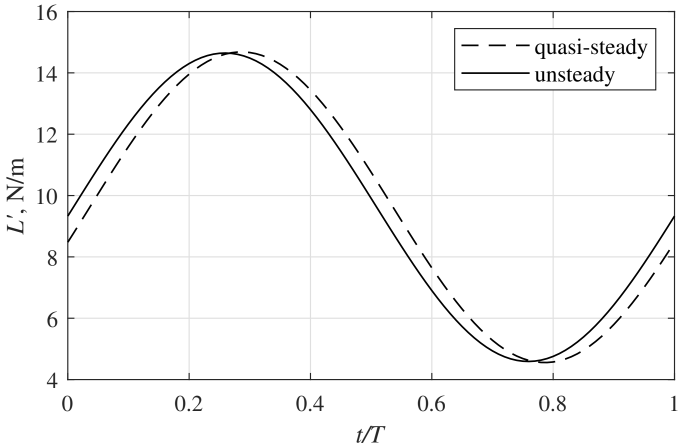

Figure 4.16: Quasi-steady and unsteady lift acting on the wing section over the period

CLOSURE OF COLLAR'S TRIANGLE

After the three forces in the dynamic aeroelastic interaction are determined based on the LPT measurements, the results can be compared with each other to validate the physical models based on the equilibrium of forces. The aerodynamic and inertial forces on the segment are determined directly with a spanwise integration of the obtained results between z_1 to z_2. For the determination of the elastic force on the segment, the amplitude of the dynamic motion of the FE degrees of freedom $\boldsymbol{\xi}_{\text{amp}}$ is combined with the solution in the case of steady inflow $\boldsymbol{\xi}_0$ to yield the dynamic result $\boldsymbol{\xi}(t) = \boldsymbol{\xi}_0 + \boldsymbol{\xi}_{\text{amp}} e^{i\omega_g t+\phi}$, that is used to calculate the shear forces $Q(z_1, t)$ and $Q(z_2, t)$ with finite differences. The results for the three forces on the investigated wing segment are shown in Fig. 4.17. Additionally, the value of the residual Δ_F is shown over the period.

The maximum absolute value of Δ_F over the period is 0.158 N at $t/T = 0.23$, which is near the maximum values of the elastic and aerodynamic force magnitudes. The RMS value of Δ_F over the period is 0.0964 N, which corresponds to an error of 11.72% of the reference force from the balance, which is the mean value over the period of the measured root shear force, scaled by the fraction of the investigated wing section. This value of the error in the dynamic aeroelastic test case is very similar to the value of the error in the static aeroelastic test case. It can therefore be assumed that the sources of error are the same as in the static case, especially when considering that the result from the static test case has been used to obtain the result for the dynamic shear force. As a consequence, it is noted that the added complexity of the dynamic test case, with considerable unsteady aerodynamic and inertial forces, is suitably accounted for with the applied methods and does not lead to significant additional sources of error.

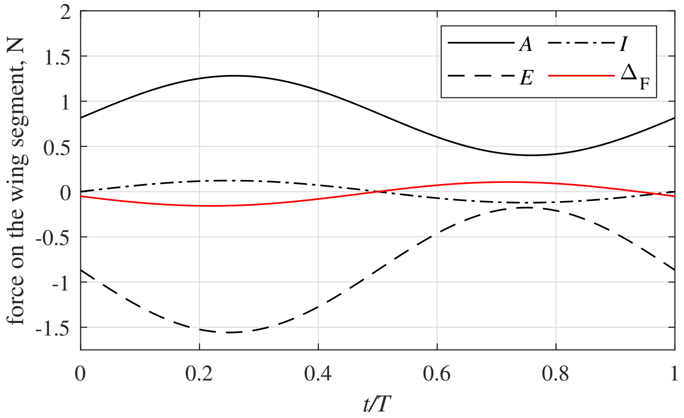

Figure 4.17: Three forces in Collar's triangle A, E, I as determined from the integrated optical measurements and the measurement residual $\Delta_F = A + E + I$

4.5. CONCLUDING REMARKS

The characterization of the aeroelastic response of a flexible wing, in terms of all three force components in Collar's triangle, based on integrated optical measurements was demonstrated by analyzing a section of a flexible wing. After applying custom post-processing procedures for the particle tracks of the flow and structure separately, the three different forces in the aeroelastic interaction were determined using three different methods. The sectional inertial force was determined as the product of mass and acceleration of the wing based on the deformation measurements, while the aerodynamic force was determined from the flow field measurements with an unsteady potential flow model, and the elastic force was determined by fitting an FE beam model to the deformation measurements. The physical agreement of the three forces, based on the equilibrium of forces in Collar's triangle, was similar to the agreement between the elastic force and the reference data from the balance measurements. This observation supports the results for the aerodynamic and inertial forces and indicates that the fidelity of the inverse structural modeling approach should be improved to achieve a better characterization result.

For the proof of concept that was presented in this chapter, the physical models that were used to determine the forces from the measurement data were of relatively low complexity. However, the complexity of the physical models that are used to analyze the measurements of the integrated non-intrusive measurement approach could be increased if required. This would be necessary in the case of considerable non-linear aerodynamic effects due to flow separation, or very large structural deformations that cannot be modeled with the linear theory of small deflections. Yet, the inverse structural modeling has been identified as the most complex and error-prone aspect of the aeroelastic characterization based on LPT measurements, already under the conditions encountered in this chapter. This means that for experimental test cases with more complex structural behavior, such as the highly flexible wing that is investigated in the next chapter, the elastic force cannot be determined directly from the marker measurements without the use of a more sophisticated inverse structural modeling procedure. It is therefore concluded that the elastic loads are best determined by exploiting the equilibrium of forces in Collar's triangle, thus using the other two forces (aerodynamic and inertial) to calculate the elastic force, when performing an aeroelastic characterization based on measurements with the integrated optical approach. Hence, this procedure will be followed in the next chapter.

5

APPLICATION: AEROELASTIC ANALYSIS OF A HIGHLY FLEXIBLE WING

The aeroelastic response of a highly flexible wing to steady and periodic unsteady inflow conditions is analyzed in a wind tunnel experiment. The investigated wing exhibits tip displacements of more than 24% of its span width under the considered experimental conditions. The measurements are performed with the integrated optical approach that provides measurements of the structural response of the wing and the unsteady flow field around it. The aeroelastic loads acting on the wing are derived using physical models and validated against force balance measurements, showing a good agreement for all considered inflow conditions.

Parts of this chapter have been accepted for publication in the AIAA Journal as: Mertens, C., Costa Fernández, J. L., Sodja, J., Sciacchitano, A., and van Oudheusden, B. W. (2023). Nonintrusive Experimental Aeroelastic Analysis of a Highly Flexible Wing.

5.1. BACKGROUND

Significant progress in aeroelastic research has been achieved in the past based on experimental aeroelastic studies that served as a benchmark for the development of improved simulation methods, for example in the case of the structural and aerodynamic nonlinearities that occur on high aspect ratio wings (Tang & Dowell, 2001, 2002a, 2002b). Following this tradition, a novel experimental benchmark of a highly flexible wing, known as the Pazy wing, has recently been introduced to support the development of numerical prediction models for highly flexible structures with experimental reference data (Avin et al., 2022). This wing has been observed to sustain very large deformations in the wind tunnel, with tip displacements of more than 50% of the span. Previous experimental studies on the Pazy wing were conducted at the Technion (Israel Institute of Technology) and were focused on the behavior of the wing in steady inflow and during inflow velocity sweeps and on the limit-cycle oscillation behavior of the wing (Avin et al., 2022; Drachinsky et al., 2022). Several numerical studies have followed these experimental activities, using the results as a benchmark for the validation of numerical models (Goizueta et al., 2022; Hilger & Ritter, 2021; Riso & Cesnik, 2022).

In the existing experimental studies of the Pazy wing, wind tunnel measurements were performed with strain sensors, an optical motion tracking system, and a force balance. However, no dedicated aerodynamic measurements were performed so far. In this chapter, an adapted version of the Pazy benchmark wing, the Delft-Pazy wing, is studied in a wind tunnel experiment where aeroelastic measurements are performed with the integrated optical approach. Based on the optical measurements of the flow and the structure, the aeroelastic response of the wing to steady and unsteady inflow conditions is characterized. Two different angles of attack and two different gust excitation frequencies are studied, producing different static and dynamic aeroelastic wing responses, respectively. Significant extensions to the proof of concept study in the previous chapter are the flow field measurements along the entire span width of the wing and the increased complexity of the experimental conditions, in which aerodynamic and structural nonlinearities are observed. Additionally, an extension to the integrated optical measurement approach is explored by conducting aerodynamic measurements with an infrared camera. These measurements provide insight into the boundary layer behavior of the Delft-Pazy wing, which cannot be resolved with the LPT measurements but are valuable information for the validation of numerical simulation methods.

5.2. EXPERIMENTAL SETUP AND PROCEDURES

5.2.1. DELFT-PAZY HIGHLY FLEXIBLE WING MODEL

The investigated Delft-Pazy wing is nearly identical to the benchmark Pazy wing described in detail by Avin et al. (2022). The wing has a nominal span of $s = 550\,\mathrm{mm}$, with a chord length of $c = 100\,\mathrm{mm}$ and a NACA 0018 airfoil section. The wing is furthermore equipped with a 300 mm long wingtip rod with a diameter of 10 mm and a mass of approximately 15 g that can be used to change the dynamic aeroelastic properties of the wing (see Avin et al., 2022). The wing structure consists of an aluminum spar and a 3D-printed nylon chassis that forms the leading and trailing edges as well as the ribs and is connected to a cylindrical mounting base. The main difference to the benchmark Pazy wing design is the reduced thickness of the aluminum plate representing the spar of the Delft-Pazy wing, which is 1.5 mm, as opposed to 2.25 mm for the original benchmark wing. The purpose of this design modification is to achieve similarly large deformations as observed by Avin et al. (2022) at the reduced wind tunnel speed, which is adjusted to facilitate the LPT measurements of the wing with the optical setup present in the wind tunnel test section (see Sec. 5.2.4). The mass of the wing, including the wingtip rod but without the mounting base and connectors is estimated to be 279 g, based on the information given by Avin et al. (2022) and considering the reduced plate thickness. The skin of the Delft-Pazy wing is made of Oralight black iron-on film that is applied to the chassis by thermal shrinking. The wing surface is painted with a grid of white circular markers with a diameter of 1.5 mm at the spanwise locations of the ribs and on the wingtip rod, to perform the measurements of the structural response of the wing in the wind tunnel. The wing geometry and the surface marker grid specifications are shown in Fig. 5.1.

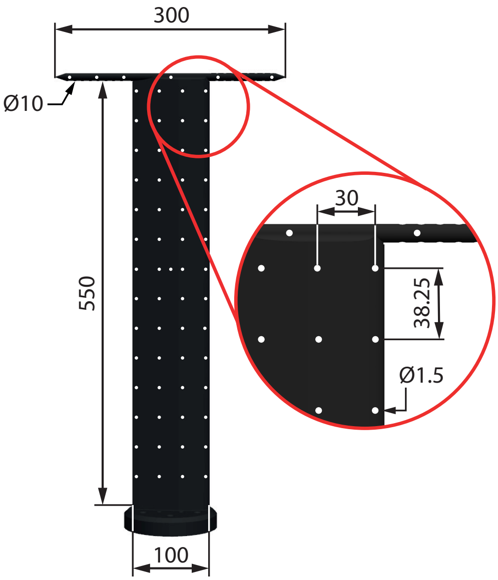

Figure 5.1: Sketch of the dimensions (in mm) of the Delft-Pazy wing with detail of the fiducial marker grid

The purpose of the structural marker measurements is threefold; firstly, marker measurements of the unloaded wing mounted in the wind tunnel are used to transform the measurement coordinate system into wind tunnel coordinates. Secondly, measurements of the wing under aerodynamic load are used to determine the deformed wing shape according to the procedure described in Sec. 5.3.2, which is in turn used for the determination of the inertial force. Additionally, the marker-based wing shape reconstruction is used for selecting the circulation integration contours during the aerodynamic load determination based on the flow field measurements. The construction process of the Delft-Pazy wing with a thin foil covering the chassis does not preserve the design airfoil shape between the ribs due to the flexibility of the foil. This means that the aerodynamic shape of the wing is altered from the design shape. To quantify this effect, a 3D-scan of the wing is performed in unloaded conditions, using a FARO Quantum Max scanner arm (maximum permissible error below 0.1 mm)[1]. The result of the shape scan is visualized in Fig. 5.2. Two cross-sectional slices of the scanned geometry are shown, section I between two ribs and section II on a rib, as well as one slice along the span at $x/c = 0.25$. The differences between the outer shape of the Delft-Pazy wing and the design shape are visible, as the maximum thickness of the wing section between the ribs is reduced by more than 10% compared to the reference NACA 0018 airfoil. Furthermore, a kink in the sectional wing shape is visible close to the leading edge for slice I. The effects of these shape alterations on the boundary layer on the suction side of the wing are quantified based on measurements with an infrared camera that is used to perform surface temperature measurements of the Delft-Pazy wing in the wind tunnel.

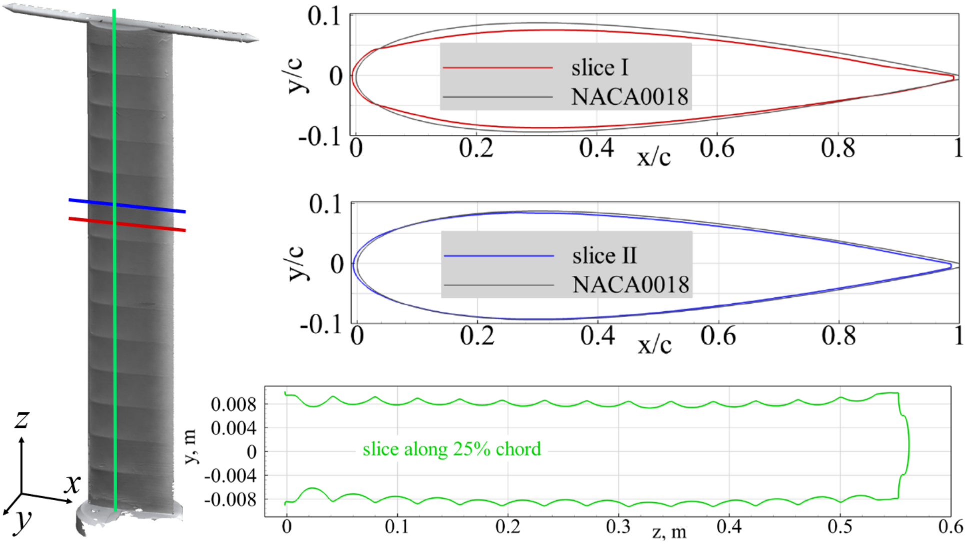

Figure 5.2: Visualization of the outer shape scan results of the Delft-Pazy wing

5.2.2. GROUND VIBRATION TEST

A ground vibration test (GVT) and a FE model simulation are used to characterize the structural dynamic behavior of the Delft-Pazy wing, in a similar approach as reported by Jaworski and Dowell (2009). The GVT measurements are conducted with a Polytec PSV-500 laser scanning vibrometer in the frequency range up to 800 Hz and post-processed with the SimCenter TestLab software. An overview of the experimental setup of the GVT is shown in Fig. 5.3(a). The vibration data is acquired at 37 different measurement points on the wing (see Fig. 5.3(b)), and the data from 10 measurements are averaged for each measurement point. The excitation of the wing model is achieved with a Maul-Theet

---

[1] https://www.faro.com/en/Products/Hardware/Quantum-FaroArms

vImpact-61 automatic modal hammer. The impact point of the modal hammer is near the leading edge of the wing at around one-quarter of the wingspan measured from the base, between the third and the fourth rib, as visible in Fig. 5.3(b).

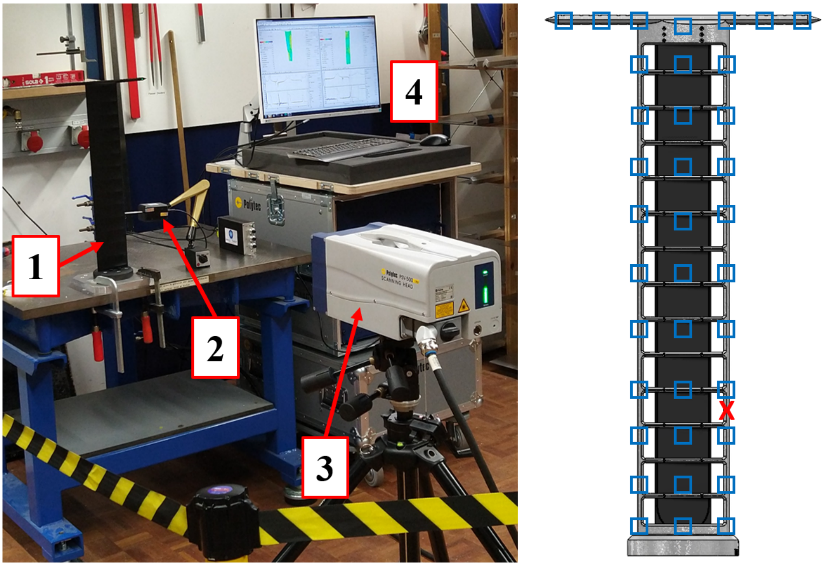

(a) (b)

Figure 5.3: Ground vibration test of the Delft-Pazy wing. (a) Experimental setup. 1: Delft-Pazy wing, 2: modal hammer, 3: laser scanning vibrometer, 4: data acquisition computer. (b) Design model of the wing without skin, with an indication of the GVT measurement points (blue squares) and the driving point (red cross)

The results of the GVT in terms of the first five mode shapes, the modal frequencies, and damping are summarized in Tab. 5.1. The GVT results are correlated with a finite element model of the wing using the correlation tool in SimCenter 3D. The finite element model of the Delft-Pazy wing was derived from the finite element model of the original Pazy wing (available through the Third Aeroelastic Prediction Workshop[2]) by adjusting the spar thickness in the model to match the reduced plate thickness comprising the spar in the Delft-Pazy wing. The comparison between the GVT and the simulation results is shown in Fig. 5.4, showing a qualitative comparison between the first five modes. The agreement between the mode shapes is very good, which is also indicated by very high values of the modal assurance criterion (MAC, Pastor et al., 2012), which is given in Tab. 5.1. The agreement between the frequencies of the finite element model, f_{FEM}, and from the GVT, f_{GVT}, for the first five modes is very good, with an average difference of around 4% of the finite element model with respect to the GVT result, $\Delta f = (f_{\mathrm{FEM}} - f_{\mathrm{GVT}})/f_{\mathrm{GVT}}$, which is similar to the agreement between the FEM and the GVT results reported by Avin et al. (2022) for the original Pazy wing and Jaworski and Dowell (2009) for a similar wing design.

---

[2] https://nescacademy.nasa.gov/workshops/AePW3/public/wg/largedeflection

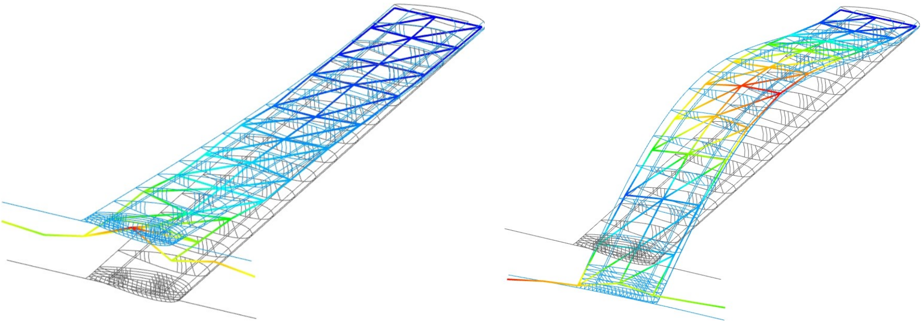

(a) first bending (b) second bending

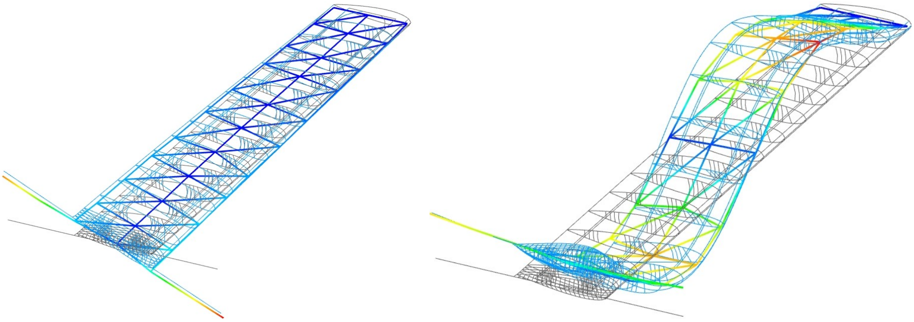

(c) first torsion (d) third bending

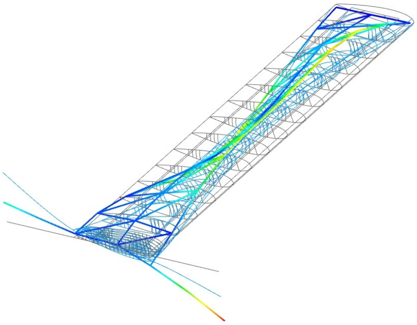

(e) second torsion

Figure 5.4: Dynamic mode shape comparison between finite element model (light blue, with undeformed reference shape in grey) and GVT result (colored by displacement)

Table 5.1: Results of the ground vibration test and comparison with finite element model

mode no.	mode type	f_{GVT}	damping ratio	f_{FEM}	Δf	MAC
1	first bending	3.2 Hz	0.54%	3.3 Hz	+2.3%	0.96
2	second bending	22.5 Hz	0.60%	21.9 Hz	-2.3%	0.99
3	first torsion	29.5 Hz	0.61%	28.1 Hz	-4.7%	0.97
4	third bending	65.0 Hz	0.60%	63.1 Hz	-2.9%	0.96
5	second torsion	119.7 Hz	0.65%	105.9 Hz	-11.5%	0.73

5.2.3. WIND TUNNEL SETUP

The wind tunnel experiment is conducted in the OJF at a freestream velocity of $U_\infty = 18.3\,\mathrm{m\,s^{-1}}$, corresponding to a Reynolds number of $\mathrm{Re} = 122\,000$ based on the wing chord. The Delft-Pazy wing model is mounted vertically in the test section on a force balance, which is attached to a rotating table that allows setting the geometric angle of attack, α, defined with respect to the steady inflow direction. The balance and the rotating table are located underneath a splitter plate to reduce wind tunnel interference effects. This part of the setup is positioned between the optical measurement setup for the LPT measurements on one side and the setup for the infrared thermography measurements on the other side. For the experiment, the same gust generator that was used in the previous chapter, consisting of two vertically mounted movable vanes that span the height of the wind tunnel nozzle (Lancelot et al., 2017), is mounted at the wind tunnel nozzle exit. The wind tunnel setup with an indication of the relevant components is sketched in Fig. 5.5.

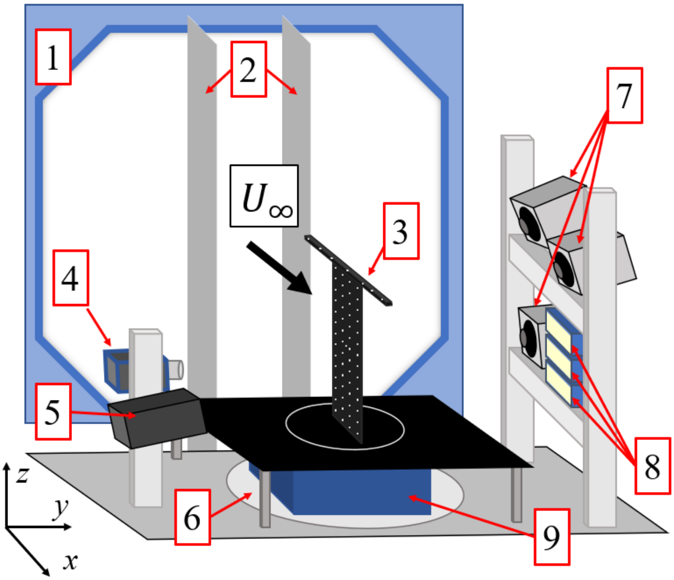

Figure 5.5: Sketch of the experimental setup in the OJF. 1: Wind tunnel nozzle exit, 2: gust generator vanes, 3: Delft-Pazy wing, 4: infrared camera, 5: heat lamp, 6: rotating table, 7: high-speed cameras, 8: LED illumination units, 9: force balance

For the infrared thermography measurements, the suction side of the wing is measured at 8 different angles of attack between $0° \leq \alpha \leq 14°$, with increments of $\Delta\alpha = 2°$, in steady inflow conditions. The infrared thermography measurement system is described in Sec. 5.2.5. For the integrated optical measurements with the LPT system (see Sec. 5.2.4), four different test conditions are considered, of which two are with steady inflow conditions and two include unsteady inflow produced by the gust generator. The conditions of the four test cases are summarized in Tab. 5.2. For the two test cases with steady inflow, the angle of attack is set to $\alpha = 5°$ and $\alpha = 10°$, respectively, achieving different lift values and thus wing deformation levels. For the test cases with gust generator operation, the unsteady inflow is generated by a continuous sinusoidal operation of the gust generator during the measurement, with the gust vane angle described by $\beta = \beta_{\text{amp}} \sin(2\pi f_g t)$, where β_{amp} and f_g are the amplitude and frequency of the gust vane motion, respectively. Different mean angles and gust frequencies are selected for the two dynamic test cases, corresponding to different levels of wing deformation and unsteadiness in the periodic inflow conditions, respectively. The first dynamic test case is selected to represent linear unsteady aerodynamic conditions because these conditions are relevant for applications in flight (see Z. Wu et al., 2019). A moderate geometric angle of attack $\alpha = 5°$ is therefore selected, while the gust frequency is determined to be high enough to reach a reduced frequency of $k = 0.1$, which is high enough to produce considerable unsteady aerodynamic effects, as observed in the previous two chapters. The second dynamic test case is selected to study the gust response involving very large deformations. The angle of attack, $\alpha = 10°$, is therefore selected to produce the maximum value of the lift to achieve a large mean deflection. Furthermore, the wing is excited with a gust frequency that corresponds to the first natural bending frequency of the Delft-Pazy wing as it is measured in the GVT, to produce large dynamic deflections around the mean deflection.

Table 5.2: Summary of the wind tunnel test conditions for the integrated optical measurements

test case	wing geometric angle of attack α	gust vane amplitude β_{amp}	gust frequency f_g	reduced frequency k
static 1	5°	N/A	N/A	0
dynamic 1	5°	5°	5.7 Hz	0.10
static 2	10°	N/A	N/A	0
dynamic 2	10°	5°	3.2 Hz	0.055

The gust vane amplitude is set to $\beta_g = 5°$ in both test cases. Based on previous studies, it can be expected that this amplitude corresponds to a variation of the inflow angle to the wing with roughly half the amplitude of the gust vane motion (Lancelot et al., 2017). This estimate can be compared to the variation of the transversal velocity component $v(t)$ in the flow, based on the ensemble-averaged LPT flow field measurements of the wing (see Sec. 5.2.4). To minimize the influence of the presence of the wing on the gust measurement, the inflow is analyzed upstream of the wing at the streamwise location $x/c = -0.75$, which corresponds to the upstream edge of the field of view of the LPT system. The phase-averaged measurements of the transversal velocity component at the considered streamwise location are averaged over an area that is centered at the mid-span of the deflected wing and spans $0.5s$ in the spanwise direction and $0.4s$ in the transversal direction over the entire gust period. The influence of the wing on the transversal flow velocity at $x/c = -0.75$ is non-zero, the transversal velocity is the sum of the contributions of the gust and the velocity induced by the wing, $v(t) = v_g(t) + v_{\text{wing}}(t)$. To determine the gust velocity only, it is assumed that the velocity induced by the wing at $x/c = -0.75$ does not vary strongly over time, such that $v_g(t) \approx v_{\text{amp}}(t) = v(t) - v_{\text{m}}(t)$. The transversal gust velocity measurements obtained with this approximation are shown for the two gusts with different frequencies in Fig. 5.6(a) and Fig. 5.6(b), respectively.

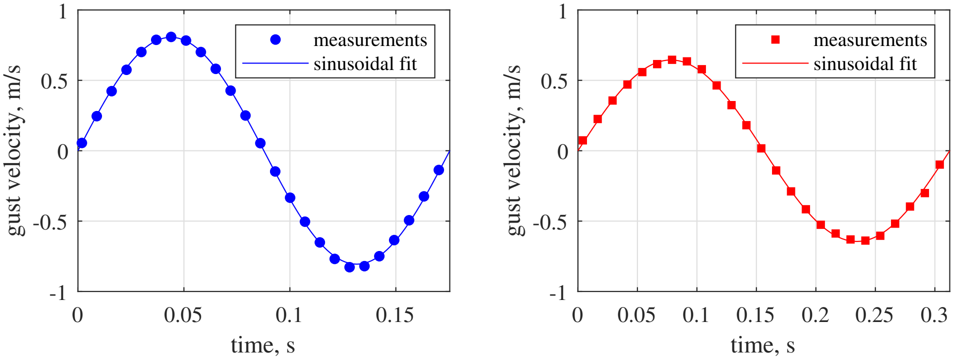

(a) $f_g = 5.7\,\text{Hz}$ (b) $f_g = 3.2\,\text{Hz}$

Figure 5.6: Measurements with sinusoidal fit of the transversal gust velocity upstream of the wing

The measurements for both gusts are well approximated with a sinusoidal fit that uses the inverse of the gust frequency as the period length. Operating the gust generator at the higher frequency of $f_g = 5.7\,\text{Hz}$ produces gust measurements with a transversal velocity amplitude of $v_{g,\text{amp}} = 0.81\,\text{m}\,\text{s}^{-1}$ (corresponding to an inflow angle variation amplitude of $\alpha_{g,\text{amp}} = 2.5°$) that is around 20% larger than the value of $v_{g,\text{amp}} = 0.65\,\text{m}\,\text{s}^{-1}$ (equivalent to $\alpha_{g,\text{amp}} = 2.0°$) that is obtained for the lower frequency of $f_g = 3.2\,\text{Hz}$. The sinusoidal fits of the gust measurements are used to align the gusts in time throughout this chapter, such that for both gust frequencies the time instant $t/T = 0$ corresponds to the time instant at which the gust arrives at the theoretical aerodynamic center of the wing at $x/c = 0.25$, based on the assumption that the gust convects downstream from the measurement location with the freestream velocity.

5.2.4. LAGRANGIAN PARTICLE TRACKING SYSTEM

For conducting the non-intrusive measurements of the flow, the freestream is seeded with HFSB, using the same seeding generator system as in the previous chapters, placed in the OJF upstream of the wind tunnel contraction. The seeding particle concentration during the experiment is on the order of $1\,\text{cm}^{-3}$. The setup for conducting the integrated non-intrusive measurements consists of three Photron Fastcam SA1.1 high-speed cameras with 50 mm lenses at a focal ratio of $f/22$. The cameras are operated at a recording frequency of 5.4 kHz with a resolution of 1024×1024 pixel (12-bit, 20 µm pixel pitch). The illumination of the HFSB flow tracers and the fiducial markers on the wing is achieved with three LaVision LED-Flashlight 300 illumination units. The LPT data acquisition is performed with the LaVision Davis 10 software. A photo of the LPT measurement setup in the wind tunnel is shown in Fig. 5.7.

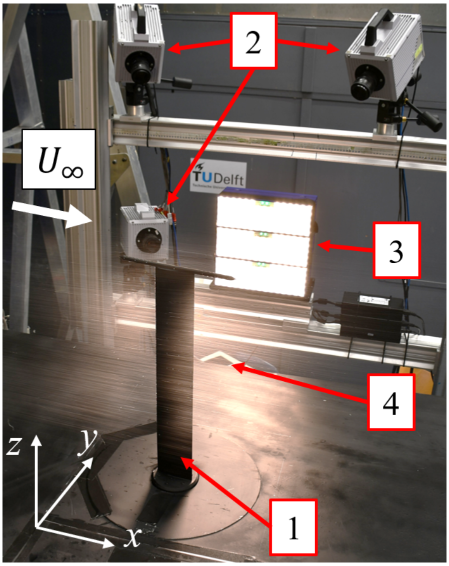

Figure 5.7: Photo of the Lagrangian particle tracking measurement setup in the wind tunnel. 1: Delft-Pazy wing, 2: high speed cameras, 3: LED illumination units, 4: stream of illuminated HFSB

The size of the measurement volume that is obtained with this setup is about 300 mm in the x, y, and z directions, respectively. To achieve the complete aeroelastic characterization of the Delft-Pazy wing, which has a span width of 550 mm, measurements of the flow field around the entire wing are necessary. Considering the measurement volume size, four separate measurements are performed for each test case. Each of the four measurements is covering roughly one quarter of the entire investigated domain: one measurement volume is placed on the suction and one on the pressure side for the upper and the lower half of the wingspan, respectively. The adjustment of the spanwise position of the measurement volume is performed by changing the position of the cameras and illumination with respect to the wing. The measurements on the suction and pressure side of the wing are performed without moving the optical measurement setup and instead by changing the angle of attack of the wing from $+\alpha$ to $-\alpha$, respectively. For the test cases with steady inflow, the four acquisitions from the four different measurement volumes are combined into an integrated, time-averaged representation during the LPT data post-processing. For the dynamic test cases, five recordings, each with a duration of 1.01 s (5457 images per recording, corresponding to the full memory of the cameras), are performed for each of the four measurement volumes. These separate measurements are then combined into a phase-averaged representation of the flow field during the post-processing, which is necessary to improve the measurement resolution, considering the limited seeding particle concentration.

The processing of the integrated optical measurements is performed analogously to the procedures described in the previous chapters. First, the images of flow and structure are separated by exploiting the different time scales of their motion. Subsequently, the data sets are processed separately and the STB algorithm is applied. The obtained LPT measurements are post-processed in a time- or phase-averaged sense, for the test cases with steady and unsteady periodic inflow, respectively. A further necessary post-processing step of the LPT data is the transformation of the measurement coordinate system to the wind tunnel coordinate system. This is achieved by acquiring a reference measurement of the structural markers on the Delft-Pazy wing without wind tunnel operation after each adjustment of the measurement volume. This data is then correlated with the reference positions of the markers painted on the model to determine the translations and rotations of the measurement coordinates with respect to the wind tunnel coordinates, which are then used to transform the LPT measurements into the wind tunnel coordinate system. The accuracy of the employed merging procedure can be assessed by comparing the measured flow velocity at corresponding positions with respect to the wing from different acquisitions. Typical values of these differences are between 1% and 3% of the local velocity magnitude. Since these values are of the same order of magnitude as when the merging of different flow measurement acquisitions is performed automatically based on position measurements with a robotic arm (see Jux et al., 2018), these differences are considered acceptable and not further investigated.

5.2.5. INFRARED THERMOGRAPHY MEASUREMENT SETUP

The setup for the infrared thermography measurements in the wind tunnel is shown in Fig. 5.8. An infrared camera is used to measure the infrared radiation emitted from the suction surface of the wing, which is proportional to the surface temperature. To facilitate the analysis of the boundary layer state on the wing based on the thermographic measurements, the wing surface is heated above the temperature of the freestream with a halogen lamp.

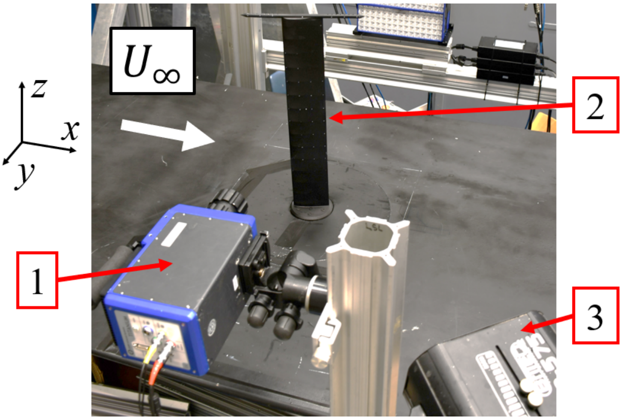

Figure 5.8: Photo of the infrared thermography measurement setup in the wind tunnel. 1: Infrared camera, 2: Delft-Pazy wing, 3: halogen lamp

The measurements are performed with a FLIR SC7300 infrared camera, which is acquiring thermographic images with a resolution of 320x256 pixels at a frame rate of 230 Hz, using an integration time of 250 µs. For each α, 100 images are taken for time-averaging. The field of view of the infrared camera captured the full span of the wing. To perform the quantitative analysis of the boundary layer, the infrared images are mapped onto the wing's reference system to account for the deflection of the wing. This is achieved by detecting the intersections of the ribs with the edges of the wing in the infrared images and mapping the image data accordingly. Since the purpose of the infrared thermography measurements is the detection of the boundary layer state, the physical values of the surface temperature are not required. Hence, no temperature calibration is performed because the data can be analyzed in terms of the infrared radiation in camera counts.

5.3. DATA PROCESSING AND ANALYSIS

The data processing steps that are applied to analyze the static and dynamic aeroelastic behavior of the Delft-Pazy wing are described in this section. First, a discussion on the aerodynamic and structural loads determination methods that are applied in this chapter is provided in Sec. 5.3.1. The post-processing of the LPT measurements to obtain the wing shape reconstruction and the ensemble-averaged volumetric flow fields are then described in Sec. 5.3.2 and Sec. 5.3.3, respectively. The latter also contains an analysis of the unsteady flow fields with respect to the effective inflow angles to the wing. The results for the wing shapes and the flow fields are subsequently analyzed to achieve the characterization of the aeroelastic loads acting on the wing. To validate these results, a comparison is made to force balance measurements in terms of the root force on the wing. The processing of the force balance measurements is described in Sec. 5.3.4. The data analysis of the infrared thermography measurements for characterizing the boundary layer on the Delft-Pazy wing is described in Sec. 5.3.5.

5.3.1. AEROELASTIC LOADS DETERMINATION METHODS

The three aeroelastic forces are derived from the integrated optical measurements using physical principles. However, the aerodynamic and inertial loads are derived from the measurements using appropriate physical models, while the elastic force is evaluated from the other two forces based on the equilibrium of the three forces acting on the wing in this chapter (see Sec. 2.3).

The determination of the aerodynamic lift force follows the same procedure that is described in Sec. 4.2.1, using the circulation-based method that was introduced in Sec. 3.4.2. The drag force is not analyzed, as the lift is the component of the aerodynamic force that determines the aeroelastic response of the wing, which is predominantly constituted by the out-of-plane deflection. This is a result of the specific angles of attack that are considered (see Tab. 5.2), for which the lift-to-drag ratio is around 35 based on Xfoil (Drela, 1989) calculations, and the wing chord is still approximately aligned with the freestream, meaning that the lift force contributes much more effectively to the out-of-plane deflection. Both effects combined mean that the lift force contributes approximately 400 times more than the drag force to the out-of-plane deflection at $\alpha = 5^\circ$, and about 200 times more at $\alpha = 10^\circ$.

Also for the characterization of the inertial force, only the dominant motion degree of freedom is considered, which is the deflection w of the wing in the direction perpendicular to the wing chord. In the same way as in Sec. 4.2.2, a simplified one-dimensional model of the wing with a single coordinate z along the span is considered for the inertial load determination, where the inertial force per unit span I' on the wing can be determined with Eq. (4.1) as the product of mass density and acceleration, which is calculated from the time series of reconstructed wing shapes using a second-order central finite difference scheme.

The elastic force, as the third relevant aeroelastic force in a dynamic aeroelastic interaction, can be determined from the equilibrium of the three forces acting on the wing, $E = -A - I$. When the sectional aerodynamic and inertial forces have been determined along the span, these two forces can therefore be used to calculate the shear force distribution along the span of the wing. In this chapter, the elastic force is determined only in an integral sense at the root of the wing, to perform a comparison of the non-intrusive measurements with force balance measurements. The force measurements that are obtained with a balance that is attached to the root of the wing, F_{root}, correspond to the reaction force to the (elastic) shear force, so that $F_{\text{root}} = -E$. In accordance with the discussion on the dominant aerodynamic and inertial force contributions, the dominant root force component in the wind tunnel reference system is the root force in the y-direction, which is determined by adding the y-components of the aerodynamic and inertial loads and integrating the sum along the span:

$$F_{\text{root},y}(t) = \int_0^s \left(L'(z,t) + I'(z,t)\cos\alpha\right) dz. \tag{5.1}$$

The sectional lift force acts perpendicular to the direction of the freestream and is aligned with the y-direction of the wind tunnel reference system, whereas the inertial force is determined by considering the out-of-plane deflection in the reference system of the wing. To obtain the integral force in the y-direction, this contribution is therefore reduced by a factor of $\cos\alpha$, where α is the geometric angle of attack of the wing.

5.3.2. WING SHAPE RECONSTRUCTION

After the LPT measurements of the surface markers on the wing are transformed into the wind tunnel coordinate system, the position measurements of the markers are used to determine the deformed shape of the wing. This is achieved by calculating an average local deflection $w(z)$ for each spanwise section where the markers are painted (i.e., the ribs of the wing) from the measurements and then fitting a polynomial curve through these measurements along the spanwise direction. Following this procedure, the polynomial curve fit can be used to approximate the reference spanwise axis to calculate the deformed wing shape. A fourth-order polynomial is used for the curve fit, which satisfies the geometric boundary conditions of the wing that is clamped at the root, $w(z=0) = 0$ and $\partial w/\partial z(z=0) = 0$, and is defined as:

$$w(z) = P_1 z^4 + P_2 z^3 + P_3 z^2, \tag{5.2}$$

where the coefficients P_1, P_2, and P_3 are optimized to provide the best fit to the experimental wing shape measurements in a least-squares sense.

The results of the polynomial curve fit to the measurements for the two test cases with steady inflow are shown in Fig. 5.9. The length of the polynomial curve is adjusted to match the undeformed shape by numerically integrating the length of the polynomial curve to determine the value of z_{tip} in the deformed case that corresponds to an arc length that is equal to the span s of the undeformed wing.

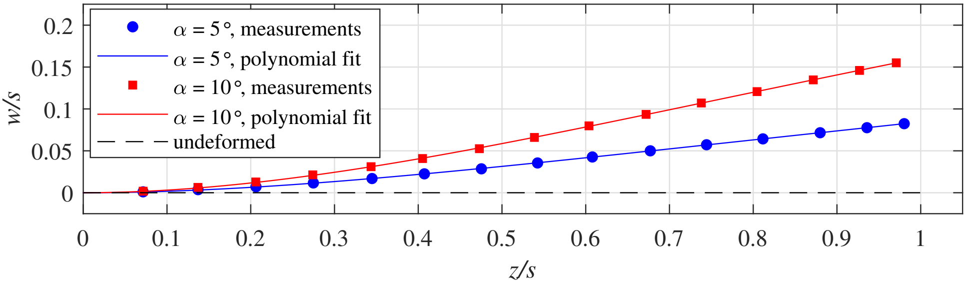

Figure 5.9: Deflection measurements in steady inflow with polynomial curve fit

The measurements of the marker positions that are shown in Fig. 5.9 are averaged from 1000 images acquired in the wind tunnel to reduce the effect of measurement noise and small-scale vibrations of the wing during the experiment. Furthermore, the deflection measurements obtained from the eight markers that are distributed along the chord on both sides of the wing are averaged to produce only one measurement data point per spanwise location. With this approach, the standard deviation of the residual between the 15 measurement data points along the span and the curve fit is $\sigma = 0.13\,\text{mm}$ for $\alpha = 5°$ and $\sigma = 0.25\,\text{mm}$ for $\alpha = 10°$, corresponding to less than 0.5% of the respective wingtip displacement.

To fully describe the deformed wing shape, the torsional deformation in terms of a twist angle θ of the wing around the reference axis is required as well. The twist angle can be estimated from the marker measurements with the average displacements of the marker measurements near the leading edge (LE) and the trailing edge (TE) as:

$$\theta(z) = \arctan\left(\frac{y_{TE}(z) - y_{LE}(z)}{x_{TE}(z) - x_{LE}(z)}\right). \tag{5.3}$$

The experimental wingtip twist angles that are found using Eq. (5.3) are below $\theta_{tip} < 0.4°$ for both α. Even though the magnitude of these values for the twist is not necessarily negligible in an aerodynamic sense, these values are considered negligible for the wing shape reconstruction, since the twist angle of the wing is of no direct interest for the experimental load determination that is performed in this study. Employing this assumption simplifies further analysis and avoids the influence of random measurement errors of the wing twist along the span on the wing shape reconstruction.

To reconstruct the dynamic response of the wing to the periodic unsteady inflow, the marker measurements obtained in these cases are processed in a similar way as for the steady inflow but now analyzed in a phase-averaged sense, which means that measurements from different periods are collected at the respective time expressed as a fraction of the period, t/T. To reduce the effect of random measurement noise and outliers that may result from light reflections in some of the acquired images, a temporal smoothing procedure using a sinusoidal curve fit is applied. The wing is expected to oscillate around the static deflected shape, the temporal smoothing is therefore performed after transforming the marker measurements per wing section into the reference system of the static deflected wing shape at the respective angle of attack. The displacement measurements in their local coordinate system and the corresponding sinusoidal fits are shown for two spanwise locations for both dynamic test cases in Fig. 5.10. For reference, the measured gust inflow is indicated in the figures as well.

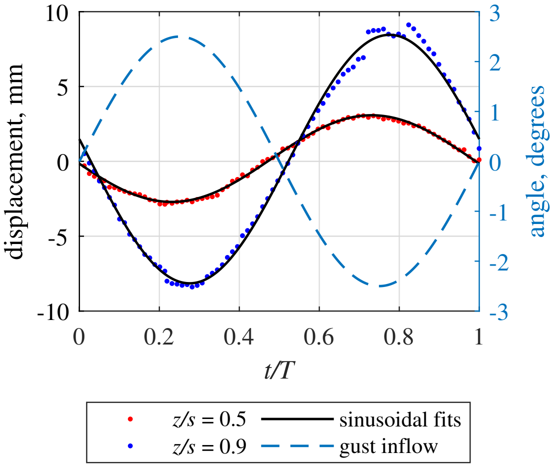

(a) $\alpha = 5°$ and $f_g = 5.7\,\mathrm{Hz}$

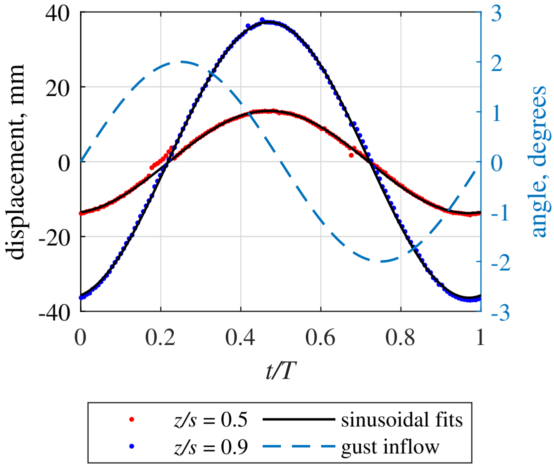

(b) $\alpha = 10°$ and $f_g = 3.2\,\mathrm{Hz}$

Figure 5.10: Measurements of the dynamic displacement increments with sinusoidal fits

With this approach, the sinusoidal curve fit provides a good approximation of the temporal behavior, with a standard deviation of the residual of the sinusoidal fit around $\sigma = 0.1\,\text{mm}$ for the $f_g = 5.7\,\text{Hz}$ gust at $\alpha = 5^\circ$ and $\sigma = 0.2\,\text{mm}$ for the $f_g = 3.2\,\text{Hz}$ gust at $\alpha = 10^\circ$. The twist angle of the wing varies between $0^\circ < \theta < 0.5^\circ$ in the first case and $0^\circ < \theta < 1^\circ$ in the second case, which is, as in the cases with steady inflow, considered sufficiently small to be neglected for the purpose of this study. After the phase-averaged marker measurements per spanwise location are determined based on the respective sinusoidal fits, the smoothed measurements are transformed back into the wind tunnel coordinate system and subsequently, the same polynomial curve fitting procedure as in the steady cases is applied for each phase instant of the dynamic response. The time series of the fitting coefficients obtained with this procedure allows the reconstruction of a smooth deformed wing shape variation over the entire period, yielding the phase-averaged behavior of the wing deformation in response to the gust. As an illustration, the reconstructed wing shapes at the phase instants with the minimum and maximum deflection are shown in Fig. 5.11 for the two dynamic test cases. The reconstructed wing shapes are used to compute the inertial loads acting on the wing along the span, to define the circulation integration contours for the lift determination from the flow field, and in the following for characterizing the dynamic wing response to the gust forcing.

The main features of the structural response of the wing to steady and unsteady inflow conditions, as determined based on the wing shape reconstructions, are summarized in Tab. 5.3. As expected, the higher geometric angle of attack produces larger deflections in steady inflow, with the wingtip deflection scaling nearly linearly with the angle of attack. On the other hand, the dynamic response to the two gusts is different in terms of both the deflection amplitude as well as the phase shift Φ that is calculated with respect to the gust arriving at the wing, despite the identical gust forcing amplitudes. These differences can be attributed to the different forcing frequencies of the gust with respect to the frequencies of the dynamic modes of the Delft-Pazy wing that were identified in the GVT (see Tab 5.1). The first gust frequency of $f_g = 5.7\,\text{Hz}$ is well above the first bending frequency of the wing, but clearly below the second bending and first torsion modal frequencies. As a result, the dynamic response of the wing is relatively small in amplitude, with a phase shift of nearly $\phi \approx \pi$ with respect to the gust forcing. For the second gust case, the gust frequency is identical to the frequency of the first bending mode, $f_g = 3.2\,\text{Hz}$. In this case, the dynamic response is observed to be much larger in amplitude and shifted in phase by around $\phi \approx 0.5\pi$. Overall, these observations are in close correspondence to the theoretical frequency response of a harmonically forced system (see Weaver Jr et al., 1991).

Table 5.3: Summary of the structural response of the wing to steady and unsteady inflow

geometric angle of attack	static tip deflection	gust frequency	dynamic tip deflection amplitude	phase shift to gust inflow
$\alpha = 5^\circ$	$w_{\text{tip}}/s = 8.5\%$	$f_g = 5.7\,\text{Hz}$	$w_{\text{tip,amp}}/s = 1.8\%$	$\phi = -0.95\pi$
$\alpha = 10^\circ$	$w_{\text{tip}}/s = 15.9\%$	$f_g = 3.2\,\text{Hz}$	$w_{\text{tip,amp}}/s = 8.2\%$	$\phi = 0.55\pi$

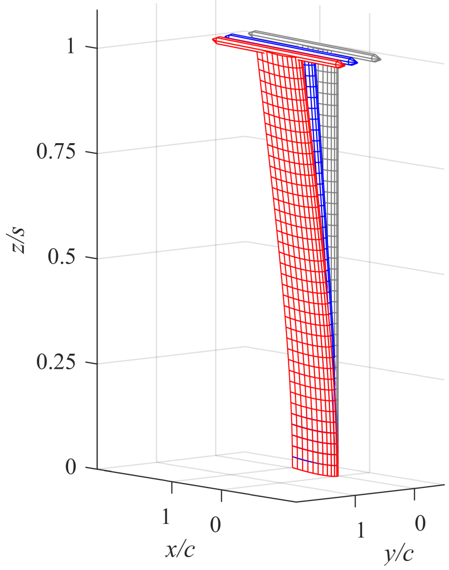

(a) $\alpha = 5°$ and $f_g = 5.7\,\mathrm{Hz}$

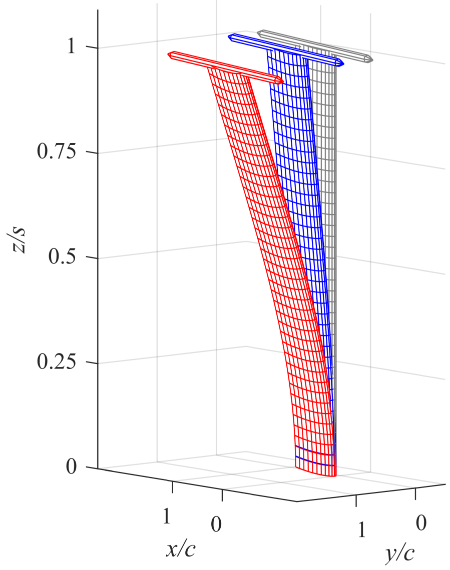

(b) $\alpha = 10°$ and $f_g = 3.2\,\mathrm{Hz}$

Figure 5.11: Wing shape reconstructions based on optical deflection measurements, red: maximum deflection, blue: minimum deflection, gray: undeformed reference

5.3.3. FLOW FIELD PROCESSING AND ANALYSIS

The particle tracks of the flow tracers obtained from the LPT analysis provide the time series of a large number of discrete measurements of the flow velocity, obtained in the measurement coordinates of the LPT system. These measurements are first transformed into the coordinate system of the wind tunnel (see Sec. 5.2.4). Subsequently, the measurements are ensemble-averaged onto a Cartesian grid. A Cartesian grid with a grid spacing of 3.75 mm is used, and an overlap of 75% is applied in the ensemble averaging. The three-dimensional flow field that results from this procedure is visualized in Fig. 5.12 for the test cases with steady inflow at $\alpha = 5°$ and $\alpha = 10°$. The plots show the marker-based reconstruction of the deformed wing shape together with the ensemble-averaged flow field, which is visualized in five slices along the span and with two isosurfaces of the streamwise velocity. It is evident in the flow visualizations that the increase in the angle of attack from $\alpha = 5°$ to $\alpha = 10°$ corresponds to enlarged areas of accelerated flow on the suction side (indicated by the red isosurface) and decelerated flow near the stagnation point on the pressure side of the wing (indicated by the blue isosurface). Furthermore, the formation of a region of decelerated flow near the trailing edge on the suction side of the wing is visible in Fig. 5.12(b), which is a result of the boundary layer that forms on the wing and increases in thickness with increasing α, thus having a stronger effect on the flow field at $\alpha = 10°$ than at $\alpha = 5°$. The flow fields for both angles of attack exhibit little spanwise variation, except for the regions in the vicinity of the wing root and tip, which could not be fully captured due to the size limitations of the LPT measurement volumes.

For the test cases with unsteady periodic inflow, the particle tracks from the LPT analysis are analyzed in a phase-averaged manner. The ensemble averaging is therefore performed for 25 temporal bins distributed over the period, each spanning a fraction of 4% of the respective period. For each subset of the LPT data that is collected in one temporal bin, the ensemble averaging is performed in the same way as for the test cases with steady inflow. The results of the flow data post-processing for the test cases with unsteady inflow are visualized in Figs. 5.13 and 5.14, where the phase-averaged flow field is shown together with the reconstructed wing section for four different phase instants at mid-span. The four plots in Fig. 5.13 show no appreciable variation in the location of the wing section over the period, but the flow fields exhibit a notable variation over the gust cycle, where the regions of accelerated and decelerated flow are enlarged at $t/T = 0.25$ and reduced at $t/T = 0.75$ when compared to the flow fields at $t/T = 0$ and $t/T = 0.5$, which appear as similar. These effects can be directly linked to the sinusoidal gust inflow and explained with linear aerodynamics theory. The observations for the flow fields shown in Fig. 5.14 are different; while the location of the wing section varies more than in Fig. 5.13 due to the different gust frequency, the flow fields, in this case, remain nearly unchanged over the period. The explanation for this difference between the aerodynamic response of the wing to the two gusts is twofold. Firstly, the geometric angle of attack of $\alpha = 10°$ for the second gust is outside of the linear lift regime, while the flow on the wing is still mostly attached. This means that at this particular angle of attack, the lift is less sensitive to changes in α, and changes in the inflow angle do not translate directly into enlarged regions of acceleration and deceleration around the wing. Secondly, the influence of the wing motion on the effective inflow angle that is experienced by the wing differs between the two gusts, due to the differences in the structural response.

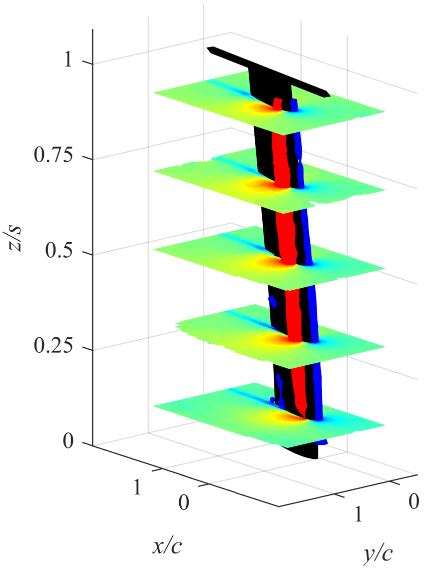

(a) $\alpha = 5°$

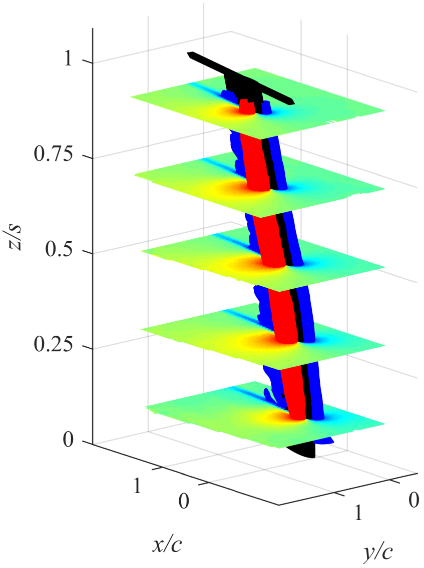

(b) $\alpha = 10°$

Figure 5.12: Reconstructed Wing shape with five slices of the streamwise velocity field and isosurfaces of the streamwise velocity (blue: $0.75U_\infty$, red: $1.25U_\infty$)

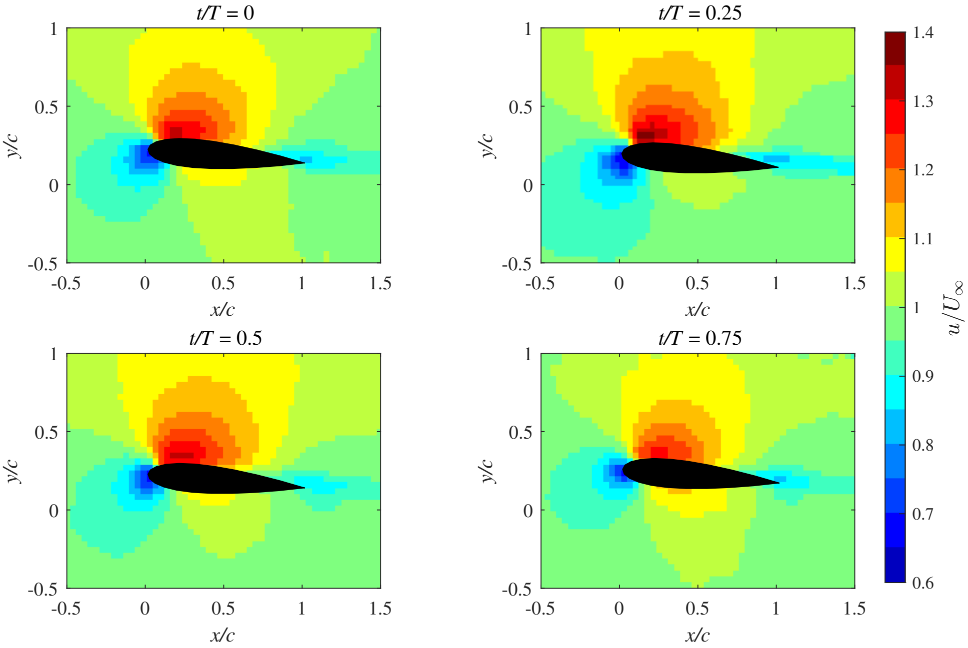

Figure 5.13: Ensemble-averaged streamwise velocity fields at $z/s = 0.5$ at $\alpha = 5°$ for the gust with $f_g = 5.7\,\text{Hz}$

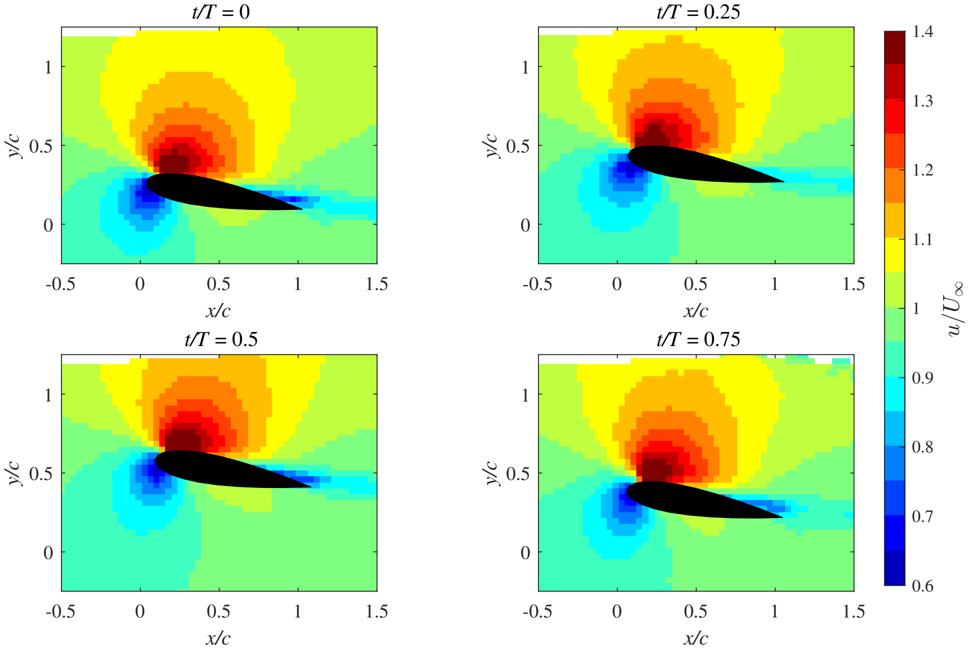

Figure 5.14: Ensemble-averaged streamwise velocity fields at $z/s = 0.5$ at $\alpha = 10°$ for the gust with $f_g = 3.2\,\text{Hz}$

The effective inflow angle is calculated as

$$\alpha_e(z,t) = \alpha + \alpha_g(t) + \alpha_v(z,t), \tag{5.4}$$

where α is the geometric angle of attack of the wing, α_g is the inflow angle of the gust, and α_v is the inflow angle induced by the motion of the wing:

$$\alpha_v(z,t) = -\arctan\left(\dot{w}(z,t)\cos\alpha / U_\infty\right). \tag{5.5}$$

The different contributions to the effective inflow angles are shown in Fig. 5.15 for the two dynamic test cases.

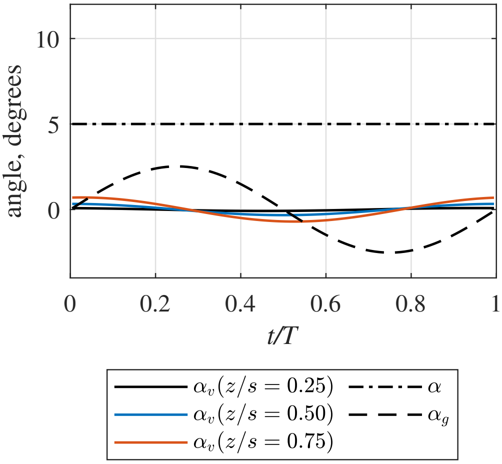

(a) $\alpha = 5°$ and $f_g = 5.7\,\mathrm{Hz}$

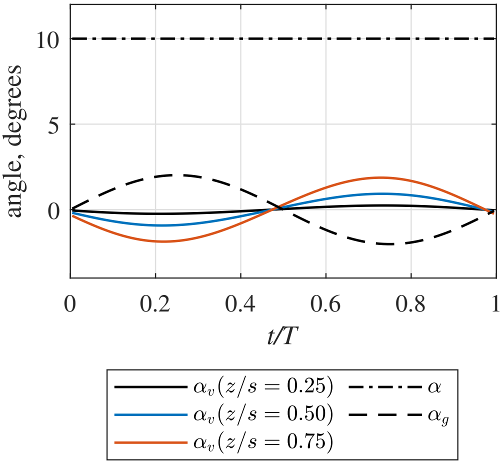

(b) $\alpha = 10°$ and $f_g = 3.2\,\mathrm{Hz}$

Figure 5.15: Separate contributions to the effective inflow angle for the two dynamic test cases

It can be observed that geometric angle α is constant, while the gust inflow angle α_g varies sinusoidally, as determined based on the measurements of the gust inflow. The inflow angles induced by the wing motion α_v are calculated from the transversal velocity $v_{\text{wing}} = \dot{w}(z,t)\cos\alpha$ of the reconstructed wing shapes at three different spanwise locations. The results for the effective inflow angles over the period for these three locations are shown in Fig. 5.16. In Fig. 5.16(a), it is visible that all curves are similar, implying that the influence of the wing motion on the inflow angle for the gust with $f_g = 5.7\,\text{Hz}$ is relatively small. The effects of the wing motion are a lag in the effective inflow with respect to the gust inflow ($|\Delta t/T| < 0.1$) and an increase in amplitude ($|\Delta\alpha_e| < 0.5°$) of the inflow angle towards the wingtip. For the gust with $f_g = 3.2\,\text{Hz}$, the effect of the wing motion on α_e is substantially larger, as visible in Fig. 5.16(b). In this case, the inflow angle induced by the wing motion α_v is in anti-phase with the gust inflow and large enough in amplitude to considerably reduce the variation in α_e and to invert the phase angle of the variation of α_e towards the wingtip. These differences in the behavior of the effective inflow angle between the two gusts are in direct correspondence to the different aerodynamic behavior shown in Fig. 5.13 and Fig. 5.14.

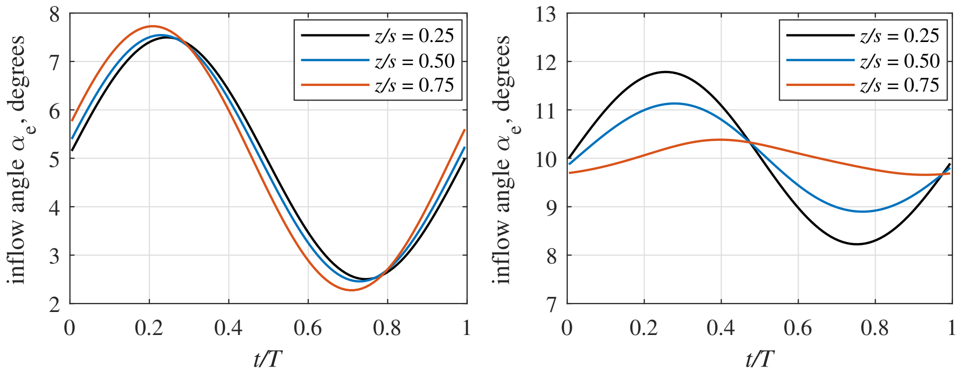

(a) $\alpha = 5°$ and $f_g = 5.7\,\text{Hz}$ (b) $\alpha = 10°$ and $f_g = 3.2\,\text{Hz}$

Figure 5.16: Effective inflow angles at different spanwise locations for the two dynamic test cases

5.3.4. FORCE BALANCE DATA PROCESSING

The balance data are acquired at a sampling rate of 100 Hz, simultaneously with the optical measurements, which means that there are four measurements for each test case with steady inflow, corresponding to the four different measurement volumes, and 20 separate measurements for each of the test cases with dynamic inflow (five acquisitions for each of the four measurement volumes). For the test cases with steady inflow, the balance measurements of the root force in the y-direction of the wind tunnel coordinate system from the different acquisitions are first averaged in time, and then the mean and standard deviation of the four acquisitions are calculated to be used as a reference for the non-intrusive loads.

For the dynamic test cases, the balance measurements are phase-averaged using 25 temporal bins, analogous to the phase-averaging procedure applied for the LPT data. The results from the phase-averaging of the root force measured with the balance are shown for both test cases in Fig. 5.17. The mean and the standard deviation of all 20 phase-averaged measurements are depicted as solid lines with error bars, while the individual measurements are plotted in shaded colors, corresponding to the respective test case. The root force measurements with the balance show little variation over the period for the dynamic inflow with $f = 5.7\,\text{Hz}$ at $\alpha = 5°$. For the dynamic inflow with $f = 3.2\,\text{Hz}$ at $\alpha = 10°$, the force shows a cosine-shaped variation over the period. Despite the phase-averaging that is applied to the individual measurements, the balance measurements still show a considerable variation between different acquisitions for the same test condition, with standard deviations of the root force around $\sigma = 0.6\,\text{N}$ in both test cases.

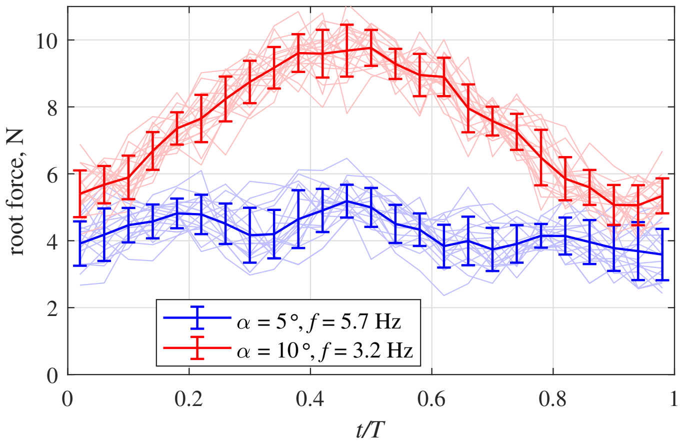

Figure 5.17: Phase-averaged root force in the y-direction measured with the balance for the dynamic test cases

5.3.5. INFRARED THERMOGRAPHY DATA ANALYSIS

The mapped and time-averaged thermographic images measured at eight angles of attack α are shown in Fig. 5.18. For $\alpha = 0°$, a region of increased surface temperature is present between $0.55 < x/c < 0.75$, which is relatively uniform along the span (the decrease in overall temperature for $y/s > 0.75$ can be attributed to the non-uniform external heating). The reduced convective heat transfer in this region can be explained by the presence of a laminar separation bubble, which is known to occur on the NACA 0018 airfoil in the considered Reynolds number regime (Gerakopulos et al., 2010). The main features of a laminar separation bubble are the laminar separation, transition within the separated shear layer, and turbulent reattachment. At $\alpha = 0°$, the spanwise variation of the sectional shape of the wing has little influence on the boundary layer flow and a spanwise relatively uniform laminar separation bubble is observed. With increasing α, the wing shape variations cause differences in the spanwise flow pattern. The main effect is a reduced surface temperature downstream of the leading edge between the rib locations. This can be explained when considering the distorted wing shape between the ribs, where the design shape is not preserved. The kink in the sectional wing shape causes the boundary layer to transition to turbulence, increasing the skin friction and thus the convective heat transfer when compared to a laminar boundary layer state. This effect sets in locally at individual spanwise locations at $\alpha = 2°$, it is established along all spanwise sections at $\alpha = 4°$, and further increases with increasing α. For very high values of α, the flow over the wing appears as fully turbulent at $\alpha = 12°$, before at $\alpha = 14°$ the wing stalls and flow separation effects cause an increased surface temperature at some sections of the span, in comparison to the turbulent attached flow.

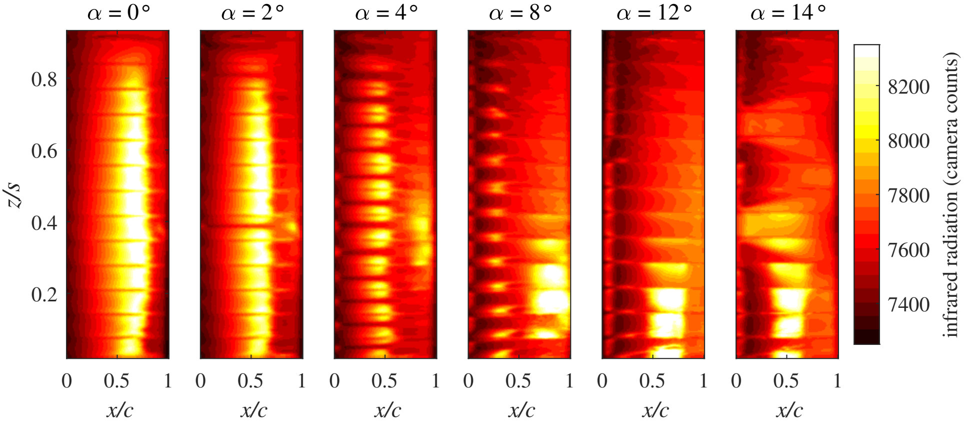

Figure 5.18: Infrared thermography images of the Delft-Pazy wing for $0° \leq \alpha \leq 14°$

The quantitative locations of the three characteristic features of a laminar separation bubble (separation, transition, reattachment) can be extracted from thermographic measurements by analyzing the chordwise temperature gradient (Grille Guerra et al., 2023). The procedure for this is illustrated in Fig. 5.19 for $\alpha = 4°$ at the two sections of the wing shown in Fig. 5.2, where section I corresponds to the center between two ribs and section II is on a rib, both approximately at mid-span. As the boundary layer thickness increases along the chord, the velocity gradient at the wall decreases. The skin friction is proportional to the velocity gradient and linked to the convective heat transfer through the Reynolds analogy (see Carlomagno and Cardone, 2010). Therefore, the surface temperature is generally increasing with x for a wing that is heated above the temperature of the freestream. However, a turbulent boundary layer produces significantly larger skin friction values compared to a laminar boundary layer at the same Re_x. When the transition occurs over a laminar separation bubble, the surface temperature is maximal inside the bubble, where the flow speed is lowest. The laminar-turbulent transition location is therefore considered to be the position of the minimum of the chordwise temperature gradient. When a separation bubble is present, the separation location can be determined as the position of the local maximum of the temperature gradient upstream of the transition location. When the flow reattaches, the chordwise temperature trend reverses from decreasing to increasing again. The reattachment location is therefore the position where the chordwise gradient becomes positive again (Grille Guerra et al., 2023).

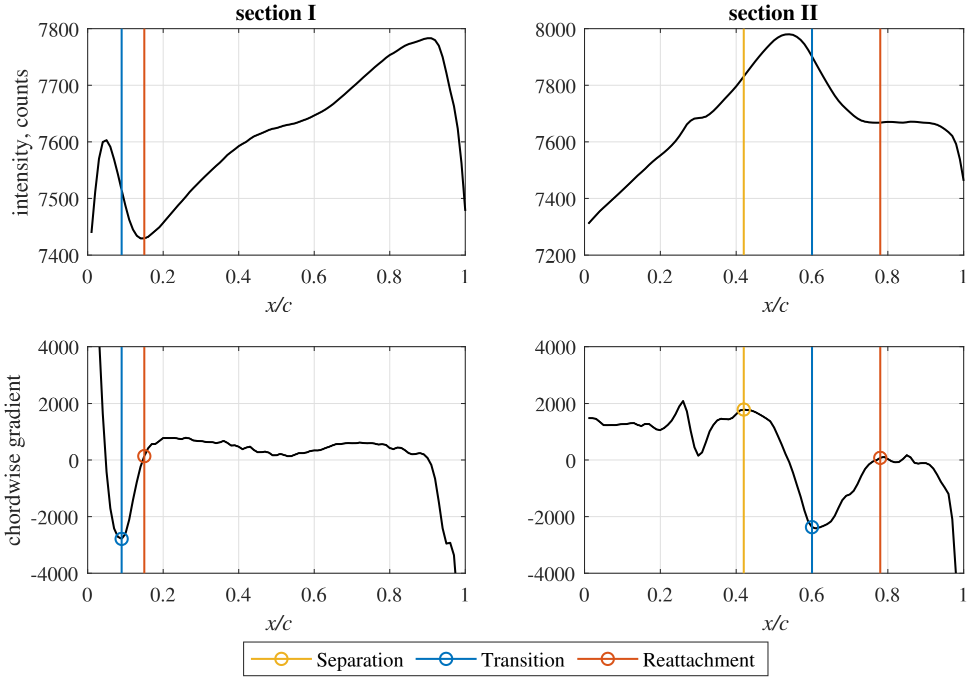

Figure 5.19: Infrared thermography-based boundary layer state detection, for steady inflow at $\alpha = 4°$ (the separation point for section I is near the leading edge and cannot be detected with the gradient-based method)

As observed in Fig. 5.19, the determination of the separation location with this approach fails when the transition occurs very close to the leading edge (section I), as there is no detectable local maximum of the gradient. It is, however, likely that the boundary layer separates due to the kink near the leading edge. The detection of the reattachment is problematic when the laminar separation bubble is located further downstream (section II) because the non-uniformity of the external heating causes a reduction in the temperature increase near the trailing edge. Due to the challenges with determining the separation and reattachment locations, the quantitative results of this study are limited to the transition location, x_{tr}.

5.4. RESULTS

5.4.1. STATIC AEROELASTIC CHARACTERIZATION

In steady flow conditions, the lift per unit span L' is determined from the time-averaged flow field measurements using the Kutta-Zhukovsky theorem and measurements of the circulation by line integration of the velocity field (Eq. (2.12) and Eq. (2.13)). Different rectangular integration contours with a distance d from the wing surface as a fraction of the chord length c varying between $d_{min}/c = 0.1$ and $d_{min}/c = 0.3$ in all four directions, as illustrated in Fig. 5.20, are used for each spanwise section of the wing.

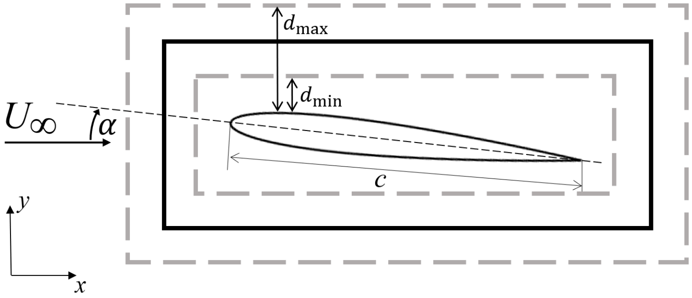

Figure 5.20: Wing section with an example rectangular integration contour (black) and the limits of the range of the different contours (gray dashed)

To illustrate the sensitivity of the lift to the position of the integration contour, the sectional lift in terms of the lift coefficient as determined when using different contours for the integration of the circulation for $\alpha = 5°$ at $z/s = 0.5$ is shown in Fig. 5.21(a). The 25 different integration contours that are considered are obtained by independently varying the distances d from the wing surface in 5 steps from $0.1c$ to $0.3c$ in the x- and y-directions, respectively. Overall, the variation of C_ℓ as a function of the circulation integration contour is small, with a standard deviation of $\sigma = 0.002$, corresponding to 0.5% of the lift coefficient in this case. The only consistent trend that is visible is a small increase of the lift for the largest contour in the y-direction. Because there is no physical explanation for this variation of the lift, this effect is likely to be caused by systematic measurement errors towards the edge of the measurement volume. Hence, a reference value for the lift, $C_{\ell,\mathrm{ref}}$, is computed as the average of the 16 integration contours in the range $0.1 < d/c < 0.25$. To further analyze the sensitivity of the lift to the properties of the experimental data, the effect of the particle concentration and the number of circulation integration contours used for averaging on the result for the lift coefficient is shown in Fig. 5.21(b). The particle concentration is varied by deleting particles from the original distribution, which has a concentration of $1278\,\mathrm{cm}^{-3}$ for the investigated section of the data set. The effect of averaging multiple integration contours is shown by using an increasing number of contours, between 1 and 16, for the averaging, selected at random from the range $0.1c < d < 0.25c$. The result is quantified in terms of the lift residual Δ_L, which is defined with respect to the reference lift coefficient:

$$\Delta_L = \frac{|C_\ell - C_{\ell,\mathrm{ref}}|}{C_{\ell,\mathrm{ref}}}. \tag{5.6}$$

The lift residual generally decreases with increasing the particle concentration and the number of integration contours, however, a consistent trend is observed mainly for the particle concentration, where the residual decreases by several orders of magnitude with an increasing number of particles. On the other hand, the difference between the lift result that is obtained using the largest amount of data (16 integration contours with particle concentration $1278\,\mathrm{cm}^{-3}$), which is $C_{\ell,\mathrm{ref}} = 0.408$, and the lift result from a much smaller amount of data (one integration contour with particle concentration $60\,\mathrm{cm}^{-3}$), which is $C_\ell = 0.414$, is relatively small at around 1.4%.

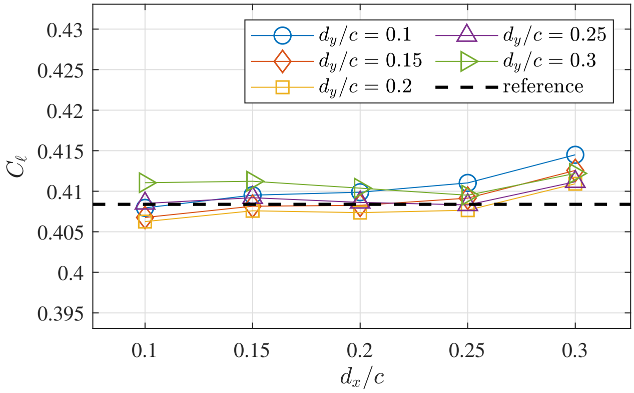

(a) lift coefficient for different circulation integration contours

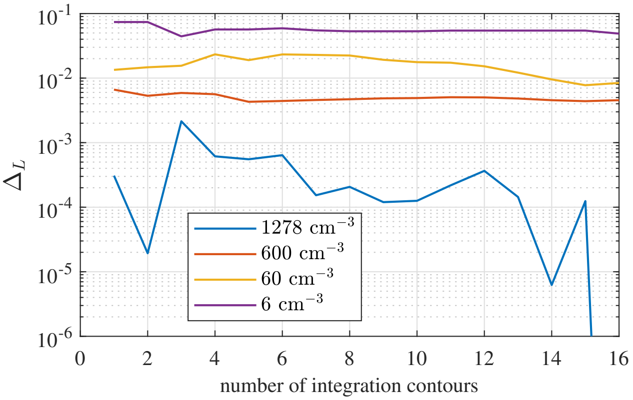

(b) residual over the number of contours and particle concentration

Figure 5.21: Sensitivity analysis of the lift coefficient to the integration contour and particle concentration

Following the sensitivity analysis of the sectional lift to the position of the integration contour, the sectional lift is determined as the average of the 16 circulation integration contours with the distances to the wing varying between $d_{min}/c = 0.1$ and $d_{max}/c = 0.25$ in all four directions, using all available particle data. This procedure is applied along the entire span. To obtain a smooth spanwise lift distribution, the results from all contours are averaged over a range of 5% of the span. The lift distributions for both α using this approach are shown in Fig. 5.22. As expected, the lift is generally higher for $\alpha = 10°$, but the two lift distributions are qualitatively similar. Both lift curves show a gradual drop of lift towards the tip, as expected from aerodynamics theory (see Anderson Jr., 2011). A small drop of lift towards the root is visible for $\alpha = 5°$ that can be associated with the presence of a boundary layer on the table on which the wing is mounted. The drop of lift towards the root is more pronounced for $\alpha = 10°$, which is likely caused by the strong deformations of the wing section shape near the root as the wing is bending, providing a less effective aerodynamic shape in this region of the wing.

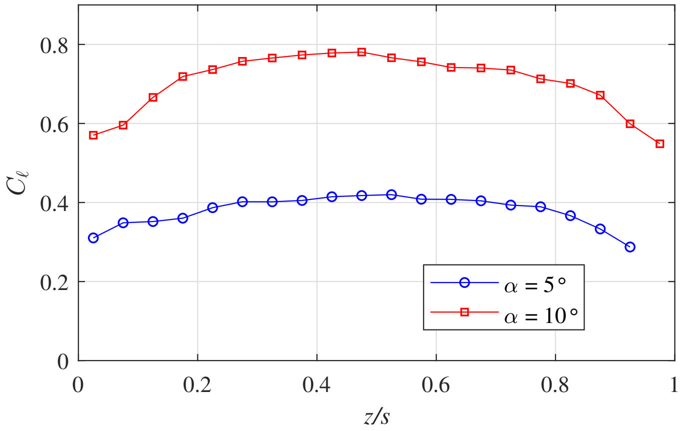

Figure 5.22: Spanwise lift distributions for the test cases with steady inflow

To perform a quantitative assessment of the results for the lift, the lift distributions for both α values are integrated along the span and compared to the measurements of the force at the root with the balance. The results of this comparison are shown in Tab. 5.4. The agreement of the root force values measured non-intrusively and with the balance is very good, with differences around 1% of the root force. These differences are in the same order of magnitude as the standard deviation of the balance measurements from different measurement acquisitions.

Table 5.4: Comparison of the root force measured with the integrated approach and the balance in steady inflow conditions

geometric angle of attack	root force (non-intrusive)	root force (balance)	relative difference $\Delta F_y / F_{y,\text{B}}$
$\alpha = 5°$	$F_y = 4.14\,\text{N}$	$F_{y,\text{B}} = 4.12\,\text{N} \pm 0.17\,\text{N}$	+0.6%
$\alpha = 10°$	$F_y = 7.77\,\text{N}$	$F_{y,\text{B}} = 7.64\,\text{N} \pm 0.10\,\text{N}$	+1.7%

The quantitative values of the boundary layer transition location along the span that are extracted from the infrared thermography measurements are shown in Fig. 5.23. The locations of the ribs of the Delft-Pazy wing are indicated as well. For all angles $\alpha \geq 4°$, it can be observed that the boundary layer transition to turbulence is triggered by the shape distortion of the wing between the ribs. The shape is preserved near the rib locations, where the transition occurs significantly further downstream. With increasing α and thus increasing adverse pressure gradients on the suction side of the wing, the transition location on the ribs moves gradually upstream. Furthermore, the spanwise extent of the region around the ribs where the transition is delayed reduces and the region where turbulent flow is triggered near the leading edge covers a larger fraction of the span width.

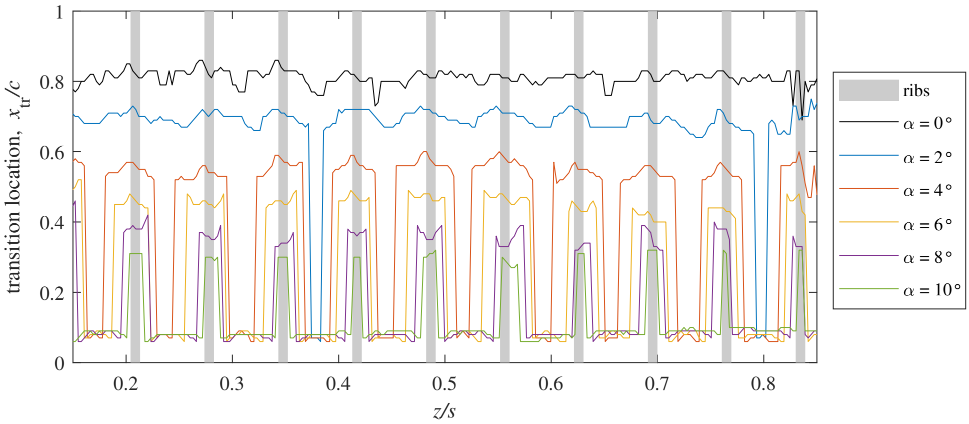

Figure 5.23: Boundary layer transition location along the span of the Delft-Pazy wing for $0° < \alpha < 10°$

5.4.2. DYNAMIC AEROELASTIC CHARACTERIZATION

For the test cases with dynamic inflow, the aerodynamic load is determined by using Eq. (3.10), with additional circulation integration contours to obtain the partial circulation along the chord. Apart from the inclusion of the additional unsteady term, the calculations of the lift distributions along the span for each phase instant of the dynamic cases follow the same procedure as in the static cases. The results for the lift distributions at four phase instants are shown for both dynamic test cases in Fig. 5.24. The standard deviations of the lift variation due to the choice of the integration contour have been assessed to be not significant, having typical values of less than 1% of the lift for both dynamic test cases.

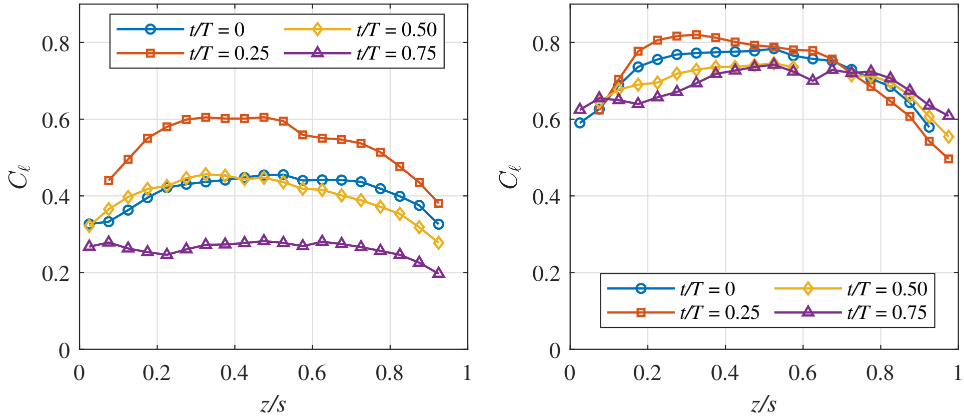

(a) $\alpha = 5°$ and $f_g = 5.7\,\text{Hz}$ (b) $\alpha = 10°$ and $f_g = 3.2\,\text{Hz}$

Figure 5.24: Spanwise lift distributions in dynamic inflow conditions for both test cases

As visible in Fig. 5.24(a), the four lift distributions along the span for the different phase instants are qualitatively similar for $\alpha = 5°$ and $f_g = 5.7\,\mathrm{Hz}$ but vary in lift magnitude. From the four phase instants that are shown, the highest lift occurs at $t/T = 0.25$ over the entire span width. In contrast, the spanwise lift distributions for $\alpha = 10°$ and $f_g = 3.2\,\mathrm{Hz}$ in Fig. 5.24(b) do not vary strongly in magnitude but exhibit qualitatively different behavior depending on the phase instant. It is visible that for $t/T = 0.25$, the maximum lift over the span occurs relatively close to the root at around $z/s = 0.3$, whereas for $t/T = 0.75$ the spanwise maximum of the lift is around $z/s = 0.75$.

Further analysis of the unsteady lift behavior is provided in Fig. 5.25, where the temporal behavior of the lift is shown for three spanwise locations of the wing for both dynamic test cases. Following the behavior of the spanwise lift distributions and the analysis of the effective inflow angles in Sec. 5.3.3, the temporal behavior of the lift for $\alpha = 5°$ and $f_g = 5.7\,\mathrm{Hz}$ is sinusoidal for each spanwise location. The effect of the unsteady lift terms on the temporal behavior of the lift is indicated in the plot as well. In this test case, the unsteady lift contribution due to the circulation in the wake is noticeable and causes a lag of the lift with respect to the quasi-steady lift due to the bound circulation. For the test case with $\alpha = 10°$ and $f_g = 3.2\,\mathrm{Hz}$ that is shown in Fig. 5.25(b), the temporal behavior of the lift is sinusoidal only near the root and shows less temporal variation for the outer part of the wing, which is in agreement with the analysis of the effective inflow angles (see Fig. 5.16(b)). In this case, the lift variation is smaller than in the other test case and further decreased compared to the analysis of the effective inflow angles due to the nonlinear lift behavior that occurs for the range of α_e of this test case. Furthermore, the gust frequency is lower, which leads to an overall decreased significance of the unsteady lift contributions, in particular for the outer part of the wing.

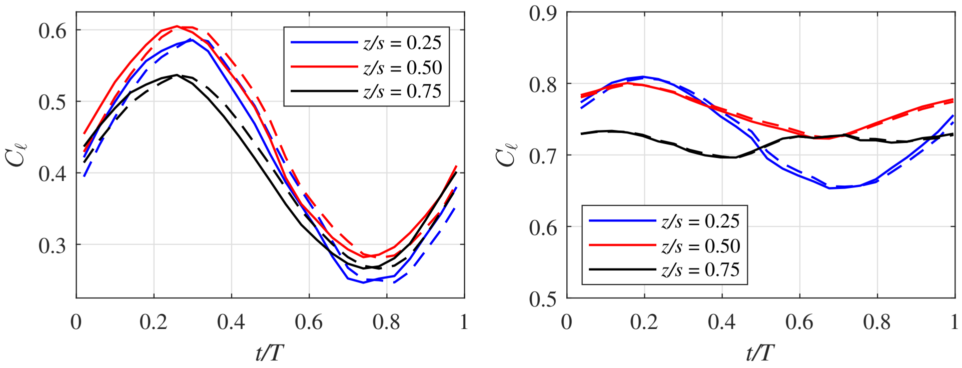

(a) $\alpha = 5°$ and $f_g = 5.7\,\mathrm{Hz}$ (b) $\alpha = 10°$ and $f_g = 3.2\,\mathrm{Hz}$

Figure 5.25: Unsteady lift (solid lines) and quasi-steady lift (dashed lines) over the period

For performing the comparison between the non-intrusive load measurements and the root force measured with the force balance, the lift distributions for both dynamic test cases are integrated along the span. The temporal variation of the spanwise-integrated lift force is shown for both test cases in Fig. 5.26. The variation of the lift is considerably larger for the gust with $f_g = 5.7\,\mathrm{Hz}$ at $\alpha = 5°$, with a peak-to-peak amplitude of almost

3 N, compared to less than 1 N for the gust with $f_g = 3.2$ Hz at $\alpha = 10°$. The analysis of the separate contributions of the unsteady and quasi-steady terms to the lift reveals that the unsteady terms cause a phase lag of the lift for the gust with $f_g = 5.7$ Hz of $\Delta t/T = 0.029$, compared to the quasi-steady lift. For the gust with $f_g = 3.2$ Hz, the contribution of the unsteady terms to the overall lift is always below 0.1 N and thus negligible.

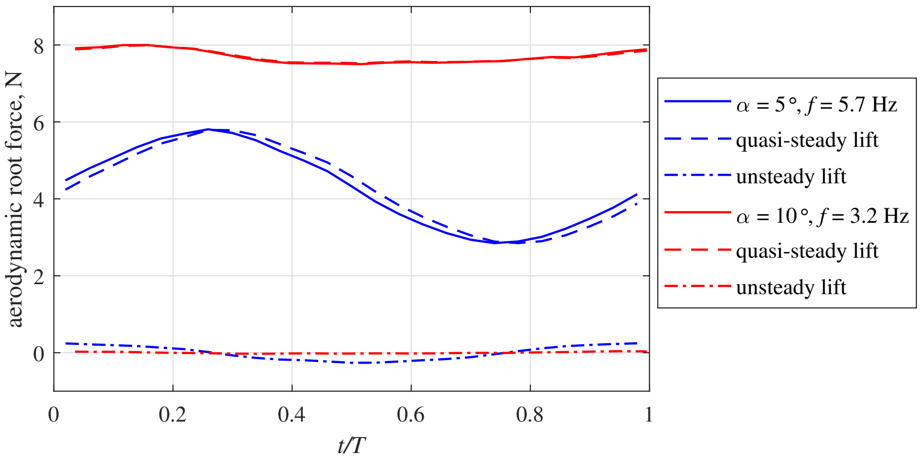

Figure 5.26: Root force over the period resulting from the aerodynamic load for both dynamic test cases

The inertial loads as determined from the time series of the wing shape reconstructions and Eq. (4.1) are shown in Fig. 5.27 for the two dynamic test cases. The plots show the variation of the sectional inertial force over the period at three spanwise locations. The temporal behavior of the inertial load is qualitatively identical along the span, with the load magnitude increasing as the dynamic deflection amplitude increases with the spanwise coordinate.

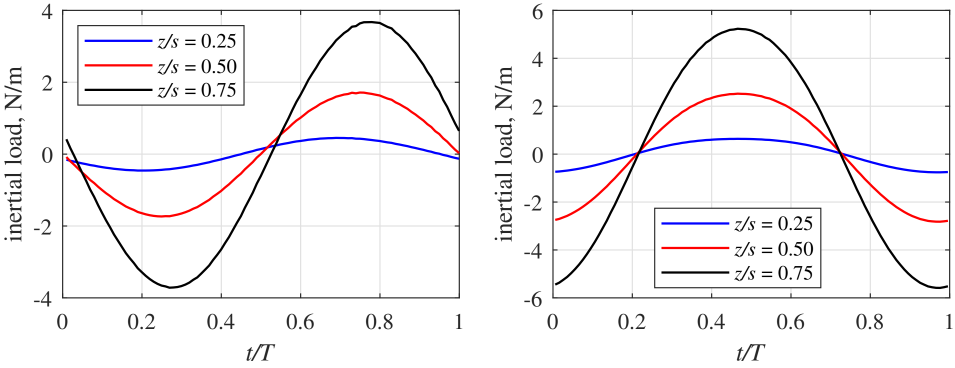

(a) $\alpha = 5°$ and $f_g = 5.7$ Hz (b) $\alpha = 10°$ and $f_g = 3.2$ Hz

Figure 5.27: Inertial loads at different spanwise locations for both dynamic test cases

As for the aerodynamic load, the inertial load is integrated along the span to validate the non-intrusive measurements with the force balance, as shown in Fig. 5.28. The magnitudes of the inertial force are similar for both test cases. When compared to the aerodynamic force, the amplitudes of the inertial force are significant; for the gust with $f_g = 5.7\,\mathrm{Hz}$ the amplitude of the inertial force is around 37% of the temporal mean of the aerodynamic force, and for the gust with $f_g = 3.2\,\mathrm{Hz}$ the inertial force amplitude is 29% of the aerodynamic force. The phase difference between the inertial force of the two cases is around a quarter of the period as a result of the phase lag differences in the wing dynamic response (see Tab. 5.3).

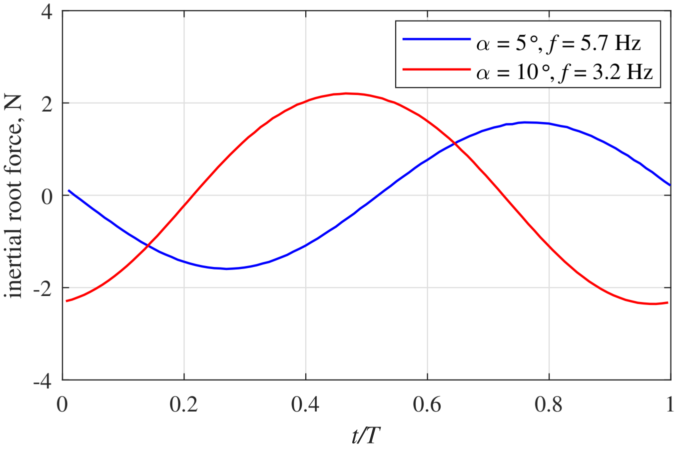

Figure 5.28: Root force over the period resulting from the inertial load for both dynamic test cases

The root forces obtained with the integrated measurement approach in terms of the aerodynamic force and the sum of aerodynamic and inertial forces according to Eq. (5.1) are compared to the force balance measurements for the two dynamic test cases in Fig. 5.29. The dynamic behavior clearly differs between the two test cases. In the first case (Fig. 5.29(a)), the inertial force nearly balances the dynamic variation of the aerodynamic force over the period, such that the root force is approximately constant. In the second case (Fig. 5.29(b)), a strong dynamic variation of the root force is observed, which is mainly contributed by the variation of the inertial force, whereas the aerodynamic force is approximately constant. A good agreement between the results from the integrated measurement approach and the force balance is observed in both dynamic test cases. The root mean square of the difference between the non-intrusive measurement and the force balance is 0.56 N for the gust with $f_g = 5.7\,\mathrm{Hz}$, which corresponds to 13.1% of the mean root force over the period measured with the force balance in this case. For the gust with $f_g = 3.2\,\mathrm{Hz}$, the root mean square difference between the measurements is 0.28 N, which corresponds to 3.8% of the mean root force measured with the balance. The differences between non-intrusive and balance measurements are mostly within the standard deviation of the balance measurements, indicated by the error bars.

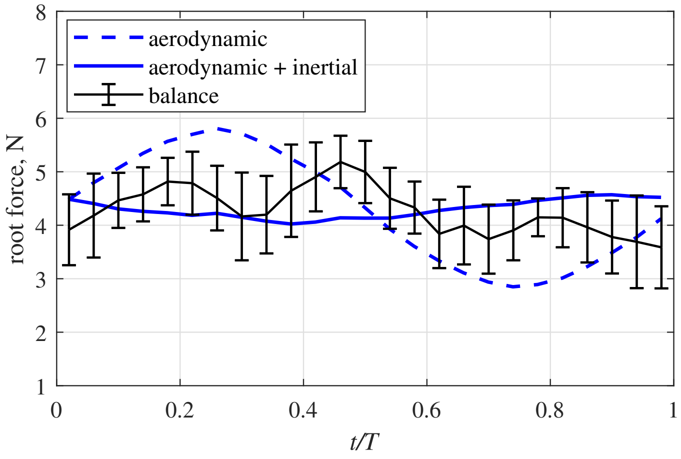

(a) $\alpha = 5°$ and $f_g = 5.7\,\mathrm{Hz}$

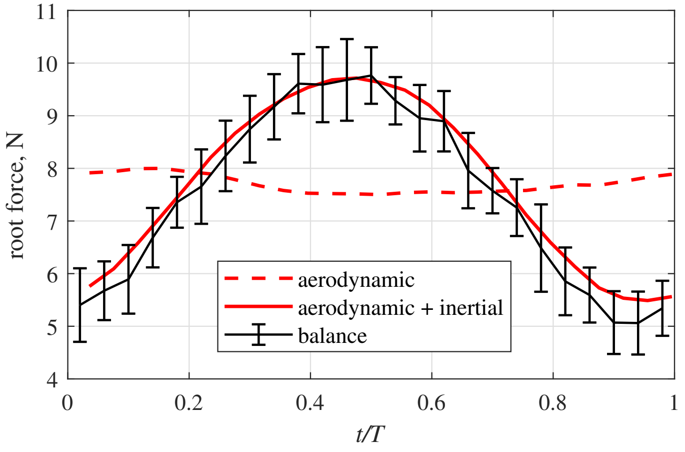

(b) $\alpha = 10°$ and $f_g = 3.2\,\mathrm{Hz}$

Figure 5.29: Comparison of the root forces measured non-intrusively and with the balance

The relatively larger differences between the force balance measurements and the non-intrusive measurements for the gust with $f_g = 5.7\,\mathrm{Hz}$ are presumed to be due to higher frequency contents of the structural response of the wing to the gust excitation. The higher frequency content of the structural response is not captured by the non-intrusive load measurements because the data are analyzed using a phase-averaging approach based on the gust excitation frequency. However, even in this case, the root mean square of the difference between the two measurements is smaller than the standard deviation of the balance measurements from different acquisitions of the same test condition, which is 0.6 N.

5.5. CONCLUDING REMARKS

In this chapter, the aeroelastic response of a highly flexible wing to steady and periodic unsteady inflow was determined experimentally in a wind tunnel test. The wing that was investigated is the Delft-Pazy wing, an adaptation of the Pazy aeroelastic benchmark wing to be tested at lower freestream velocities. Two static test cases with different angles of attack and two dynamic test cases with different gust frequencies were considered for measurements with the integrated optical measurement approach. These measurements were post-processed to obtain a reconstruction of the wing shape as well as the phase-averaged flow field. Additionally, infrared thermography measurements were conducted to gain insights into the boundary layer behavior of the wing.

After the post-processing of the optical measurements, the aerodynamic loads and, in the dynamic test cases, the inertial loads acting on the wing were determined through the application of physical models to the measured data. In the test cases with steady inflow, the obtained lift distributions were integrated along the span and compared to the reference measurements with a force balance, yielding excellent agreements with differences around 1%. The analysis of the lift distribution on the wing during the periodic gust encounter revealed that for small wing deflections, the lift variation is sinusoidal and can thus be directly linked to the gust forcing. For the dynamic test case with larger deflections, the temporal behavior of the lift varied depending on the spanwise location. The results of the analysis of the unsteady aerodynamic and inertial loads were compared to force balance measurements in terms of the force at the root of the wing, yielding differences between around 4% and 13%. A potential reason for these remaining differences is the phase-averaging approach, which was used in this study to merge information from different measurement volumes and thus inherently limits the temporal resolution of the measurement.

Based on the infrared thermography measurements, it could be observed that the aerodynamic performance of the Delft-Pazy wing differs significantly from the design shape. The construction method of using a thin shrinking foil as wing skin does not preserve the aerodynamic shape between the ribs of the wing, which causes a premature transition of the boundary layer to turbulence near the leading edge in those areas. These insights into the boundary layer behavior of the Delft-Pazy wing provide a reference data set that can be used for the validation of numerical aeroelastic simulation tools, in particular for those involving high-fidelity aerodynamic models that are capable of resolving the boundary layer flow. The comparison of the results from such high-fidelity models with the results from the optical measurement approach is desirable as well, specifically to compare the flow field and aerodynamic loads characteristics outside of the linear aerodynamic regime, where flow separation occurs. In the context of providing experimental reference data, the infrared measurements are therefore considered a valuable addition to the flow field measurements.

6

CONCLUSIONS AND OUTLOOK

In the final chapter of this thesis, conclusions are drawn based on the results and findings that were presented in the previous chapters and an outlook on the opportunities for future research related to this thesis is given. This chapter begins with a summary of the findings of the previous three chapters. Subsequently, the most important limitations of the developed measurement approach are discussed and some suggestions for improvement are provided. This thesis is concluded with a discussion of the future applications of the integrated optical measurement approach for aeroelastic characterization.

6.1. SUMMARY OF FINDINGS

The previous chapters have introduced a novel approach to performing an experimental aeroelastic characterization based on optical measurements. The main steps of the approach are the following: first, integrated measurements of the object under investigation and the flow around it are conducted. These measurements are implemented with high-speed cameras that acquire images of illuminated seeder particles in the flow and circular markers on the surface of the object. Subsequently, the acquired image data are processed and analyzed to obtain the volumetric flow velocity field and the structural displacements. For this, the images containing both structural markers and flow tracers are split up with data filtering operations that make use of the different time scales of the flow and the structural motion. After that, a Lagrangian particle tracking algorithm is used to determine the time-resolved position and velocity of the structural markers and the flow tracer particles, based on which the aeroelastic characterization can be realized.

In this thesis, the integrated measurement approach was first applied to a rigid, rectangular wing with a movable trailing edge flap. The measurements were conducted while the wing was undergoing a harmonic pitching motion. Two different test cases were considered; one test case where the trailing edge flap was fixed and one test case with an actuation of the trailing edge flap, which was designed to reduce the aerodynamic loads on the wing. Based on the performed measurements, the structural motion of the wing was determined in terms of the angle of attack and the flap deflection angle by fitting the marker measurements to a rigid body model of the wing using a regression. These measurements were compared to the motion that was imposed on the wing and the flap by the respective actuator mechanism to validate the method. The agreement that was obtained for the angle of attack during the pitching motion of the wing was very good, with differences around 0.03°. The differences to the reference were larger for the flap deflection angle but still considered satisfactory for validating the method. For the same two test cases, the aerodynamic loads in terms of the lift and the pitching moment were determined from the flow velocity field using physical models based on unsteady thin airfoil theory, employing the assumptions of potential flow. Two different load determination methods were applied, a pressure-based and a circulation-based approach, and the results were compared to the reference measurements that were acquired with surface pressure sensors. Both measurement approaches provided satisfactory results, with typical errors on the order of 0.01 coefficient counts for both lift and moment. Based on these results, the circulation-based approach was favored because its implementation is simpler than that of the pressure-based approach. In the pressure-based approach, the presence of the boundary layer on the suction side of the wing had to be accounted for with an additional data processing step that included an extrapolation procedure from the irrotational region of the flow field to the wing surface.

After demonstrating the measurement approach for the rigid body motion and unsteady aerodynamic loads of a pitching wing, the next step was the proof of concept study for a dynamic aeroelastic characterization, where all three forces in Collar's triangle were determined. This study was implemented by analyzing the loads on a section of a flexible wing that was subjected to a periodic gust. The aerodynamic loads were determined from the flow velocity field with the circulation-based approach and the structural forces were determined from the displacement measurements of the surface markers. To determine the inertial force, the time series of the wing displacement measurements was used to calculate the acceleration, which yielded the inertial load when multiplied by the mass of the wing section. The determination of the elastic force from the marker measurements was found to be more complex and was achieved by fitting a finite element beam model to the measurements. The use of this model was connected to strong assumptions about the structural properties and the external load distribution, which caused a relatively large uncertainty on the results for the elastic force. The physical agreement between the three determined forces (that should add up to zero) was found to be satisfactory, with a measurement residual on the order of 0.1 N, corresponding to about 10% of the considered reference force acting on the analyzed wing section that was estimated based on force balance measurements. This measurement residual was mainly accredited to the overestimation of the elastic force by the structural model, which was also observed in a comparison between the root loads from the finite element model and the force balance measurements. Nevertheless, meaningful results were obtained for all three forces in Collar's triangle, such that the proof of concept of an aeroelastic characterization was achieved.

In the next stage, the aeroelastic characterization approach was applied to analyze the gust response of a highly flexible wing. The design of this wing replicates the Pazy experimental benchmark wing that was developed to provide experimental reference data for the development of computational aeroelastic prediction methods. The measurements were conducted under two different gust conditions; the first gust condition was in the linear unsteady aerodynamic regime and the second gust condition was selected to produce aerodynamic and structural nonlinearities. The aeroelastic characterization was performed by determining the aerodynamic load from the measured flow fields and the inertial loads from the surface marker tracking data. In contrast to the proof of concept, the elastic loads were not determined using a finite element model, instead, they were calculated from the other two forces using the equilibrium of forces in Collar's triangle. Using force balance measurements as a reference, it was found that the accuracy of the aeroelastic characterization was about 13% for the first test case (linear unsteady aerodynamics regime) with a gust frequency between the first two eigenfrequencies of the wing, and below 4% for the second test case (nonlinear aeroelastic regime) with a gust excitation at the first eigenfrequency. The latter value is considered very good, even though the source of the remaining difference is not obvious, considering the long chain of data processing of the measurement approach. The reduced accuracy for the higher frequency case was presumed to result from higher frequency content in the aeroelastic response (from the higher order structural modes), which could not be captured experimentally due to the phase-averaging procedure that was employed. The occurrence of nonlinear aerodynamic effects, i.e. the onset of stall, on the other hand, was not found to be detrimental to the performance of the non-intrusive approach, as the second test case with the better accuracy was conducted at a higher geometric angle of attack that corresponded to the maximum lift angle. In addition to the measurements with the integrated optical approach, measurements with an infrared camera were conducted to characterize the boundary layer flow over the wing. It was found that the flexibility of the wing skin causes significant differences in the boundary flow pattern on the wing with respect to the design shape of the wing. These additional aerodynamic measurements are a valuable addition to the aeroelastic characterization results when a comparison between the experimental data and numerical simulation results is performed.

Overall, the presented results demonstrate that the research objective of developing an aeroelastic characterization approach based on integrated optical measurements was achieved successfully. The developed approach uses only a single, optical measurement system, which reduces the setup complexity and data processing efforts of aeroelastic wind tunnel experiments. After processing these measurements, relatively simple physical models can be used to determine all three forces in Collar's triangle in good agreement with reference data. While the physical models were first demonstrated on two simplified test cases, it was proven that the aeroelastic characterization approach can be used to conduct experimental research on challenging nonlinear aeroelastic problems by performing measurements on the gust response of a highly flexible wing.

6.2. CURRENT LIMITATIONS AND SUGGESTED IMPROVEMENTS

The main challenges in aeroelastic experiments from the measurement perspective are related to the scale of the test object. Aeroelastic experiments are typically performed at the largest possible scale that is permitted by the wind tunnel test facility because the simultaneous downscaling of all relevant aerodynamic and structural properties is difficult. For optical measurements of the flow, this is unfavorable due to the limitations of the experimental hardware, in particular the limited spatial resolution of the high-speed cameras, the limited power output of the illumination sources, and the limited seeding particle concentration. This problem is particularly relevant for the investigation of high aspect ratio wings, where the span width determines the scale of the wind tunnel setup, whereas the measurement scale that is most relevant for the aerodynamic behavior is the much smaller chord length. As a result of this complication, the analysis of the results in Ch. 5 had to be restricted to a phase-averaged analysis, because measurements from different volumes had to be conducted subsequently and then combined in post-processing. This means that the scale of the experimental model was effectively limiting the temporal resolution of the results.

The above limitations could be overcome with the use of improved hardware with respect to the equipment that was used in this thesis, for example with cameras that offer a significantly higher resolution and/or acquisition frequency. However, the availability of such equipment is currently not given on the market. Alternatively, a larger number of cameras and light sources could be used as well; however, this increases the complexity of the experimental setup and the requirements in terms of resources that are necessary to conduct the experiment. These are both hindering factors for the application of the proposed aeroelastic characterization approach. Instead, an interesting pathway to overcoming the challenges connected to the large range of relevant length scales of aeroelastic experiments is to complement the optical measurement approach with additional optical measurements using an infrared camera. Measurements with an infrared camera, which also require no model instrumentation, provide insights into the boundary layer state, which is an important parameter of the wing aerodynamics that cannot be analyzed with the large-scale flow field measurements because the boundary layer thickness is much smaller than the geometric scale of the wing. The infrared thermography measurement technique can thus be seen as a suitable complement to the integrated measurement approach for overcoming one of the challenges associated with the measurement scale.

While the preceding discussion was focused on the aerodynamic measurements, the limitations and possible advancements of the loads determination methods have to be discussed in the context of both structural (i.e., elastic and inertial) and aerodynamic loads. The inertial loads could be determined reliably from the surface marker measurements for various experimental conditions, using structural models of low complexity. Regarding the elastic loads, a main observation that was made based on the published literature and also within the proof of concept study in this thesis was that the inverse modeling approach using a structural model in combination with the surface marker measurements is an ill-suited approach to perform a load estimation. Furthermore, it cannot be expected that increasing the complexity of the finite element model (e.g. by using a shell model) would improve the accuracy of the results because the density and accuracy of the position measurements of the wing surface are not sufficient to model the structural behavior without employing further simplifying assumptions. This is an inherent feature of the optical measurement approach based on surface marker tracking that cannot be overcome without additional measurements using, for example, strain gauges. However, it is important to consider that the use of a higher fidelity structural model is essential when a determination of the stresses inside the structure is required. For such studies, it is therefore not recommended to attempt the determination of the elastic loads solely based on the marker measurements, but instead to use the aerodynamic and inertial loads that are obtained from the proposed approach and apply those as external loading to the structural model to obtain these quantities.

For the aerodynamic loads determination, the Navier-Stokes equations can be used in the future as a higher fidelity model for the determination of the pressure field and/or the integral forces from the flow field measurements. This could be useful to generalize the approach for flow situations that do not satisfy the assumptions made in unsteady potential flow theory, which was used in this thesis. The disadvantage of the Navier-Stokes equations is that their evaluation requires the determination of several spatial gradients of the flow field, which poses a more demanding requirement on the quality of the measurement, compared to the loads determination based on unsteady potential flow theory, which only requires the velocity field. This means that the accuracy of the aerodynamic loads that result from the application of the Navier-Stokes equations is more likely to suffer from the amplification of measurement errors and can therefore only be justified when it is clear that considered flow conditions disqualify the use of the simpler potential flow model. For the incompressible flow around wings, the flow region that is affected by the acting of viscosity is limited to the boundary layer. As long as the flow remains mostly attached, the flow field is mostly irrotational, which means the application of the potential flow model is justified. Some studies in the published literature have demonstrated that the Kutta-Zhukovsky theorem is suitable as a lift determination method based on flow field measurements, also for wings that have entered full stall (Olasek & Karczewski, 2021). The applicability of the loads determination methods based on unsteady thin airfoil theory in situations with dynamic flow separation is therefore suggested as a topic for future research.

6.3. FUTURE APPLICATIONS

Two different directions of research can be envisioned to benefit from the application of the aeroelastic characterization approach in the future. The first direction is the study of more fundamental problems in aeroelasticity, driven by the same motivation as in the study of the highly flexible benchmark wing in Ch. 5, which is providing experimental insights and reference data for the development of aeroelastic simulation models. An example of a possible future study in this research direction is the study of limit cycle oscillations. A number of experimental studies on limit cycle oscillations have been conducted in the past (e.g., Tang and Dowell, 2002b), in which a large majority of the measurements were carried out with conventional measurement tools. The use of these measurement tools was limiting the experimental insights that could be gained into, for example, the occurrence of stall. Such measurements, using accelerometers and a force balance, have also been performed on the limit cycle oscillation behavior of the Pazy wing at the Technion (see Drachinsky et al., 2022). Time-resolved, volumetric flow field measurements have, to the author's knowledge, so far never been conducted for a wing undergoing a limit cycle oscillation, meaning that the aeroelastic characterization approach could provide novel insights into the unsteady aerodynamic behavior during a limit cycle oscillation. The highly flexible Delft-Pazy wing presents itself as an interesting test case for such a study because the analysis of the limit cycle oscillations of the Pazy wing that was conducted by Drachinsky et al. (2022) suggests that aerodynamic stall was limiting the amplitude of the oscillations, without providing aerodynamic measurement data. These nonlinear effects could be quantified and their effect on the aeroelastic behavior could be analyzed in detail based on measurements with the integrated optical approach.

The second research direction is the research on novel aeroelastic technological concepts, in which the aeroelastic characterization approach could be used to support the advancement of the TRL. With the ongoing development of novel aircraft designs, as discussed in Ch. 1, such concepts are expected to emerge more regularly in the future. To advance from the concept stage in the laboratory (TRL 2 to 4) to the first implementation on a prototype (TRL 5 and higher), an aeroelastic concept needs to be subjected to wind tunnel testing, for which the developed aeroelastic characterization approach could be a valuable tool. One example of such a novel concept is the hinged folding wingtip in the context of civil aviation. In this context, the folding wingtip was first developed for the Boeing 777X series (Smith et al., 1995), to make use of the benefit for aerodynamic efficiency of a large aspect ratio wings (Anderson Jr., 2011) and still comply with aircraft size limitations on the ground at airports. More recently, Airbus proposed the concept of active aeroelastic wingtips that can be used for load alleviation purposes (Wilson et al., 2017). In this concept, the folding wingtip can be released in flight to reduce the peak loads on the wing structure during extreme load events, such as a gust encounter. The load alleviation potential of this approach has been demonstrated successfully in several preliminary studies, where, among others, the timing of the hinge release with respect to the gust encounter has been identified as an important performance parameter (Carrillo et al., 2022; Castrichini et al., 2016; Cheung et al., 2018, 2020). The integrated optical measurement approach is suitable for an experimental aeroelastic characterization study of this parameter in the wind tunnel.

BIBLIOGRAPHY

Abbott, I. H., Von Doenhoff, A. E., & Stivers Jr., L. S. (1945). *Summary of airfoil data* (tech. rep. No. 824). National Advisory Committee for Aeronautics. https://ntrs.nasa.gov/citations/19930090976

Adrian, R. J. (1991). Particle-imaging techniques for experimental fluid mechanics. *Annual Review of Fluid Mechanics*, *23*, 261–304. https://doi.org/10.1146/annurev.fl.23.010191.001401

Adrian, R. J. (2005). Twenty years of particle image velocimetry. *Experiments in Fluids*, *39*, 159–169. https://doi.org/10.1007/s00348-005-0991-7

Adrian, R. J., & Westerweel, J. (2011). *Particle Image Velocimetry*. Cambridge University Press.

Agüera, N., Cafiero, G., Astarita, T., & Discetti, S. (2016). Ensemble 3D PTV for high resolution turbulent statistics. *Measurement Science and Technology*, *27*, 124011. https://doi.org/10.1088/0957-0233/27/12/124011

Anderson Jr., J. D. (2011). *Fundamentals of Aerodynamics* (5th edition). McGraw-Hill.

Avin, O., Raveh, D. E., Drachinsky, A., Ben-Shmuel, Y., & Tur, M. (2022). Experimental aeroelastic benchmark of a very flexible wing. *AIAA Journal*, *60*(3), 1745–1768. https://doi.org/10.2514/1.J060621

Ballmann, J., Dafnis, A., Korsch, H., Buxel, C., Reimerdes, H. G., Brakhage, K. H., Olivier, H., Braun, C., Baars, A., & Boucke, A. (2008). Experimental analysis of high Reynolds number aero-structural dynamics in ETW. *46th AIAA Aerospace Sciences Meeting and Exhibit, 7 - 10 January 2008, Reno, Nevada, USA*. https://doi.org/10.2514/6.2008-841

Banks, J., Marimon Giovannetti, L., Soubeyran, X., Wright, A. M., Turnock, S. R., & Boyd, S. W. (2015). Assessment of digital image correlation as a method of obtaining deformations of a structure under fluid load. *Journal of Fluids and Structures*, *58*, 173–187. https://doi.org/10.1016/j.jfluidstructs.2015.08.007

Baqersad, J., Poozesh, P., Niezrecki, C., & Avitabile, P. (2017). Photogrammetry and optical methods in structural dynamics – a review. *Mechanical Systems and Signal Processing*, *86*, 17–34. https://doi.org/10.1016/j.ymssp.2016.02.011

Barlas, T. K., & van Kuik, G. A. M. (2010). Review of state of the art in smart rotor control research for wind turbines. *Progress in Aerospace Sciences*, *46*(1), 1–27. https://doi.org/10.1016/j.paerosci.2009.08.002

Barrows, D. A., Olson, L., Abrego, A., & Burner, A. W. (2011). Blade displacement measurements of the full-scale UH-60A airloads rotor. *29th AIAA Applied Aerodynamics Conference, 27 - 30 June 2011, Honolulu, Hawaii, USA*. https://doi.org/10.2514/6.2011-3655

Batchelor, G. K. (1967). *An Introduction to Fluid Dynamics*. Cambridge University Press.

Baur, T., & Könteger, J. (1999). PIV with high temporal resolution for the determination of local pressure reductions from coherent turbulence phenomena. *Proceedings of* *the 3rd International Workshop on PIV, 16 - 18 September 1999, Santa Barbara, California, USA*. https://www.yumpu.com/en/document/read/3642130/piv-with-high-temporal-resolution-for-the-determination-of-local-

Bazilevs, Y., Takizawa, K., & Tezduyar, T. E. (2013). *Computational fluid-structure interaction: Methods and applications*. John Wiley & Sons.

Bell, J., & Burner, A. W. (1998). Data fusion in wind tunnel testing - combined pressure paint and model deformation measurements. *20th AIAA Advanced Measurement and Ground Testing Technology Conference, 15 - 18 June 1998, Albuquerque, New Mexico, USA*. https://doi.org/10.2514/6.1998-2500

Bernhammer, L. O., De Breuker, R., & Karpel, M. (2017). Geometrically nonlinear structural modal analysis using fictitious masses. *AIAA Journal*, *55*(10), 3584–3593. https://doi.org/10.2514/1.J054787

Bisplinghoff, R. L., Ashley, H., & Halfman, R. L. (1955). *Aeroelasticity*. Addison–Wesley.

Black, J. T., Pitcher, N. A., Reeder, M. F., & Maple, R. C. (2010). Videogrammetry dynamics measurements of a lightweight flexible wing in a wind tunnel. *Journal of Aircraft*, *47*(1), 172–180. https://doi.org/10.2514/1.44545

Bosbach, J., Kühn, M., & Wagner, C. (2009). Large scale particle image velocimetry with helium filled soap bubbles. *Experiments in Fluids*, *46*, 539–547. https://doi.org/10.1007/s00348-008-0579-0

Brown, O. C., Mehta, R. D., & Cantwell, B. J. (1997). Low-speed flow studies using the pressure sensitive paint technique. *AGARD Conference for Advanced Aerodynamic Measurement Technology, 22- 25 September 1997, Seattle, Washington, USA*. https://ntrs.nasa.gov/citations/19980204016

Burner, A. W., Lokos, W. A., & Barrows, D. A. (2003). In-flight aeroelastic measurement technique development. *Proceedings SPIE 5191, Optical diagnostics for Fluids, Solids, and Combustion II , 10 November 2003, San Diego, California, USA*, *5191*, 186–199. https://doi.org/10.1117/12.504157

Caridi, G. C. A., Ragni, D., Sciacchitano, A., & Scarano, F. (2016). HFSB-seeding for large-scale tomographic PIV in wind tunnels. *Experiments in Fluids*, *57*, 190. https://doi.org/10.1007/s00348-016-2277-7

Carlomagno, G. M., & Cardone, G. (2010). Infrared thermography for convective heat transfer measurements. *Experiments in Fluids*, *49*, 1187–1218. https://doi.org/10.1007/s00348-010-0912-2

Carrillo, X., Mertens, C., Sciacchitano, A., van Oudheusden, B. W., De Breuker, R., & Sodja, J. (2022). Wing stiffness and hinge release threshold effects on folding wingtip gust load alleviation. *AIAA SciTech Forum, 3 - 7 January 2022, San Diego, California, USA and Online*. https://doi.org/10.2514/6.2022-1559

Castrichini, A., Hodigere Siddaramaiah, V., Calderon, D., Cooper, J. E., Wilson, T., & Lemmens, Y. (2016). Nonlinear folding wing tips for gust loads alleviation. *Journal of Aircraft*, *53*(5), 1391–1399. https://doi.org/10.2514/1.C033474

Cheung, R. C., Rezgui, D., Cooper, J. E., & Wilson, T. (2018). Testing of a hinged wingtip device for gust loads alleviation. *Journal of Aircraft*, *55*(5), 2050–2067. https://doi.org/10.2514/1.C034811

Cheung, R. C., Rezgui, D., Cooper, J. E., & Wilson, T. (2020). Testing of folding wingtip for gust load alleviation of flexible high-aspect-ratio wing. *Journal of Aircraft*, *57*(5), 876–888. https://doi.org/10.2514/1.C035732

Chin, D. D., & Lentink, D. (2019). Fluid moment and force measurement based on control surface integration. *Experiments in Fluids*, *61*, 18. https://doi.org/10.1007/s00348-019-2838-7

Collar, A. R. (1946). The expanding domain of aeroelasticity. *The Aeronautical Journal*, *50*(428), 613–636. https://doi.org/10.1017/S0368393100120358

D'Aguanno, A., Quesada Allerhand, P., Schrijer, F. F. J., & van Oudheusden, B. W. (2023). Characterization of shock-induced panel flutter with simultaneous use of DIC and PIV. *Experiments in Fluids*, *64*, 15. https://doi.org/10.1007/s00348-022-03551-1

David, L., Jardin, T., & Farcy, A. (2009). On the non-intrusive evaluation of fluid forces with the momentum equation approach. *Measurement Science and Technology*, *20*, 095401. https://doi.org/10.1088/0957-0233/20/9/095401

de Kat, R., & van Oudheusden, B. W. (2011). Instantaneous planar pressure determination from PIV in turbulent flow. *Experiments in Fluids*, *52*, 1089–1106. https://doi.org/10.1007/s00348-011-1237-5

DeVoria, A. C., Carr, Z. R., & Ringuette, M. J. (2014). On calculating forces from the flow field with application to experimental volume data. *Journal of Fluid Mechanics*, *749*, 297–319. https://doi.org/10.1017/jfm.2014.237

DeVoria, A. C., & Ringuette, M. J. (2013). On the flow generated on the leeward face of a rotating flat plate. *Experiments in Fluids*, *54*, 1495. https://doi.org/10.1007/s00348-013-1495-5

Dimitriadis, G. (2017). *Introduction to nonlinear aeroelasticity*. Wiley & Sons.

Drachinsky, A., Avin, O., Raveh, D. E., Ben-Shmuel, Y., & Tur, M. (2022). Flutter tests of the Pazy wing. *AIAA Journal*, *60*(9), 5414–5421. https://doi.org/10.2514/1.J061717

Drachinsky, A., & Raveh, D. E. (2020). Modal rotations: A modal-based method for large structural deformations of slender bodies. *AIAA Journal*, *58*(7), 3159–3173. https://doi.org/10.2514/1.J058899

Drela, M. (1989). XFOIL: An analysis and design system for low Reynolds number airfoils. In T. J. Mueller (Ed.), *Low Reynolds number aerodynamics. Lecture Notes in Engineering, Vol. 54*. Springer. https://doi.org/10.1007/978-3-642-84010-4_1

Elsinga, G. E., Scarano, F., Wieneke, B., & van Oudheusden, B. W. (2006). Tomographic particle image velocimetry. *Experiments in Fluids*, *41*, 933–947. https://doi.org/10.1007/s00348-006-0212-z

Engler Faleiros, D. (2021). *Soap bubbles for large-scale PIV: Generation, control and tracing accuracy* (Doctoral dissertation). Delft University of Technology. https://doi.org/10.4233/uuid:c579128f-9e96-4e9e-9997-6ce9486e1e25

Engler Faleiros, D., Tuinstra, M., Sciacchitano, A., & Scarano, F. (2019). Generation and control of helium-filled soap bubbles for PIV. *Experiments in Fluids*, *60*, 40. https://doi.org/10.1007/s00348-019-2687-4

Fernández Barrio, J., Mertens, C., Ragni, D., Schiacchitano, A., & van Oudheusden, B. W. (2020). Pressure based active load control of a blade in dynamic stall conditions.

Journal of Physics: Conference Series, *1618*. https://doi.org/10.1088/1742-6596/1618/2/022003

Fujisawa, N., Tanahashi, S., & Srinivas, K. (2005). Evaluation of pressure field and fluid forces on a circular cylinder with and without rotational oscillation using velocity data from PIV measurement. *Measurement Science and Technology*, *16*, 989–996. https://doi.org/10.1088/0957-0233/16/4/011

Gerakopulos, R., Boutilier, M., & Yarusevych, S. (2010). Aerodynamic characterization of a NACA 0018 airfoil at low Reynolds numbers. *40th Fluid Dynamics Conference and Exhibit, 28 June - 1 July 2010, Chicago, Illinois, USA*. https://doi.org/10.2514/6.2010-4629

Gharali, K., & Johnson, D. A. (2014). PIV-based load investigation in dynamic stall for different reduced frequencies. *Experiments in Fluids*, *55*, 1803. https://doi.org/10.1007/s00348-014-1803-8

Gherlone, M., Cerracchio, P., & Mattone, M. (2018). Shape sensing methods: Review and experimental comparison on a wing-shaped plate. *Progress in Aerospace Sciences*, *99*, 14–26. https://doi.org/10.1016/j.paerosci.2018.04.001

Gherlone, M., Cerracchio, P., Mattone, M., Di Sciuva, M., & Tessler, A. (2014). An inverse finite element method for beam shape sensing: Theoretical framework and experimental validation. *Smart Materials and Structures*, *23*(045027). https://doi.org/10.1088/0964-1726/23/4/045027

Goizueta, N., Wynn, A., Palacios, R., Drachinsky, A., & Raveh, D. E. (2022). Flutter predictions for very flexible wing wind tunnel test. *Journal of Aircraft*, *59*(4), 1082–1097. https://doi.org/10.2514/1.C036710

Grewe, V., Gangoli Rao, A., Grönstedt, T., Xisto, C., Linke, F., Melkert, J., Middel, J., Ohlenforst, B., Blakey, S., Christie, S., Matthes, S., & Dahlmann, K. (2021). Evaluating the climate impact of aviation emission scenarios towards the Paris agreement including COVID-19 effects. *Nature Communications*, *12*(1), 1–10. https://doi.org/10.1038/s41467-021-24091-y

Grille Guerra, A., Mertens, C., Little, J. C., & van Oudheusden, B. W. (2023). Experimental characterization of an unsteady laminar separation bubble on a pitching wing. *Experiments in Fluids*, *64*(1), 16. https://doi.org/10.1007/s00348-022-03564-w

Gurka, R., Liberzon, A., Hefetz, D., Rubinstein, D., & Shavit, U. (1999). Computation of pressure distribution using piv velocity data. *Proceedings of the 3rd International Workshop on PIV, 16 - 18 September 1999, Santa Barbara, California, USA*. http://www.openpiv.net/openpiv-pressure/files/PIV_99_paper_OCR.pdf

Ha, N. S., Vang, H. M., & Goo, N. S. (2015). Modal analysis using digital image correlation technique: An application to artificial wing mimicking beetle's hind wing. *Experimental Mechanics*, *55*, 989–998. https://doi.org/10.1007/s11340-015-9987-2

Haigermoser, C. (2009). Application of an acoustic analogy to piv data from rectangular cavity flows. *Experiments in Fluids*, *47*, 145–157. https://doi.org/10.1007/s00348-009-0642-5

Héder, M. (2017). From NASA to EU: The evolution of the TRL scale in Public Sector Innovation. *The Innovation Journal*, *22*(2), 3. https://www.innovation.cc/discussion-papers/2017_22_2_3_heder_nasa-to-eu-trl-scale.pdf

Heinold, M., & Kähler, C. J. (2018). Aerodynamic investigation of the free flapping flight of a Saker falcon with the help of 3D multi-view reconstruction method. *AIAA Aviation Forum, 25 - 29 June 2018, Atlanta, Georgia, USA*. https://doi.org/10.2514/6.2018-3173

Helfrick, M. N., Niezrecki, C., Avitabile, P., & Schmidt, T. (2011). 3D digital image correlation methods for full-field vibration measurement. *Mechanical Systems and Signal Processing*, *25*(3), 917–927. https://doi.org/10.1016/j.ymssp.2010.08.013

Hilger, J., & Ritter, M. R. (2021). Nonlinear aeroelastic simulations and stability analysis of the pazy wing aeroelastic benchmark. *Aerospace*, *8*(10), 308. https://doi.org/10.3390/aerospace8100308

Hodges, D. H., & Pierce, G. A. (2011). *Introduction to structural dynamics and aeroelasticity* (2nd Edition). Cambridge University Press.

Hoffman, J. D., & Frankel, S. (2018). *Numerical methods for engineers and scientists*. CRC press.

Imai, M., Nakakita, K., & Kameda, M. (2022). Random-dot pressure-sensitive paint for time-resolved measurement of deformation and surface pressure of transonic wing flutter. *Experiments in Fluids*, *63*, 174. https://doi.org/10.1007/s00348-022-03527-1

Jaworski, J. W., & Dowell, E. H. (2009). Comparison of theoretical structural models with experiment for a high-aspect-ratio aeroelastic wing. *Journal of Aircraft*, *46*(2), 708–713. https://doi.org/10.2514/1.39244

Jux, C., Sciacchitano, A., & Scarano, F. (2020). Flow pressure evaluation on generic surfaces by robotic volumetric PTV. *Measurement Science and Technology*, *31*, 104001. https://doi.org/10.1088/1361-6501/ab8f46

Jux, C., Sciacchitano, A., Schneiders, J. F. G., & Scarano, F. (2018). Robotic volumetric PIV of a full-scale cyclist. *Experiments in Fluids*, *59*, 74. https://doi.org/10.1007/s00348-018-2524-1

Kantor, E., Raveh, D. E., & Cavallaro, R. (2019). Nonlinear structural, nonlinear aerodynamic model for static aeroelastic problems. *AIAA Journal*, *57*(5), 2158–2170. https://doi.org/10.2514/1.J057309

Katz, J., & Plotkin, A. (2001). *Low-speed aerodynamics* (2nd Edition). Cambridge University Press.

Klein, C., Engler, R. H., Henne, U., & Sachs, W. E. (2005). Application of pressure-sensitive paint for determination of the pressure field and calculation of the forces and moments of models in a wind tunnel. *Experiments in Fluids*, *39*, 475–483. https://doi.org/10.1007/s00348-005-1010-8

Kurtulus, D. F., Scarano, F., & David, L. (2006). Unsteady aerodynamic forces estimation on a square cylinder by TR-PIV. *Experiments in Fluids*, *42*, 185–196. https://doi.org/10.1007/s00348-006-0228-4

Lancelot, P. M. G. J., Sodja, J., Werter, N. P. M., & Breuker, R. D. (2017). Design and testing of a low subsonic wind tunnel gust generator. *Advances in aircraft and spacecraft science*, *4*(2), 125–144. https://doi.org/10.12989/aas.2017.4.2.125

Lee, D. S., Fahey, D. W., Skowron, A., Allen, M. R., Burkhardt, U., Chen, Q., Doherty, S. J., Freeman, S., Forster, P. M., Fuglestvedt, J., Gettelman, A., De Leon, R. R., Lim, L. L., Lund, M. T., Millar, R. J., Owen, B., Penner, J. E., Pitari, G., Prather, M. J., . . .

Wilcox, J. (2021). The contribution of global aviation to anthropogenic climate forcing for 2000 to 2018. *Atmospheric Environment*, *244*, 117834. https://doi.org/10.1016/j.atmosenv.2020.117834

Lee, T., & Su, Y. Y. (2012). Low Reynolds number airfoil aerodynamic loads determination via line integral of velocity obtained with particle image velocimetry. *Experiments in Fluids*, *53*, 1177–1190. https://doi.org/10.1007/s00348-012-1353-x

Leishman, J. G. (2006). *Principles of helicopter aerodynamics* (2nd Edition). Cambridge University Press.

Lind, A. H., Lefebvre, J. N., & Jones, A. R. (2014). Time-averaged aerodynamics of sharp and blunt trailing-edge static airfoils in reverse flow. *AIAA Journal*, *52*(12), 2751–2764. https://doi.org/10.2514/1.J052967

Liu, T., Barrows, D. A., Burner, A. W., & Rhew, R. D. (2002). Determining aerodynamic loads based on optical deformation measurements. *AIAA Journal*, *40*(6), 1105–1112. https://doi.org/10.2514/2.1759

Liu, T., Burner, A. W., Jones, T. W., & Barrows, D. A. (2012). Photogrammetric techniques for aerospace applications. *Progress in Aerospace Sciences*, *54*, 1–58. https://doi.org/10.1016/j.paerosci.2012.03.002

Liu, T., Montefort, J., Gregory, J., Palluconi, S., Crafton, J., & Fonov, S. (2011). Wing deformation measurements from pressure sensitive paint images using videogrammetry. *41st AIAA Fluid Dynamics Conference and Exhibit, 27 - 30 June 2011, Honolulu, Hawaii, USA*. https://doi.org/10.2514/6.2011-3725

Liu, T., Sullivan, J. P., Asai, K., Klein, C., & Egami, Y. (2005). *Pressure and temperature sensitive paints*. Springer.

Liu, X., & Katz, J. (2006). Instantaneous pressure and material acceleration measurements using a four-exposure PIV system. *Experiments in Fluids*, *41*, 227–240. https://doi.org/10.1007/s00348-006-0152-7

Maas, H. G., Gruen, A., & Papantoniou, D. (1993). Particle tracking velocimetry in three-dimensional flows: Part 1. Photogrammetric determination of particle coordinates. *Experiments in Fluids*, *15*, 133–146. https://doi.org/10.1007/BF00190953

Malik, N. A., Dracos, T., & Papantoniou, D. A. (1993). Particle tracking velocimetry in three-dimensional flows: Part 2. particle tracking. *Experiments in Fluids*, *15*, 279–294. https://doi.org/10.1007/BF00223406

Marimon Giovannetti, L. (2017). *Fluid structure interaction testing, modelling and development of passive adaptive composite foils* (Doctoral dissertation). University of Southampton. https://eprints.soton.ac.uk/412651/

Marimon Giovannetti, L., Banks, J., Turnock, S. R., & Boyd, S. W. (2017). Uncertainty assessment of coupled Digital Image Correlation and Particle Image Velocimetry for fluid-structure interaction wind tunnel experiments. *Journal of Fluids and Structures*, *68*, 125–140. https://doi.org/10.1016/j.jfluidstructs.2016.09.002

Martínez Gallar, B., van Oudheusden, B. W., Sciacchitano, A., & Karásek, M. (2019). Large-scale volumetric flow visualization of the unsteady wake of a flapping-wing micro air vehicle. *Experiments in Fluids*, *61*, 16. https://doi.org/10.1007/s00348-019-2854-7

McLachlan, B. G., Bell, J. H., Park, H., Kennelly, R. A., Schreiner, J. A., Smith, S. C., Strong, J. M., Gallery, J., & Gouterman, M. (1995). Pressure-sensitive paint measurements on a supersonic high-sweep oblique wing model. *Journal of Aircraft*, *32*(2), 217–227. https://doi.org/10.2514/3.56921

McLachlan, B. G., & Bell, J. H. (1995). Pressure-sensitive paint in aerodynamic testing. *Experimental thermal and fluid science*, *10*(4), 470–485. https://doi.org/10.1016/0894-1777(94)00123-P

Mitrotta, F. M. A., Sodja, J., & Sciacchitano, A. (2022). On the combined flow and structural measurements via robotic volumetric PTV. *Measurement Science and Technology*, *33*, 045201. https://doi.org/10.1088/1361-6501/ac41dd

Mohebbian, A., & Rival, D. E. (2012). Assessment of the derivative-moment transformation method for unsteady-load estimation. *Experiments in Fluids*, *53*, 319–330. https://doi.org/10.1007/s00348-012-1290-8

Murua, J., Palacios, R., & Graham, J. M. R. (2012). Applications of the unsteady vortex-lattice method in aircraft aeroelasticity and flight dynamics. *Progress in Aerospace Sciences*, *55*, 46–72. https://doi.org/10.1016/j.paerosci.2012.06.001

Nakakita, K., & Asai, K. (2002). Pressure sensitive paint application to a wing-body model in a hypersonic shock tunnel. *22nd AIAA Aerodynamic Measurement Technology and Ground Testing Conference, 24 - 26 June 2002, St. Louis, Missouri, USA*. https://doi.org/10.2514/6.2002-2911

Nishino, K., Kasagi, N., & Hirata, M. (1989). Three-dimensional particle tracking velocimetry based on automated digital image processing. *Journal of Fluids Engineering*, *111*(4), 384–391. https://doi.org/10.1115/1.3243657

Noca, F., Shiels, D., & Jeon, D. (1997). Measuring instantaneous fluid dynamic forces on bodies, using only velocity fields and their derivatives. *Journal of Fluids and Structures*, *11*(3), 345–350. https://doi.org/10.1006/jfls.1997.0081

Noca, F., Shiels, D., & Jeon, D. (1999). A comparison of methods for evaluating time-dependent fluid dynamic forces on bodies, using only velocity fields and their derivatives. *Journal of Fluids and Structures*, *13*(5), 551–578. https://doi.org/10.1006/jfls.1999.0219

Noll, T. E., Brown, J. M., Perez-Davis, M. E., Ishmael, S. D., Tiffany, G. C., & Gaier, M. (2004). *Investigation of the helios prototype aircraft mishap* (tech. rep.). NASA. https://www.nasa.gov/pdf/64317main_helios.pdf

North, D. D., Busan, R. C., & Howland, G. (2021). Design and fabrication of the LA-8 distributed electric propulsion vtol testbed. *AIAA SciTech Forum, 11 – 15 and 19 – 21 January 2021, Virtual Event*. https://doi.org/10.2514/6.2021-1188

Olasek, K., & Karczewski, M. (2021). Velocity data-based determination of airfoil characteristics with circulation and fluid momentum change methods, including a control surface size independence test. *Experiments in Fluids*, *62*, 108. https://doi.org/10.1007/s00348-021-03193-9

Pan, B. (2018). Digital image correlation for surface deformation measurement: Historical developments, recent advances and future goals. *Measurement Science and Technology*, *29*, 082001. https://doi.org/10.1088/1361-6501/aac55b

Paris Agreement, 2015, http://unfccc.int/resource/docs/2015/cop21/eng/l09r01.pdf

Pastor, M., Binda, M., & Harčarik, T. (2012). Modal assurance criterion. *Procedia Engineering*, *48*, 543–548. https://doi.org/10.1016/j.proeng.2012.09.551

Prasad, A. K. (2000). Stereoscopic particle image velocimetry. *Experiments in Fluids*, *29*, 103–116. https://doi.org/10.1007/s003480000143

Raffel, M., Willert, C. E., Scarano, F., Kähler, C. J., Wereley, S., & Kompenhans, J. (2018). *Particle image velocimetry: A practical guide* (3rd Edition). Springer. https://doi.org/10.1007/978-3-319-68852-7

Ragni, D., Ashok, A., van Oudheusden, B. W., & Scarano, F. (2009). Surface pressure and aerodynamic loads determination of a transonic airfoil based on particle image velocimetry. *Measurement Science and Technology*, *20*, 074005. https://doi.org/10.1088/0957-0233/20/7/074005

Rajpal, D., Mitrotta, F. M. A., Socci, C. A., Sodja, J., Kassapoglou, C., & De Breuker, R. (2021). Design and testing of aeroelastically tailored composite wing under fatigue and gust loading including effect of fatigue on aeroelastic performance. *Composite Structures*, *275*, 114373. https://doi.org/10.1016/j.compstruct.2021.114373

Riso, C., & Cesnik, C. E. (2022). Impact of low-order modeling on aeroelastic predictions for very flexible wings. *Journal of Aircraft*. https://doi.org/10.2514/1.C036869

Rival, D. E., & van Oudheusden, B. W. (2017). Load-estimation techniques for unsteady incompressible flows. *Experiments in Fluids*, *58*, 20. https://doi.org/10.1007/s00348-017-2304-3

Rommel, B. A., & Dodd, A. J. (1984). Practical considerations in aeroelastic design. *Proceedings of a Symposium on Recent Experiences in Multi-disciplinary Analysis and Optimization*. https://ntrs.nasa.gov/citations/19870002287

Roy, J. P., Liu, T., & Britcher, C. P. (2006). Extracting dynamic loads from optical deformation measurements. *47th AIAA/ASME/ASCE/AHS/ASC Structures, Structural Dynamics and Materials Conference, 01 - 04 May 2006, Newport, Rhode Island, USA*. https://doi.org/10.2514/6.2006-2187

Scarano, F. (2013). Tomographic PIV: Principles and practice. *Measurement Science and Technology*, *24*, 012001. https://doi.org/10.1088/0957-0233/24/1/012001

Scarano, F., Ghaemi, S., Caridi, G. C. A., Bosbach, J., Dierksheide, U., & Sciacchitano, A. (2015). On the use of helium-filled soap bubbles for large-scale tomographic PIV in wind tunnel experiments. *Experiments in Fluids*, *56*, 42. https://doi.org/10.1007/s00348-015-1909-7

Schairer, E. T., & Hand, L. A. (1999). Measurements of unsteady aeroelastic model deformation by stereo photogrammetry. *Journal of Aircraft*, *36*(6), 1033–1040. https://doi.org/10.2514/2.2545

Schanz, D., Gesemann, S., & Schröder, A. (2016). Shake-the-box: Lagrangian particle tracking at high particle image densities. *Experiments in Fluids*, *57*, 70. https://doi.org/10.1007/s00348-016-2157-1

Schanz, D., Gesemann, S., Schröder, A., Wieneke, B., & Novara, M. (2013). Non-uniform optical transfer functions in particle imaging: Calibration and application to tomographic reconstruction. *Measurement Science and Technology*, *24*, 024009. https://doi.org/10.1088/0957-0233/24/2/024009

Schneiders, J. F. G., Scarano, F., Jux, C., & Sciacchitano, A. (2018). Coaxial volumetric velocimetry. *Measurement Science and Technology*, *29*, 065201. https://doi.org/10.1088/1361-6501/aab07d

Schröder, A., & Schanz, D. (2023). 3D Lagrangian particle tracking in fluid mechanics. *Annual Review of Fluid Mechanics*, *55*, 511–540. https://doi.org/10.1146/annurev-fluid-031822-041721

Schröder, A., Schanz, D., Bosbach, J., Novara, M., Geisler, R., Agocs, J., & Kohl, A. (2022). Large-scale volumetric flow studies on transport of aerosol particles using a breathing human model with and without face protections. *Physics of Fluids*, *34*, 035133. https://doi.org/10.1063/5.0086383

Schütte, A., Hummel, D., & Hitzel, S. M. (2010). Numerical and experimental analyses of the vortical flow around the SACCON configuration. *28th AIAA Applied Aerodynamics Conference, 28 June - 01 July 2010, Chicago, Illinois, USA*. https://doi.org/10.2514/6.2010-4690

Sciacchitano, A., & Scarano, F. (2014). Elimination of PIV light reflections via a temporal high pass filter. *Measurement Science and Technology*, *25*, 084009. https://doi.org/10.1088/0957-0233/25/8/084009

Sharma, S. D., & Deshpande, P. J. (2012). Kutta–Joukowsky theorem in viscous and unsteady flow. *Experiments in Fluids*, *52*, 1581–1591. https://doi.org/10.1007/s00348-012-1276-6

Simão Ferreira, C. J., van Bussel, G. J. W., van Kuik, G. A. M., & Scarano, F. (2011). On the use of velocity data for load estimation of a VAWT in dynamic stall. *Journal of Solar Energy Engineering*, *133*, 011006. https://doi.org/10.1115/1.4003182

Smith, M. H., Renzelmann, M. E., & Marx, A. D. (1995). Folding wing-tip system (U.S. Patent No. 5381986A). https://worldwide.espacenet.com/patent/search?q=pn%3DUS5381986A

Sterenborg, J. J. H. M., Lindeboom, R. C. J., Simão Ferreira, C. J., van Zuijlen, A. H., & Bijl, H. (2014). Assessment of PIV-based unsteady load determination of an airfoil with actuated flap. *Journal of Fluids and Structures*, *45*, 79–95. https://doi.org/10.1016/j.jfluidstructs.2013.12.001

Sterenborg, J. J. H. M., van Zuijlen, A. H., & Bijl, H. (2014). Experimental benchmark of a free plunging wing with imposed flap oscillations. *Journal of Fluids and Structures*, *49*, 338–359. https://doi.org/10.1016/j.jfluidstructs.2014.05.001

Stodieck, O., Cooper, J., Neild, S., Lowenberg, M., & Iorga, L. (2018). Slender-wing beam reduction method for gradient-based aeroelastic design optimization. *AIAA Journal*, *56*(11), 4529–4545. https://doi.org/10.2514/1.J056952

Tang, D., & Dowell, E. H. (2001). Experimental and theoretical study on aeroelastic response of high-aspect-ratio wings. *AIAA journal*, *39*(8), 1430–1441. https://doi.org/10.2514/2.1484

Tang, D., & Dowell, E. H. (2002a). Experimental and theoretical study of gust response for high-aspect-ratio wing. *AIAA journal*, *40*(3), 419–429. https://doi.org/10.2514/2.1691

Tang, D., & Dowell, E. H. (2002b). Limit-cycle hysteresis response for a high-aspect-ratio wing model. *Journal of Aircraft*, *39*(5), 885–888. https://doi.org/10.2514/2.3009

Tang, D., & Dowell, E. H. (2016). Experimental aeroelastic models design and wind tunnel testing for correlation with new theory. *Aerospace*, *3*(2), 12. https://doi.org/10.3390/aerospace3020012

Tessler, A. (2007). Structural analysis methods for structural health management of future aerospace vehicles. *Key Engineering Materials*, *347*, 57–66. https://doi.org/10.4028/www.scientific.net/kem.347.57

Unal, M. F., Lin, J. C., & Rockwell, D. (1997). Force prediction by PIV imaging: A momentum-based approach. *Journal of Fluids and Structures*, *11*(8), 965–971. https://doi.org/10.1006/jfls.1997.0111

van Oudheusden, B. W. (2013). PIV-based pressure measurement. *Measurement Science and Technology*, *24*, 032001. https://doi.org/10.1088/0957-0233/24/3/032001

van Oudheusden, B. W., Scarano, F., Roosenboom, E. W. M., Casimiri, E. W. F., & Souverein, L. J. (2007). Evaluation of integral forces and pressure fields from planar velocimetry data for incompressible and compressible flows. *Experiments in Fluids*, *43*, 153–162. https://doi.org/10.1007/s00348-007-0261-y

Villegas, A., & Diez, F. J. (2014a). Evaluation of unsteady pressure fields and forces in rotating airfoils from time-resolved PIV. *Experiments in Fluids*, *55*, 1697. https://doi.org/10.1007/s00348-014-1697-5

Villegas, A., & Diez, F. J. (2014b). On the quasi-instantaneous aerodynamic load and pressure field measurements on turbines by non-intrusive PIV. *Renewable Energy*, *63*, 181–193. https://doi.org/10.1016/j.renene.2013.09.015

Walker, S. M., Thomas, A. L. R., & Taylor, G. K. (2009). Photogrammetric reconstruction of high-resolution surface topographies and deformable wing kinematics of tethered locusts and free-flying hoverflies. *Journal of the Royal Society Interface*, *6*(33), 351–366. https://doi.org/10.1098/rsif.2008.0245

Wang, J., Zhang, C., & Katz, J. (2019). GPU-based, parallel-line, omni-directional integration of measured pressure gradient field to obtain the 3d pressure distribution. *Experiments in Fluids*, *60*, 58. https://doi.org/10.1007/s00348-019-2700-y

Weaver Jr, W., Timoshenko, S. P., & Young, D. H. (1991). *Vibration problems in engineering*. John Wiley & Sons.

Westerweel, J., Elsinga, G. E., & Adrian, R. J. (2013). Particle image velocimetry for complex and turbulent flows. *Annual Review of Fluid Mechanics*, *45*, 409–436. https://doi.org/10.1146/annurev-fluid-120710-101204

White, F. M. (2006). *Viscous fluid flow* (3rd Edition). McGraw-Hill.

Wieneke, B. (2008). Volume self-calibration for 3D particle image velocimetry. *Experiments in Fluids*, *45*, 549–556. https://doi.org/10.1007/s00348-008-0521-5

Wieneke, B. (2012). Iterative reconstruction of volumetric particle distribution. *Measurement Science and Technology*, *24*, 024008. https://doi.org/10.1088/0957-0233/24/2/024008

Wilson, T., Herring, M., Pattinson, J., Cooper, J., Castrichini, A., Ajaj, R., & Dhoru, H. (2017). An Aircraft Wing With Moveable Wing Tip Device for Load Alleviation (International Patent No. WO2017118832A1). https://worldwide.espacenet.com/patent/search?q=pn%3DWO2017118832A1

Wolf, C. C., Schwarz, C., Kaufmann, K., Gardner, A. D., Michaelis, D., Bosbach, J., Schanz, D., & Schröder, A. (2019). Experimental study of secondary vortex structures in a rotor wake. *Experiments in Fluids*, *60*, 175. https://doi.org/10.1007/s00348-019-2807-1

Wu, J.-Z., Pan, Z.-L., & Lu, X.-Y. (2005). Unsteady fluid-dynamic force solely in terms of control-surface integral. *Physics of Fluids*, *17*, 098102. https://doi.org/10.1063/1.2055528

Wu, P., Ifju, P., & Stanford, B. (2010). Flapping wing structural deformation and thrust correlation study with flexible membrane wings. *AIAA Journal*, *48*(9), 2111–2122. https://doi.org/10.2514/1.J050310

Wu, Z., Cao, Y., & Ismail, M. (2019). Gust loads on aircraft. *The Aeronautical Journal*, *123*(1266), 1216–1274. https://doi.org/10.1017/aer.2019.48

Yorita, D., Henne, U., & Klein, C. (2017). Improvement of lifetime-based PSP technique for industrial wind tunnel tests. *55th AIAA Aerospace Sciences Meeting, 9 - 13 January 2017, Grapevine, Texas, USA*. https://doi.org/10.2514/6.2017-0703

Yuan, J., & Olinger, D. J. (2005). Ultrasonic lift measurement technique for flow-induced structural vibrations. *Journal of Aerospace Engineering*, *18*(2), 111–119. https://doi.org/10.1061/(asce)0893-1321(2005)18:2(111)

Zhang, P., Peterson, S. D., & Porfiri, M. (2019). Combined particle image velocimetry/digital image correlation for load estimation. *Experimental Thermal and Fluid Science*, *100*, 207–221. https://doi.org/10.1016/j.expthermflusci.2018.09.011

ACKNOWLEDGEMENTS

Remember to let her under your skin
Then you'll begin to make it
Better, better, better, ...

Paul McCartney

Just like any other Ph.D. thesis, this little book has only one name printed on the cover, and just like any other Ph.D. thesis, you would not be able to hold this book in your hands without a whole list of other people that took part in this work in one way or the other. I am grateful to these people for their contributions to my work and would like to acknowledge them here.

First and foremost, I want to acknowledge my team of supervisors, my promotor Bas and my co-promotors Andrea and Jurij. I am very grateful that you have allowed me to come up with and pursue many own ideas over the last four years. And when it happened that I went to far off track, you have kept the overview and brought me back smoothly. Whenever I needed your help or feedback, I could rely on receiving very sophisticated input in a timely and professional manner, which I appreciated a lot. I would like to express a distinct appreciation to Bas, for supporting the Arizona project, to Andrea for creating a friendly and valuable team environment with the large-scale PIV group, and to Jurij, for always keeping the doors open for me at the aeroelasticity group, which has helped me enormously on several occasions.

I would also like express my gratitude towards the external members of my graduation committee. Thank you very much for taking the time and effort to review my work, the valuable feedback, and for taking part in my Ph.D. defense ceremony.

During my Ph.D., I had the honor and pleasure to collaborate and exchange ideas with many experts and great researchers in the field. I have been very fortunate to conduct my research within the framework of the HOMER project and I would like to thank all participants of the project for the interesting discussions we had at the workshops and teleconferences. During the second half of my Ph.D., I have been extremely lucky to be introduced to the Large Deflection Working Group of the Third Aeroelastic Prediction Workshop. This cooperative platform for exchanging ideas and results has meant a great deal for my research and for me personally. It has been an absolute pleasure to interact with all members, but in particular, I would like to thank Markus Ritter from DLR as coordinator of the group for welcoming me so warmly, Daniella Raveh and Ariel Drachinsky from the Technion for sharing the Pazy wing drawings and the tips and tricks for building one myself, and Michael Fehrs from DLR and Pawel Chwalowski from NASA Langley for the fruitful collaboration on the boundary layer analysis.

My Ph.D. research would have likely turned out completely different if I had not had the opportunity to work with 7 young, bright minds as a supervisor of their M.Sc. thesis. Jorge, Tomás, Louis, José Luis, Xavier, Adrián, and Fabio, it has been a pleasure to work with you all and I have learned incredibly much from you. Special thanks go to Tomás and José Luis, whose results contributed directly to this thesis, and Jorge and Adrián for contributing their extraordinarily proficient assistance in the wind tunnel.

I would also like to acknowledge the technical and administrative support I have received from the aerodynamics staff in the HSL. As for many before me, and many coming after me, a Ph.D. cannot be successful here without the help of Colette, Peter, Frits, Dennis, Nico, and Henk-Jan. In terms of practical support, it is also important to mention the contribution provided by the coordinator of our Faculty Graduate School, Laurike, and its director Piero. Your efforts to improve the experience of Ph.D. candidates at our faculty together with the members (and my fellow alumni) of the Ph.D. council are highly appreciated.

I definitely cannot imagine how different my experience as a Ph.D. candidate would have been without all the Ph.D. colleagues at TU Delft. Thanks for having shared this journey, Adrián, Alberto, Alessandro, Alexander, Ata, Babak, Constantin, David, Edoardo, Firoozeh, Gabriel, Giulia, Giulio, Guanqun, Hasse, Haris, Ilda, Jane, Jordi, Kaisheng, Kherlen, Kushal, Luis, Luuk, Marina, Mengjie, Michele, Ming, Mohamad, Renzhi, Ruiying, Sagar, Sven, Thomas, Tiago, Tyler, Varun, Weibo, Wencan, Wouter, Xiaodong, Yi, Yu, and Zeno. There could have been no more convincing lesson on how valuable this community is than the Covid-19 pandemic, during which we all suddenly found ourselves without it. Unfortunately I did not manage to visit even a single conference together with any of you, and hopefully I can remain a single outlier in the history books of the Aerodynamics Ph.D.s at TU Delft with that.

Apart from the professional side, I would also like to acknowledge my friends who provided me with many fun moments and experiences during the last four years. I have a lot of good memories of amazing Karaoke nights, humiliating board game victories and defeats, countless beers, hundreds of kilometers of running and rowing, thousands of kilometers of cycling, and a good number of trips to Berlin, Hamburg, Munich, Dortmund, Cologne, Frankfurt, Sindelfingen, Vienna, Venice, Bruges, Thessaloniki, Playa del Carmen and last but not least of course the Veluwe. There is no point in listing any names here because those who are meant will know when they read this.

Of course this acknowledgement is not complete without expressing my warmest gratitude towards Alessia- you inspired me to begin this Ph.D., and towards Sofja- you inspired me to finish it. Last but not least, I would like to acknowledge my family, my parents Claudia and Heiko, and my brother Jan, you have been there for me during the entire journey that brought me here. Thank you.

Christoph Mertens
Delft, May 2023

CURRICULUM VITÆ

Christoph MERTENS

1992	Born in Hamburg, Germany

EDUCATION

2011–2016	B.Sc. in Aerospace Engineering Technische Universität Berlin
2016–2018	M.Sc. in Aerospace Engineering Delft University of Technology
2019–2023	Ph.D. in Aerospace Engineering Delft University of Technology

PROFESSIONAL EXPERIENCE

02/2015– 12/2015	Research Assistant The University of Arizona, Tucson, USA
07/2017– 12/2017	Technology Research Intern Airbus, Munich, Germany
03/2018– 11/2018	Research Assistant German Aerospace Center (DLR), Göttingen, Germany
Since 2023	Research and Development Engineer Netherlands Aerospace Center (NLR), Amsterdam, The Netherlands

LIST OF PUBLICATIONS

JOURNAL ARTICLES

7. Carrillo Córcoles, X., **Mertens, C.**, Sciacchitano, A., van Oudheusden, B. W., De Breuker, R. and Sodja, J. (2023) Effect of Wing Stiffness and Folding Wingtip Release Threshold on Gust Loads. *In press at* Journal of Aircraft.

6. **Mertens, C.**, Costa Fernández, J. L., Sodja, J., Sciacchitano, A. and van Oudheusden, B. W. (2023) Nonintrusive Experimental Aeroelastic Analysis of a Highly Flexible Wing. *In press at* AIAA Journal.

5. Grille Guerra, A., **Mertens, C.**, Little, J. C. and van Oudheusden, B. W. (2023) Experimental characterization of an unsteady laminar separation bubble on a pitching wing. Experiments in Fluids **64(1)**:16.

4. **Mertens, C.**, de Rojas Cordero, T., Sodja, J., Sciacchitano, A. and van Oudheusden, B. W. (2022) Aeroelastic Characterization of a Flexible Wing Using Particle Tracking Velocimetry Measurements. AIAA Journal **60(1)**:276-286.

3. **Mertens, C.**, Sciacchitano, A., van Oudheusden, B. W. and Sodja, J. (2021) An integrated measurement approach for the determination of the aerodynamic loads and structural motion for unsteady airfoils. Journal of Fluids and Structures **103**:103293.

2. **Mertens, C.**, Wolf, C. C., Gardner, A. D., Schrijer, F. F. J. and van Oudheusden, B. W. (2020) Advanced infrared thermography data analysis for unsteady boundary layer transition detection. Measurement Science and Technology **31(1)**:015301.

1. Wolf, C. C., **Mertens, C.**, Gardner, A. D., Dollinger, C. and Fischer, A. (2019) Optimization of differential infrared thermography for unsteady boundary layer transition measurement. Experiments in Fluids **60(1)**:19.

CONFERENCE PAPERS AND PROCEEDINGS

14. Ritter, M. R., Fehrs, M. and **Mertens, C.** (2023) Aerodynamic and Static Coupling Simulations of the Pazy Wing with Transitional CFD for the Third Aeroelastic Prediction Workshop. *AIAA SciTech Forum*, 23-27 January 2022, National Harbor, Maryland, USA and Virtual.

13. **Mertens, C.**, Grille Guerra, A., van Oudheusden, B. W., Fehrs, M. and Ritter, M. R. (2022) Analysis of the Boundary Layer on a Highly Flexible Wing based on Infrared Thermography Measurements. *23rd STAB/DGLR Symposium*, 9-10 November 2022, Berlin, Germany.

12. Grille Guerra, A., **Mertens, C.**, Little, J. C. and van Oudheusden, B. W. (2022) Investigation of the Unsteady Behaviour of a Laminar Separation Bubble Using Infrared Thermography. *20th International Symposium on Application of Laser and Imaging Techniques to Fluid Mechanics*, 11-14 July 2022, Lisbon, Portugal.

11. Fehrs, M., Ritter, M. R., Helm, S. and **Mertens, C.** (2022) CFD Simulations of the Pazy Wing in Support of the Third Aeroelastic Prediction Workshop. *International Forum on Aeroelasticity and Structural Dynamics*, 13-17 June 2022, Madrid, Spain.

10. **Mertens, C.**, Costa Fernández, J. L., Sodja, J., Sciacchitano, A. and van Oudheusden, B. W. (2022) Integrated Aeroelastic Measurements of the Periodic Gust Response of a Highly Flexible Wing. *International Forum on Aeroelasticity and Structural Dynamics*, 13-17 June 2022, Madrid, Spain.

9. Carrillo Córcoles, X., **Mertens, C.**, Sciacchitano, A., van Oudheusden, B. W., De Breuker, R. and Sodja, J. (2022) Wing Stiffness and Hinge Release Threshold Effects on Folding Wingtip Gust Load Alleviation. *AIAA SciTech Forum*, 3-7 January 2022, Virtual Event and San Diego, California, USA.

8. **Mertens, C.**, Sodja, J., Sciacchitano, A. and van Oudheusden, B. W. (2022) Experimental Aeroelastic Characterization of a Very Flexible Wing in Steady and Unsteady Inflow. *AIAA SciTech Forum*, 3-7 January 2022, Virtual Event and San Diego, California, USA.

7. **Mertens, C.**, Costa Fernández, J. L., Sciacchitano, A., van Oudheusden, B. W. and Sodja, J. (2021) Gridless Determination of Aerodynamic Loads Using Lagrangian Particle Tracks. *14th International Symposium on Particle Image Velocimetry*, 1-5 August 2021, Virtual Event.

6. **Mertens, C.**, de Rojas Cordero, T., Sodja, J., Sciacchitano, A. and van Oudheusden, B. W. (2021) Determination of Collar's Triangle of Forces on a Flexible Wing based on Particle Tracking Velocimetry Measurements. *AIAA SciTech Forum*, 11-15 and 19–21 January 2021, Virtual Event.

5. Fernández Barrio, J., **Mertens, C.**, Ragni, D., Sciacchitano, A. and van Oudheusden, B. W. (2020) Pressure based active load control of a blade in dynamic stall conditions. *TORQUE 2020 Conference*, 28 September – 2 October 2020, Virtual Event.
   Published in: Journal of Physics: Conference Series (2020) **1618**:022003

4. **Mertens, C.**, Sciacchitano, A., van Oudheusden, B. W. and Sodja, J. (2020) Non-intrusive determination of the unsteady surface pressure and aerodynamic loads on a pitching airfoil. *10th EASN International Conference*, 2–4 September 2020, Virtual Event.
   Published in: IOP Conference Series Materials Science and Engineering (2021) **1024**:012051

3. **Mertens, C.**, Wolf, C. C. and Gardner, A. D. (2018) Unsteady Boundary Layer Transition Detection with Local Infrared Thermography. *21st STAB/DGLR Symposium*, 6–7 November 2018, Darmstadt, Germany.
   Published in: New Results in Numerical and Experimental Fluid Mechanics XII (2020)

2. Wolf, C. C., **Mertens, C.**, Gardner, A. D., Dollinger, C. and Fischer, A. (2018) Optimisation of differential infrared thermography for unsteady boundary layer transition measurement. *44th European Rotorcraft Forum*, 18–21 September 2018, Delft, The Netherlands.

1. **Mertens, C.**, Pineda, S., Agate, M., Little, J. C., Fasel, H. F., and Gross, A. (2016) Effects of Structural Motion on the Aerodynamics of the X-56A Airfoil. *AIAA SciTech Forum*, 4–8 January 2016, San Diego, California, USA.